SCUOLA DI DOTTORATO
UNIVERSITÀ DEGLI STUDI DI MILANO-BICOCCA

Dipartimento di / Department of

Scienza dei Materiali

Dottorato di Ricerca in / PhD program Scienza e Nanotecnologia dei Materiali Ciclo / Cycle XXXVI

ADVANCES IN MOLECULAR DOPING OF N-TYPE ORGANIC SEMICONDUCTORS

Cognome / Surname Pallini Nome / Name Francesca

Matricola / Registration number 789707

Tutore / Tutor: Prof. Luca Beverina

Coordinatore / Coordinator: Prof. Francesco Montalenti

ANNO ACCADEMICO / ACADEMIC YEAR 2022-2023

Contents

Chapter 1

Introduction

The development of modern electronics was based on the use of inorganic semiconductors.[1] Despite the excellent performances of these materials, their energy-intensive and expensive processing and their mechanical rigidity make the use of inorganic semiconductor troublesome for large-area applications, particularly on flexible surfaces such as those required for wearable devices.[2] Interest in the so called plastic electronic has however grown massively in the last decades, especially with the expansion of nowadays technologies, consisting in a web of connected displays, sensors and devices called Internet of Things (IoT), for which cheap, abundant easily processable, printable and flexible materials are a requirement.[3,4] In this scenario, the intrinsic properties of organic semiconductors (OSC) i.e. mechanical flexibility, lightweight, solution processability, low cost and easy tunability of their optoelectronic properties via structural modification, paved the way for their use in these applications for which the established inorganic counterpart is less attractive.[5–7]

In analogy to the inorganic semiconductors field, the development of performing organic based optoelectronic devices requires control of the doping process as a fundamental tool to tune charge transport and energy level alignment with respect to metal contacts. Since the first controlled synthesis and doping with halogens of polyacetylene in 1977 by Heeger, Shirakawa and MacDiarmid,[8] many progresses have been made in the field and it was, for example, thanks to doping that Organic Light Emitting Diodes (OLED) reached the performance level required for industrialization.[9,10] Doping plays a role also in Organic Photovoltaics (OPVs)[11] and Organic Field Effect Transistors (OFETs)[12,13] and is crucial for Organic Thermoelectric Generators (OTEGs), that recently gained interest as a promising energy harvesting solution for low consumption self-powered electronics.[4] To reach a performance level suitable for the industrialization of this wider plethora of applications, both efficient electron-transporting (n-type) and hole transporting (p-type) materials are required. However, the poorer performances and air instability issues of n-type materials and dopants are still one of the main bottlenecks for the further development of OSCs based technology. More effort is thus required in the field.

Finding efficient semiconductor/dopant systems is however not an easy target. This is mainly due to the nature of the processes underlying OSCs doping, that make each host/dopant combination ruled by specific interactions. In this contest, unexplored, possibly general, and more efficient strategies are thus required to reach better performances, and this research work tries to move towards this goal. Before going into details, it is necessary to give an overview of the doping process in organic semiconductors. In this first Chapter, I will thus briefly describe the fundamental properties of organic semiconductors and the principles of doping processes, together with its main benefits in applications, and its main challenges. I will then explain in more details the specific challenges of doping n-type semiconductors with molecular dopant precursors like 4-(1,3-Dimethyl-2,3-dihydro-1H-benzimidazol-2-yl)-N,N-dimethylaniline, also known as N-DMBI-H.

1.1 Intrinsic OSC electrical properties

The figure of merit describing the electrical transport properties of a material is the electrical conductivity (σ), i.e., according to **equation 1.1**,[14] the capability of the material to conduct an electrical current (J, current per unit surface) under an electric field E:

$$J = \sigma E \tag{1.1}$$

σ can be defined as[6]

$$\sigma = ne\mu \tag{1.2}$$

where n is the charge carrier density, e is the elementary charge and μ is the material charge carrier mobility, a parameter describing how fast carriers can move through it. To understand the key aspects of OSCs doping, a (brief) description of the electrical properties of the intrinsic materials is firstly required. These can be mainly understood looking at their electronic structure and at their charge transport properties.

1.1.1 Organic semiconductors electronic structure

Organic semiconductors are materials (either small molecules or polymers) characterized by highly π-conjugated backbones that make them capable of absorbing/emitting light in the UV-Vis-NIR wavelength region and of conducting charges. This π-conjugation is due to overlap of p-orbitals of successive atoms of the backbone and leads to charge delocalization over the molecular structure.[15] As the conjugation length of the molecule increases, the delocalization level increases as well. At the same time, the occupied bonding and unoccupied anti-bonding π-molecular orbital energy manifold become denser and the energy gap between the Frontiers Orbitals (FO) of the material, i.e. the Highest Occupied Molecular Orbital (HOMO) and the Lowest Unoccupied Molecular Orbital (LUMO) shrinks, giving the material a progressively less insulating

behavior. In the limit case of conductive polymers, where the conjugation length is very high, this leads to band like structure formation, with the definition of a filled Valence Band (VB) and an empty Conduction Band (CB) (see **Figure 1.1**).[16]

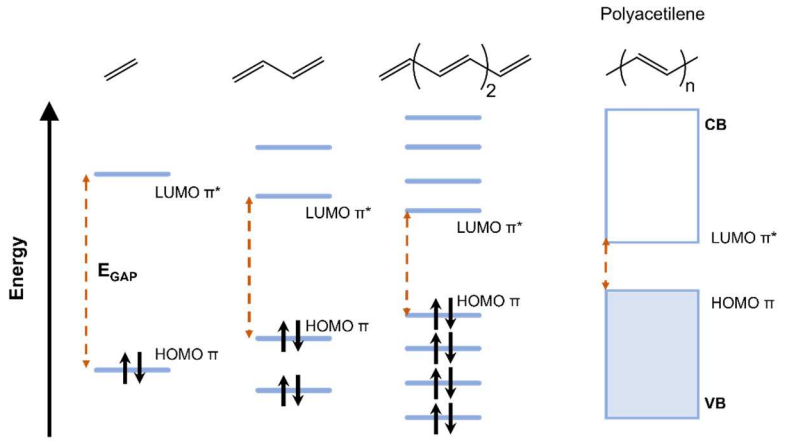

Figure 1.1 Electronic state distribution as a function of the number of conjugated double bonds. Valence band (VB) and Conduction Band (CB) form in the limit of conjugated polymers. The energy gap shrinkage is highlighted with orange arrows.

When we move from the single molecules to the solid state, which is where charge carriers conduction happens, the HOMO and LUMO levels position and the energy gap further change due to the energetic contribution of the interaction between the individual molecules forming the material.[6] Molecular solids are however held together by weak forces, mainly Van der Waals and π-π interactions, which make electronic coupling between the orbitals of the individual constituents low. The OSC material electronic structure and the conduction and valence states of the solid can thus generally be understood and discussed by looking at those of the individual molecules.[17]

The position of the FMOs levels and the entity of the energy gap mainly determine the electronic properties of an organic material.[6] The energy gap in particular defines the conducting behavior in terms of intrinsic free charge carriers density n. Depending on the desired property, the synthetic versatility of OSC allows for an easy tuning of the energy gap via functionalization of the molecule conjugated backbone.[18] Nonetheless, the gaps obtainable in OSC materials are in the order of 1-3 eV*.[16,17] Intrinsic organic semiconductors are thus quite insulating, since the energy requirement for an electron to move from the valence state to the conduction one is particularly high to make the occupation of the latter statistically relevant at room temperature. The main feature used to classify intrinsic OSC electrical properties is thus their capability to transport

* According to the Peierls distorsion theorem,[122] a 1D metal cannot exists. For this reason, even in the case of an infinite number of conjugated bonds, a gap always opens between the VB and the CB of a conjugated material, giving it a semiconductor behaviour. Even in those systems where this effect is mitigated, limits to the energy gap reduction are posed by low solubility and poor stability of highly conjugated structures.[16]

injected charges (for example at electrodes or via photoexcitation), i.e. their mobility μ.

1.1.2 Charge transport in organic semiconductors

Depending on the nature of the majority carriers, organic semiconductors are classified as p and n-type materials, in analogy with their inorganic counterparts. This feature is determined by the material FMOs position. The HOMO level is associated with an Ionization Energy (IE), which is the energy required to remove an electron from the molecule and bring it to an unbound state (vacuum level). The LUMO level is instead associated with the energy released when an electron is added from an unbound state to the molecule, which is called Electron Affinity (EA). p-type OSCs are materials characterized by high HOMO levels (low IE), from which is easy to extract electron. They thus can transport positive charges (holes). n-type OSC, are instead electron deficient materials having low LUMO levels (high EA) and in which is easy to introduce electrons. They thus transport negative charges.

The introduction of a charge in an organic semiconductor π-conjugated structure is accompanied by a local lattice polarization and distortion of the molecular structure. The unpaired charge and the polarization cloud are defined collectively as polaron and can be experimentally detected via spectroscopic techniques, due to the formation of intragap states, which change the optical properties of the material (see **Figure 1.2**). [19] Charge transport in OSC is accompanied by this polaron motion[6,20] and the transport efficiency is determined by the electronic coupling between adjacent molecules and by their distance.[6] As we discussed, OSC materials are held together by weak interactions and the electronic coupling between adjacent molecular orbitals is low, so that charge delocalization along the solid is limited. This is a very different situation with respect to the covalent crystalline lattices of inorganic semiconductor, where charges are highly delocalized and "free" to move. In such scenario, the molecules solid state arrangement highly impacts the charge transport properties. Along ordered crystalline regions a certain level of charge delocalization is possible and in very crystalline materials, band-like

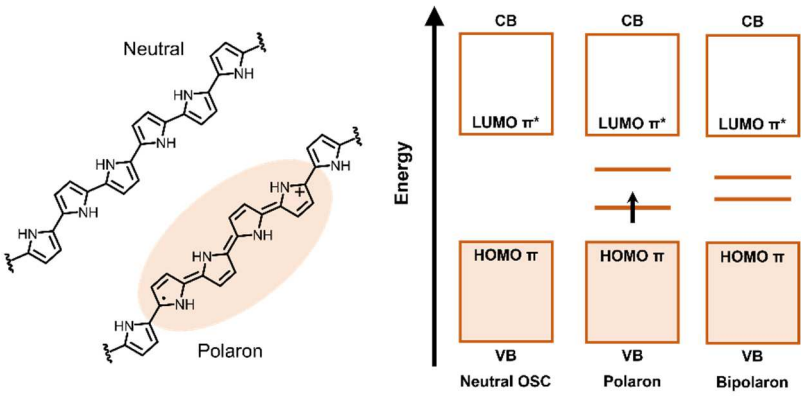

Figure 1.2 Left: graphical description of positive polaron formation in the case of polypyrrole. The molecular structure distortion (quinoidization) associated with the introduced positive charge is highlighted in red. Right: electronic structure of intragap energy states associated with polaron formation. The addition of a second charge on the same chain is also possible, with formation of a bipolaron.

transport can be obtained, giving rise to carrier mobilities exceeding 10 $cm^2V^{-1}s^{-1}$, thus higher than those of amorphous silicon.[21] This is the case for example of single crystal solids.[22] However, organic materials are generally obtained as thin films characterized by high disorder, with microstructures based on crystalline regions separated by amorphous ones and were charge delocalization interests only coherent polymeric chains or small ordered portion of the material. This situation is depicted in **Figure 1.3** and is particularly true for polymeric materials, whose higher adaptability to solution processing techniques and higher mechanical flexibility with respect to small molecules based one are also connected to a more disordered structure.[23] In such disordered systems, intermolecular charge transport is mainly described as thermally activated hopping of the charge from one molecule to another. The low charge delocalization, the high disorder and the intrinsic barrier to motion offered by the polaronic distortion highly impacts carrier mobilities of common organic semiconductors, which are typically below 10 $cm^2V^{-1}s^{-1}$, [22,24] far lower with respect to those of highly crystalline intrinsic inorganic semiconductors (10^2-10^4 $cm^2V^{-1}s^{-1}$).[25]

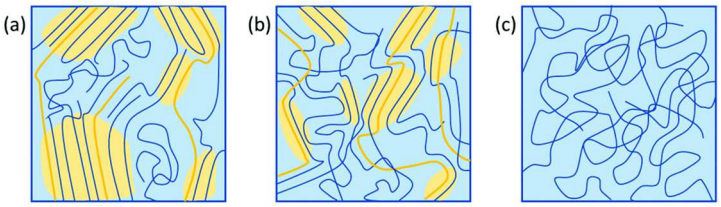

Figure 1.3 Cartoon of typical polymeric OSCs microstructures: Semicrystalline material (a), partially ordered materials with short-range aggregation (b) and amorphous materials (c). Yellow color indicates ordered regions. Yellow polymeric chains represent path where charge is delocalized in π-conjugation and that improve charge transport between ordered regions. Adapted from reference 24 with permission of the Royal Society of Chemistry.

Due to the aforementioned low charge carriers density and the generally poor mobilities, intrinsic OSCs show then moderate electrical performances, with conductivities in the order of 10^{-10} and 10^{-6} Scm^{-1},[19] which limits their application. In sight of better performances, doping thus offer a strategy to tune σ toward higher values.

1.2 Principles of organic semiconductor doping

The concept of doping was firstly introduced in the field of inorganic semiconductors and consists in increasing charge carriers density n and, as a consequence, conductivity of a material via introduction of impurities that can either donate (n-type doping) or accept (p-type doping) electrons.[26]

In the case of inorganic semiconductors, doping is made possible by controlled addition in the material crystal lattice of substitutional or interstitial atomic impurities bearing more valence electrons (donor atom) or less valence electrons (acceptor atom) with respect to the intrinsic atoms. The introduction of these extrinsic charges then cause a shift of the Fermi energy level, i.e. the energy level associated with 50% probability of being occupied by an electron, towards the material empty conduction band and filled Valence band respectively (see **Figure 1.4**).[1,26] This doping process is extremely efficient and the obtained n basically coincides with the added impurity concentration, so

that small amount of dopant, in the orders of few ppm (10^{-3}-10^{-6} doping ratio), are sufficient to reach target conductivities, without significant perturbation of the crystalline structure of the material.[27]

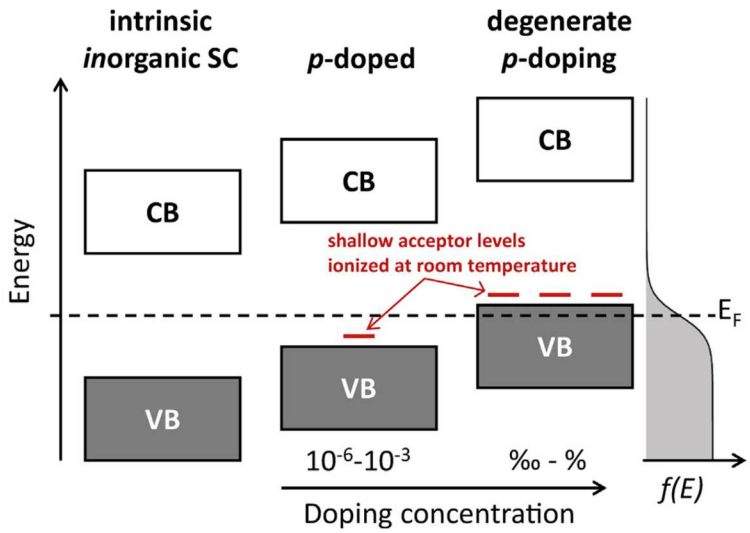

Figure 1.4 Schematic energy level diagram for a p-doped inorganic semiconductor as a function of dopant concentration. E_F is the fermi energy level and f(E) is the Fermi function describing the electron distribution in the material electronic states. Adapted from Reference 27.

Due to the very different nature and structure of organic semiconductor, their doping processes is different and harder to control. Doping is in this case generally obtained via blending with compounds capable of introducing positive or negative charges into the semiconductor via oxidation (p-type doping) or reduction (n-type doping) reactions. The consequences of these reactions are the same of inorganic semiconductor doping, i.e. growth of charge carrier concentration and Fermi energy level shift toward HOMO or LUMO levels. Due to the low mobilities of OSC however, high carrier concentrations are needed to reach decent performances, with the consequence that dopants amounts in the order of % molar ratio with respect to the conductive unit need to be added to the semiconductor host, reaching also 10-40% for those applications requiring high conductivities (for example >10 Scm^{-1} for thermoelectric devices).[17,27–31] This means that the effect of dopants introduction on the OSC matrix microstructure is not negligible. Moreover, dopants and semiconductors molecules are not bound covalently as it is for the inorganic semiconductors, but only via coulomb forces or weak interactions, which can make dopant diffusion processes possible, and device operational stability limited. For all these reasons, doping is way harder to control in OSCs than in silicon. A detailed knowledge of the organic semiconductors doping principles is thus the starting point for understanding the nature of dopant/host interactions and obtaining performing OSCs.

1.2.1 Early doping approaches

The first examples of OSC doping mainly exploited inorganic redox active derivatives. These were strong oxidants, like halides (I_2, Br_2),[8,32] in the case of p-type doping and strong electron rich reductants, like alkali metals (Li, K, Cs)[33–35] in the case of n-type doping. However, due to their small dimensions and the weak noncovalent interactions with the host, these metals and halides-based dopants tend to diffuse within the material, leading to thermal and operational instability of the obtained devices and dedoping effects. Other classes of inorganic dopants have been reported in more recent

years, like, for example Lewis acid salt ($FeCl_3$)[36] or oxides (WO_3)[37] but their use is limited by sensitivity to moisture or lack of solution processability.
Molecular dopants were introduced as valuable alternative to inorganic ones, since they are larger in dimension and their bulkiness limits diffusion.[6,27] Furthermore, the possibility of tuning their properties via synthetic strategies and their higher solubility/easier processing versatility made this class of materials particularly interesting. This project will thus mainly discuss this second approach.

1.2.2 Molecular doping processes

Molecular doping processes mainly happen via two mechanisms, here schematized in **Figure 1.5**: *ion-pair* formation or *Charge Transfer Complex* (CTC) formation. Ion pair formation is probably the most common and better understood process.[6,27,38–40] It involves an integer charge transfer between the dopant and the OSC with formation of a cation and an anion that interact coulombically afterward. The process is highly driven by the energy level difference between the dopant and the semiconductor. In the case of p-type doping the electron transfer occurs from an electron rich semiconductor to a dopant acceptor with an electron affinity higher or equal than the OSC ionization potential or, in other words, a LUMO level energetically lower than the HOMO level of the semiconductor. Chemically speaking, the process is an oxidation that leaves a hole in the OSC conjugated structure. In the case of n-type doping it is

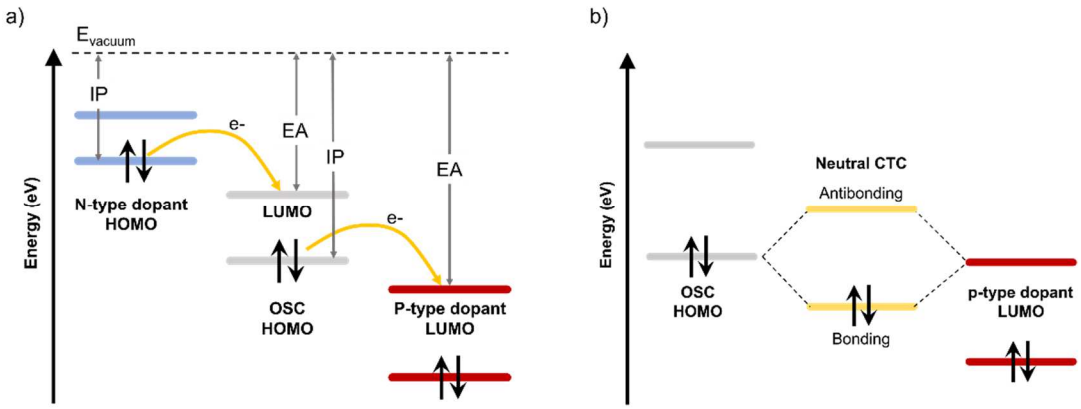

Figure 1.5 a) ion pair formation mechanisms. Integer charge transfer processes are highlighted via yellow arrows; b) schematization of charge transfer complex (CTC) formation in the case of p-type doping. HOMO bonding and LUMO antibonding CTC levels are highlighted in yellow.

the other way around: an electron rich dopant donor transfers an electron to an electron poor semiconductor (dopant IP ≤ OSC EA), which is then negatively charged, following a reduction reaction. In the case of CTC formation, doping instead happens via hybridization of the OSC and dopant molecular orbitals, with formation of a neutral complex characterized by its own HOMO and LUMO levels (**Figure 1.5b**).[6,27,41,42] The process does not require a specific energy level mismatch between the HOMO and LUMO levels of the species involved in it. The electrons of the donor compound are thus shared within the molecular orbital of the obtained complex and the charge transfer is only partial and not integer, with no formation of radicals and charged species.

The CTC can eventually be ionized via transfer of an integer charge transfer to/from another semiconductor unit, even if this process generally requires activation energy and is not as efficient as the basic ion pair formation reaction.[6]

There are then dopants for which charge transfer processes are coupled to more complex chemical reactions. Doping mediated by proton transfer,[43] interaction with Lewis acid/base[44,45] and strong nucleophilic anions[46] or hydride transfer[47] are some of the most common examples. As we will deepen later in this chapter, this project will deal with compounds belonging to this last class. It is however worth mentioning that the doping mechanism is not strictly defined and highly depends on the nature of the specific semiconductor/dopant interactions: the same dopant can work differently depending on the semiconductor counterpart.[47,48] Whichever the selected dopant/host system, a deep knowledge of doping mechanism is then required to predict the outcome of doping processes in applications.

1.2.3 Doping efficiency: definition, limiting factors and strategies to improve it

It is not granted that all dopants introduce charge carriers in the semiconductor counterpart. The efficiency of a doping process μ_{eff} is thus defined as the number of free charge carriers (N_{free}) introduced in the semiconductor per number of dopant molecules (N_{dopant}).[6]

$$\mu_{eff} = \frac{N_{free}}{N_{dopant}} \tag{1.3}$$

The generation of the free charge carriers follows a two-step process.[49,50] The first step is the ionization of the dopant, with charge transfer (electron or hole) to the OSC and formation of an ion pair. The formed polaron is however coulombically bound to the dopant counterion and must dissociate to become a free charge carrier actually contributing to electrical conductivity. The doping efficiency is then on the overall determined by that of the dopant ionization step and the ion pair dissociation process.

With few exceptions[51,52], doping efficiency is generally low, not overcoming 10-20% values in many cases,[13] due to factors limiting these two steps (**Figure 1.6**).
Low charge dissociation efficiencies are one of the main factors limiting μ_{eff}, in some cases even reducing it to values below 5% in system with 100% of dopant ionization efficiency (**Figure 1.6a**).[53,54] This is mainly because organic semiconductors possess low dielectric constants, which inhibits electrostatic screening. The Coulombic binding energies between ionized dopant and charge carriers are thus quite high (typically ~ 0.2-0.5 eV) with respect to the thermal energy at room temperatures (k_BT=25 meV, where k_B is the Boltzman constant),[49,53,55] and dopant counterions can thus act as traps for the polarons. The effect is reduced by energetic disorder[49] and by coulomb potentials overlap.[55]

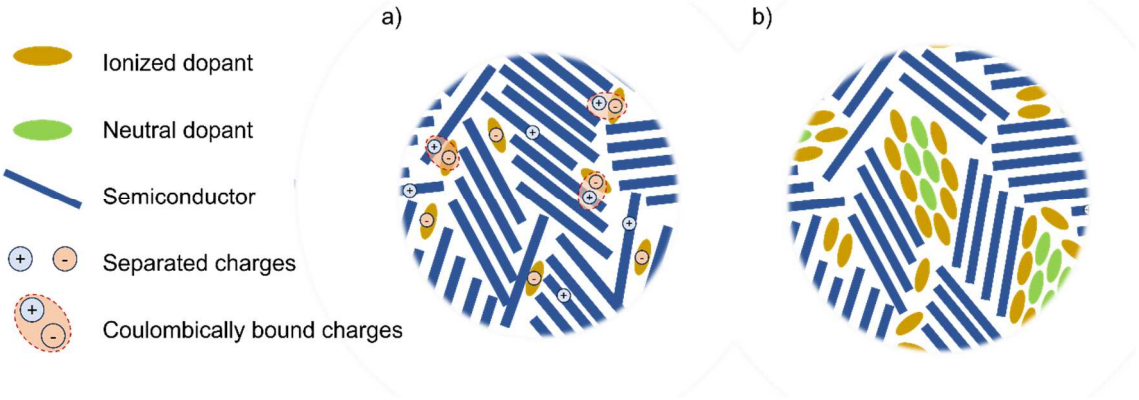

Figure 1.6. sketch of possible situations leading to lower doping efficiencies: coulomb trapping of charge carriers after ion pair formation (a); formation of segregated dopant domains in highly doped semiconductors.

Concerning the dopant ionization step, its efficiency highly depends on the thermodynamically driving force of the charge transfer reactions.[56,57] High ionization efficiency can thus be generally obtained by selecting dopant and semiconductors systems with high EA and IP differences. Even when the energy levels alignment requirement is satisfied, low miscibility of the dopant in the semiconductor host can however severely limits the efficiency of the process. In such scenario in fact, after reaching a certain dopant concentration threshold, phase separation of the dopant and the host occurs, leading to a condition in which only the dopant fraction at the interface of the segregated domains and in contact with the semiconductor matrix is actually active in the charge transfer process (**Figure 1.6b**).[6,58]

Ideally one would like to achieve organic semiconductors with good electrical performances at low dopant concentration. Addition of high dopant concentration to a semiconductor host leads in fact inevitably to a severe decrease of the carrier's mobility μ, due to introduction of Coulomb scattering sites and severe disruption of the OSC molecular packing, which, as already discussed, determines the charge transport properties.[6,59] Highly efficient doping processes are thus required. Several approaches are possible to counteract the phenomena limiting μ_{eff}. Structural modification of the semiconductor and/or dopant to improve mutual miscibility is an efficient way to reduce dopant segregation impact (we will further deepen this concept in Chapter 4).[29,60–64] Introduction of Polyethylene glycol (PEG) polar chains on the semiconductor structure was for example demonstrated to work particularly well in this direction, since the dopants tend to be more soluble in such polar environment.[61,62,64] The same strategy can be exploited to reduce Coulomb trapping effects as well, since polar side chains increase the medium dielectric constant and can confine the dopant at higher distances with respect to the polaron,[65,66] thus reducing Coulomb forces. Development of bulkier dopants is another efficient way to reduce coulomb interactions via better spatial separation of counterions from the charged OSC.[51,56,67] Structural modification of the semiconductor and addition of bulky dopants can in some cases however also impacts the morphology of the obtained conductive blend and lead to disruption of semiconductor packing or higher density of grain boundaries within the material.[10,28,66,68–71] The close

interplay between doping and microstructure within each specific dopant/semiconductor system must then be taken into consideration to obtain an optimal trade-off between good doping efficiencies and carrier mobilities. It this sense, it is worth mentioning that processing techniques can highly help in obtaining ordered OSC morphology and reducing the OSC structural disruption related to dopant addition. For example, sequential doping techniques, which consist in obtaining OSC films and subsequently expose them to dopant containing solution, can mitigate the negative effect of molecular dopant addition with respect to doping obtained via semiconductor and dopant solution mixing.[31]

1.2.4 A few words on doping in device applications

When moving to devices application, we deal with heterostructures characterized by interfaces between different organic layers and organic layers and electrodes. The devices performances are then determined by the efficiency of charge injection between these interfaces, which are highly dependent on energy level alignment, and on the transport properties of the bulk materials in the single layers. An efficient doping can thus lead to several benefits in applications:[6,10]

- it increases electrical conductivity, which reduce bulk Ohmic losses in transport layers and devices operating voltages;[10]
- it can increase carriers mobility via filling of trap energy state;[72]
- Via tuning of the Fermi energy levels alignment, it can facilitate charge injection at semiconductor/electrode or organic/organic junctions.[73,74] Even in the case of energy level alignment mismatch at semiconductor/electrode junctions, doping can lead to formation of Ohmic contacts by thinning of charge space regions forming at these interfaces, i.e. insulating regions generating due to charge exchanges between the two materials. The space charge region is associated with a barrier for charge injection, but tunneling of carriers through it is possible if it is very thin. The width of the space charge region decreases at higher charge carrier densities, and as such, higher doping levels, according to the equation[6,75]

$$w = \sqrt{\frac{2\varepsilon V_{bi}}{eN_D}} \tag{1.4}$$

where ε is the semiconductor dielectric constant, V_{bi} is the built-in potential, i.e. the voltage change across the depletion region, e is the elementary charge and N_D is the ionized dopant density.[74]

All these effects have been efficiently exploited to increase performances of several optoelectronic devices of which **Figure 1.7** collect some of the most common architectures. In OLED, for example, holes and electrons need to be efficiently injected at the electrodes via application of a voltage bias and then transported to the emissive active layer, where they recombine to emit light. In this devices, the use of efficiently doped electron transport (ETL) and hole transport layers (HTL) exhibiting high conductivi-

ties and low charge injection barriers demonstrated to increase performances.[10] A similar effect can be obtained in the case of OPVs. The working principle is in this device opposite and hole-electron pairs forming in the active layer via light absorption need to be separated before recombination and extracted at the electrodes. Again, highly conductive doped ETL and HTL can help in increasing the efficiency of the process.[6] Doping of the bulk heterojunction (BHJ) photoactive layer also demonstrated to lead to BHJ improved morphology and reduced charge carriers recombination.[6,11]

OFET working principle is based on the modulation of the conductivity of a semiconductor channel between a source and a drain electrode by application of an external

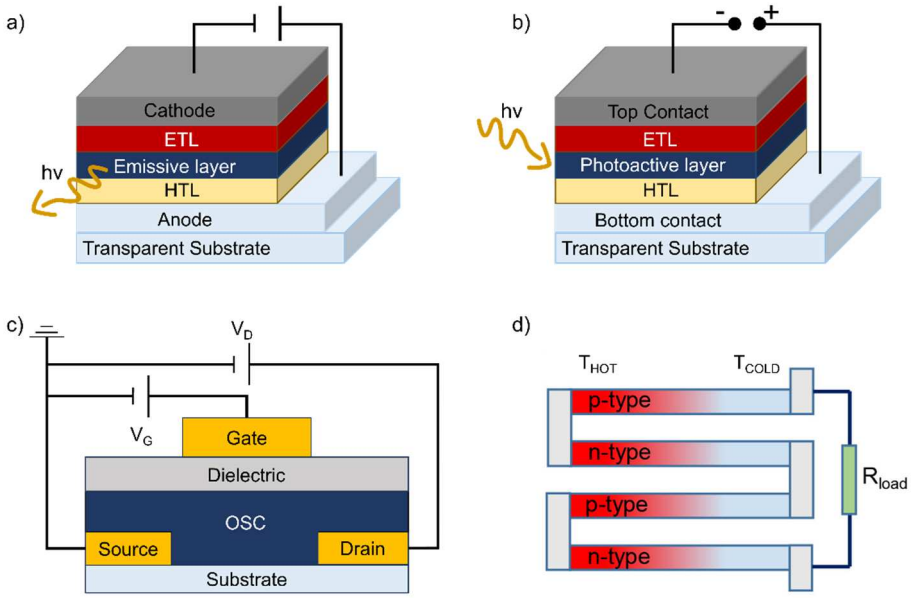

Figure 1.7 Examples of organic semiconductor-based devices in typical configurations: OLED (a), Conventional architecture of Organic solar cell (b), OFET in Top-Gate-Bottom-Contact configuration, where Drain voltage and Gate voltage are indicated as V_D and V_G respectively (c), and p-n leg OTEG (d). Adapted with permission from reference 6. Copyright 2023 American Chemical Society.

gate voltage V_G. The threshold voltage V_T, i.e. the gate voltage at which the transistor switches on, is affected by several factors, like presence of charge carriers traps and high contact resistance. These effects can be controlled via selective doping of electrode/semiconductor contact regions[12] or trap filling with addition of small dopant amount.[6,76]

The interest in doping for Organic Thermoelectric Generators (OTEG) field has also increased in the last decades since these devices are considered among the most promising energy harvester for the IoT technologies.[4,77] TEGs exploit the Seebeck effect, i.e. the generation of an electric potential difference in the presence of a thermal gradient in a material. The performances of TEGs are determined by the dimensionless figure of merit zT

$$zT = \frac{\sigma S^2}{k_e + k_l} T \tag{1.5}$$

where T is the temperature, σ is the electrical conductivity, S is the Seebeck coefficient, k_e is the charge carrier component of thermal conductivity, and k_l is its lattice component. Typically, organic semiconductors display very low thermal conductivities (between 0.1-1.0 $Wm^{-1}K^{-1}$) due to their structural disorder. As such, efforts to increase OTEGs performances mainly focus on maximizing the Power Factor (PF), which is defined as $PF = \sigma S^2$. For obtaining decent power factors high conductivities are thus required and doping can clearly increase OTEG performances. It is however worth mentioning that the Seeback effect empirically shows a proportionality to $\sigma^{-\frac{1}{4}}$ and, as such, a trade-off is required between the two parameters.[4,78,79]

For all the cited applications both n-type and p-type semiconductors having good transport properties are necessary in sight of more efficient applications. Both efficient ETL and HTL layers are required to balance injection or extraction of electrons and holes from or to the electrodes in OLEDs and OPVs. OTEGs are generally based on arrays of p- and n- doped OSCs.[4] In the field of OFETs, complementary logic circuits built with matched p- and n- type materials are required to fasten circuit speed and lower power consumptions.[24]
As aforementioned, finding p- and n- type materials with comparable performances is however not straightforward and is one of the main challenges in the field of organic optoelectronics.

1.3 The n-Type doping challenge

1.3.1 p-Type vs n-Type doping: two different stories

After the discovery of polyacetylene doping in 1977, the field of p-type semiconductors saw a continuous growth and several efficient dopants have been developed. The most used and widespread known molecular p-type dopant is probably 2,3,5,6-tetrafluoro-tetracyanoquinodimethane, or F4-TCNQ.[39,70,80] This is a tetracyanoquinodimethane derivative introduced in the field in 1998,[80] which possesses appropriate solubility, good air stability and a pretty high electron affinity of 5.24 eV, properties that made it a very good candidate for applications.[40] A plethora of new dopants followed and some of these examples are reported in **Figure 1.8**. Air stable TCNQ derivatives with larger structures like F6-TCNNQ[†] where, for example, synthesized to overcome the detected high diffusivity of F4-TCNQ from doped films.[81] Bulkier compound, like $Mo(tfd)_3$ allowed further improvements in this direction.[82] Derivatives having very high EA and capable of doping also semiconductor with very deep HOMO levels inaccessible to F4-TCNQ were also reported, like radialene based compounds or tris(4-bromophenyl)ammoniumyl hexachloroantimonate (Magic Blue).[57,83] Lewis acids also showed to work in this sense.[84]

[†] 2,2'-(1,3,4,5,7,8-Hexafluoro-2,6-naphthalenediylidene)bis-propanedinitrile

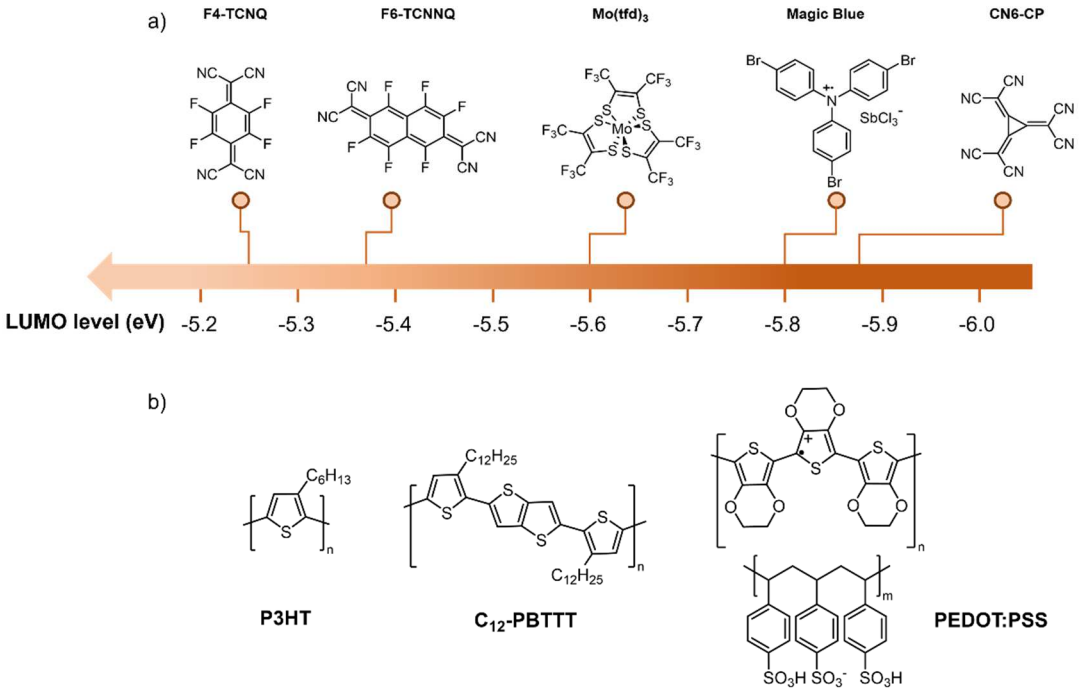

Figure 1.8. a) Molecular structure of different p-type dopants reported together with their LUMO levels; b) molecular structure of the cited p-type polymers.

The extended effort in the field, the good air stability of most doped p-type polymers and the development of so many different dopants, lead to the achievement of good p-type semiconductor performances. With the right processing conditions, efficient polymer/dopant systems showing conductivities higher than 500 Scm^{-1} were obtained. For example, doping of P3HT[‡] polymer with a $Mo(tfd)_3$ derivative or with Magic Blue lead to a conductivity of 681 Scm^{-1} and over 3000 Scm^{-1} respectively,[85,86] while aligned PBTTT[§] films doped with F6-TCNNQ reached values as high as 2400 Scm^{-1}.[87] The development of the conductive polyelectrolyte PEDOT:PSS,[**] where polystyrene sulfonic acid acts as dopant, has then given a great push to the filed, due to its good filming properties, high transparency, good thermal stability and the easy tuning of its electrical transport properties.[88] The conductivity of this material today can reach values of 4380 Scm^{-1} via secondary acid doping.[89]

When looking instead at the n-type organic semiconductor field, the difference in performances is obvious. The majority of n-type OSC/dopant systems reported in the literature show low doping efficiencies and conductivities in the order of 10^{-3}-10 Scm^{-1}, [90] with only a bunch of materials reaching values higher than 10 Scm^{-1}. [67,91,92] Only very recently some examples of semiconductor/dopant systems with conductivities of 100-150 Scm^{-1} were described,[93–95] and a newly synthesized in-situ doped poly(benzodifurandione) polymer (PBFDO, vide infra **Figure 1.10**) was reported to reach a conductivity of 2000 Scm^{-1}, [96] becoming a possible candidate to close the gap between n-

[‡] Poly(3-hexylthiophene-2,5-diyil)
[§] Poly(2,5-bis(3-alkylthiophen-2-yl)thieno[3,2-b]thiophene)
[**] Poly(3,4-ethylenedioxythiophene) polystyrene sulfonate

and p- type materials. However, especially for those applications in which high conductivities values are required, like OTEGs, more effort is necessary to extend the library of performing n-type semiconductors.

The reason behind the smaller number of good n-type OSCs candidates lies in the difficulty of obtaining the required good solubility, high mobility, good doping efficiencies and deep LUMO levels simultaneously integrated in the same material.[23] Moreover, even when the electrical performances are fair, in most cases n-type doped semiconductors and n-type dopants are particularly unstable under air, which is still one of the main challenge to overcome for devices applications.[90]

1.3.2 The air sensitivity issue

The air sensitivity of doped n-type semiconductors is due to redox reactions with O_2 and moisture. A look at the reduction potentials of these species, reported in **Figure 1.9a**, suggest that an n-type semiconductor should have a LUMO level below -4.9 eV to be air stable in its doped state.[24,97] Presence of overpotentials, i.e., free activation energies required for the reduction to proceed, can mitigate this requirement making semiconductors with LUMO levels below -4.0 eV decently air stable.[97] For application in which the carrier injection and transport is concluded within minutes, like OFETs, materials with LUMO levels below -4.0 eV are indeed known to work under ambient conditions. However for applications requiring high conductivities for prolonged time, only semiconductors having LUMO levels deeper than -4.7 eV show good performances.[90] Nonetheless, LUMO levels of benchmark and commercial n-type materials

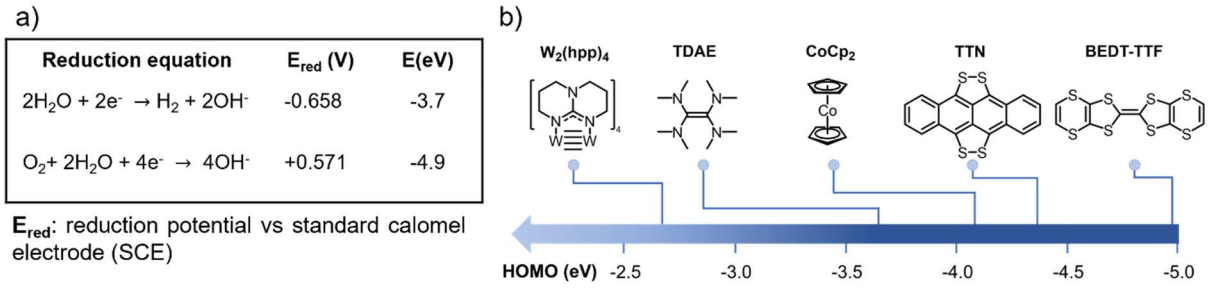

Figure 1.9 Reduction equations related to H_2O and O_2 redox processes causing instability of n-doped semiconductors and dopants and redox potentials (E_{red}) at which they happen(a); common n-type dopants working via direct electron transfer processes. Their HOMO level energy is highlighted via blue lines (b)

reside within the electrochemical window of O_2 and H_2O reduction reactions. For instance, the LUMO level of the widespread fullerene acceptor Phenyl-C61-butyric acid methyl ester (PCBM) is localized at -3.90[90] eV and also the well-known donor-acceptor polymer poly{[N,N′-bis(2-octyldodecyl)-naphthalene-1,4,5,8-bis(dicarboximide)-2,6-diyl]-alt-5,5′-(2,2′-bithiophene), better known as P(NDI2OD-T2) or N2200, has a LUMO level of -3.91 eV.[98]

The air sensitivity issue is even more relevant for n-type dopants. To obtain the required driving force for efficient charge transfer, dopants should in fact have HOMO levels higher that the LUMO of the semiconductor counterpart. First molecular n-type

dopants thus either suffered of low doping efficiencies due to too high ionization potentials or of high oxygen sensitivity, which posed serious difficulties in their synthesis, handling and storage. For example n-type dopants like tetrathiafulvalene derivative BEDT-TTF[99] and tetrathianaphthacene (TTN)[100,101] possess decent air stability but are not enough reducing to dope most of n-type semiconductors; other reported organometallics based compounds[102,103] and amine-based dopants, like tetrakis (dimethylamino)ethylene, or TDAE,[104,105] are instead strong reductants but highly susceptible to oxidation (**Figure 1.9b**).

To deal with the air sensitivity issue while at the same time increasing the doping efficiency, both OSC with deeper LUMO levels and efficient but oxygen/water tolerant dopants are then required.

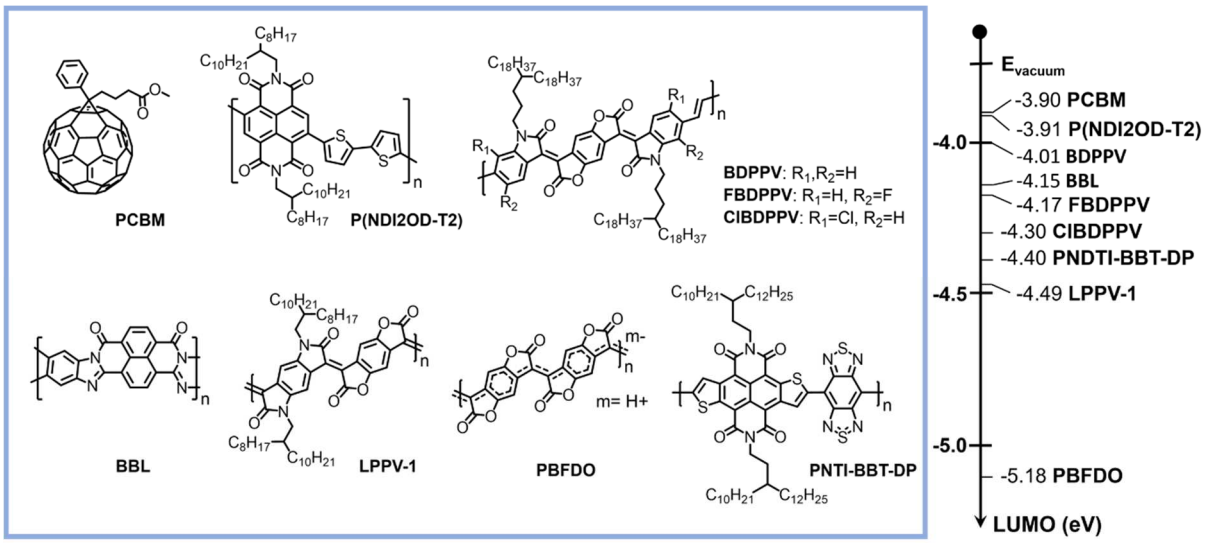

Figure 1.10 Representatives of different classes of n-type semiconductors, reported with their LUMO level: fullerenes derivatives (PCBM), naphtalenediimides derivatives (P(NDI2OD-T2)), naphtodithiophenediimide derivatives (PNDTI-BBT-DT), polylactam/polylactons (BDPPV derivatives), fully fused acceptor-acceptor based polymers (BBL, LPPV and PBFDO)

For what concern the semiconductor side, several strategies have been applied to lower LUMO levels while keeping good transport properties: design of planar and rigid conjugated backbones, like those of polylactons/polylactams or naphtodithiophenediimides polymers, addition of more electron-withdrawing group on such structures, and synthesis of highly rigid, fully fused copolymers based only on electron deficient moieties (acceptor-acceptor copolymers) are just some examples.[24,90] **Figure 1.10** collects structures of some of the developed materials**,** together with a comparison of their LUMO level energy with respect to that of benchmark n-type semiconductors (PCBM and P(NDI2OD-T2)). Among all the reported derivatives however, only the in-situ doped PBFDO polymer show high prolonged air stability thank to its record LUMO energy level of -5.18 eV.[24,90] Other strategies have thus been developed to counteract the air sensitivity of doped OSC, like self-encapsulation.[90] The deepening of this topic however goes beyond the purpose of this manuscript.

For what concern the dopant side, the most important step in the field was instead the

development of n-type dopant precursors.

1.3.3 The dopant precursors route

Dopant precursors are kinetically air stable compounds whose ionization potential is too high to give direct electron transfer to a semiconductor but that can form highly reducing species under thermal treatment or light irradiation once directly in contact with the acceptor counterpart. The formation of the actual dopant species is generally accompanied by complex reactions involving chemical bond cleavage or formation. The air stability of these compounds allows their easy handling and even the possibility of performing some of the device processing steps in air, a great advantage with respect to the traditional highly reducing but unstable dopants.

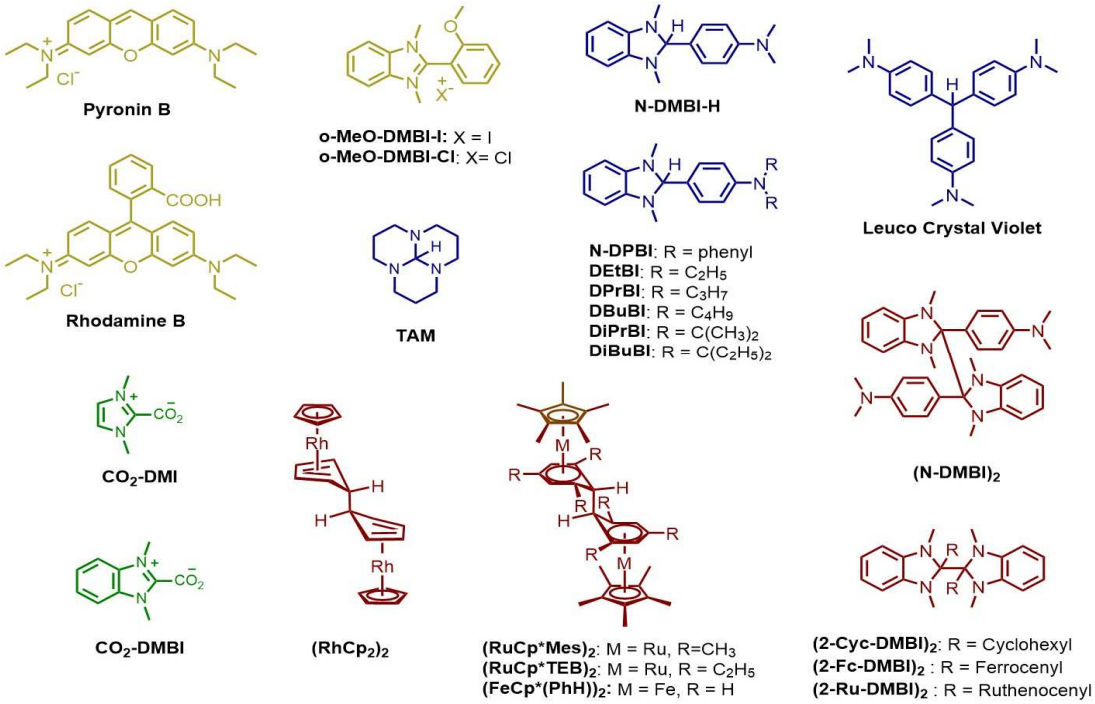

Figure 1.11 examples of n-type dopant precursors: cationic salts (yellow), hydride donors (blue), dimers (red), carbene forming derivatives (green).

The first ever reported dopant precursors were Pyronin B and Rhodamine B, two cationic dyes capable of doping fullerenes by formation of their more electron rich *leuco* form during co-evaporation with the acceptor.[106,107] These compounds however can only work via vacuum processing and lead to formation of side-products. After this pioneering work, a series of classes of dopant precursors were then developed to extend and improve the method. A classification based on the doping pathway is here attempted in **Figure 1.11**. We can recognize:

- Cationic salts, like the benzimidazole based O-MeO-DMBI-I and O-MeO-DMBI-Cl.[108,109] These turn into unknown highly reducing intermediates during vacuum

processing. Their limit is, in analogy to cationic dyes, that they can't be solution processed.

- Hydride donors, like Leuco crystal violet (LCV),[110] the benzoimidaozoline-based dopant N-DMBI-H[111] and its derivatives[29,58] and the more recently reported triaminomethane based dopant (TAM).[112] These dopant precursors work via hydride or hydrogen atom transfer and are solution processable. There is however the possibility of side product formation due to unwanted hydrogenation reactions;[47]
- Dimeric dopants. These are organometallic based compounds like rhodocene, ruthenium and ferrocene dimers, or dimers of organic radicals, like the N-DMBI-H derived $(N\text{-}DMBI)_2$ or $(2\text{-}Cyc\text{-}DMBI)_2$. Firstly introduced by Marder group,[78,113,114] these dopants are solution and vacuum processable and they are capable of transferring two electrons per dopant molecules under thermal activation, thus increasing doping efficiency at lower dopant concentration.[115] Their drawback is that the metal containing ones are mostly based on rare expensive transition metals and that their synthesis is in all cases based on hazardous liquid alkali-metal reductants like Na-Hg.
- Carbenes forming dopants with activation based on decarboxylation reactions, like CO_2-DMI e CO_2-DMBI. These compounds were very recently introduced. They are processable from solution and show good generality of application.[116]

Depending on the semiconductor and the application, one dopant precursor might be a better choice with respect to another. The most known and used precursor dopants are, however, benzimidazoline based ones, and in particular 4-(1,3-Dimethyl-2,3-dihydro-1H-benzimidazol-2-yl)-N,N-dimethylaniline, i.e. N-DMBI-H.

1.3.4 Challenges of N-DMBI-H - the scope of this work

Introduced for the first time by Bao group in 2010, N-DMBI-H became the benchmark n-type dopant precursor, due to its relative air stability, good solubility in common processing solvents, its commercial availability and its capability to dope a wide number of semiconductors. This compound has in fact been successfully applied for the doping of different classes of small molecules[111,117,118] and polymeric n-type semiconductors,[58,91,94] graphene,[119] carbon nanotubes[120] and perovskite layers,[121] for applications in solar cells, organic field effect transistors and organic thermoelectrics. N-DMBI-H appears then to possess many of the characteristics required from an excellent n-type dopant. Despite is success, there are however some issues that still limit its efficient use and that requires to be solved toward performances improvement.
On the one side, a full rationalization of its doping mechanism is still missing and it is required for a better use of this compound.[117] We will deepen these concepts in Chapter 2.

On the other side this dopant shows very low doping efficiencies and high concentrations of N-DMBI-H are generally required to reach good electrical performances, sometimes even surpassing the 50% molar content (with respect to the polymer repeating unit). [29,78] This is mainly due to its poor miscibility with common semiconductors, that causes its segregation and out-diffusion from the host matrix, limiting the amount of available compound during doping activation.

Several successful approaches have already been developed to deepen the knowledge of N-DMBI-H doping mechanism and to improve its miscibility with the semiconductor host. I will give more details about these in the next chapters. Nonetheless, these well-known challenges still offer a playground for the exploration of new approaches toward more efficient n-type organic semiconductors doping and for the definition of design guidelines for new and more performing n-type dopants.

This work fits within this scope. In this manuscript, I will indeed show how we dealt with N-DMBI-H issues and how, by doing this, we developed original strategies for the investigation of doping mechanisms and the improvement of n-type dopants efficiencies. Firstly, I will showcase the use of molecular hydrogen detection techniques as a novel approach for the investigation of N-DMBI-H doping mechanism and for the more general analysis of semiconductor doping processes mediated by hydrogen atoms transfers (Chapter 2). I will then present new ways to deal with the problem of N-DMBI-H segregation, either based on the addition of third elements, i.e. nucleating agents, in the semiconductor/dopant matrix (Chapter 3) or on the design and synthesis of new N-DMBI-H derivatives (Chapter 4).

1.4 Bibliography

1 I. Salzmann, G. Heimel, M. Oehzelt, S. Winkler and N. Koch, *Acc. Chem. Res.*, 2016, **49**, 370–378.

2 M. Riede, B. Lüssem, K. Leo and A. Z. M. S. Rahman, in *Reference Module in Materials Science and Materials Engineering*, Elsevier, 2018.

3 M. Jahandar, S. Kim and D. C. Lim, *ChemSusChem*, 2021, **14**, 3449–3474.

4 N. Pataki, P. Rossi and M. Caironi, *Appl. Phys. Lett.*, 2022, **121**, 1–12.

5 H. Liu, D. Liu, J. Yang, H. Gao and Y. Wu, *Small*, 2023, **19**, 1–27.

6 A. D. Scaccabarozzi, A. Basu, F. Aniés, J. Liu, O. Zapata-Arteaga, R. Warren, Y. Firdaus, M. I. Nugraha, Y. Lin, M. Campoy-Quiles, N. Koch, C. Müller, L. Tsetseris, M. Heeney and T. D. Anthopoulos, *Chem. Rev.*, 2022, **122**, 4420–4492.

7 J. S. Chang, A. F. Facchetti and R. Reuss, *IEEE J. Emerg. Sel. Top. Circuits Syst.*, 2017, **7**, 7–26.

8 H. Shirakawa, E. J. Louis, A. G. MacDiarmid, C. K. Chiang and A. J. Heeger, *J. Chem. Soc. Chem. Commun.*, 1977, 578–580.

9 X. Zhou, M. Pfeiffer, J. Blochwitz, A. Werner, A. Nollau, T. Fritz and K. Leo, *Appl. Phys. Lett.*, 2001, **78**, 410–412.

10 K. Walzer, B. Männig, M. Pfeiffer and K. Leo, *Chem. Rev.*, 2007, **107**, 1233–1271.

11 Y. Lin, Y. Firdaus, M. I. Nugraha, F. Liu, S. Karuthedath, A. H. Emwas, W. Zhang, A. Seitkhan, M. Neophytou, H. Faber, E. Yengel, I. McCulloch, L. Tsetseris, F. Laquai and T. D. Anthopoulos, *Adv. Sci.*, 2020, **7**, 1–9.

12 M. Waldrip, O. D. Jurchescu, D. J. Gundlach and E. G. Bittle, *Adv. Funct. Mater.*, 2020, **30**, 1–31.

13 B. Lüssem, C. M. Keum, D. Kasemann, B. Naab, Z. Bao and K. Leo, *Chem. Rev.*, 2016, **116**, 13714–13751.

14 G. Woan, *The Cambridge Handbook of Physics Formulas*, Cambridge University press, 2003.

15 A. J. Heeger, *J. Phys. Chem. B*, 2001, **105**, 8475–8491.

16 M. C. Scharber and N. S. Sariciftci, *Adv. Mater. Technol.*, 2021, **6**, 1–9.

17 B. Russ, A. Glaudell, J. J. Urban, M. L. Chabinyc and R. A. Segalman, *Nat. Rev. Mater.*, 2016, **1**, 1–14.

18 J. Roncali, *Macromol. Rapid Commun.*, 2007, **28**, 1761–1775.

19 T. H. Le, Y. Kim and H. Yoon, *Polymers (Basel).*, 2017, **9**, 1–32.

20 I. I. Fishchuk, A. Kadashchuk, S. T. Hoffmann, S. Athanasopoulos, J. Genoe, H. Bässler and A. Köhler, *Phys. Rev. B - Condens. Matter Mater. Phys.*, 2013, **88**, 1–11.

21 R. Street, *Technology and Applications of Amorphous Silicon*, Springer, 2000.

22 P. Hu, X. He and H. Jiang, *InfoMat*, 2021, **3**, 613–630.

23 H. Sun, X. Guo and A. Facchetti, *Chem*, 2020, **6**, 1310–1326.

24 S. Griggs, A. Marks, H. Bristow and I. McCulloch, *J. Mater. Chem. C*, 2021, **9**, 8099–8128.

25 M. Levinshtein, S. Rumyantsev and M. Shur, *Handbook Series on Semiconductors parameters*, World Scientific, 2000.

26 S. M. Sze and K. K. Ng, in *Physics of Semiconductor Devices*, Jhon Wiley & Sons, 2007.

27 I. Salzmann and G. Heimel, *J. Electron Spectros. Relat. Phenomena*, 2015, **204**, 208–222.

28 I. E. Jacobs and A. J. Moulé, *Adv. Mater.*, 2017, **29**, 1–39.

29 B. Saglio, M. Mura, M. Massetti, F. Scuratti, D. Beretta, X. Jiao, C. R. McNeill, M. Sommer, A. Famulari, G. Lanzani, M. Caironi and C. Bertarelli, *J. Mater. Chem. A*, 2018, **6**, 15294–15302.

30 Y. Zeng, W. Zheng, Y. Guo, G. Han and Y. Yi, *J. Mater. Chem. A*, 2020, **8**, 8323–8328.

31 W. Zhao, J. Ding, Y. Zou, C. Di and D. Zhu, *Chem. Soc. Rev.*, 2020, **49**, 7210–7228.

32 T. Minakata, I. Nagoya and M. Ozaki, *J. Appl. Phys.*, 1991, **69**, 7354–7356.

33 G. Parthasarathy, C. Shen, A. Kahn and S. R. Forrest, *J. Appl. Phys.*, 2001, **89**, 4986–4992.

34 A. Ali Benamara, M. Galtier and A. Montaner, *Synth. Met.*, 1991, **41**, 45–48.

35 P. Piromreun, H. S. Oh, Y. Shen, G. G. Malliaras, J. C. Scott and P. J. Brock, *Appl. Phys. Lett.*, 2000, **77**, 2403–2405.

36 T. Sakanoue and H. Sirringhaus, *Nat. Mater.*, 2010, **9**, 736–740.

37 J. Meyer, S. Hamwi, S. Schmale, T. Winkler, H. H. Johannes, T. Riedl and W. Kowalsky, *J. Mater. Chem.*, 2009, **19**, 702–705.

38 T. Glaser, S. Beck, B. Lunkenheimer, D. Donhauser, A. Köhn, M. Kröger and A. Pucci, *Org. Electron.*, 2013, **14**, 575–583.

39 W. Gao and A. Kahn, *J. Appl. Phys.*, 2003, **94**, 359–366.

40 K. H. Yim, G. L. Whiting, C. E. Murphy, J. J. M. Halls, J. H. Burroughes, R. H. Friend and J. S. Kim, *Adv. Mater.*, 2008, **20**, 3319–3324.

41 E. F. Aziz, A. Vollmer, S. Eisebitt, W. Eberhardt, P. Pingel, D. Neher and N. Koch, *Adv. Mater.*, 2007, **19**, 3257–3260.

42 H. Méndez, G. Heimel, S. Winkler, J. Frisch, A. Opitz, K. Sauer, B. Wegner, M. Oehzelt, C. Röthel, S. Duhm, D. Többens, N. Koch and I. Salzmann, *Nat. Commun.*, 2015, **6**, 1–11.

43 S. Nam, J. Kim, H. Lee, H. Kim, C. S. Ha and Y. Kim, *ACS Appl. Mater. Interfaces*, 2012, **4**, 1281–1288.

44 B. Yurash, D. X. Cao, V. V. Brus, D. Leifert, M. Wang, A. Dixon, M. Seifrid, A. E. Mansour, D. Lungwitz, T. Liu, P. J. Santiago, K. R. Graham, N. Koch, G. C. Bazan and T. Q. Nguyen, *Nat. Mater.*, 2019, **18**, 1327–1334.

45 S. Guha, F. S. Goodson, L. J. Corson and S. Saha, *J. Am. Chem. Soc.*, 2012, **134**, 13679–13691.

46 C. D. Weber, C. Bradley and M. C. Lonergan, *J. Mater. Chem. A*, 2014, **2**, 303–307.

47 B. D. Naab, S. Guo, S. Olthof, E. G. B. Evans, P. Wei, G. L. Millhauser, A. Kahn, S. Barlow, S. R. Marder and Z. Bao, *J. Am. Chem. Soc.*, 2013, **135**, 15018–15025.

48 F. Ghani, A. Opitz, P. Pingel, G. Heimel, I. Salzmann, J. Frisch, D. Neher, A. Tsami, U. Scherf and N. Koch, *J. Polym. Sci. Part B Polym. Phys.*, 2015, **53**, 58–63.

49 M. L. Tietze, J. Benduhn, P. Pahner, B. Nell, M. Schwarze, H. Kleemann, M. Krammer, K. Zojer, K. Vandewal and K. Leo, *Nat. Commun.*, 2018, **9**, 1–8.

50 H. Yan and W. Ma, *Adv. Funct. Mater.*, 2022, **32**, 1–12.

51 T. J. Aubry, J. C. Axtell, V. M. Basile, K. J. Winchell, J. R. Lindemuth, T. M. Porter, J. Y. Liu, A. N. Alexandrova, C. P. Kubiak, S. H. Tolbert, A. M. Spokoyny and B. J. Schwartz, *Adv. Mater.*, 2019, **31**, 1–8.

52 D. Kiefer, R. Kroon, A. I. Hofmann, H. Sun, X. Liu, A. Giovannitti, D. Stegerer, A. Cano, J. Hynynen, L. Yu, Y. Zhang, D. Nai, T. F. Harrelson, M. Sommer, A. J. Moulé, M. Kemerink, S. R. Marder, I. McCulloch, M. Fahlman, S. Fabiano and C. Müller, *Nat. Mater.*, 2019, **18**, 149–155.

53 P. Pingel and D. Neher, *Phys. Rev. B - Condens. Matter Mater. Phys.*, 2013, **87**, 1–9.

54 A. Jha, H. G. Duan, V. Tiwari, M. Thorwart and R. J. D. Miller, *Chem. Sci.*, 2018, **9**, 4468–4476.

55 A. Mityashin, Y. Olivier, T. Van Regemorter, C. Rolin, S. Verlaak, N. G. Martinelli, D. Beljonne, J. Cornil, J. Genoe and P. Heremans, *Adv. Mater.*, 2012, **24**, 1535–1539.

56 Z. Liang, Y. Zhang, M. Souri, X. Luo, A. M. Boehm, R. Li, Y. Zhang, T. Wang, D. Y. Kim, J. Mei, S. R. Marder and K. R. Graham, *J. Mater. Chem. A*, 2018, **6**, 16495–16505.

57 Y. Karpov, T. Erdmann, I. Raguzin, M. Al-Hussein, M. Binner, U. Lappan, M. Stamm, K. L. Gerasimov, T. Beryozkina, V. Bakulev, D. V. Anokhin, D. A. Ivanov, F. Günther, S. Gemming, G. Seifert, B. Voit, R. Di Pietro and A. Kiriy, *Adv. Mater.*, 2016, **28**, 6003–6010.

58 R. A. Schlitz, F. G. Brunetti, A. M. Glaudell, P. L. Miller, M. A. Brady, C. J. Takacs, C. J. Hawker and M. L. Chabinyc, *Adv. Mater.*, 2014, **26**, 2825–2830.

59 W. Zhao, J. Ding, Y. Zou, C. A. Di and D. Zhu, *Chem. Soc. Rev.*, 2020, **49**, 7210–7228.

60 J. Liu, B. Van Der Zee, D. R. Villava, G. Ye, S. Kahmann, M. Kamperman, J. Dong, L. Qiu, G. Portale, M. A. Loi, J. C. Hummelen, R. C. Chiechi, D. Baran and L. J. A. Koster, *ACS Appl. Mater. Interfaces*, 2021, **13**, 29858–29865.

61 L. Qiu, J. Liu, R. Alessandri, X. Qiu, M. Koopmans, R. W. A. Havenith, S. J. Marrink, R. C. Chiechi, L. J. Anton Koster and J. C. Hummelen, *J. Mater. Chem. A*, 2017, **5**, 21234–21241.

62 D. Kiefer, A. Giovannitti, H. Sun, T. Biskup, A. Hofmann, M. Koopmans, C. Cendra, S. Weber, L. J. Anton Koster, E. Olsson, J. Rivnay, S. Fabiano, I. McCulloch and C. Müller, *ACS Energy Lett.*, 2018, **3**, 278–285.

63 R. Kroon, D. Kiefer, D. Stegerer, L. Yu, M. Sommer and C. Müller, *Adv. Mater.*, 2017, **29**, 35–37.

64 J. Liu, L. Qiu, R. Alessandri, X. Qiu, G. Portale, J. J. Dong, W. Talsma, G. Ye, A. A. Sengrian, P. C. T. Souza, M. A. Loi, R. C. Chiechi, S. J. Marrink, J. C. Hummelen and L. J. A. Koster, *Adv. Mater.*, 2018, **30**, 1–9.

65 J. Liu, S. Maity, N. Roosloot, X. Qiu, L. Qiu, R. C. Chiechi, J. C. Hummelen, E. von Hauff and L. J. A. Koster, *Adv. Electron. Mater.*, 2019, **5**, 1–8.

66 J. Liu, G. Ye, H. G. O. Potgieser, M. Koopmans, S. Sami, M. I. Nugraha, D. R. Villalva, H. Sun, J. Dong, X. Yang, X. Qiu, C. Yao, G. Portale, S. Fabiano,

T. D. Anthopoulos, D. Baran, R. W. A. Havenith, R. C. Chiechi and L. J. A. Koster, *Adv. Mater.*, 2021, **33**, 1–9.

67 Y. Lu, Z. Di Yu, Y. Liu, Y. F. Ding, C. Y. Yang, Z. F. Yao, Z. Y. Wang, H. Y. You, X. F. Cheng, B. Tang, J. Y. Wang and J. Pei, *J. Am. Chem. Soc.*, 2020, **142**, 15340–15348.

68 A. Giovannitti, I. P. Maria, D. Hanifi, M. J. Donahue, D. Bryant, K. J. Barth, B. E. Makdah, A. Savva, D. Moia, M. Zetek, P. R. F. Barnes, O. G. Reid, S. Inal, G. Rumbles, G. G. Malliaras, J. Nelson, J. Rivnay and I. McCulloch, *Chem. Mater.*, 2018, **30**, 2945–2953.

69 D. T. Scholes, S. A. Hawks, P. Y. Yee, H. Wu, J. R. Lindemuth, S. H. Tolbert and B. J. Schwartz, *J. Phys. Chem. Lett.*, 2015, **6**, 4786–4793.

70 I. E. Jacobs, E. W. Aasen, J. L. Oliveira, T. N. Fonseca, J. D. Roehling, J. Li, G. Zhang, M. P. Augustine, M. Mascal and A. J. Moulé, *J. Mater. Chem. C*, 2016, **4**, 3454–3466.

71 C. Liu, J. Jang, Y. Xu, H. J. Kim, D. Khim, W. T. Park, Y. Y. Noh and J. J. Kim, *Adv. Funct. Mater.*, 2015, **25**, 758–767.

72 S. Olthof, S. Mehraeen, S. K. Mohapatra, S. Barlow, V. Coropceanu, J. L. Brédas, S. R. Marder and A. Kahn, *Phys. Rev. Lett.*, 2012, **109**, 1–5.

73 M. H. Futscher, T. Schultz, J. Frisch, M. Ralaiarisoa, E. Metwalli and M. V Nardi, .

74 J. H. Lee and J. J. Kim, *Phys. Status Solidi Appl. Mater. Sci.*, 2012, **209**, 1399–1413.

75 H. Ishii, N. Hayashi, E. Ito, Y. Washizu, K. Sugi, Y. Kimura, M. Niwano, Y. Ouchi and K. Seki, *Phys. Status Solidi Appl. Res.*, 2004, **201**, 1075–1094.

76 J. H. Oh, P. Wei and Z. Bao, *Appl. Phys. Lett.*, 2010, **97**, 243305.

77 M. Massetti, F. Jiao, A. J. Ferguson, D. Zhao, K. Wijeratne, A. Würger, J. L. Blackburn, X. Crispin and S. Fabiano, *Chem. Rev.*, 2021, **121**, 12465–12547.

78 H. I. Un, S. A. Gregory, S. K. Mohapatra, M. Xiong, E. Longhi, Y. Lu, S. Rigin, S. Jhulki, C. Y. Yang, T. V. Timofeeva, J. Y. Wang, S. K. Yee, S. Barlow, S. R. Marder and J. Pei, *Adv. Energy Mater.*, 2019, **9**, 1–10.

79 C. Y. Yang, W. L. Jin, J. Wang, Y. F. Ding, S. Nong, K. Shi, Y. Lu, Y. Z. Dai, F. D. Zhuang, T. Lei, C. A. Di, D. Zhu, J. Y. Wang and J. Pei, *Adv. Mater.*, 2018, **30**, 1–9.

80 M. Pfeiffer, A. Beyer, T. Fritz and K. Leo, *Appl. Phys. Lett.*, 1998, **73**, 3202–3204.

81 P. K. Koech, A. B. Padmaperuma, L. Wang, J. S. Swensen, E. Polikarpov, J. T. Darsell, J. E. Rainbolt and D. J. Gaspar, 2010, 3926–3932.

82 A. M. Kandabarow, Y. Qi, T. Sajoto, M. Kr, W. Park, S. Barlow, E. Kim, L. Wielunski, L. C. Feldman, R. A. Bartynski, J. Br, S. R. Marder and A. Kahn, 2010, **4**, 524–531.

83 A. I. Hofmann, R. Kroon, S. Zokaei, E. Järsvall, C. Malacrida, S. Ludwigs, T. Biskup and C. Müller, 2020, **6**, 1–8.

84 P. Zalar, M. Kuik, Z. B. Henson, C. Woellner, Y. Zhang, A. Sharenko, G. C. Bazan and T. Q. Nguyen, *Adv. Mater.*, 2014, **26**, 724–727.

85 V. Untilova, J. Hynynen, A. I. Hofmann, D. Scheunemann, Y. Zhang, S. Barlow, M. Kemerink, S. R. Marder, L. Biniek, C. Mu and M. Brinkmann, 2020, **53**, 6314–6321.

86 Y. Zhong, V. Untilova, D. Muller, S. Guchait, C. Kiefer, L. Herrmann, N. Zimmermann, M. Brosset, T. Heiser and M. Brinkmann, *Adv. Funct. Mater.*, 2022, **32**, 1–11.

87 V. Vijayakumar, P. Durand, H. Zeng, V. Untilova, L. Herrmann, A. Patrick, L. Nicolas and M. Brinkmann, *J. Mater. Chem. C*, 2020, **8**, 16470–16482.

88 H. Shi, C. Liu, Q. Jiang and J. Xu, 2015, 1–16.

89 N. Kim, S. Kee, S. H. Lee, B. H. Lee, Y. H. Kahng, Y.-R. Jo, B.-J. Kim and K. Lee, *Adv. Mater.*, 2014, **26**, 2268–2272.

90 D. Yuan, W. Liu and X. Zhu, *Chem. Soc. Rev.*, 2023, 3842–3872.

91 K. Shi, F. Zhang, C. A. Di, T. W. Yan, Y. Zou, X. Zhou, D. Zhu, J. Y. Wang and J. Pei, *J. Am. Chem. Soc.*, 2015, **137**, 6979–6982.

92 Y. Lu, Z. Di Yu, H. I. Un, Z. F. Yao, H. Y. You, W. Jin, L. Li, Z. Y. Wang, B. W. Dong, S. Barlow, E. Longhi, C. an Di, D. Zhu, J. Y. Wang, C. Silva, S. R. Marder and J. Pei, *Adv. Mater.*, 2021, **33**, 1–7.

93 H. Guo, C. Y. Yang, X. Zhang, A. Motta, K. Feng, Y. Xia, Y. Shi, Z. Wu, K. Yang, J. Chen, Q. Liao, Y. Tang, H. Sun, H. Y. Woo, S. Fabiano, A. Facchetti and X. Guo, *Nature*, 2021, **599**, 67–73.

94 K. Feng, W. Yang, S. Y. Jeong, S. Ma, Y. Li, J. Wang, Y. Wang, H. Y. Woo, P. Kwok, L. Chan, G. Wang and X. Guo, 2023, **2210847**, 1–9.

95 S. Deng, J. Liu, B. Meng, J. Liu and L. Wang, *ACS Appl. Mater. Interfaces*, 2023, **15**, 45190–45200.

96 H. Tang, Y. Liang, C. Liu, Z. Hu, Y. Deng, H. Guo, Z. Yu, A. Song, H. Zhao, D. Zhao, Y. Zhang, X. Guo, J. Pei, Y. Ma, Y. Cao and F. Huang, *Nature*,

2022, **611**, 271–277.

97 D. M. de Leeuw, M. M. J. Simenon, A. R. Brown and R. E. F. Einerhand, *Synth. Met.*, 1997, **87**, 53–59.

98 Z. Chen, Y. Zheng, H. Yan and A. Facchetti, *J. Am. Chem. Soc.*, 2009, **131**, 8–9.

99 A. Nollau, M. Pfeiffer, T. Fritz and K. Leo, *J. Appl. Phys.*, 2000, **87**, 4340–4343.

100 H. Ishii, K. Sugiyama, D. Yoshimura, E. Ito, Y. Ouchi and K. Seki, *IEEE J. Sel. Top. Quantum Electron.*, 1998, **4**, 24–32.

101 S. Tanaka, K. Kanai, E. Kawabe, T. Iwahashi, T. Nishi, Y. Ouchi and K. Seki, *Japanese J. Appl. Physics, Part 1 Regul. Pap. Short Notes Rev. Pap.*, 2005, **44**, 3760–3763.

102 C. K. Chan, F. Amy, Q. Zhang, S. Barlow, S. Marder and A. Kahn, *Chem. Phys. Lett.*, 2006, **431**, 67–71.

103 T. Menke, D. Ray, J. Meiss, K. Leo and M. Riede, *Appl. Phys. Lett.*, 2012, **100**, 1–4.

104 M. Fujitsuka, C. Luo and O. Ito, *J. Phys. Chem. B*, 1999, **103**, 445–449.

105 Y. M. Gross, D. Trefz, C. DIngler, D. Bauer, V. Vijayakumar, V. Untilova, L. Biniek, M. Brinkmann and S. Ludwigs, *Chem. Mater.*, 2019, **31**, 3542–3555.

106 A. G. Werner, F. Li, K. Harada, M. Pfeiffer, T. Fritz and K. Leo, *Appl. Phys. Lett.*, 2003, **82**, 4495–4497.

107 A. Werner, F. Li, K. Harada, M. Pfeiffer, T. Fritz, K. Leo and S. Machill, *Adv. Funct. Mater.*, 2004, **14**, 255–260.

108 P. Wei, T. Menke, B. D. Naab, K. Leo, M. Riede and Z. Bao, *J. Am. Chem. Soc.*, 2012, **134**, 3999–4002.

109 M. Schwarze, B. D. Naab, M. L. Tietze, R. Scholz, P. Pahner, F. Bussolotti, S. Kera, D. Kasemann, Z. Bao and K. Leo, *ACS Appl. Mater. Interfaces*, 2018, **10**, 1340–1346.

110 F. Li, A. Werner, M. Pfeiffer, K. Leo and X. Liu, *J. Phys. Chem. B*, 2004, **108**, 17076–17082.

111 P. Wei, J. H. Oh, G. Dong and Z. Bao, *J. Am. Chem. Soc.*, 2010, **132**, 8852–8853.

112 C. Y. Yang, Y. F. Ding, D. Huang, J. Wang, Z. F. Yao, C. X. Huang, Y. Lu, H. I. Un, F. D. Zhuang, J. H. Dou, C. an Di, D. Zhu, J. Y. Wang, T. Lei and

J. Pei, *Nat. Commun.*, 2020, **11**, 1–10.

113 S. Guo, S. B. Kim, S. K. Mohapatra, Y. Qi, T. Sajoto, A. Kahn, S. R. Marder and S. Barlow, *Adv. Mater.*, 2012, **24**, 699–703.

114 B. D. Naab, S. Zhang, K. Vandewal, A. Salleo, S. Barlow, S. R. Marder and Z. Bao, *Adv. Mater.*, 2014, **26**, 4268–4272.

115 S. Zhang, B. D. Naab, E. V. Jucov, S. Parkin, E. G. B. Evans, G. L. Millhauser, T. V. Timofeeva, C. Risko, J. L. Brédas, Z. Bao, S. Barlow and S. R. Marder, *Chem. - A Eur. J.*, 2015, **21**, 10878–10885.

116 F. Aniés, M. I. Nugraha, A. Fall, J. Panidi, Y. Zhao, P. Vanelle, L. Tsetseris, J. Broggi, T. D. Anthopoulos and M. Heeney, *Adv. Funct. Mater.*, 2023, **33**, 1–10.

117 S. Jhulki, H. I. Un, Y. F. Ding, C. Risko, S. K. Mohapatra, J. Pei, S. Barlow and S. R. Marder, *Chem*, 2021, **7**, 1050–1065.

118 J. Xie, W. Lin, G. C. Bazan, T. Pullerits, K. Zheng and Z. Liang, *J. Mater. Chem. A*, 2022, **10**, 18845–18855.

119 W. Xu, T.-S. Lim, H.-K. Seo, S.-Y. Min, H. Cho, M.-H. Park, Y.-H. Kim and T.-W. Lee, *Small*, 2014, **10**, 1999–2005.

120 H. Wang, P. Wei, Y. Li, J. Han, H. R. Lee, B. D. Naab, N. Liu, C. Wang, E. Adijanto, B. C. K. Tee, S. Morishita, Q. Li, Y. Gao, Y. Cui and Z. Bao, *Proc. Natl. Acad. Sci. U. S. A.*, 2014, **111**, 4776–4781.

121 L. Lanzetta, L. Gregori, L. H. Hernandez, A. Sharma, S. Kern, A. M. Kotowska, A. H. Emwas, L. Gutiérrez-Arzaluz, D. J. Scurr, M. Piggott, D. Meggiolaro, M. A. Haque, F. De Angelis and D. Baran, *ACS Energy Lett.*, 2023, **8**, 2858–2867.

122 R. E. Peierls, *Quantum theory of solids*, Oxford University Press, 1955.

Chapter 2

H_2 detection as a tool for the characterization of the doping process

---

Part of the results of this work has been published in a paper: F. Pallini, S. Mattiello, N. Manfredi, S. Mecca, A. Fedorov, M. Sassi, K. Al Kurdi, Y.F. Ding, C.K. Pan, J. Pei, S. Barlow, S.R. Marder, T.Q. Nguyen, and L. Beverina, "Direct detection of molecular hydrogen upon p and n-doping of organic semiconductors with complex oxidants or reductants".

J. Mater. Chem. A, **2023**, 11, 8192

The first step for an efficient use of a dopant, is understanding the corresponding doping mechanism. This first experimental-related chapter thus deals with 4-(1,3-Dimethyl-2,3-dihydro-1H-benzimidazol-2-yl)-N,N-dimethylaniline (N-DMBI-H) complex doping mechanism and its investigation. After a brief introduction on the possible doping pathways of DMBI based dopants, the innovative application of H_2 detection techniques as direct method to investigate doping processes is showcased and new insights on the doping mechanism are provided. The generality and potentiality of the proposed method are then demonstrated in the study of another dopant and in the use of the same technique for the characterization of N-DMBI-H doping processes happening in thermally activated solutions.

This work was performed in collaboration with the Laboratory for Nanostructure Epitaxy and Spintronics on Silicon (L-NESS) of Como, Thuc-Quyen Nguyen's research group at the Center for Polymers and Organic Solids (CPOS, University of California, Santa Barbara), Seth R. Marder's group at University of Colorado, Boulder and the Italian Institute of Technology of Milan(IIT). Synthesis of BDOPV acceptors was performed by Jian Pei's group at Peking University. EPR measurements were performed by Professor Massimiliano D'Arienzo at the University of Milano-Bicocca.

2.1 N-DMBI-H doping: a complex process

As aforementioned, N-DMBI-H is a dopant precursor and its doping process does not happen as a direct electron transfer (ET). If feasible with compounds having very high electron affinities, this pathway is in fact highly endergonic in the case of most n-type OSC, since the HOMO level of N-DMBI-H (~ -4.6 eV)[1] is far lower with respect to their LUMO level, in most cases located at higher energies (~ -4.0 eV).[2] The charge transfer process in the case of this dopant is thus coupled to more complex chemical reactions that do not depend solely on the energy level alignment of the species involved and that generally (few exceptions are described)[3–5] require some energy to be activated. There isn't universal consensus regarding to the mechanism behind the overall doping process, including the side products not directly involved in the electron transfer steps. More than one pathway has been proposed and the factors influencing the electron transfer efficiency, or the doping possible side-reactions are still under investigation.

2.1.1 N-DMBI-H possible doping mechanisms

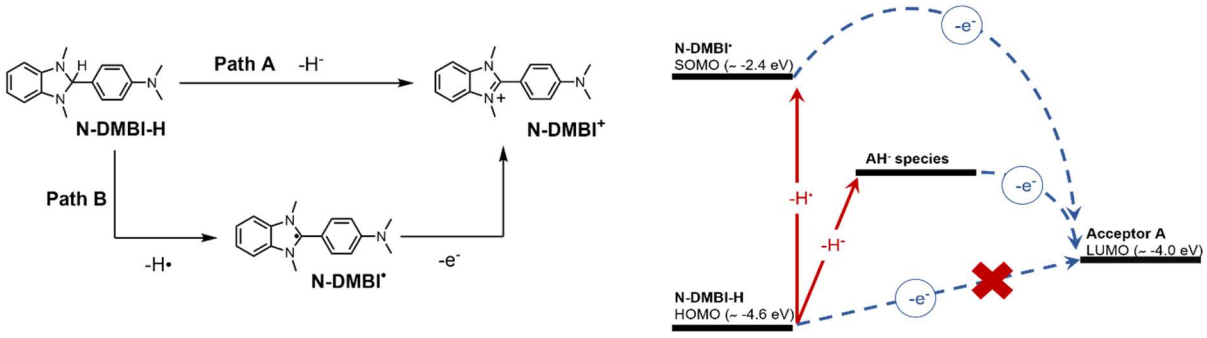

Figure 2.1 Left: plausible doping pathways of N-DMBI-H: hydride transfer (Path A) or hydrogen atom transfer (Path B). Right: energy level alignment of N-DMBI-H and of the species obtained via hydride or hydrogen atom transfer processes (AH^- and N-DMBI$^\bullet$) with respect to common OSC LUMO levels. ET processes are highlighted with dashed blue arrows.

Two plausible mechanisms have been proposed for N-DMBI-H doping (**Figure 2.1a**), based on its organic hydride donor nature.[5–7]One consists in a direct hydride transfer (H^-) from the dopant to the acceptor with formation of **N-DMBI$^+$** cation and the hydrogenated species **AH^- (Figure 2.1a, Path A)**. The other is instead the homolytic cleavage of the C-H aminal bond of N-DMBI-H, with consequent transfer of hydrogen ($H^\bullet$) to the acceptor and formation of the **N-DMBI$^\bullet$** radical (**Figure 2.1a, Path B**). The hydrogenated species **AH^-** and the **N-DMBI$^\bullet$** radical, whose Singly Occupied Molecular Orbital (SOMO) level is around -2.4 eV,[1] are both more electron rich species than N-DMBI-H. The electron transfer from these derivatives to the acceptor is thus feasible and can efficiently lead to formation of the acceptor polaron **$A^{\bullet-}$ (Figure 2.1b)**.

Whether the mechanism happens via hydride transfer or hydrogen removal is still debated and only for a few derivatives there is conclusive evidence of the preferred pathway. In the case of fullerenes derivatives, like [6,6]-phenyl-C61-butyric acid methyl

ester ($PC_{61}BM$), or benzodifurandione-based oligo(p-phenylene vinylene) derivatives (BDOPV), experimental and computational studies confirmed hydride transfer to be the first step of the process, at least when this happens in solution and at room temperature.[5,7,8] In other works, homolytic cleavage with N-DMBI$^{\bullet}$ radical formation was instead proposed as main doping mechanism, even if without much experimental evidence.[1,9,10]

Determining a dominant doping reaction is indeed not straightforward: the doping mechanisms seems in fact to depend much on the selected semiconductor target.[7] Computational studies in fact suggest that the specific nature of the interaction between the dopant and the acceptor can define, under an energetic point of view, which is the dominant process[4]. The hydride accepting capability of the semiconductors is also considered as another factor influencing the doping pathway and efficiency.[11]

2.1.2 The fate of the hydrogen atom

Whichever the mechanism, N-DMBI-H mediated doping processes involves transfers of hydrogen atoms or ions to the acceptor in one of the reaction steps, since N-DMBI^{+} is always among the reaction products. Hydrogenation of the acceptor **A** structure with formation of **AH$^{\bullet}$** species should thus in principle happens as result of all the previously discussed doping pathways, as depicted in **Figure 2.2.** In the case of hydride transfer mediated doping (**Path A**), **AH$^{\bullet}$** forms as a result of ET from **AH-** to a neutral acceptor; if the process happens via hydrogen atom transfer (**Path B**), **AH$^{\bullet}$** should form due to **H$^{\bullet}$** transfer from the dopant to **A**; even in the less plausible case of a doping mediated by direct electron transfer (**Path C**), **AH$^{\bullet}$** is expected to form via H atom abstraction from the **N-DMBI-H$^{+\bullet}$** radical formed after the initial ET.
The fate of the hydrogen atom thus formed is mostly ignored in the dedicated literature.

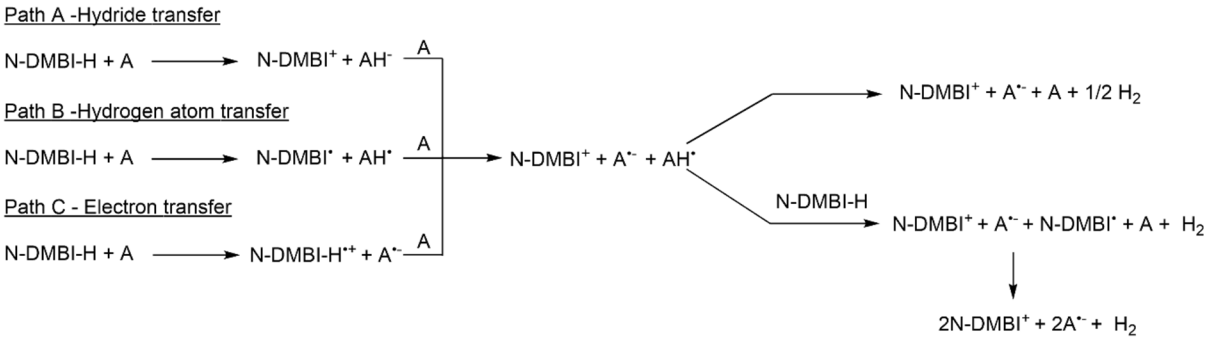

Figure 2.2 Mechanism of the formation of hydrogenated semiconductor species AH$^{\bullet}$ via doping initiated by hydride transfer (Path A), hydrogen atom transfer (Path B) or electron transfer (Path C). The proposed mechanism for molecular H_2 formation is reported as well.

The incorporation of hydrogen in the acceptor structure is one of the possible answers and was experimentally demonstrated as consequence of the doping of specific materials. This is the case for example of fullerenes derivatives and $PC_{61}BM$, for which formation of $PC_{61}BMH_x$ and $C_{60}H_x$ hydrides has been reported.[7] Fullerenes are however known to easily undergo hydrogenation reactions.[12] Apart from these few examples,

hydrogenated derivatives have not been directly detected in the study of other semiconductors doping. Fast interaction of two AH$^{\bullet}$ species or of an AH$^{\bullet}$ species and a N-DMBI-H molecule, with formation of molecular hydrogen was thus proposed as another possible doping outcome based on computational studies (**Figure 2.2**).[5] This H_2 evolution has been demonstrated in transition-metal catalysed doping processes.[13] Still no direct evidence of molecular hydrogen formation has been given in non-catalysed N-DMBI-H mediated doping.

The destiny of the H atom in N-DMBI-H mediated doping is not an irrelevant question. Hydrogenation of the acceptor structure might create defects in the conjugation of the doped semiconductor and impact its transport properties. Gaseous H_2 evolution would instead leave unaltered the conductive structure. Further investigation of this possible side-reaction, and its dependence on the semiconductor choice, is thus required to guide in the selection of the right dopant/host combination.

2.2 Aim of the work

When working with molecular dopants, a deep understanding of how the charge injection process happen is fundamental to obtain good performances in devices applications. A good knowledge of the mechanisms helps in fact in selecting the best dopant/semiconductor systems and processing conditions for obtaining efficient doping and high performances. Looking at the literature, it appears evident that there are still some open questions on the working mechanism on N-DMBI-H that need to be answered for a better use of this dopant, especially in relation of its possible side-reactions.

In this work, we thus aimed at investigating the doping mechanism of N-DMBI-H n-type dopant and the fate of the H atom involved in the process. For the purpose, we adapted two different H_2 detection techniques: Gas Chromatography (GC) and Residual Gas Analysis associated with low Mass Spectrometry detector (RGA-MS). We firstly dedicated at experimentally demonstrating H_2 evolution as possible outcome of the doping and at studying this reaction dependence on the semiconductor counterpart. We then aimed at investigating the specific reactive sites involved in the H_2 evolution mechanism. The generality of the GC-H_2 detection method was then further tested in the study of doping mechanisms mediated by other dopants.

While using the GC-H_2-detection technique we became aware of its advantages as a possible semiconductor doping characterization method. We therefore further extended the application of the approach in the study of thermally activated N-DMBI-H doping happening in highly concentrated solution.

2.3 Before starting: a warning on palladium impurities

As aforementioned, H_2 evolution has been demonstrated as outcome of N-DMBI-H doping processes catalysed by gold nanoparticles in a recent work by Facchetti's group.

In the same work, the possibility of catalysing the process with Palladium based catalyst is also showcased.[13] In a previous work by Thorn's group, the reaction between N-DMBI-H derivatives and Pd^{2+} species is reported to form Pd(0) species, that can hereinafter trigger H_2 evolution.[14] This scenario raises an issue for the analysis of H_2 evolution in uncatalyzed N-DMBI-H doping since palladium and other metal-based catalyst are widely used for the synthesis of conjugated molecules and organic semiconductors.[15] Presence of unwanted metal traces in the samples might indeed alter the result of the H_2 detection experiments. Purification from residual catalyst appears then to be of extreme importance for the purpose. For this reason, whenever we used non-commercial batches of semiconductors synthesized via metal-catalysed reactions (this is the case for example of P(NDI2OD-T2) polymer), we carefully purified the product to remove catalyst traces and subsequently analysed the obtained material via Inductively Couple Plasma coupled to Optical Emission Spectroscopy (ICP-OES) to verify the content of residual Pd to be below the detection limit (100 ppb).

2.4 Investigation of N-DMBI-H doping via Gas Chromatography- H_2 detection

We firstly approached the investigation of N-DMBI-H doping by using a Gas Chromatographic (GC) setup calibrated for the detection of H_2, O_2 and N_2. The details of the instrumental features are reported in **Figure 2.3.**

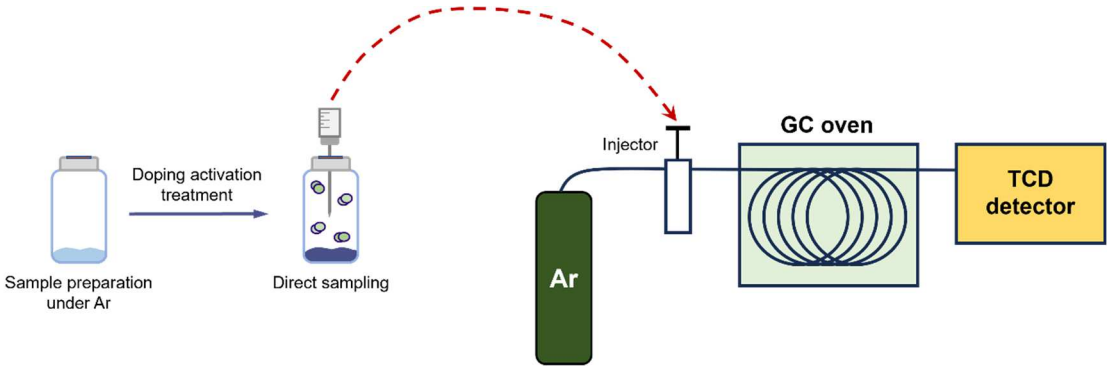

Figure 2.3 Experimental setup used for GC based H_2 detection experiments.

The setup is equipped with a gas chromatographic column made of molecular sieves and a thermal conductivity detector (TCD). The TCD produces voltage signals in response to changes in thermal conductivity of the carrier gas (argon) due to elution of gaseous analytes. Each analysed sample was prepared under argon atmosphere in a GC-MS vial, sealed with a PTFE/silicone septum equipped with a crimp cap. After the required treatment, the head space of the vial was sampled via a gas-tight volumetric syringe and analysed using the GC instrument. The calibration of the GC setup, allowed then to estimate the amount of detected H_2 via chromatogram peak area integration. Further details on the instrument and on the experimental procedure are reported in the experimental methods section.

2.4.1 Study of doping of P(NDI2OD-T2) polymer

We selected the N-DMBI-H/P(NDI2OD-T2) blend as first reference system for our study due to the vast literature dedicated to the doping of P(NDI2OD-T2) polymer.[16,17] Since the doping of this semiconductor is generally activated in the solid state, we started investigating processes happening in such conditions. Our setup is not sensitive enough to allow the detection of H_2 from doping of thin films, due to the very small amount of gas that would evolve from such small amounts of material. We thus decided to work on powder mixtures and help the dopant/semiconductor blending using small volumes of chlorobenzene, which was subsequently dried under N_2 flow.
We firstly analysed a blend of N-DMBI-H/P(NDI2ODT2) in 2:1 molar ratio. We used N-DMBI-H in large excess to guarantee its easy interaction with the semiconductor. Since the doping process of P(NDI2OD-T2) is reported as thermally activated, we subjected the sample to a 2 hours thermal treatment at 150 °C. Such conditions correspond to a common thermal treatment reported in the literature to lead to the maximum increase in the conductivity of N-DMBI-H/P(NDI2OD-T2) films.[16] Moreover, this treatment ensures further mixing of the two powders, being the melting point of N-DMBI-H around 110 °C.[9] The obtained results are collected in **Figure 2.4**, together with the molecular structure of all the compounds used for the experiment. Control experiments on samples of pure N-DMBI-H and P(NDI2OD-T2) under the same conditions were performed as well.

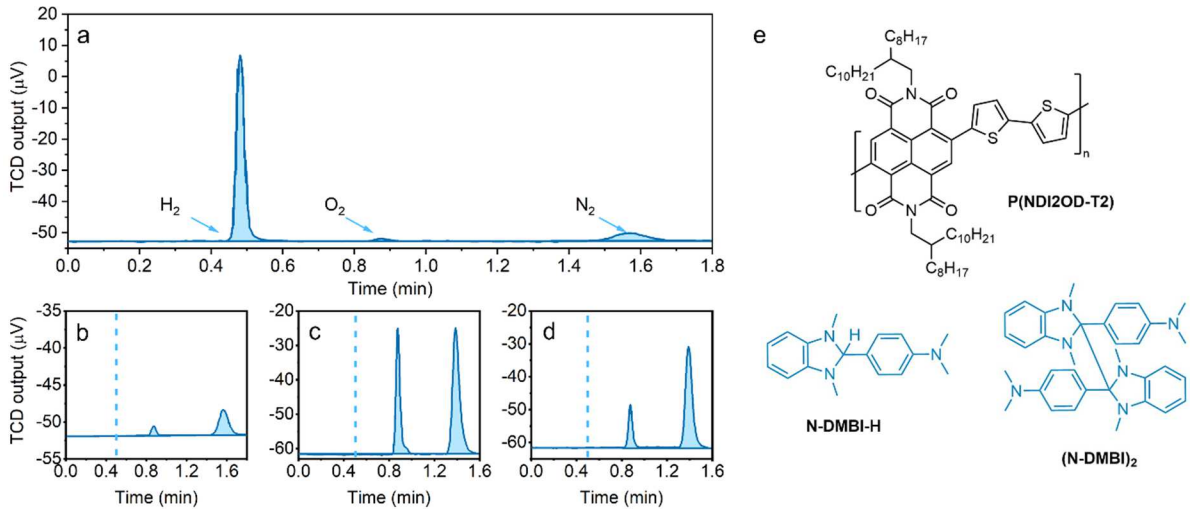

Figure 2.4 GC traces corresponding to the atmosphere of sealed vials containing: N-DMBI-H/P(NDI2OD-T2) 2:1 blend (a); pure N-DMBI-H (b); pure P(NDI2OD-T2) (c); $(N\text{-DMBI})_2$/P(NDI2OD-T2) 1:1 blend (d). Light blue arrows indicate peaks corresponding to H_2, O_2 and N_2 in (a). H_2 retention time is highlighted with a light blue dashed lines in all the other graphs. Molecular structure of P(NDI2OD-T2), N-DMBI-H and $(NDMBI)_2$ (e).

The gas chromatogram related to N-DMBI-H/P(NDI2OD-T2) blend (**Figure 2.4a**) shows an intense H_2 related peak at 0.48 minutes of retention time, demonstrating formation of molecular hydrogen during the process. Two less intense peaks related to oxygen and nitrogen are present at 0.88 minutes and 1.57 minutes of retention time respectively. Their presence is due to contamination with the air naturally present in the syringe needle while sampling the GC-Vial atmosphere. The two control experi-

ments (**Figure 2.4b** and **c**) show instead no sign of H_2 formation, confirming that molecular hydrogen evolution is the consequence of the interaction between the dopant and the n-type polymer. To further confirm that H_2 formation is triggered by the transfer of H atoms/ions from N-DMBI-H to the semiconductor during the doping, we repeated the experiment using a dimeric dopant, $(N\text{-}DMBI)_2$, whose doping mechanism is known to happen via clean electron transfer.[18] Again, no molecular hydrogen was detected during the experiment, confirming the origin of the H_2 evolution (**Figure 2.4d**).

Via chromatogram peak area integration, we estimated the concentration of H_2 to be around 6000 ppm[††] in the vial containing the P(NDI2OD-T2)/N-DMBI-H blend. Considering the volume of the vial (2 mL), this value corresponds to 0.54 µmol of evolved H_2. The analysed blend contained 19 mg of polymer (19 µmol of repeat units) and 11 mg of N-DMBI-H (41 µmol). According to the hypothesized H_2 formation mechanisms previously shown in **Figure 2.2**, for every mole of H_2 formed two moles of N-DMBI-H should be consumed and two moles of polarons ($A^{\bullet-}$) should be obtained. Since we observed that no H_2 forms by heating N-DMBI-H alone and, in our experiment, the P(NDI2OD-T2) repeat unit is the limiting reagent, the maximum theoretical amount of H_2 expected is 9.6 µmol. This value is eighteen times greater than what we measured and suggest that we reached a polymer doping level of 5.6% during our experiment. This discrepancy can be explained in two ways. On one side, doping side reaction leading to acceptor hydrogenation (AH_x) and not involving molecular hydrogen formation cannot be completely excluded: these might lead to underestimated values. On the other hand, the maximum doping level of P(NDI2OD-T2) like derivatives reported in the literature is between 1%[17] and 13%,[19] based on Electron Paramagnetic Resonance (EPR) and electrical measurements. The value we measured is thus pretty much in line with this limit, suggesting that this GC-based method has the potentiality to estimate the amount of activated N-DMBI-H.

2.4.2 Doping mechanism of semiconductors having different molecular structure

After having experimentally demonstrated H_2 formation as a collateral process of doping of P(NDI2OD-T2) with N-DMBI-H, we decided to test the generality of the method on semiconductors having different structure and characteristics. For the purpose, we selected five different semiconductor molecules, whose structure is reported in **Figure 2.5**. The derivatives choice was dictated by two reasons:

- they represent classes of n-dopable semiconductors usually investigated as electron-transport materials: fullerene derivatives ($PC_{61}BM$), naphthalenediimide derivatives (2CN-NDI-C6, and NDI-C8) and extended isoindigos BDOPV derivatives (2CN-BDOPV and 4CN-BDOPV).

[††] Part per millions of H_2 moles with respect to argon moles inside the analysed gas volume.

- Previous works by Marder's group have already analysed the doping mechanisms and kinetics of such compounds (except for 4CN-BDOPV). A comparison with these results can allow for a better interpretation of the H_2 evolution data.[5]

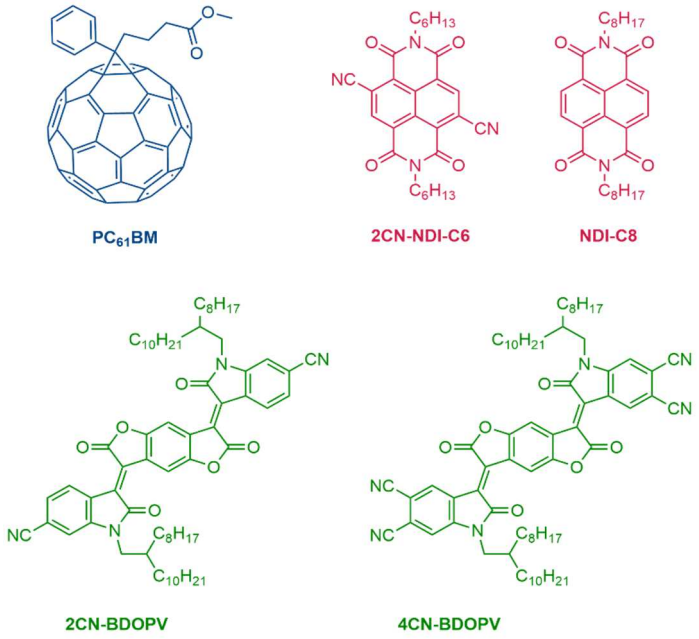

Figure 2.5 chemical structure of the selected N-type semiconductors. Fullerene derivatives are highlighted in blue, naphtalenediimide derivatives in red and extended isoindigo derivatives in green.

The doping mechanism was investigated both in annealed blends and in solution kept at room temperature, to address the effect of the activation conditions on the process.

2.4.2.1 Thermally activated doping in solid blends

We firstly analysed H_2 evolution from solid blends of the selected acceptor and N-DMBI-H. To be consistent with previous experiment on P(NDI2OD-T2) polymer, we firstly prepared the blends and treated the obtained samples under the same conditions. However, previous works on these derivatives suggest that the process can be activated also at room temperature, in the presence of a solvent, with noticeable differences in rates depending on the acceptor used. This means that when preparing blends, molecular H_2 might evolve also prior to solvent evaporation under N_2 flow and, if the doping process is fast enough, most of it might get lost during drying of the sample. This is true in particular for BDOPV derivatives, that showed fast doping kinetics during in-solution studies.[5] For this reason, H_2 detection experiments were performed both on dry blends and on not dried wet blends containing small amounts of chlorobenzene. Both samples were thermally annealed at 150°C for 2 hours before GC analysis. The obtained GC traces are reported in **Figure 2.6**, and the detected H_2 concentrations are collected in **Table 2.1**. Since no noticeable differences were detected in the two set of experiments, I only report here GC traces related to dry blends.

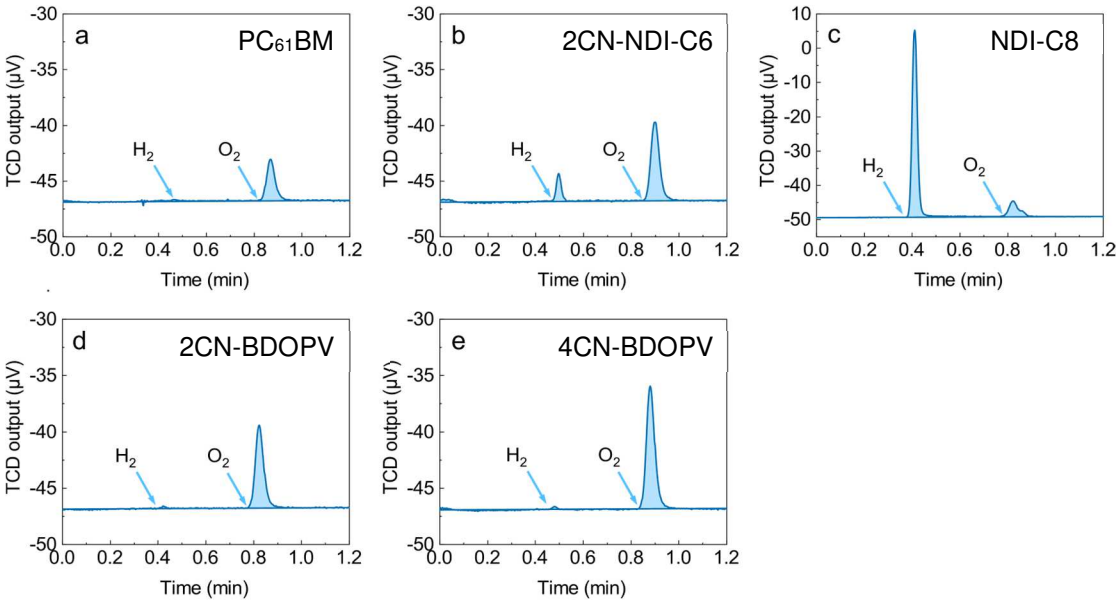

Figure 2.6 GC traces corresponding to the atmosphere of sealed vials containing blends of N-DMBI-H with different acceptors (2:1 mol:mol): $PC_{61}BM$ (a); 2CN-NDI-C6 (b); NDI-C8 (c); 2CN-BDOPV (d); 4CN-BDOPV(e). Light blue arrows indicate peaks corresponding to H_2 and O_2. Small differences in retention time are due to delays in manual injection.

Table 2.1 H_2 concentration values detected in the atmosphere of vials containing blends of different acceptor and N-DMBI-H. Both results of dry and wet blends are here reported.

Acceptor	**N-DMBI-H (molar eq.)**	**H_2 in dry blends (ppm)**	**H_2 in wet blends (ppm)**
$PC_{61}BM$	2	0	0
2CN-NDI-C6	2	85	108
NDI-C8	2	2000	1620
2CN-BDOPV	2	2	18
2CN-BDOPV	0.65	-	0
4CN-BDOPV[a]	2	6	18

[a] This blend was prepared using 0.011 mmol of acceptor instead of 0.015 mmol.

In the case of sample containing $PC_{61}BM$, we did not detect any H_2. This result is in line with previous studies since, as already mentioned, formation of stable hydrogenated $PCBMH_x$ derivatives has been experimentally demonstrated.[7] Our data then confirm that H atoms are incorporated in the structure of the acceptor and do not give rise to H_2 evolution in the case of this class of compounds.

In samples containing BDOPV derivatives, only traces of H_2 were detected. The value is modestly higher in the case of wet blends, which suggest that either the H_2 forms immediately after blending or that its evolution is helped by the presence of a solvent. Still, the concentration detected is extremely low. These compounds are known to be good hydride acceptors and hydrogenated $[2CN\text{-}BDOPV\text{-}H]^-$ species have been ob-

served via NMR as product of N-DMBI-H doping processes, confirming a hydride transfer mediated doping mechanism.[5] The poor H_2 evolution detected is in line with this observation and suggests that most likely the [xCN-BDOPV-H]$^-$ species form and further react to give BDOPVH_x hydrogenated species. However, according to the results of the same reference work, the reaction kinetic of [2CN-BDOPV-H]$^-$ (and plausibly [4CN-BDOPV-H]$^-$) formation is much faster than the following electron transfer from this specie to a neutral acceptor molecule. In the presence of excess dopant, the first hydride transfer step might thus be so fast that no more neutral acceptor remains to be doped in a subsequent ET step, with consequent no formation of 2CN-BDOPV-H$^\bullet$ radical and no H_2 evolution. Our experimental conditions resemble this situation. We thus performed one more experiment preparing a wet blend of 2CN-BDOPV containing sub-stoichiometric amount of N-DMBI-H (0.65 molar eq., see **Table 2.1,** entry 5). This experiment showed again no H_2 production, corroborating the hypothesis that, at least in our experimental conditions, H_2 evolution is not the dominant doping process for these compounds or, if the reaction between [2CN-BDOPV-H]$^-$ and the corresponding undoped 2CN-BDOPV happens, it is very slow.

Concerning naphtalenediimide derivatives, both the analysed acceptors show evident H_2 evolution. The H_2 concentration detected in dry and wet blends is within the same order of magnitude, with variations for the single acceptor probably connected to differences in blends homogeneity and dopant distribution in the sample. The detected amount of H_2 is however very different for the two derivatives: samples containing 2CN-NDI-C6 show H_2 concentration levels in the order of 85-100 ppm, while for NDI-C8 acceptors detected values are between 1600 and 2000 ppm. 2CN-NDI-C6 and NDI-C8 hydrogenated derivatives have never been detected in previous studies on doping happening in solution, but the formation of an NDI-H$^-$ or NDI-H$^\bullet$ like intermediates was confirmed by incorporation of deuterium in the product obtained from doping with deuterated N-DMBI-D.[5] It was thus hypothesized that hydride/H atom transfer happens as first step of the doping and that the hydrogenated intermediates then fast interact to give formation of H_2. Our data on 2CN-NDI-C6 agree with this hypothesis, but the low amount of detected H_2 suggests that either the doping is not particularly efficient, or it happens both via formation of unknown hydrogenated species and molecular

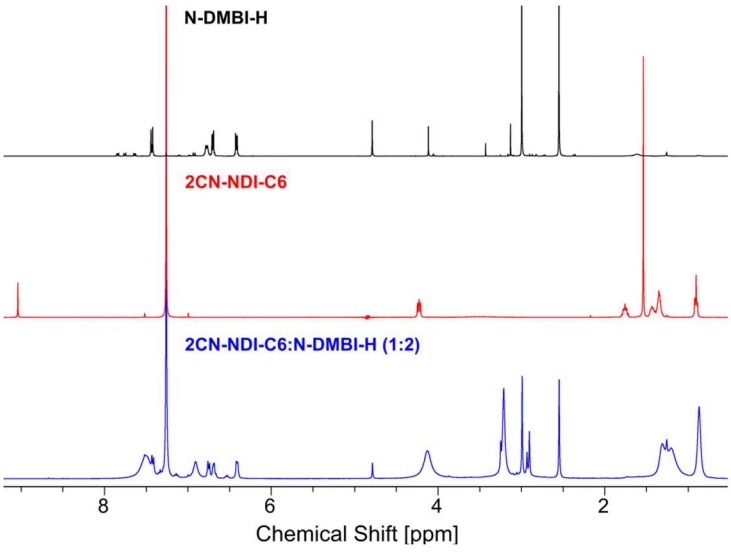

Figure 2.7 solution ^{1}H-NMR spectra of N-DMBI-H (black), 2CN-NDI-C6 (red) and their 1:2 molar blend after thermal annealing (blue) in $CDCl_3$. Peaks appearing after thermal treatment around 3 ppm are related to formation of oxidation products of N-DMBI-H (see chapter 3 and reference 23 for comparison).

H_2. Since previously reported studies on 2CN-NDI-C6 suggest its doping to be more efficient than that of NDI-C8, we consider the second hypothesis to be more likely. To demonstrate the hydrogenation of this acceptor, we tried to characterize the analysed blend via solution NMR. The obtained spectrum is reported in **Figure 2.7,** together with that of N-DMBI-H and pristine 2CN-NDI-C6. Presence of the doped 2CN-NDI-C6 paramagnetic radical anions however leads to shifting/broadening of 2CN-NDI-C6 and N-DMBI-H NMR peaks,[20] making identification of hydrogenated species impossible.

For NDI-C8 instead, the amount of H_2 evolved is closer to that obtained with P(NDI2OD-T2) which hints at a predominant H_2 evolution for this naphthalenediimide derivative. A possible reason behind the different behaviour of these two acceptor is that 2CN-NDI-C6 is a better hydride and hydrogen acceptor than NDI-C8 and the formation of AH^- species is, for this compound, energetically favoured, at least according to computational studies analysing doping in solution.[5] The former acceptor might then form more stable hydrogenated species. However, further studies are required to confirm this speculation.
On the overall, these results support the conclusions of previous studies performed on the same compounds, confirming that the doping mechanism is strongly dependent on the semiconductor and suggesting that the fate of the hydrogen atoms its dictated by hydride accepting capability of the target semiconductor.

2.4.2.2 Doping in solution at room temperature

We then moved to the analysis of doping of the same derivatives in solutions at room temperature. For the purpose we prepared 10mM solutions in chlorobenzene, in the presence of 1 molar equivalent of N-DMBI-H and stored the samples for 2 days under inert atmosphere before sampling for the GC analysis. These conditions were selected to reproduce those of previous works analysing doping mechanisms and kinetics on these compounds.[5] In the case of 2CN-BDOPV, we again considered that dopant stoichiometry might affect the outcome of the experiment, so we prepared also a sample containing 0.5 molar equivalent of N-DMBI-H. The obtained H_2 concentrations are reported in **Table 2.2**. Since no H_2 or only traces of molecular hydrogen were detected for the whole set of experiments, no GC trace is here reported. It is worth mentioning that H_2 leakage from the used GC-MS vials is not fast enough to highly affect the results of this set of experiments within a time span of two days and as such, the obtained data are a reliable picture of the doping process outcome (the

Table 2.2: H_2 concentration values detected in the atmosphere of vials containing 10 mM solutions of different acceptor in chlorobenzene added with 1 molar equivalent of N-DMBI-H

Acceptor	N-DMBI-H (molar eq.)	H_2 concentration (ppm)
$PC_{61}BM$	1	0
2CN-BDOPV	1	0
2CN-BDOPV	0.5	0
2CN-NDI-C6	1	6
NDI-C8	1	2

reader is addressed to **Appendix A** for a detailed description of the H_2 leakage evaluation).

According to Marder's studies on doping of 2CN-BDOPV and $PC_{61}BM$, the kinetic of the process in solution is quite fast for these derivatives and complete conversion of the acceptor to the corresponding radical anion should be obtained within less than one day. Since we analysed samples after 2 days from preparation, data obtained for $PC_{61}BM$ and 2CN-BDOPV again support the results previously reported for such derivatives, hinting that these semiconductors doping happens via hydride transfer and subsequent formation of stable hydrogenated species. In the case of naphtalenediimide derivatives, previous data suggest that the rate of the doping reaction is very slow in solution at room temperature, requiring days to reach completion. This is especially true for the NDI-C8 derivative, for which conversion to the radical anion was reported to be almost negligible even after a timespan of several days.[5] A possible explanation of the low H_2 concentration detected in our set of experiments is then a consequent very slow kinetic for the H_2 formation reaction, due to very low concentration of NDI-H^- and NDI-$H^\bullet$ like species in the reaction environment. In the case of the previously analysed solid blends, where the species were in close proximity one with another and the process was thermally activated, the reaction rate was likely accelerated, which would explain the different amount of H_2 detected. A thermal treatment in principle could increase the rate of the process happening in solution as well.

The obtained results are not conclusive, but they are coherent with those of previous works studying the doping semiconductor dependence and reactions kinetics. Moreover, they further confirm that the doping outcome depends on the activation conditions.

2.5 RGA – H_2 detection: investigation of reactive sites involved in H_2 evolution mechanism

To further investigate the reactive sites involved in the H_2 evolution mechanism, we adapted a homemade setup composed of a high vacuum chamber connected to a Residual Gas Analysis – Mass Spectrometer, a low mass detector capable of discriminating the presence of three hydrogen isotopologues H_2, H-D and D_2. We equipped the vacuum chamber with a remotely controlled lamp heater and a thermocouple, to be capable of heating our samples while monitoring at the same time the temperature inside the chamber and the partial pressure variation of the low mass gases evolved during the doping process. **Figure 2.8** shows a picture of the setup. For the purpose, we

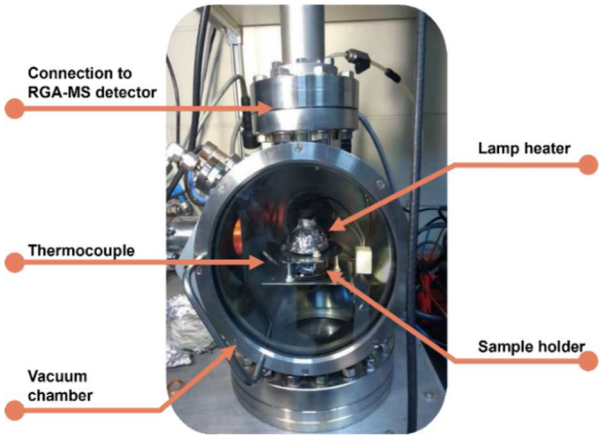

Figure 2.8 Picture of the setup used for RGA-MS H_2 detection experiments.

synthesized the deuterated dopant N-DMBI-D. Since the setup is suitable only for non-volatile samples, we focused the attention on doping of solid blends of P(NDI2OD-T2) polymer, as according to our previous GC-H_2 detection experiments this compound shows the largest H_2 evolution values in such conditions.

We thus prepared a P(NDI2OD-T2)/N-DMBI-D 1:2 (mol:mol) blend and heated the sample at a constant rate of 10°Cmin^{-1} from 50°C to 160°C, while monitoring the partial pressure of H_2, D_2 and H-D inside the vacuum chamber. Since H_2 is known to desorb from thermally treated metals under high vacuum,[21] we also performed a control experiment using only P(NDI2OD-T2), to verify if the amount of H_2 evolving from the chamber walls can affect the experimental result. The obtained partial pressure evolution is reported in **Figure 2.9**. We observed evolution of all the H_2 isotopologues, with the highest intensity in the case of H-D, and the lowest in the case of H_2. Control experiment only show negligible H_2 evolution, confirming that the detected H_2 is mainly the result of the doping process. This result, is a further confirmation that molecular hydrogen forms due to H atom transfer from the dopant molecule, since deuterium atoms can only come from N-DMBI-D. We explain the formation of H_2 and H-D considering the hypothesized pathways for H_2 formation (see **Figure 2.2**). D_2 can form via reaction of two AD$^{\bullet}$ species or reaction of a N-DMBI-D molecule and AD$^{\bullet}$. However, if the D$^{\bullet}$ transferred to the acceptor is bound to a carbon atom also bearing an H atom, the loss of an H$^{\bullet}$ can in principle happen as well and, according to a primary isotope kinetic effect,[7,22] it should even be more favourable. H-D and H_2 can then form according to the following reactions:

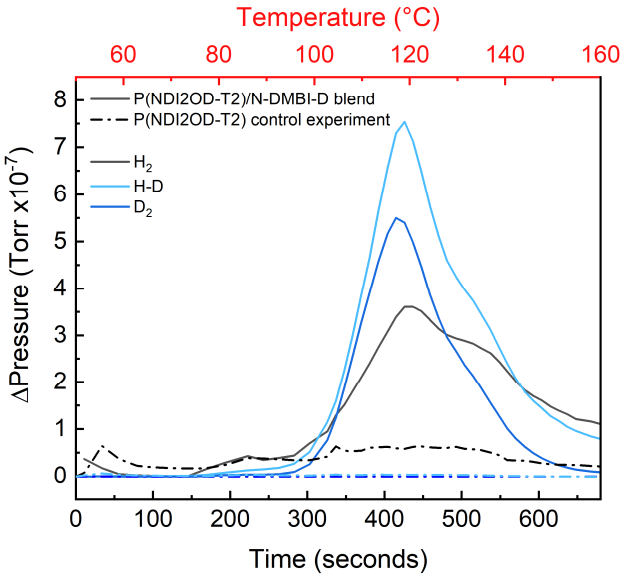

Figure 2.9 Partial pressure variation of H_2 (black lines) H-D (light-blue line) and D_2 (blue line) detected while heating a P(NDI2OD-T2)/N-DMBI-D 1:2 solid blend (solid lines) under a constant rate of 10°Cmin^{-1}. Results related to P(NDI2OD-T2) control experiments are reported as well (dot-dashed lines).

Interaction between AD$^{\bullet}$ and another N-DMBI-D molecule

AHD$^{\bullet}$ + N-DMBI-D ⟶ D_2 or HD

Interaction between two AD$^{\bullet}$ molecules

AHD$^{\bullet}$ + AHD$^{\bullet}$ ⟶ D_2 or HD or H_2

The formation of H_2 and HD is thus a confirmation that the doping happens via first H atom/hydride transfer to the acceptor.

The detected partial pressure variations show that H_2 evolution begins at a temperature

around 90°C and is complete at 160°C, with a peak at 120°C. This is in line with previous works reporting temperatures ≥ 90°C-100°C as a requirement for N-DMBI-H activation in the solid state.[8,23] Apparently the process happens in two steps, one peaking around 120°C and the second peaking at 135°C. The relative intensity of H_2, D_2 and H-D peaks changes at the second step: H_2 peak intensity is comparable, the H-D one is weaker and the D_2 one is barely noticeable. We explain this behaviour with the already mentioned known tendency of N-DMBI-H to segregate from the polymeric matrix, especially at high dopant concentrations.[16,17] The first step can be related to a first doping process happening at the interface between segregated dopant domains and the polymer, which is a D rich region (high concentration of N-DMBI-D and AD$^\bullet$) and where the formation of D_2 is thus more likely. The second step instead presumably happens far from this interface, in the bulk of the host. Thermally promoted diffusion of D$^\bullet$ and H$^\bullet$ atoms between neighbouring acceptor A sites is in fact in principle possible, with isotope kinetic effects again favouring the H$^\bullet$ transfer. The concentration of D atoms then should decrease when going from the D rich interfacial region to the H rich bulk of the acceptor, where the H_2 evolution becomes thus more likely. This phenomenon is pictured in **Figure 2.10**.

When interfacial N-DMBI-D has been completely activated, the hydrogen evolution prevalently occurs in the bulk regions, thus explaining the difference in the relative H_2, D_2 and H-D peak intensity. These results then are a circumstantial evidence that N-DMBI-H doping in the solid state is an interfacial phenomenon happening at the interphase between segregated dopant domains and the host material.

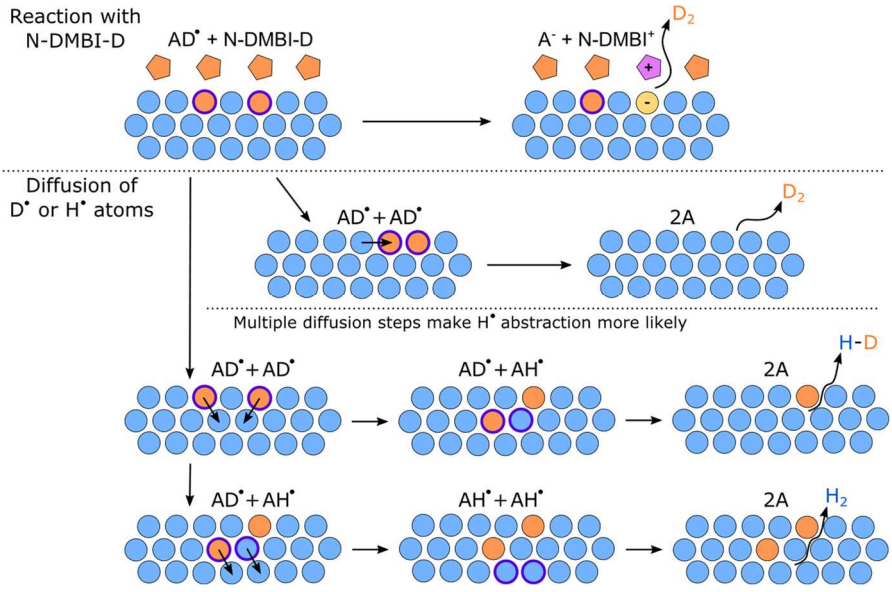

Figure 2.10. Reactions leading to H_2, D_2 and H-D formation after the first doping step at the interface between N-DMBI-D domains (pentacles) and the acceptor A (circles). Light blue circles indicate presence of H atoms only, orange circles indicate presence of D atom on the species while purple contour highlights radical species.

It cannot be excluded that part of these AH$^\bullet$ radicals do not find another species to react to give H_2 formation when they get far from the interfacial area, thus evolving in multiple hydrogenated AH_x species.

2.6 Generality of the method: investigation of BCF doping

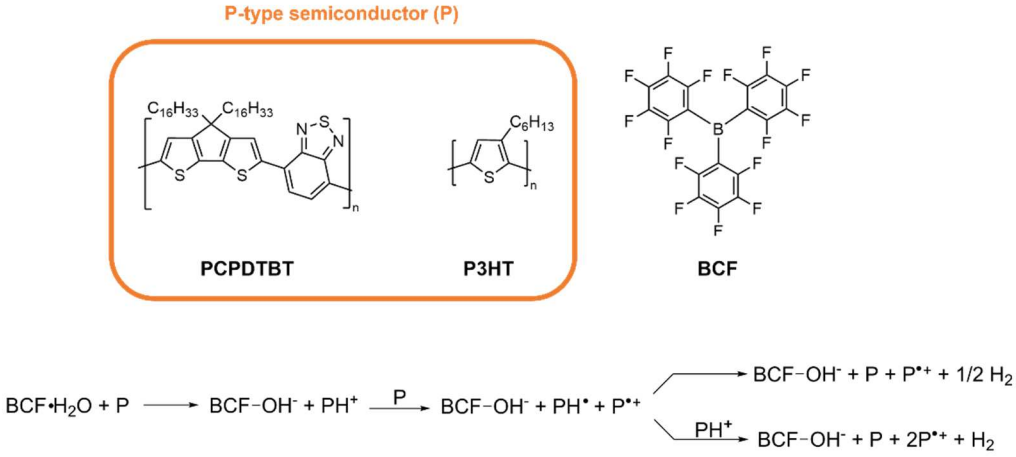

Figure 2.11 Molecular structures of BCF and p-type polymers used during this study. A scheme of the hypothesized doping mechanism leading to H_2 production is reported as well.

The results obtained in the study of N-DMBI-H showed the potentiality and versatility of H_2 detection techniques in the investigation of hydride/H atom transfer mediated doping processes. H_2 evolution has however been proposed also as outcome of other doping processes. We thus decided to test the generality of the GC-H_2 detection method in the investigation of another debated doping mechanism, the one of the Lewis acid p-type dopant trispentafluorophenylborane (BCF). First works on BCF doping mechanism reported it to happen via formation of charge transfer complexes with p-type semiconductors having Lewis base behaviour. The obtained complex would then act as dopant.[24,25] Based on previous studies on oxidation of metallocenes by BCF complexes with water,[26] it was however recently suggested that, in the presence of water traces, BCF mediated doping happens via formation of BCF $\bullet$ H_2O complexes, subsequently acting as Brønsted acids in proton transfer reactions to a target p-type semiconductor **P (Figure 2.11)**.[‡‡]

The obtained protonated p-type semiconductor ($\mathbf{PH^+}$) then oxidizes a second neutral **P** molecule, with formation of the positive polaron $P^{\bullet+}$ and the hydrogenated species $PH^{\bullet}$.[27,28] In analogy to N-DMBI-H doping, interaction of $PH^{\bullet}$ with a second $PH^{\bullet}$ species, with regeneration of the starting semiconductor P and H_2 formation was then hypothesized.[27,28] The formation of PH^+ species was supported by comparative studies with other Brønsted acid.[27] The subsequent H_2 evolution, even if hypothesized in different studies, has instead never been demonstrated. We thus decided to apply our H_2 detection in the study of BCF mediated doping of two well-known p-type polymers: poly[2,6-

[‡‡] Computational studies suggest the overall process to be more exergonic if two $BCF(OH_2)$ complexes interact during the first protonation step, with formation of $[BCF(OH)(OH_2)BCF]^-$ or $[BCF(OH)BCF]^-$ complexes.[27] Since the identification of these species is beyond the scope of this work, we here write $BCF(OH)^-$ for simplicity.

(4,4-bis(2-hexadecyl)-4Hcyclopenta[2,1-b;3,4-b′]dithiophene)-alt-4,7(2,1,3benzothiadiazole)] (PCPDTBT) and poly(3-hexylthiophene) (P3HT). Chemical structure of all the compound used in the following experiments is reported in **Figure 2.11**.

2.6.1 Investigation of doping in solid blends

As first attempt, we performed GC-H_2 detection experiments on wet solid blends of PCPDTBT polymer and BCF. We selected this p-type polymer because of the numerous works studying its doping process.[27,29] We prepared two samples, adding small amounts of chlorobenzene to help the materials blending. We used anhydrous chlorobenzene in one case (Sample A) and chlorobenzene saturated with water in the other (Sample B), to analyse the impact of water presence on the doping outcome. **Figure 2.12** shows the obtained GC traces. No hydrogen was detected in Sample A, prepared in the absence of water. Very small amounts of molecular hydrogen (11 ppm, 0.49 nmol) were instead detected in Sample B. This result suggests that H_2 can form due to the interaction between BCF and PCPDTBT, and that the process is affected by water presence. The amount of hydrogen detected is anyway almost negligible and the result does not demonstrate H_2 evolution to be the dominant doping outcome for this dopant. It is worth noting that p-type doping of PCPDTBT via BCF is generally activated in solution[29] and the same is for other p-type polymers, like P3HT.[28,30] We speculate that the doping requires the presence of a solvent due to the need for an equilibrium protonation of the polymer chain which, based on previous computational studies,[27] is the process rate limiting step. The condition we selected for these experiments might thus not be optimal for studying doping processes mediated by BCF. We then decided to move to the investigation of doping happening in solution.

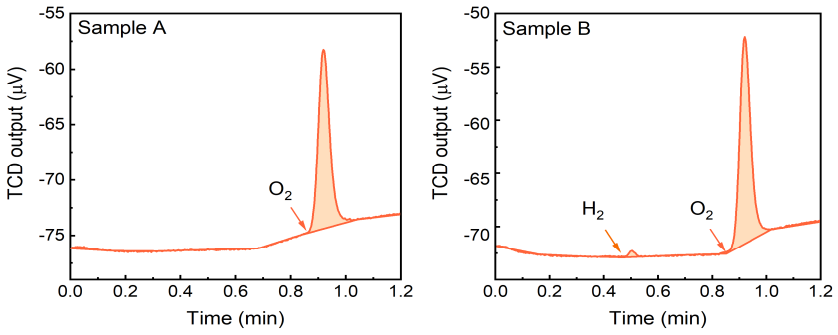

Figure 2.12: GC traces corresponding to the atmosphere of vials containing blends of BCF and PCPDTBT (2:1 mol:mol) in the absence (Sample A) and presence (Sample B) of water traces. Retention times of H_2 and O_2 are highlighted with orange arrows. Samples were analysed 18 hours after preparation.

2.6.2 Investigation of doping processes in solution

We firstly focused on analysing the doping outcome on solutions of PCPDTBT in chlorobenzene in the presence of 2 molar equivalents of BCF. Again, we prepared two different solutions using anhydrous chlorobenzene and chlorobenzene saturated with water to analyse the impact of water traces on the doping process. The solutions were let equilibrate for 24 hours before GC injection. The obtained GC traces (see **Figure 2.13a** and **b**) show sizable H_2 evolution only in sample containing water, corroborating

conclusions of previous works on the impact of H_2O in the doping process. The H_2 detected amount is twenty times higher with respect to samples obtained in wet solid blends (230 ppm, 10.24 nmol), and support the proposed doping mechanism reported in **Figure 2.11**. We then analysed the time dependence of H_2 generation and the effect of BCF stoichiometry on the doping process. To do so, we prepared two different solutions using chlorobenzene saturated with water and containing different BCF amounts (1 and 2 molar equivalents with respect to PCPDTBT repeat units). We then performed GC-injections at different times after sample preparation. The detected H_2 concentrations are reported in **Figure 2.14** and show that the process clearly depends on BCF stoichiometry and requires over 48 hours to reach completion. This is in line with other group previous observations and with common procedures followed in devices preparation, as generally BCF and semiconductor solutions are reported to require several hours of equilibration for efficient doping activation before use.[28,30] We performed the same experiment also on P3HT polymer, to test the generality of the doping mechanism (**Figure 2.14**). Data demonstrate H_2 evolution to be also the outcome of the doping of P3HT, suggesting a possible generality of the phenomenon. The H_2 generation has a similar time dependence for the two polymers and the process is slightly more efficient in the case of P3HT. Again, there is a clear dependence on BCF stoichiometry. It is worth noting that these data are reliable enough for our conclusions, but do not represent a quantitative measurement and a real kinetic analysis. In fact, for these experiments we performed multiple injections on the same samples, withdrawing 250µl of gas each time, which corresponds to ¼ of the free vial volume. This of course leads to leakages and systematic errors inevitably affecting the measurements results.

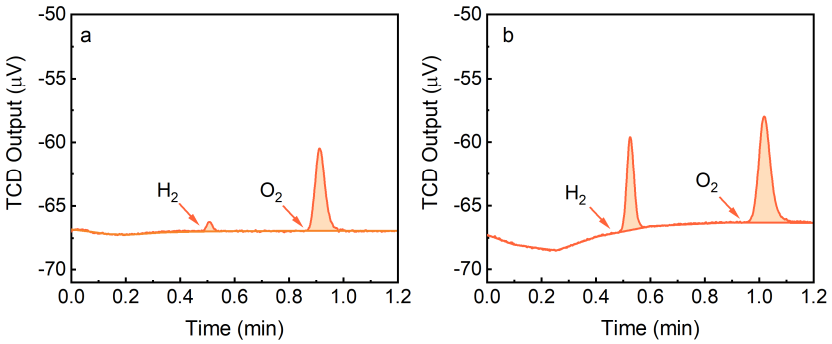

Figure 2.13 GC traces corresponding to the atmosphere of samples containing 9 mM solutions of PCPDTBT and 2 molar equivalents of BCF and obtained using anhydrous chlorobenzene (a) and chlorobenzene saturated with H_2O(b).

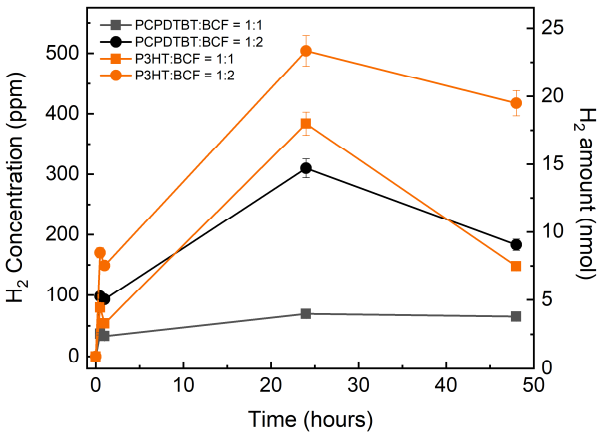

Figure 2.14 H_2 generation as a function of time in samples containing 9 mM PCPDTBT (black) and P3HT (orange) solutions with 1 (squares) and 2 (circles) equivalents of BCF respectively.

2.6.3 A warning on contaminations: BCF control experiments

To confirm that H_2 generation is the result of the doping process, we performed control experiments on solutions containing only the analysed p-type polymers and solutions containing only BCF. As reported in **Figure 2.15**, GC traces of samples containing only PCPDTBT or P3HT showed, as expected, no H_2 generation. In the case of BCF instead we unexpectedly detected H_2 in some of the analysed samples. As the unknown process behind this molecular hydrogen evolution might have affected our GC detection experiments, we performed different tests to further analyse the phenomenon. We firstly repeated the control experiments on BCF several times, keeping the same conditions of previous experiments performed on polymers, to see the if the average amount of detected H_2 is, statistically, in the same order of magnitude of that detected during doping of P3HT and PCPDTBT. The obtained H_2 amount is below 100 ppm for most of the samples. However, for two of them we detected values in the order of 200-250 ppm, close to those obtained during our doping experiments. We then evaluated the influence of different factors on the amount of detected hydrogen, like the specific solvent used, water presence in the sample, contamination of the solution with materials of the vial cap septum or of the thermoplastic adhesive used to seal it. The obtained data are collected in **Figure 2.16**.

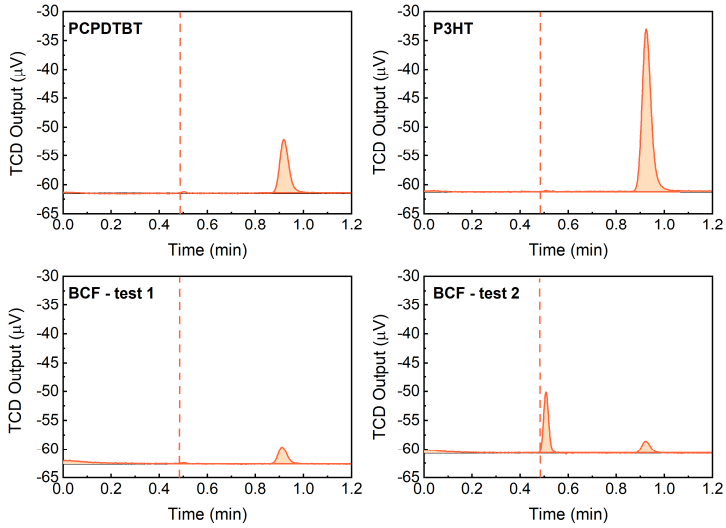

Figure 2.15. GC traces corresponding to the atmosphere of control experiments performed on PCPDTBT, P3HT and BCF solutions. Results of two different tests on BCF solutions are reported. Retention time of H_2 is highlighted with orange dashed lines. Samples were analysed 24 hours after preparation.

Experiments performed using anhydrous toluene saturated with water in place of chlorobenzene again showed random values of H_2, so confirming that the parasitic hydrogen evolution is not associated to the solvent used. Same is for data obtained with anhydrous chlorobenzene, that suggest that H_2 evolution is not the results of simple interaction of BCF with H_2O, since amounts of molecular hydrogen higher than 100 ppm are detected even in such dry condition. Both experiments performed dissolving a piece of thermoplastic adhesive in the sample showed no or negligible amounts of H_2, confirming that the H_2 evolution is not due to sample contamination with this material. Experiments performed adding pieces of the vial septum in the solution showed instead sizable H_2 evolution, one of the samples even reaching around 450 ppm of detected H_2. These data hint that reaction of the BCF solution with the septum might be the reason

behind this unexpected H_2 generation. Several works report H_2 generation in BCF catalysed coupling reactions of hydrosilanes with silanoles or secondary alchools.[31,32] The same was reported for catalysed attachments of these species to silica.[33,34] As part of the GC-Vial septum is made of silicones, we speculate that presence of residual silanoles and hydrosilanes is the reason behind the unexpected H_2 formation. We then performed four more experiments trying to avoid as much as possible contact between the septum and BCF solution, and rinsing syringes with clean solvent before use, to avoid contacts with possible unknown lubricants. Following this procedure, 3 over 4 of the prepared samples showed no or negligible H_2 evolution (<10 ppm). Still, one sample showed H_2 concentrations higher than 100 ppm. Complete avoidance of H_2 evolution with this experimental setup is thus not straightforward.

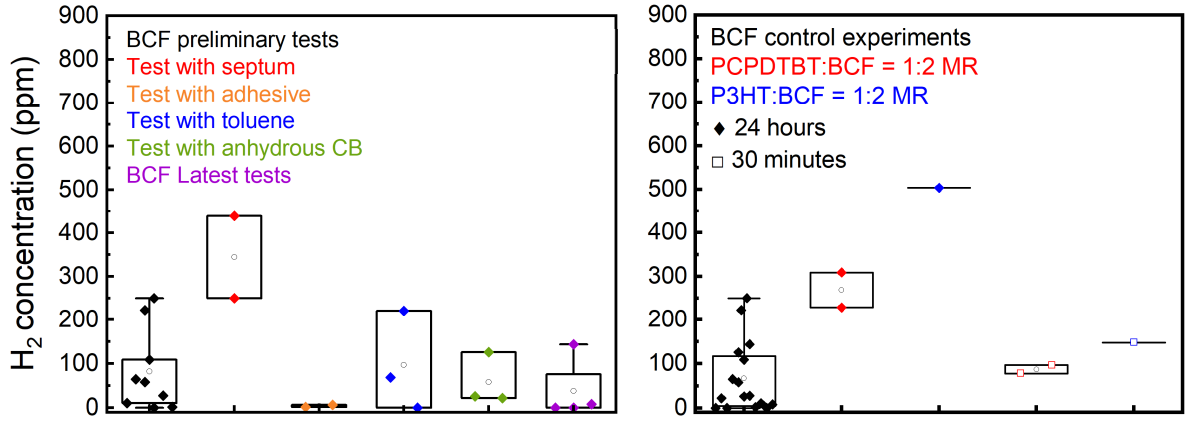

Figure 2.16 Left: distribution of H_2 concentrations detected during BCF control experiments prepared in the same conditions of previous experiments (black), in the presence of pieces of vial septum (red), contaminated with thermoplastic adhesive (orange), prepared using toluene saturated with H_2O (blue), prepared in anhydrous chlorobenzene (green) and latest samples prepared avoiding contact with the septum/lubricants (purple); Right: distribution of H_2 concentrations detected during all BCF control experiments prepared in the same conditions of doping experiments (black), doping experiments on PCPDTBT (red) and doping experiments involving P3HT (blue). Values detected after 24 hours from sample preparations are indicated with diamonds, while values detected after 30 minutes from sample preparations are indicated with empty squares. In both sets average values are highlighted with white circles.

It is however worth noting that the H_2 amounts detected in our doping experiments are always higher with respect to the average values obtained when only the dopant is present in the sample (**Figure 2.16, right**). Moreover, results of GC-injections performed 30 minutes after samples preparation on solutions containing P3HT and PCPDTBT show H_2 concentrations equal or higher with respect to average H_2 concentrations detected in control experiments, always analysed 24 hours after preparation. These considerations, together with the fact that the results of control experiments are very random suggest that these side reactions might contribute to the total amount of molecular hydrogen detected while analysing doping processes of p-type polymers, but that the doping itself generates H_2.

2.7 Conclusions

With this work, we gave the first experimental demonstration of H_2 evolution as possible outcome of uncatalyzed doping processes mediated by N-DMBI-H, confirming previously only hypothesized doping mechanisms. With an innovative GC based H_2-detection approach, we corroborated previous observation and results on doping dependence on the semiconductor counterpart and on the activation conditions. With the use of a deuterium labelled dopant and a low mass detector, we then deepened the nature of the reactive sites involved in the H_2 generation and demonstrated hydrogen atom/hydride transfer from the dopant to the acceptor to be one of the steps of the process, confirming previously suggested pathways. We then further showed the generality and powerfulness of the GC-H_2 detection approach in the study of BCF doping mechanism, demonstrating for the first time H_2 evolution during doping of different p-type semiconductors and confirming previous spectroscopic observation on the impact of water on the process efficiency.

On the overall our results are in line with those obtained by other groups using more common doping characterization techniques. This work then paves the way for the use of H_2-detection techniques as a method to characterize organic semiconductor doping processes mediated by H atoms or ions.

2.8 Extending the applications of the GC-H_2 detection method

The results obtained in the study of doping mechanism demonstrate the potentiality of the GC-H_2 detection method and highlight some advantages of the approach:

- it can work on different types of samples (solutions and solid blends) reproducing the conditions of the main devices preparation steps (concentrations, doping activation treatments);
- for processes happening via H_2 evolution, it allows a direct estimate of the amount of activated dopant.

This is not the case for all common techniques used for semiconductor doping characterization. For example, in the case of Electron Paramagnetic Resonance spectroscopy (EPR) and UV-Vis-NIR absorption spectroscopy, it is generally not straightforward to analyse processes happening in solutions obtained at the same concentration of device preparation procedures (semiconductor concentration: 10^{-3}-10^{-2} M), due to the too high absorbance and the higher impacts of broadening and spin-pairing effects characteristics of highly concentrated samples. In the case of EPR, these effects can also affect spin density determination.[35] The doping then needs to be activated in more diluted solutions or else dilution steps of pristine solutions are required before the characterization. The advantageous features of the GC-H_2 detection method then suggest that it could be especially useful in the characterization of doping processes happening in such conditions, not suitable for direct measurement with common spectroscopic techniques.

We thus decided to test the approach in the study of N-DMBI-H doping happening in solution of the same concentrations (8-10 mM) of those used during typical devices preparation procedures. We considered of particular interest the thermally activated doping under such conditions for two reasons:

- As aforementioned doping of some semiconductors is known to require thermal activation in the solid state. The possibility of activating the process in solution via thermal treatment has however not been much investigated. Only few works analysing doping happening in diluted solutions via UV-Vis-NIR spectroscopy exist and state that N-DMBI-H activation in thermally treated solution is negligible.[36] Since N-DMBI-H doping reaction is known to possess a second order kinetic,[§§5,7] the outcome of the process can however be different in highly concentrated samples.
- Deepening the effect of such treatments might have relevant impacts in the definition of better guidelines for the use of N-DMBI-H. As mentioned in the first chapter, N-DMBI-H doping efficiency is limited by its segregation from the semiconductor matrix, which reduces the amount of activated dopant during thermal treatments. The activation of the doping in a homogeneous environment prior to film deposition might result in a strategy to mitigate the impact of this phenomenon.

[§§] The rate r depends on concentration of both the reactants A and B as r=-k[A][B], where k is the rate constant.

2.8.1 Thermally activated doping of P(NDI2OD-T2) in solution

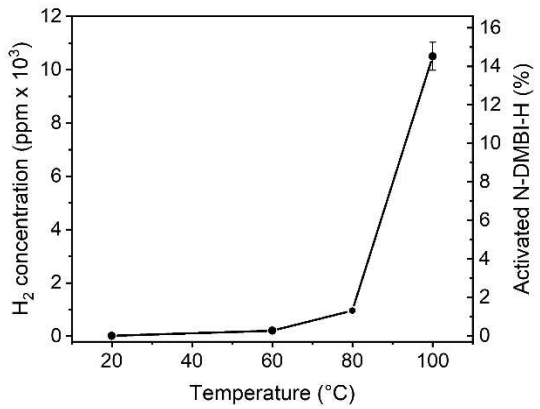

Figure 2.17. H_2 concentration detected in GC-vials containing solutions of P(NDI2OD-T2)/N-DMBI-H (1:0.8 mol:mol) in chlorobenzene treated at different temperatures for 1 hour. The corresponding percentage of activated N-DMBI-H is reported as well. A 5% error was considered for each value.

For the purpose, we then selected P(NDI2OD-T2) as the acceptor, since the doping of this polymer is known to require thermal activation and we already demonstrated that the process happens via H_2 formation in the case of solid blends. We firstly prepared 8 mM solutions of P(NDI2OD-T2) in anhydrous chlorobenzene and added them with 0.8 molar equivalent of N-DMBI-H, to reproduce conditions of common device making procedures.[16] We filled different GC-MS vials with 1 mL of these solutions under argon atmosphere and heated them at different temperatures for 1 hour to analyse the effect of the thermal treatment on the doping outcome. The detected H_2 concentrations are reported in **Figure 2.17,** together with the corresponding estimated percentage of activated N-DMBI-H.*** The obtained data show a thermally activated hydrogen formation, the process becoming particularly efficient at temperature higher than 80°C. Doping of this polymer appears then to be possible in solution as well. The sample kept at room temperature shows only traces of H_2 (19 ppm, 0.84 nmol) suggesting that the doping can happen even without thermal treatment, but that its rate is much slower. In the sample treated at 100°C, we detected around 10470 ppm, corresponding to 0.46 µmol of evolved H_2 and to around 14.3% of activated N-DMBI-H. The value is high with respect to the one we measured in annealed solid blends and with respect to the already mentioned usually reported doping level of P(NDI2OD-T2) (see section 2.4.1). This suggests a more likely interaction between the dopant and the semiconductor within the homogeneous solution environment with respect to solid blends which are affected by dopant segregation and diffusion phenomena.

2.8.2 Comparison with common doping characterization techniques

To further corroborate these results, we compared them with those obtained with UV-Vis-NIR absorption spectroscopy and EPR. For the aim we prepared solution in the same conditions of those used for our H_2 detection experiments and again treated them

*** This was evaluated considering 1 mL of free volume in the GC-vial and that around 6.4 µmol of N-DMBI-H were added in each sample, making the maximum theoretical H_2 evolution of 3.2 µmol.

at different temperatures. The measurements then required dilution of the samples. The results are collected in **Figure 2.18**. UV-Vis-NIR absorption spectra of the thermally treated solutions show the quenching of the neutral polymer charge-transfer absorption band, located around 700 nm, and the appearance of two new absorption features at 500 nm and above 800 nm, attributed in the literature to the P(NDI2OD-T2) polaron formation. The blueshift of the π-π* band located at 390 nm is also generally connected to the polymer radical anion formation.[37,38] These features become evident when the solution is treated at temperature higher or equal to 70-80°C, suggesting a more efficient doping, which is in line with the results of the H_2-detection experiments reported in **Figure 2.17**. Also, the peak related to N-DMBI-H absorption (**~** 325 nm) disappears at temperatures higher than 80°C, suggesting higher conversion to N-DMBI$^+$ cation, whose absorption in chlorobenzene is reported to peak around 360 nm.[39]

EPR spectrum of solutions containing only P(NDI2OD-T2) and treated at 100°C for 1 hour show no paramagnetic signal as expected since only the neutral non-doped species

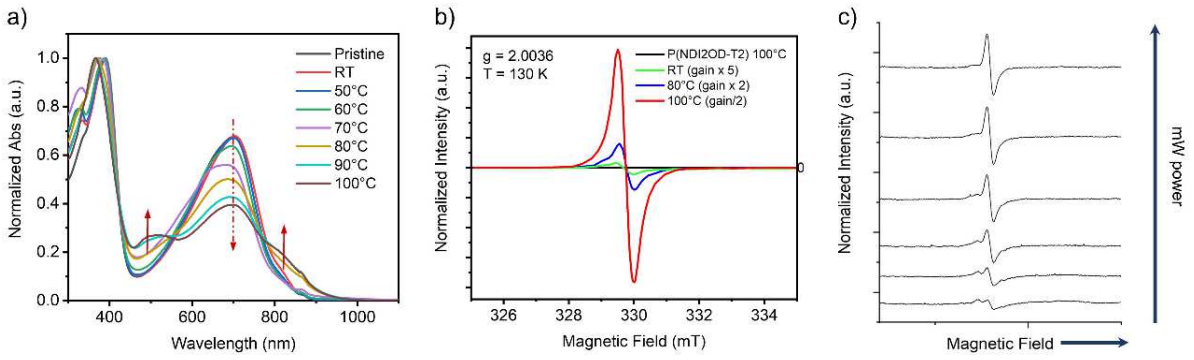

Figure 2.18 a) Normalized UV-Vis-Absorption spectra of solutions of P(NDI2OD-T2)/N-DMBI-H (1:0.8) in chlorobenzene heated at different temperatures for 1 hour and diluted to 0.1 mgmL^{-1}. The spectrum of a solution containing the pristine polymer is reported as well; Quenching of P(NDI2OD-T2) charge transfer band and appearance of polaronic features are highlighted with red arrows b) EPR spectra of 1mgmL^{-1} solutions of the same composition kept at RT (green line), treated at 80°C (blue line) and at 100°C (red line) together with the spectrum of a P(NDI2OD-T2) solution heated at 100°C for 1 hour (black line); c) EPR spectra obtained via microwave power sweep measurements on the sample kept at room temperature. All EPR measurements were performed at 130 K.

is present in this control experiment. When N-DMBI-H is added to the solution, the appearance of a signal at g = 2.0036, corresponding to P(NDI2OD-T2) radical anion is instead detected.[40] The intensity of this peak, very weak in solutions kept at room temperature (RT), increases with the temperature of the thermal treatment, with a behaviour again in line with the one of H_2-detection experiments. The signal appears anisotropic in samples kept at RT or treated at 80°C but not in sample treated at 100°C. Microwave power sweep reveals a different saturation behaviour for the superimposed anisotropic signal (see **Figure 2.18c**), thus suggesting presence of two different paramagnetic species in the sample.[41] Such an EPR spectrum structure has already been observed in P(NDI2OD-T2) films doped with octaphenylrhodocene and has been possibly connected to partial molecular ordering in the polymeric solid film.[42] P(NDI2OD-T2) is known to retains partial aggregation in chlorobenzene at RT.[37] The polymer progressively disaggregates instead at higher temperatures (see experimental

methods, section **2.10.5**, for characterization of P(NDI2OD-T2) aggregation behaviour in chlorobenzene). We thus speculate that this second anisotropic species might be due to presence of ordered polymer aggregates during doping, whose order level is instead reduced when the thermal treatment temperature increases. The in-depth analysis of this unknown species is however beyond our scope.
The obtained results confirm that N-DMBI-H doping of P(NDI2OD-T2) can happen in solution and that it is a thermally activated process. Moreover, they highlight a clear a correspondence between H_2 generation efficiency and charge injection efficiency in the semiconductor, which further corroborate the previously hypothesized H_2 formation mechanism.

2.9 Conclusions

In conclusions, via the use of our H_2-detection method, we successfully demonstrated that N-DMBI-H doping can be thermally activated in solution in the case of P(NDI2OD-T2) polymer, a conclusion potentially extendable also to other semiconductors. The process appears more efficient than when activated in the solid state, which is probably due to a better interaction between the polymer and N-DMBI-H in the solution homogeneous environment. This result might be relevant for applications and suggest that annealing of dopant/semiconductor solution prior to film deposition might be a strategy to improve this dopant efficiency.

These results, obtained using our H_2 detection method, are corroborated by more commonly used spectroscopic techniques, which further demonstrates the correlation between H_2 evolution and charge injection. The possibility of using H_2-detection techniques for the characterization of doping processes is thus showcased, suggesting it to be particularly useful in those situations in which a direct measurement with more traditional approaches is precluded.

2.10 Experimental methods

P(NDI2OD-T2) polymer batch used for H_2-GC detection experiments was purchased by Flexterra (Mn=34.7 kDa, PDI=1.9). A second batch was synthesized following a procedure previously reported in the literature,[43] and then purified from palladium traces via two consecutive chromatographic filtration on silica. This batch was used for RGA-MS experiments and for GC based analysis of thermal activation of N-DMBI-H in solution. Anhydrous chlorobenzene (99.8%) and toluene were purchased from ACROS. $PC_{60}BM$ was purchased from Solarmer Energy Inc. BCF dopant (95%) and P3HT (regioregular, average Mw 20-45 kDa, PDI ≤ 6.0) were purchased from Sigma-Aldrich. PCPDTBT was purchased from 1-Material. Unless otherwise stated, all the materials were used as received.

N-DMBI-H was synthesized according to the procedure reported in Chapter 4, Experimental methods section. $(N\text{-DMBI})_2$ was synthesized according to a literature procedure.[39] The same for N-DMBI-D.[7] All N-DMBI like derivatives were stored under inert atmosphere before use. NDI-C8 and 2CN-NDI-C6 acceptors were as well synthesized according to literature procedures.[44–46]

2.10.1 Synthesis of BDOPV acceptors

BDOP acceptors were synthesized following the synthetic pathway reported in **Scheme 2.1**. 2CN-BDOPV was prepared according to the literature.[5] The synthetic procedure followed for the synthesis of 4CN-BDOPV is described in the following paragraphs.

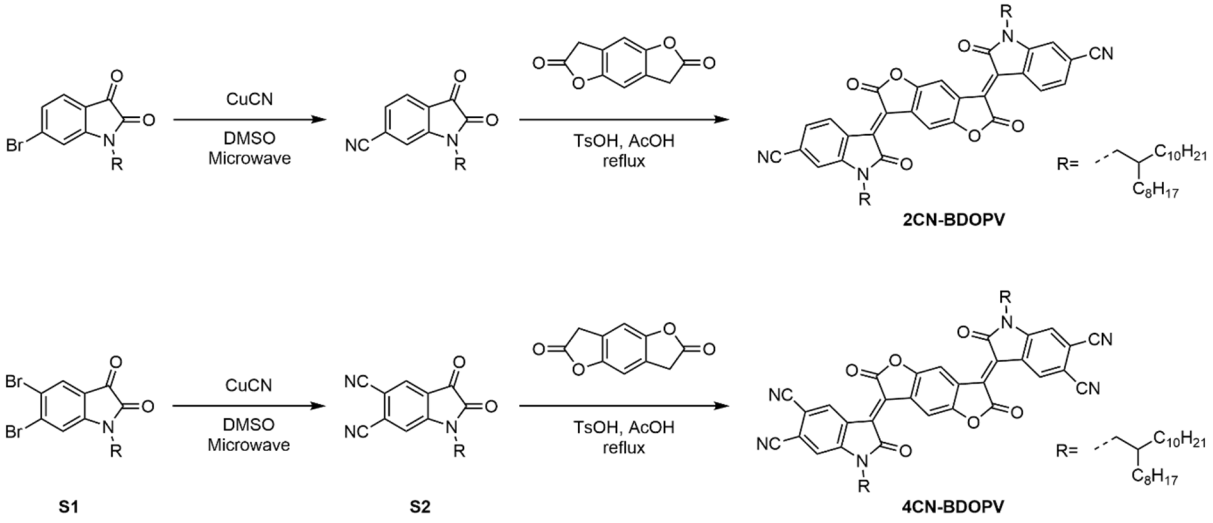

Scheme 2.1: synthetic pathway for the preparation of 2CN-BDOPV and 4CN-BDOPV.

2.10.1.1 Synthesis of derivative S2

5,6-Bromo-1-(2-octyldodecyl)indoline-2,3-dione (1.17 g, 2 mmol), CuCN (0.90 g, 10 mmol) and DMSO (15 mL), were sealed in a microwave vessel under N_2 atmosphere. The vessel was then heated in a microwave reactor at 170 °C for 5 min, and then at

190 °C for 1 h. The reaction mixture was then poured into chloroform (100 mL) and then filtered. The filtrate was washed with water and brine, and dried over anhydrous Na_2SO_4. After removal of the solvent under reduced pressure, the residue was purified via silica gel chromatography, using chloroform as eluent, to afford an orange solid.

^{1}H NMR ($CDCl_3$, 400 MHz): δ 7.94 (s, 1H), 7.25 (s, 1H), 3.65 (d, J = 7.4 Hz, 2H), 1.83 (m, 1H), 1.36–1.23 (m, 32H), 0.85 (t, J = 6.7 Hz, 6H).

^{13}C{^{1}H} NMR ($CDCl_3$, 101 MHz): δ 180.43, 156.90, 153.96, 129.33, 124.18, 119.35, 114.96, 114.56, 114.50, 110.90, 45.72, 31.42, 40.01, 29.69, 29.41, 26.30, 22.77, 22.74, 14.21, 14.19

2.10.1.2 Synthesis of 4CN-BDOPV

3,7-dihydrobenzo[1,2-b:4,5-b']difuran-2,6-dione (0.19 g, 1 mmol), and p-toluenesulfonic acid monohydrate (28 mg, 0.15 mmol) were added to a solution of **S2** (0.95 g, 2 mmol) in acetic acid (15 mL). The mixture was stirred at 115 °C under nitrogen atmosphere for 24 h. Then the mixture was poured into methanol (100 mL) and filtered. The recovered solid was washed with methanol to remove the acetic acid and then purified by silica gel chromatography using hot chloroform as eluent. 4CN-BDOPV was obtained as a dark green solid (0.49 g, 0.44 mmol, 44% yield).

^{1}H NMR ($CDCl_3$, 400 MHz): δ 9.57 (s, 2H), 9.21 (s, 2H), 7.16 (s, 2H), 3.74 (d, J = 7.4 Hz, 4H), 1.87 (m, 2H), 1.37-1.24 (m, 64H), 0.86 (t, J = 6.8 Hz, 12H).

^{13}C{^{1}H} NMR ($CDCl_3$, 101 MHz): δ 166.61, 166.09, 153.11, 148.89, 134.62, 133.12, 131.22, 127.87, 123.89, 119.83, 115.58, 115.23, 112.70, 112.55, 109.74, 45.57, 36.48, 31.98, 31.88, 31.57, 30.09, 29.76, 29.64, 29.40, 26.43, 26.38, 22.79, 22.75, 14.25, 14.21

2.10.1.3 NMR spectra

Derivative S2

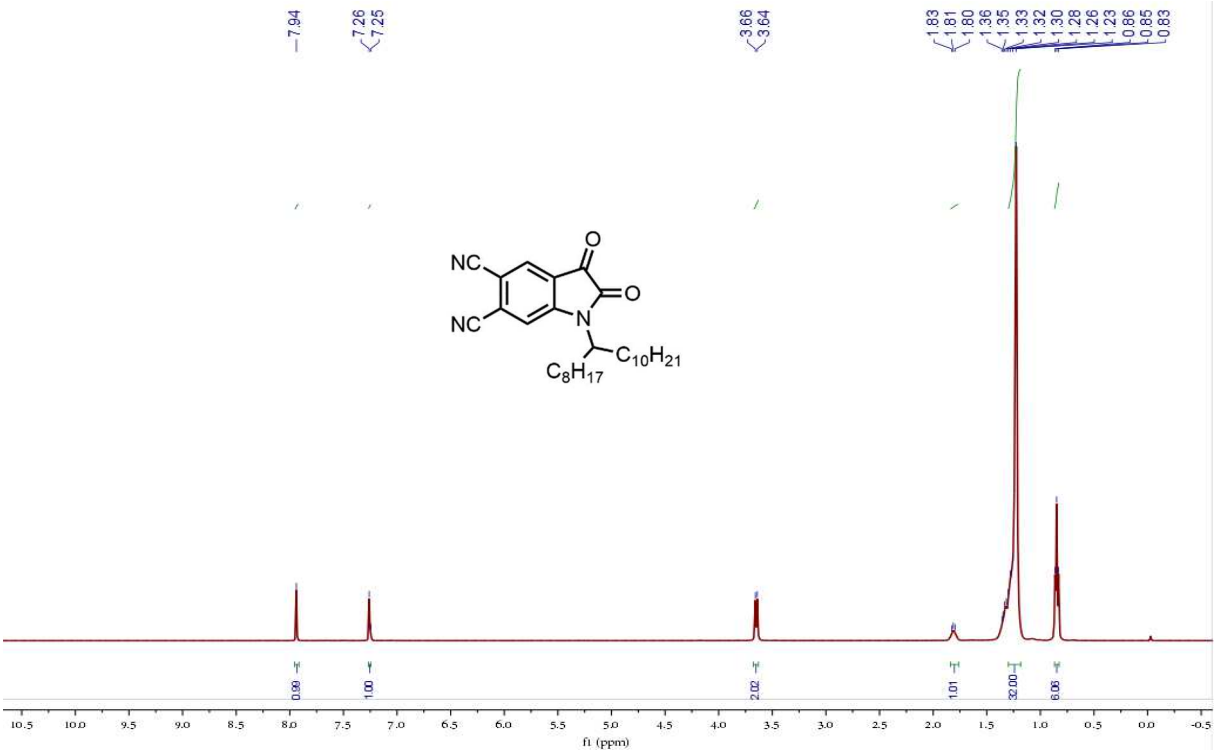

Figure 2.19: ^{1}H NMR of Derivative **S2** in $CDCl_3$

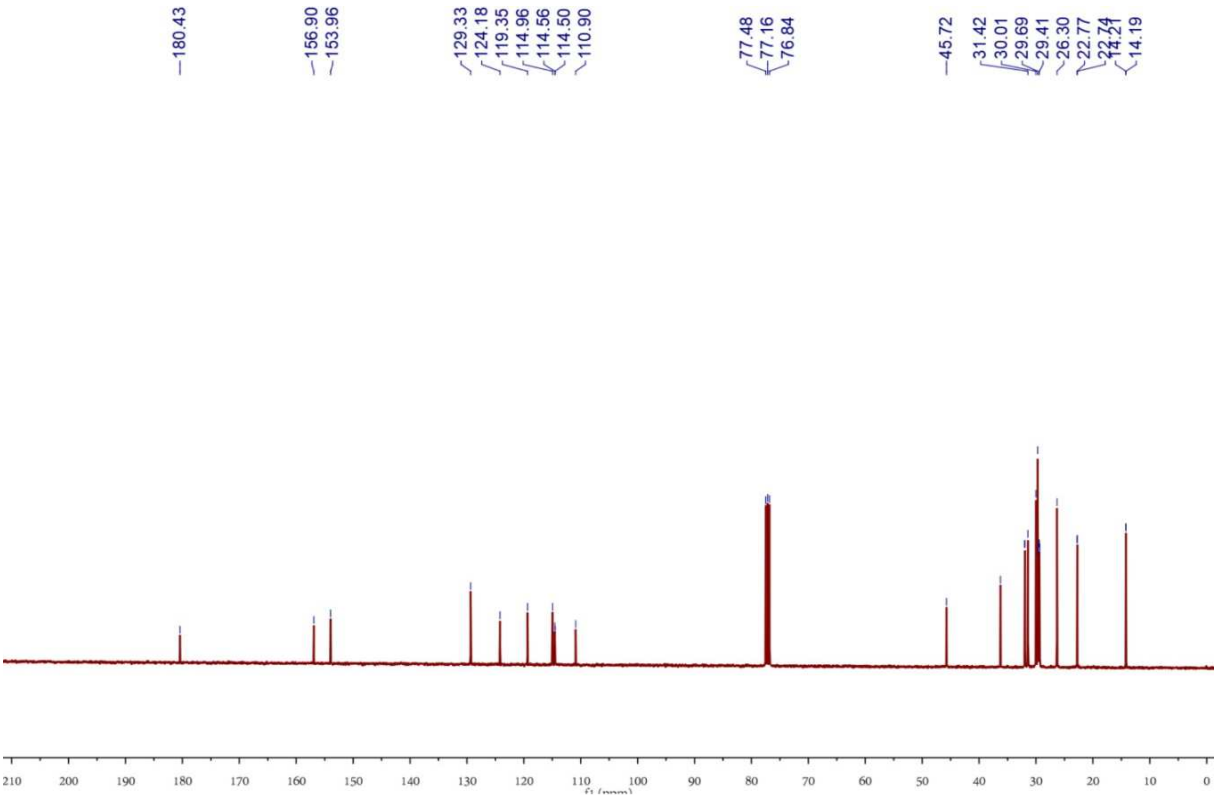

Figure 2.20: ^{13}C NMR of Derivative **S2** in $CDCl_3$

Derivative 4CN-BDOPV

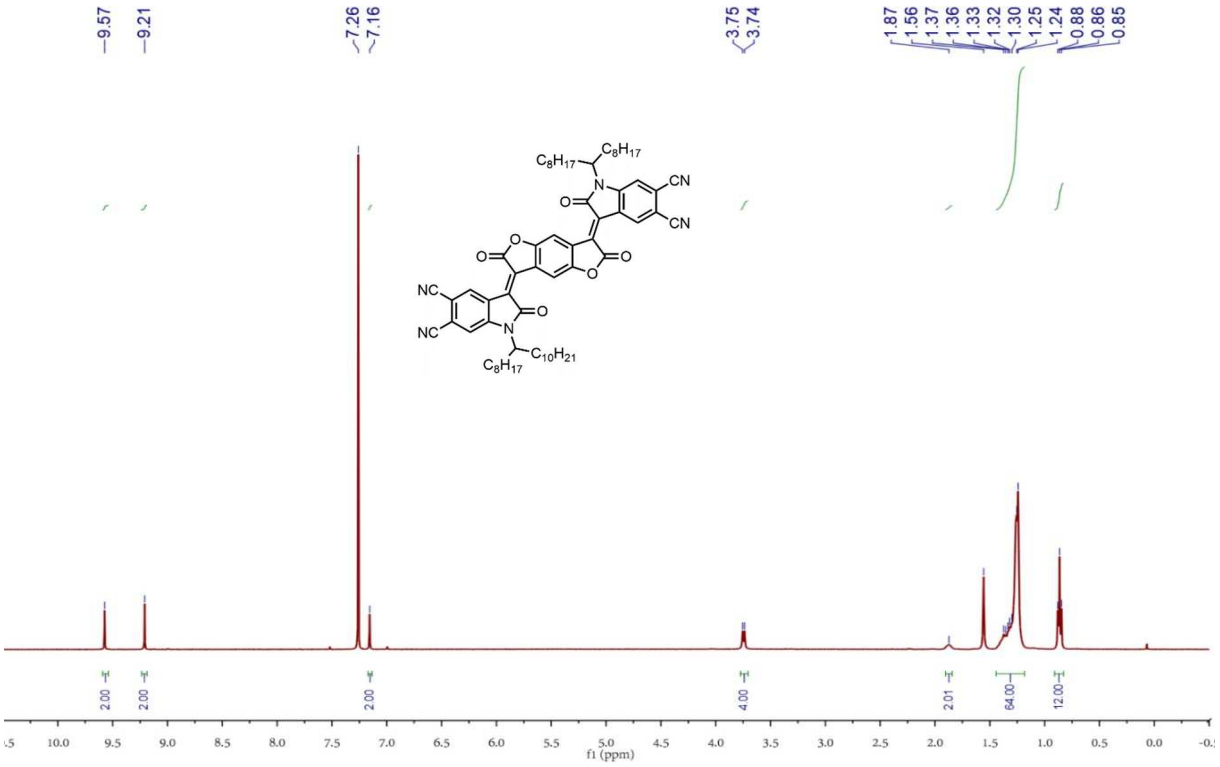

Figure 2.21: ^{1}H NMR of 4CN-BDOPV in $CDCl_3$

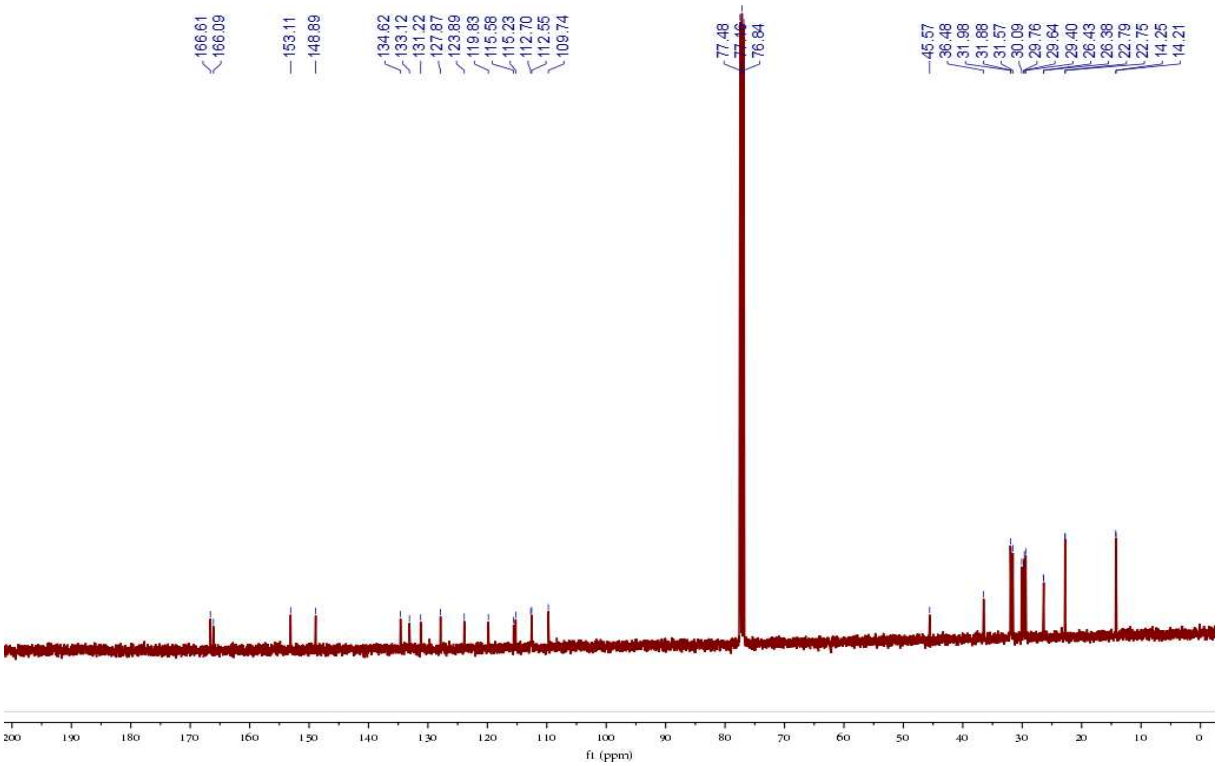

Figure 2.22: ^{13}C NMR of 4CN-BDOPV in $CDCl_3$

2.10.2 Gas Chromatography – H_2 detection experiments

Hydrogen detection experiments were performed either with an Agilent 6850 gas-chromatograph (GC) on 50 µL manual gas injections or with an Agilent 8860 GC system on 250 µL manual gas injections. Both instruments use argon as carrier gas (flow rate 25 $mLmin^{-1}$) and are equipped with a Thermal Conductivity Detector (TCD) and a molecular sieve 5 Å column (2 m × 2 mmID, temperature 70 °C).

Samples were analysed using the following Gas-Chromatographic method:

- Oven temperature: 70 °C
- Hold time: 2 min
- Run time: 2 min

Argon mixtures containing 100 ppm and 10000 ppm of H_2 were used for calibration. H_2 concentration values were then evaluated via integration of chromatograms peaks area weighed on the obtained calibration line. Concentrations of H_2 are reported in part per millions with respect to molar amount of Argon gas. A 5% instrumental error was considered for each value.

All the samples described in this section were prepared in 2 mL GC-MS glass vials with closures provided of PTFE/silicone septum. Vials were dried before use. Samples were prepared inside a glove box (argon atmosphere, $O_2 < 0.1$ ppm, $H_2O < 0.1$ ppm).

2.10.2.1 Solid blends of n-type semiconductors and N-DMBI-H

All samples described in this section were prepared mixing acceptor and dopant powder directly in the GC vial and helping the blending with addition of few droplets of anhydrous chlorobenzene. After being sealed with parafilm, all samples underwent thermal treatment at 150 °C for 2 h in an oil bath outside the glove box before GC analysis.

Unless otherwise stated, blends of acceptor and N-DMBI-H were prepared in a 1:2 molar ratio, while blends of acceptor and $(N\text{-}DMBI)_2$ were prepared in a 1:1 molar ratio. Details on each sample preparation are reported in the following paragraphs.

P(NDI2OD-T2) and N-DMBI-H blend
From P(NDI2OD-T2) powder (19 mg, 0.019 mmol) and N-DMBI-H (11 mg, 0.041 mmol). The vial was sealed and kept in the dark under inert atmosphere for 6 hours. Solvent was then evaporated under N_2 flow. The vial was then again sealed under argon and kept under inert atmosphere for 18 hours before thermal treatment.

P(NDI2OD-T2) and $(N\text{-}DMBI)_2$ blend
From P(NDI2OD-T2) powder (15 mg, 0.015 mmol) and $(N\text{-}DMBI)_2$ (9 mg, 0.016 mmol) The blend was not dried under N_2 flow to avoid any possible hydrogen loss, since the polymer had already changed colour from blue to purple after few hours, which is

usually sign of P(NDI2OD-T2) polarons formation. The blend was kept under inert atmosphere for 36 hours before thermal treatment.

N-DMBI-H control experiment
N-DMBI-H powder (10 mg, 0.037 mmol). Once sealed, the vial was kept for 24 hours in the dark under inert atmosphere before thermal treatment.

P(NDI2OD-T2) control experiment
P(NDI2OD-T2) powder (14 mg, 0.015 mmol). Once sealed, the vial was kept in the dark under inert atmosphere for 36 hours before thermal treatment.

Solid blends of N-DMBI-H and acceptors different from P(NDI2OD-T2)
Acceptor powder (0.015 mmol, 0.011 mmol of 4CN-BDOPV in the case of wet blend) was mixed with N-DMBI-H powder (0.03 mmol, 0.022 mmol with 4CN-BDOPV in the case of wet blend). The vial was then sealed under inert atmosphere. Sample storage and treatment then followed two different procedures for experiments on dry blends (**Treatment A**) and on wet blends (**Treatment B**).

Treatment A: the vial was stored at under argon, in the dark and at room temperature for 18 h. Solvent was then evaporated under N_2 flux, and the vial was sealed again under argon and kept in the dark at room temperature for 16 h before thermal treatment.

Treatment B: the vial was stored under argon and kept in the dark, at room temperature for one day before thermal treatment.

Sample containing 2CN-BDOPV and 0.65 molar equivalent of N-DMBI-H was prepared according to the same preparation procedure and following **Treatment B**.

2.10.2.2 Solutions of N-DMBI-H and n-type molecular acceptors

All samples prepared for the investigation of H_2 production from doping of molecular acceptors in solution at RT were prepared according to the following procedure.
A 0.01 M stock solution of N-DMBI-H was prepared inside an argon filled glove box using anhydrous chlorobenzene (21.40 mg of N-DMBI-H in 8 mL). Acceptor powder (0.010 mmol) was added to a GC vial. 1 mL of N-DMBI-H stock solution was added to reach a 1:1 molar ratio with respect to the acceptor. The vial was closed, sealed with parafilm and stored under argon, in the dark, at room temperature for 2 days before GC analysis.
Solution of 2CN-BDOPV and N-DMBI-H in 1:0.5 molar ratio was prepared according to the same procedure but adding 0.5 mL of N-DMBI-H stock solution and further diluting the mixture with 0.5 mL of anhydrous chlorobenzene.

2.10.2.3 Solid blends of BCF and PCPDTBT

Solid blends of BCF (9 mg, 0.018 mmol) and PCPDTBT (7 mg, 0.009 mmol) were prepared weighting the polymer and dopant powders directly in a GC vial. 3-4 droplets of

chlorobenzene were added to guarantee mixing of species. Two samples were prepared, in one case using anhydrous chlorobenzene (**Sample A**) and in the second case using anhydrous chlorobenzene saturated with water (**Sample B**).

The two samples were sealed under argon and kept at room temperature under inert atmosphere for 18 hours before Gas Chromatographic analysis.

2.10.2.4 Solutions of BCF and p-type polymers

Unless otherwise stated, all samples of this section were prepared using anhydrous chlorobenzene saturated with degassed water as solvent. After preparation, samples were stored and analysed following two different protocols.

Protocol A: the sample was stored under inert atmosphere and was analysed after 24 hours from preparation. 4 different GC injections were performed and the one giving the highest H_2 concentration is here reported.

Protocol B: this is the protocol used for GC experiments analysing H_2 evolution from BCF doping in time. The first GC injection was performed 30 min after sample preparation. After that, H_2 detection experiments were repeated after 1 h, 24 h, and 48 h. After each GC injection, samples were again sealed with a thermoplastic adhesive and kept at room temperature under air before the following experiment.

Samples containing PCPDTBT and BCF

7 mg (0.009 mmol) of PCPDTBT were weighed inside a GC vial. 0.53 mL of chlorobenzene and 0.47 mL of a 20 $mgml^{-1}$ stock BCF solution were added to the vial to obtain a polymer concentration of 9×10^{-3} *M* (BCF:PCPDTBT = 2:1 in molar ratio). Chlorobenzene was added as first step, the vial was closed, then BCF solution was added via syringe and eventually the septum was sealed with a thermoplastic adhesive. The procedure was repeated twice, in one case using degassed chlorobenzene saturated with degassed water, in the other case using anhydrous chlorobenzene as solvent. These samples were analysed following **Protocol A**.

Samples for analysis of time dependence of H_2 generation were obtained according to the same preparation procedure but chlorobenzene and the stock BCF solution were added in different amounts to obtain 1 and 2 molar equivalents of BCF with respect to the polymeric repeating unit. These samples were analysed following **Protocol B.**

Samples containing P3HT and BCF

A 5 $mgml^{-1}$ stock solution of P3HT in chlorobenzene was prepared. This solution, chlorobenzene, and a 20 $mgml^{-1}$ stock BCF solution were added in different amounts to a GC vial to obtain samples containing a 1 and 2 molar equivalents of BCF with respect to the polymeric repeating unit (P3HT overall concentration: 9×10^{-3} *M).* P3HT solution was added as first step, then chlorobenzene, the vial was closed, BCF solution was added via syringe and eventually the septum was sealed with a thermoplastic adhesive. These two samples were analysed according to **Protocol B**.

PCPDTBT control experiment

7 mg of PCPDTBT were added to a GC vial. 1mL of Chlorobenzene was added to obtain a PCPDTBT 9×10^{-3} M solution (7 $mgmL^{-1}$). The vial was closed and shaken to help the polymer dissolution and eventually the septum was sealed with a thermoplastic adhesive. GC analysis was performed according to **Protocol A.**

P3HT control experiment

A 5 $mgml^{-1}$ stock solution of P3HT (0.31 ml, 1.55 mg) and chlorobenzene (0.69 mL) were added to a GC vial to obtain a sample containing P3HT in 9×10^{-3} M concentration. The vial was closed and eventually the septum was sealed with a thermoplastic adhesive. GC analysis was performed according to **Protocol A.**

BCF control experiments

0.53 mL of chlorobenzene were added to a GC vial. The vial was closed and then 0.47 mL of a 20 $mgml^{-1}$ BCF stock solution was added via syringe. Eventually the septum was sealed with a thermoplastic adhesive. Variation on this preparation procedure were performed to test the impact of different factors on H_2 formation during control experiments:

- Three samples were prepared using anhydrous toluene saturated with water in place of chlorobenzene;
- Three samples were prepared using anhydrous chlorobenzene (no water added);
- Two samples were prepared adding a piece of thermoplastic adhesive to the sample;
- Two samples were prepared adding a piece of the vial septum to the sample;
- Four samples were prepared adding solution to the vial before closing them instead of adding BCF solution through syringes to already sealed vials, so to minimize contact with the vial septum; syringes were also rinsed with clean solvents before use.

All samples were then analysed according to **Protocol A**.

2.10.2.5 Thermal activation of N-DMBI-H doping in solution

Samples for the GC-H_2 analysis of N-DMBI-H thermal activation in solution were prepared according to the following procedure.

A 10 $mgml^{-1}$ stock solution of N-DMBI-H was prepared in anhydrous chlorobenzene. 8 mg of P(NDI2OD-T2) (0.008 mmol) were added to a GC vial, followed by 0.83 mL of chlorobenzene and 0.174 mL of N-DMBI-H stock solution to reach a P(NDI2OD-T2):N-DMBI-H molar ratio of 1:0.8. The vial was closed and sealed under argon using a thermoplastic adhesive. The vial was then heated in an oil bath for 1 hour at the desired temperature (60°C, 80°C, or 100°C depending on the sample) before undergoing GC analysis. One sample was kept at room temperature and was not heated up before being analysed.

2.10.3 RGA-MS – Hydrogen detection experiments

The setup for the RGA-MS experiments is here described. A vacuum chamber was directly connected to a Residual Gas Analysis (RGA) quadrupole mass spectrometer (SPECTRA, Microvision Plus) equipped with dual Faraday and electron multiplier detector and capable of discriminating masses in the order of 2, 3 and 4 amu. The sample container was covered with a heater (lamp with reflector) connected to an external Sorensen adjustable DC power supply and controller. A thermocouple was connected to the sample holder to monitor temperature inside the chamber. Sample powder was placed in an aluminium foil, which was punctured to let formed gases flow freely during the detection experiment. The aluminium foil containing the sample was then placed inside a tantalum container positioned in the vacuum chamber of the RGA setup. Before starting the experiments, the chamber pressure was reduced to 2×10^{-6} Torr. The sample was then heated with a rate of 10 °Cmin^{-1} from an initial temperature of around 50 °C to a final temperature of 160 °C. While heating, partial pressure of D_2, H_2, and H-D ions inside the chamber were monitored over time through the RGA mass spectrometer via conversion of their respective ion current against mass (vacuum pumping speed: 50 Ls^{-1}).

Preparation of samples for RGA-MS experiments

Samples used for RGA-MS analysis were prepared according to the following procedure. P(NDI2OD-T2) (38.5 mg, 0.0389 mmol) was weighed in a glass vial. N-DMBI-D (21 mg, 0.078 mmol) was dissolved in 0.3 mL of anhydrous chlorobenzene in glove box under inert atmosphere. Such solution was then added to the polymer (N-DMBI-D: P(NDI2OD-T2) = 2:1 in molar ratio) and the mixture was left resting for 3 hours under argon, in the dark at room temperature before evaporating the solvent under nitrogen flux. 49 mg of this blend were used for the RGA-MS experiment. The control experiment for the RGA-MS experiments was prepared according to a similar procedure, using no N-DMBI-D but only 60 mg of P(NDIOD-T2) and anhydrous chlorobenzene. 50 mg of this powder were analysed.

2.10.4 Electron Paramagnetic Resonance

Solution Electron paramagnetic Resonance measurements were performed with a Bruker EMX spectrometer equipped with an Oxford cryostat. Spectra were recorder at a temperature of 130K.

Preparation of samples for EPR measurements

A solution containing P(NDI2OD-T2) and N-DMBI-H in 1:0.8 molar ratio was prepared in anhydrous chlorobenzene following the procedure described in **Section 2.10.2.5** (polymer concentration: 8 mgml^{-1}). 0.125 mL of this solution were diluted to reach a final P(NDI2OD-T2) concentration of 1 mgml^{-1}. EPR tubes were filled with this second solution and were sealed with a thermoplastic adhesive under argon atmos-

phere. Two tubes were heated up for 1 hour in an oil bath, at the desired temperature (80°C and 100°C) before EPR analysis. A third sample was instead kept at room temperature for 1 hour before being analysed. Control experiment containing only P(NDI2OD-T2) was prepared with an analogue procedure, using a 1 $mgml^{-1}$ solution of P(NDI2OD-T2) in anhydrous chlorobenzene and was heated at 100°C for 1 hour.

2.10.5 Solution UV-Vis-NIR absorption measurements

In an N_2 filled glove box, a 10 $mgmL^{-1}$ N-DMBI-H solution in dichloromethane and an 8$mgmL^{-1}$ solution of P(NDI2OD-T2) solution in chlorobenzene were prepared. Aliquots of N-DMBI-H solution were added to different vials and the solvent was dried under vacuum, then aliquots of P(NDI2OD-T2) solution were added to each vial to reach a P(NDI2OD-T2):N-DMBI-H molar ratio of 1:0.8. The vials were then sealed and heated at the selected temperature on a hot plate for 1 hour (temperatures of different thermal treatments are reported in **Figure 2.18**). Temperature was monitored with a thermocouple (± 2°C). The solutions were then let cool down to room temperature and diluted to a polymer concentration of 0.1 $mgmL^{-1}$ before absorption spectrum collection. A 0.1 $mgmL^{-1}$ pristine P(NDI2OD-T2) polymer solution was analysed as well. All spectra were collected using a Perkin Elmer l1050 spectrophotometer, using 1 mm quartz cuvette. Solutions were transferred into the cuvette inside the glove box and the cuvette was carefully sealed under inert atmosphere before each spectrum acquisition.

UV-Vis-NIR analysis of P(NDI2OD-T2) aggregation in chlorobenzene

A 1 $mgmL^{-1}$ solution of P(NDI2OD-T2) was prepared in chlorobenzene. The solution was transferred into a quartz cuvette (optical path: 2 mm) and heated for 1 hour at different temperatures immediately before UV-Vis-NIR absorption measurement.

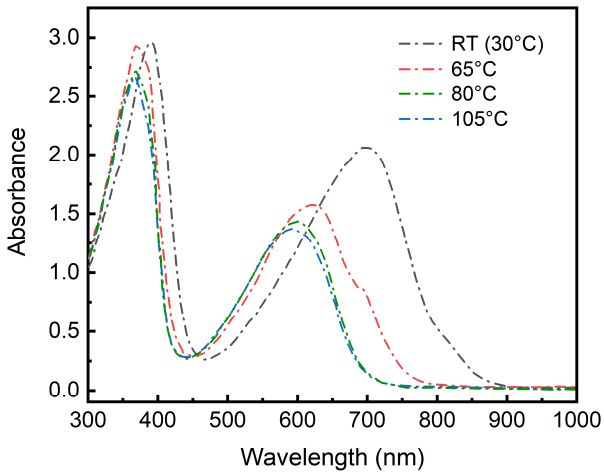

Figure 2.23 UV-Vis-NIR absorption spectra of a P(NDI2OD-T2) solution in chlorobenzene heated at different temperatures. Solution concentration: 1 $mgmL^{-1}$.

Intensity of absorption features attributed to polymers aggregates (peak at 700 nm and 800 nm) and visible in sample kept at room temperature progressively decreases when the solution is heated at higher temperatures, in agreement with previous reports.[37]

When heating at T>80°C, only the charge-transfer band (peak at 600 nm) of disaggregated polymer is visible and no aggregate is present in the solution.

2.10.6 ICP-OES measurements

ICP-OES analysis was performed by Maria Tringali (University of Milano-Bicocca). Analysis of residual palladium concentration in synthetized batch of P(NDI2OD-T2) was performed with an OPTIMA 7000 DV inductively coupled plasma-optical emission spectrophotometer by PerkinElmer. P(NDI2OD-T2) sample (100 mg) was digested by adding nitric acid (HNO_3 65%) and hydrogen peroxide (H_2O_2 30%) in an 8:2 volume ratio, using an Anton Paar multiwave 5000. The instrument vessel was kept at 220 °C for 30 minutes. Digested sample was then diluted with MilliQ water to reach a total volume of 10 mL. After centrifugation and dilution to twice the initial volume, samples were ready to be analysed by ICP-OES. Certified standard reference materials of Pd 1000 mgL^{-1} (PerkinElmer) were used for calibration and quality control. The operating parameters of the ICP-OES instrument were set up using emission line at 220.353 nm in Axial View, and sample solutions were measured in triplicate. The detection limits for Pd is 0.01 mgL^{-1}.

Appendix A - H_2 leakage from GC-Vials

Since H_2 gas leakage is very easy due to the small dimensions of hydrogen molecules, we performed an experiment to analyse the tightness of the GC-vials used and to verify if our results and conclusions might have been highly affected by H_2 losses. To do so, we introduced empty GC-vials in the same vacuum bag which was then put under vacuum. A gaseous mixture of argon and molecular hydrogen (H_2 concentration around 1% in moles) was cannulated inside the bag and the GC-Vials were closed in such atmosphere. This procedure was performed to guarantee the same initial conditions for all the samples. The H_2 content of the vials was then analysed at different times after sample preparation to evaluate the entity of H_2 loss. The analysis was performed on vials exposed to a 2 hours thermal treatments at 150°C as well, so to reproduce the conditions of experiments performed on solid blends. The obtained results are collected in **Figure 2.24**. Data shows that samples kept at room temperature are affected by an overall H_2 loss of around 25% in a 24 hours, this loss mostly happening during the first hour of storage. Only negligible losses were detected after 4 and 24 hours ($\leq$ 5%). The GC study of doping happening in solutions was performed on samples analysed at most two days after preparation. As hydrogen leakage is expected to become slower along with hydrogen level reduction, it is reasonable to consider the H_2 concentration values obtained in the analysis of such samples to be affected by an H_2 loss of 30% at most.

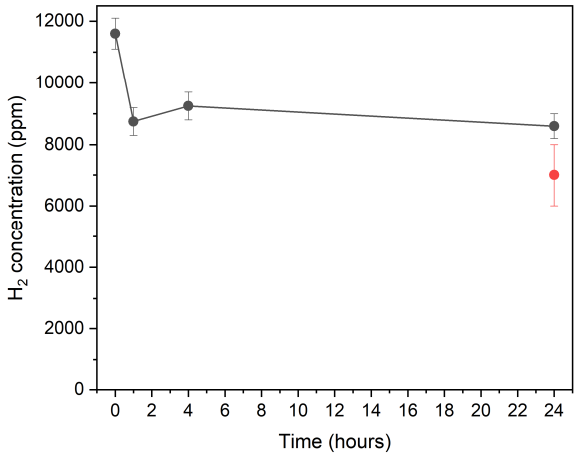

Figure 2.24: H_2 concentration variation over time for GC-vials kept at room temperature (black) and vials heated at 150°C for 2 hours (red). Data are obtained as average value between two samples analysed at each collection time.

Thermally treated samples showed an average H_2 concentration value of 7000 $\pm$ 1000 ppm, which implies an overall hydrogen loss of 40 $\pm$ 9 % with respect to the initial average hydrogen content (11600 ppm). The thermal treatment increases thus the H_2 loss of around 20 % with respect to samples analysed after 24 hours but not subjected to heating (average value: 8600 ppm). These results suggest that on the overall, the H_2 concentration detected during experiments on thermally treated samples are affected by an H_2 loss of 50% at most. Therefore, the entity of the H_2 loss does not alter the result of our experiments and the reached conclusions.

2.11 Bibliography

1 P. Wei, J. H. Oh, G. Dong and Z. Bao, *J. Am. Chem. Soc.*, 2010, **132**, 8852–8853.

2 S. Griggs, A. Marks, H. Bristow and I. McCulloch, *J. Mater. Chem. C*, 2021, **9**, 8099–8128.

3 D. Huang, H. Yao, Y. Cui, Y. Zou, F. Zhang, C. Wang, H. Shen, W. Jin, J. Zhu, Y. Diao, W. Xu, C. A. Di and D. Zhu, *J. Am. Chem. Soc.*, 2017, **139**, 13013–13023.

4 Y. Zeng, W. Zheng, Y. Guo, G. Han and Y. Yi, *J. Mater. Chem. A*, 2020, **8**, 8323–8328.

5 S. Jhulki, H. I. Un, Y. F. Ding, C. Risko, S. K. Mohapatra, J. Pei, S. Barlow and S. R. Marder, *Chem*, 2021, **7**, 1050–1065.

6 X. Q. Zhu, M. T. Zhang, A. Yu, C. H. Wang and J. P. Cheng, *J. Am. Chem. Soc.*, 2008, **130**, 2501–2516.

7 B. D. Naab, S. Guo, S. Olthof, E. G. B. Evans, P. Wei, G. L. Millhauser, A. Kahn, S. Barlow, S. R. Marder and Z. Bao, *J. Am. Chem. Soc.*, 2013, **135**, 15018–15025.

8 J. Liu, B. Van Der Zee, D. R. Villava, G. Ye, S. Kahmann, M. Kamperman, J. Dong, L. Qiu, G. Portale, M. A. Loi, J. C. Hummelen, R. C. Chiechi, D. Baran and L. J. A. Koster, *ACS Appl. Mater. Interfaces*, 2021, **13**, 29858–29865.

9 S. Riera-Galindo, A. Orbelli Biroli, A. Forni, Y. Puttisong, F. Tessore, M. Pizzotti, E. Pavlopoulou, E. Solano, S. Wang, G. Wang, T. P. Ruoko, W. M. Chen, M. Kemerink, M. Berggren, G. Di Carlo and S. Fabiano, *ACS Appl. Mater. Interfaces*, 2019, **11**, 37981–37990.

10 Z. Bin, J. Li, L. Wang and L. Duan, *Energy Environ. Sci.*, 2016, **9**, 3424–3428.

11 B. D. Naab, S. Zhang, K. Vandewal, A. Salleo, S. Barlow, S. R. Marder and Z. Bao, *Adv. Mater.*, 2014, **26**, 4268–4272.

12 J. Nossal, R. K. Saini, L. B. Alemany, M. Meier and W. E. Billups, *European J. Org. Chem.*, 2001, 4167–4180.

13 H. Guo, C. Y. Yang, X. Zhang, A. Motta, K. Feng, Y. Xia, Y. Shi, Z. Wu, K. Yang, J. Chen, Q. Liao, Y. Tang, H. Sun, H. Y. Woo, S. Fabiano, A. Facchetti and X. Guo, *Nature*, 2021, **599**, 67–73.

14 D. E. Schwarz, T. M. Cameron, P. J. Hay, B. L. Scott, W. Tumas and D. L. Thorn, *Chem. Commun.*, 2005, 5919–5921.

15 M. C. D'Alterio, E. Casals-Cruanas, N. V Tzouras, G. Talarico, S. P. Nolan and A. Poater, *Chem. Eur. J.*, 2021, **27**, 13481–13493.

16 B. Saglio, M. Mura, M. Massetti, F. Scuratti, D. Beretta, X. Jiao, C. R. McNeill, M. Sommer, A. Famulari, G. Lanzani, M. Caironi and C. Bertarelli, *J. Mater. Chem. A*, 2018, **6**, 15294–15302.

17 R. A. Schlitz, F. G. Brunetti, A. M. Glaudell, P. L. Miller, M. A. Brady, C. J. Takacs, C. J. Hawker and M. L. Chabinyc, *Adv. Mater.*, 2014, **26**, 2825–2830.

18 S. Zhang, B. D. Naab, E. V. Jucov, S. Parkin, E. G. B. Evans, G. L. Millhauser, T. V. Timofeeva, C. Risko, J. L. Brédas, Z. Bao, S. Barlow and S. R. Marder, *Chem. - A Eur. J.*, 2015, **21**, 10878–10885.

19 D. Kiefer, A. Giovannitti, H. Sun, T. Biskup, A. Hofmann, M. Koopmans, C. Cendra, S. Weber, L. J. Anton Koster, E. Olsson, J. Rivnay, S. Fabiano, I. McCulloch and C. Müller, *ACS Energy Lett.*, 2018, **3**, 278–285.

20 A. J. Pell, G. Pintacuda and C. P. Grey, *Prog. Nucl. Magn. Reson. Spectrosc.*, 2019, **111**, 1–271.

21 P. A. Redhead, *AIP Conf. Proc.*, 2003, **671**, 243.

22 F. H. Westheimer, *Chem. Rev.*, 1961, **61**, 265–273.

23 O. Bardagot, C. Aumaître, A. Monmagnon, J. Pécaut, P. A. Bayle and R. Demadrille, *Appl. Phys. Lett.*, 2021, **118**, 1–6.

24 P. Zalar, M. Kuik, Z. B. Henson, C. Woellner, Y. Zhang, A. Sharenko, G. C. Bazan and T. Q. Nguyen, *Adv. Mater.*, 2014, **26**, 724–727.

25 Y. Han, G. Barnes, Y. H. Lin, J. Martin, M. Al-Hashimi, S. Y. Alqaradawi, T. D. Anthopoulos and M. Heeney, *Chem. Mater.*, 2016, **28**, 8016–8024.

26 L. H. Doerrer and M. L. H. Green, *Dalt. Trans.*, 1999, 4325–4329.

27 P. S. Marqués, G. Londi, B. Yurash, T. Q. Nguyen, S. Barlow, S. R. Marder and D. Beljonne, *Chem. Sci.*, 2021, **12**, 7012–7022.

28 P. Pingel, M. Arvind, L. Kölln, R. Steyrleuthner, F. Kraffert, J. Behrends, S. Janietz and D. Neher, *Adv. Electron. Mater.*, 2016, **2**, 1–7.

29 B. Yurash, D. X. Cao, V. V. Brus, D. Leifert, M. Wang, A. Dixon, M. Seifrid, A. E. Mansour, D. Lungwitz, T. Liu, P. J. Santiago, K. R. Graham, N. Koch, G. C. Bazan and T. Q. Nguyen, *Nat. Mater.*, 2019, **18**, 1327–1334.

30 M. Arvind, C. E. Tait, M. Guerrini, J. Krumland, A. M. Valencia, C. Cocchi, A. E. Mansour, N. Koch, S. Barlow, S. R. Marder, J. Behrends and D. Neher, *J. Phys. Chem. B*, 2020, **124**, 7694–7708.

31 J. Zhang, Y. Chen, P. Sewell and M. A. Brook, *Green Chem.*, 2015, **17**, 1811–1819.

32 J. Cella and S. Rubinsztajn, *Macromolecules*, 2008, **41**, 6965–6971.

33 N. Moitra, S. Ichii, T. Kamei, K. Kanamori, Y. Zhu, K. Takeda, K. Nakanishi

and T. Shimada, *J. Am. Chem. Soc.*, 2014, **136**, 11570–11573.

34 D. H. Flagg and T. J. McCarthy, *Langmuir*, 2017, **33**, 8129–8139.

35 S. G. Chen, H. M. Branz, S. S. Eaton, P. C. Taylor, R. A. Cormier and B. A. Gregg, *J. Phys. Chem. B*, 2004, **108**, 17329–17336.

36 M. Xiong, X. Yan, J. Li, S. Zhang, Z. Cao, N. Prine, Y. Lu, J. Wang, X. Gu and T. Lei, *Angew. Chemie*, 2021, **60**, 8189–8197.

37 R. Steyrleuthner, M. Schubert, I. Howard, B. Klaumünzer, K. Schilling, Z. Chen, P. Saalfrank, F. Laquai, A. Facchetti and D. Neher, *J. Am. Chem. Soc.*, 2012, **134**, 18303–18317.

38 D. Trefz, A. Ruff, R. Tkachov, M. Wieland, M. Goll, A. Kiriy and S. Ludwigs, *J. Phys. Chem. C*, 2015, **119**, 22760–22771.

39 H. I. Un, S. A. Gregory, S. K. Mohapatra, M. Xiong, E. Longhi, Y. Lu, S. Rigin, S. Jhulki, C. Y. Yang, T. V. Timofeeva, J. Y. Wang, S. K. Yee, S. Barlow, S. R. Marder and J. Pei, *Adv. Energy Mater.*, 2019, **9**, 1–10.

40 S. Wang, D. Fazzi, Y. Puttisong, M. J. Jafari, Z. Chen, T. Ederth, J. W. Andreasen, W. M. Chen, A. Facchetti and S. Fabiano, *Chem. Mater.*, 2019, **31**, 3395–3406.

41 P. Olczyk, P. Ramos, M. Bernas, K. Komosinska-Vassev, J. Stojko and B. Pilawa, *Evidence-based Complement. Altern. Med.*, 2013, **2013**, 1–9.

42 D. Lungwitz, T. Schultz, C. E. Tait, J. Behrends, S. K. Mohapatra, S. Barlow, S. R. Marder, A. Opitz and N. Koch, 1–16.

43 R. Matsidik, H. Komber, A. Luzio, M. Caironi and M. Sommer, *J. Am. Chem. Soc.*, 2015, **137**, 6705–6711.

44 S. R. Greenfield, W. A. Svec, D. Gosztola and M. R. Wasielewski, *J. Am. Chem. Soc.*, 1996, **118**, 6767–6777.

45 D. T. Gryko, M. K. Rogacki, J. Klajn, M. Gałęzowski, D. K. Stępień and M. K. Cyrański, *Org. Lett.*, 2010, **12**, 2020–2023.

46 G. S. Vadehra, R. P. Maloney, M. A. Garcia-Garibay and B. Dunn, *Chem. Mater.*, 2014, **26**, 7151–7157.

Chapter 3

Impact of morphology in controlling the doping efficiency: the role of nucleating agents

---

Results of this work have been published in a paper: F. Pallini, S. Mattiello, M. Cassinelli, P. Rossi, S. Mecca, W. L. Tan, M. Sassi, G. Lanzani, C. R. McNeill, M. Caironi, and L. Beverina, "Unexpected Enhancement of Molecular n-Doping Efficiency in Polymer Thin Films by a Degradation Product".

ACS Appl. Energy Mater., **2022**, 5, 2, 2421–2429

While working with N-DMBI-H, it became clear to us that, despite the definition of air-stable dopant, this compound has a limited stability toward oxidation, especially if in solution. At the time of our investigation, the potential impact of performances of the chemical integrity of N-DMBI-H was seldomly discussed. We thus decided to systematically analyse the impact of degradation products on the performances of doped polymeric films. This chapter collects the result of such studies. I will here show that these byproducts are not detrimental for applications, but unexpectedly behave as nucleating agents for N-DMBI-H, acting on the microstructure of the dopant/polymer blend and boosting its electrical performances. The same conclusion is then extended to another nucleating agent, thus showing that the addition of the right third component in a semiconductor/dopant system can be a strategy to tune doping efficiency.

This work was performed in collaboration with Mario Caironi's research group at the Italian Institute of Technology (IIT) of Milan. The N-DMBI-H stability analysis was performed in collaboration with Dr. Sara Mattiello.

3.1 The limits of N-DMBI-H air stability

One of the main advantages of N-DMBI-H is, according to the literature, its air-stability.[1] Very recently however, some works demonstrated that this stability is limited, especially when N-DMBI-H is exposed to oxygen while in solution. In a work published in 2020 by Pei's group for example, air stability of N-DMBI-H in different solvents is investigated, with the conclusion that this compound is not stable in most of them and degrades completely within few days.[2] In a following work by Demadrille's group, the structure of different N-DMBI-H oxidation products are reported, highlighting that two possible degradation impurities can form: a oxidized cationic species (N-DMBI$^+$) and an amidic open derivative, here called DMBI-Ox (**Figure 3.1**). The same work shows that the degradation outcome highly depends on the polarity of the medium: in polar solvents, like chloroform and acetonitrile, N-DMBI$^+$ is the main degradation side-product while in apolar ones the reaction leading to DMBI-Ox formation prevails. The authors then further demonstrate that the oxidation reactions are triggered by light irradiation or heat.[3]

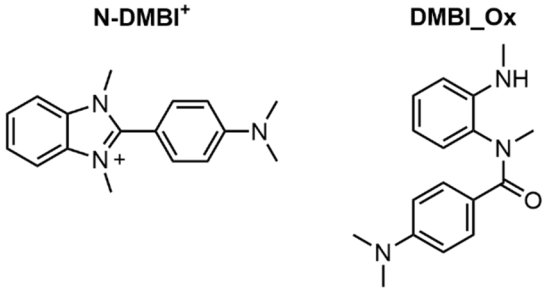

Figure 3.1: Molecular structure of N-DMBI-H possible oxidation products: the cation N-DMBI$^+$ and the amide DMBI-Ox.

These findings stated for the first time that N-DMBI-H solution should be handled under inert environment. Indeed, doping processes mediated by contaminated N-DMBI-H are expected to be less efficient, perhaps also leading to negative morphological impacts due to addition of impurities in the semiconductor host.

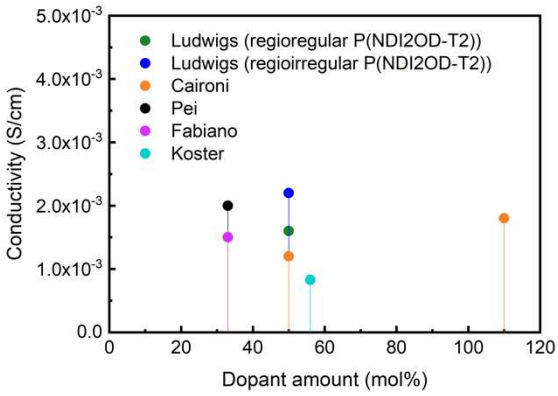

Figure 3.2 Conductivity values of N-DMBI-H doped P(NDI2OD-T2) films reported in the literature by different authors.

Before the demonstration of N-DMBI-H poor stability in solution, no precaution was suggested for the device preparation procedures encompassing the use of this compound. Still, many authors reported comparable results in doping processes performed using not preliminary characterized commercial N-DMBI-H and/or without mentioning the use of deoxygenated solvent or inert atmosphere during solution preparation, which is surprising. **Figure 3.2**. shows for examples conductivity values of P(NDI2OD-T2) polymer films doped via solution mixing with N-DMBI-H and reported by different authors:[2,4–7] the obtained performances are comparable, despite the different dopant origin and the different conditions of solution preparation. This suggests the existence of a more complex interaction between oxidation impurities and the semiconductor/dopant blend and calls for a deep investigation of the impact of oxidation side-products on N-DMBI-H mediated doping outcome.

3.2 Aim of the work

Starting from such considerations we aimed at investigating the impact of N-DMBI-H oxidation impurities on the performances of doped semiconductors.
Since the degradation outcome depends on the solvent used, we firstly analysed the dopant stability in common processing solvents and characterized the main degradation products. Then we moved to the analysis of the effects of such oxidation impurities on the electrical properties of a doped n-type polymer processed in the same solvents. The determination of how these contaminants act on the conductivity of a doped semiconductor is however not easy. In fact, the presence of such impurities makes us deal with a ternary blend problem. In such a complex system, decoupling effects related to doping processes efficiency, changes in carrier's mobility and changes in microstructure is not straightforward. A better understanding of the blends behaviour thus comes after a first deep investigation of the specific interactions playing between oxidation side products and N-DMBI-H.

3.3 N-DMBI-H stability characterization

As first step, we analysed the oxidation kinetic of N-DMBI-H under common storage and solvent processing conditions. This was done to understand the composition of the powder samples and of the solutions generally used in semiconductor doping procedures. The analysis was performed on non-commercial, carefully purified N-DMBI-H samples, synthesized according to the procedure reported in **Chapter 4**.

We firstly analysed the impact of oxidation on powder samples kept under laboratory atmosphere. The solid darkens over time, as highlighted in **Figure 3.3**. Solution NMR characterization of sample exposed to air for 1 month shows however presence of only 1-2 mol% of N-DMBI$^+$, thus confirming the decent air stability of N-DMBI-H in solid state and the possibility to handle this compound under air in such conditions (see Experimental section for NMR spectrum). Still, the analysis demonstrates that slow oxidation of solid samples happens in air and suggests inert atmosphere to be the best condition for long term storage. We thus kept our N-DMBI-H powder samples under argon.

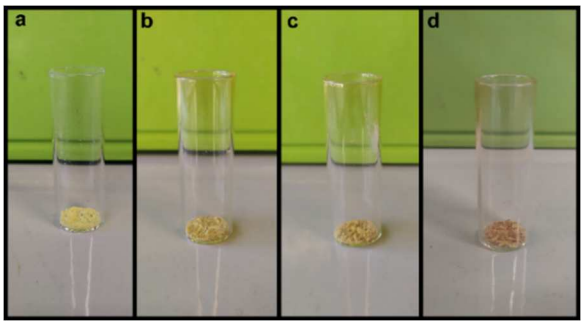

Figure 3.3 Picture of the as prepared N-DMBI-H powder (a) and of the same sample after 1 week (b), 2 weeks (c) and 3 weeks under air.

We then moved to the analysis of N-DMBI-H degradation kinetic in solution via ^{1}H NMR. We selected chlorobenzene for this experiment, since this is one of the most common processing solvents for doping procedures.[8,9] We then monitored the evolution of 10 mgmL^{-1} N-DMBI-H solutions in chlorobenzene-d_5 prepared under argon and kept

under air or under inert atmosphere (glove box under argon, $O_2 < 0.1$ ppm, $H_2O < 0.1$ ppm). The results are reported in **Figure 3.4**. The dopant oxidation is fast under air and 50% of the material is degraded within two days. Complete degradation leads to formation of a solution containing DMBI-Ox and N-DMBI$^+$ in a 9:1 molar ratio, thus showing that the amide derivative is the dominant degradation side-product in this solvent (**Figure 3.4b**). The degradation kinetic is far slower under argon, the sample showing almost no sign of degradation for the first two days of monitoring. Oxidation then slowly proceeds, probably due to oxygen traces entering the solution during sample storage and during NMR analysis. The experiment confirms the role of air in the degradation reaction. In principle however both H_2O and O_2 might cause the oxidation to occur. To get further insight into the process, we thus monitored degradation in a N-DMBI-H solution obtained using d_5-chlorobenzene saturated with D_2O and kept under laboratory atmosphere. In the presence of water, the same degradation side-products are obtained (see experimental section for NMR spectrum) but the oxidation reaction is slower. A possible explanation is that water might stabilize intermediates species forming during reaction of N-DMBI-H with O_2. A detailed characterization of the oxidation mechanism is beyond the scope of this work. Nevertheless, these data suggest that degradation is mainly due to oxygen presence and that moisture can slow down the reaction.

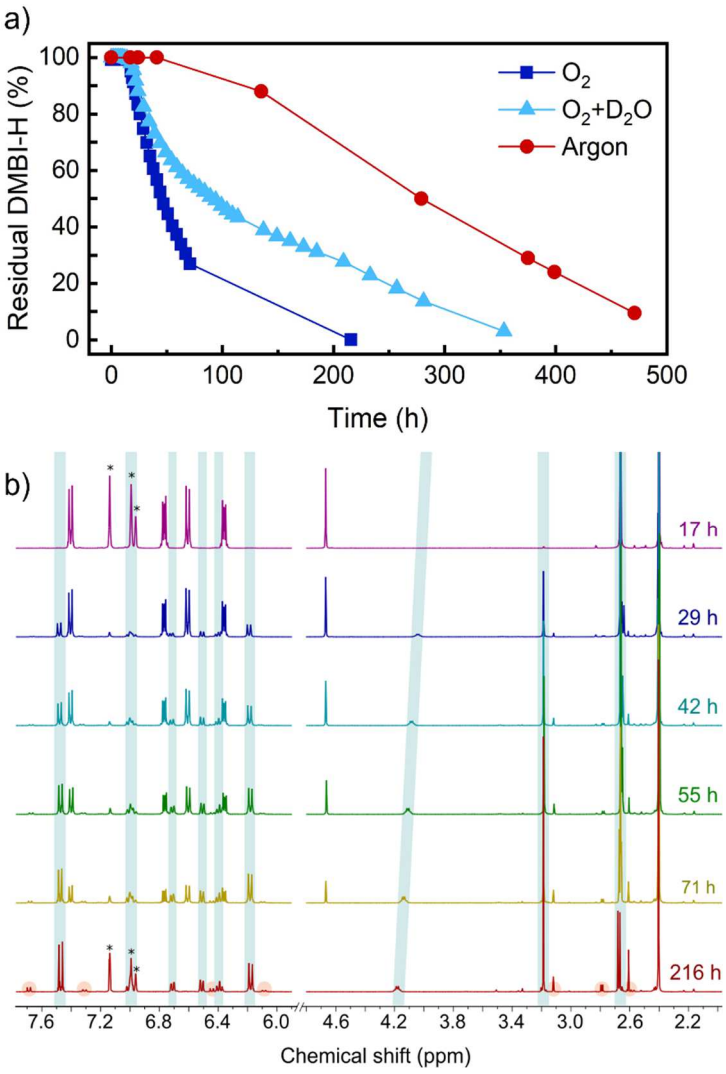

Figure 3.4 (a) Oxidation over time of N-DMBI-H in d_5-chlorobenzene solutions kept under argon (red) and under air in absence (blue) or presence (light blue) of deuterated water. Residual N-DMBI-H amount was evaluated via solution ^{1}H-NMR peaks integration; (b) evolution in time of the ^{1}H-NMR spectra of N-DMBI-H solution kept under air in the absence of water. Peaks related to DMBI-Ox and N-DMBI$^+$ are highlighted in blue and red respectively. Solvent residual peaks are indicated with asterisks. For further details on the compounds NMR see experimental section and reference 3.

The obtained results confirm that non negligible amounts of N-DMBI-H oxidation side products, mainly DMBI-Ox, form in chlorobenzene solutions in time-spans typical of doping experimental campaigns, that can usually last several days.

3.4 Impact of DMBI-Ox on P(NDI2OD-T2) electrical performances

We moved to the analysis of the impact of the detected oxidation impurities on electrical performance of doped semiconductors. For the purpose, we selected the benchmark P(NDI2OD-T2) polymer as model material. We firstly prepared solutions of this polymer in chlorobenzene in the presence of different amounts of N-DMBI-H (1%, 3%, 5%, 10% and 30% in weight with respect to P(NDI2OD-T2) respectively). We aged these solutions under inert atmosphere, reproducing the conditions of the NMR analysis of samples kept under argon. We then prepared films with these solutions after aging them for different time, we annealed the obtained films for 2 hours at 150°C to activate the doping process and eventually measured the conductivity of the doped polymer. The obtained electrical performances are collected in **Figure 3.5**. The conductivity values are in line with those previously reported for this semiconductor/dopant system in the literature.[5] Unexpectedly, the performances do not show evident drops even after 250 hours of solution aging, which corresponds, according to our NMR kinetic analysis, to 50% of oxidized N-DMBI-H (see **Figure 3.4a**). A drop in conductivity is evident only after 400 hours of solution aging and only for samples prepared with solution containing 1 wt% of N-DMBI-H. We could then not detect any negative effect related to dopant oxidation.

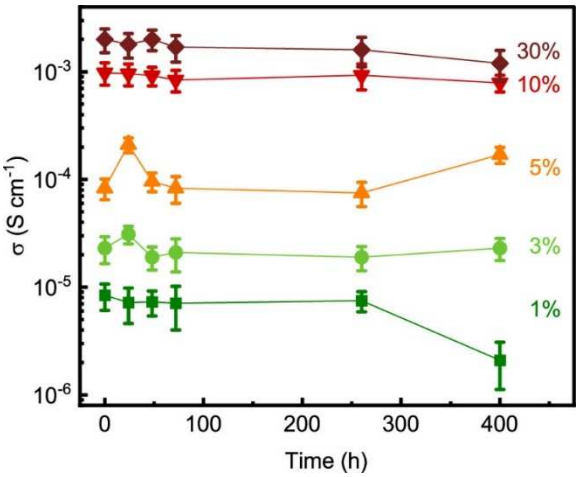

Figure 3.5: electrical conductivity of P(NDI2OD-T2) film containing different wt% amount of N-DMBI-H as a function of solution aging time. Reprinted from reference 25.

Since one cannot exclude N-DMBI-H degradation to behave differently in the presence of the polymer, we decided to directly contaminate the polymeric film with known amounts of DMBI-Ox. We then prepared a polymer film containing 10 wt% of a 20:80 N-DMBI-H:DMBI-Ox molar mixture. It is worth noting that the actual amount of pure N-DMBI-H added to the sample was of only 2 wt% with respect to P(NDI2OD-T2). This sample showed a conductivity of 9×10^{-4} Scm^{-1}, a value comparable to that obtained using 10 wt% of pure N-DMBI-H and two orders of magnitude higher than that expected from a film containing 2 wt% of active N-DMBI-H, which should be between 1×10^{-5} or 2×10^{-5} Scm^{-1} according to **Figure 3.5**. The result thus suggest that the presence of DMBI-Ox has a positive effect on the electrical performances. The conductivity improvements could be in principle connected with DMBI-Ox mediated doping of P(NDI2OD-T2), even if this is not expected from a species already obtained via oxidation reactions.

To completely rule out any such contribution, we evaluated the HOMO level of DMBI-Ox via electrochemical characterization (Differential Pulse Voltammetry and Cyclic Voltammetry, **Figure 3.6**). Both DPV and CV show two non-reversible oxidation processes of DMBI-Ox, with peaks located at +0.42 V and +0.62 V vs Fc/Fc^+. The corresponding evaluated HOMO energy level of -5.15 eV is around 1.3 eV lower than P(NDI2OD-T2) LUMO level (~ -3.9 eV)[10], which suggests that this oxidation impurity in unlikely to reduce the polymer.

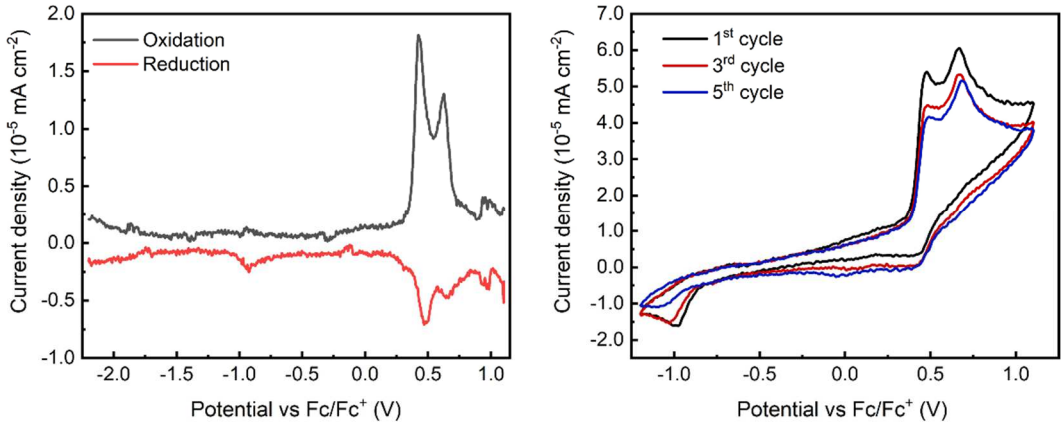

Figure 3.6 Differential pulse voltammetry (DPV, left) and Cyclic voltammetry (CV, right) analysis of DMBI-Ox. Measurements were performed using a 0.1 M solution of tetrabutylammonium perchlorate in acetonitrile as electrolyte. Potentials are reported against ferrocene redox couple ($E_{1/2}$ Fc/Fc^+= +0.397 V vs Ag/AgCl).

The presence of DMBI-Ox impurity might also change the microstructure of the polymeric film inducing higher crystallinity, a factor that, as mentioned in **Chapter 1**, can improve charge transport. A correlation between highly ordered chain packing and charge carrier mobility improvement has, indeed, been reported for P(NDI2OD-T2).[11–13] We thus evaluated the electrical properties of a P(NDI2OD-T2) film containing 30 wt% of DMBI-Ox and compared them with that of a pristine polymeric film to investigate this possibility. We obtained conductivity values of 6×10^{-6} and 3×10^{-7} Scm^{-1} respectively. These data show that the presence of this oxidation impurity alone can increase electrical performances of the polymer of one order of magnitude, which, considering the electrochemical characterization results, suggest a beneficial effect on charge mobility. Still, this improvement cannot explain by its own the striking conductivity enhancement obtained using blends of N-DMBI-H and DMBI-Ox. A more complex effect dictated by the copresence of these two compounds must then exist. As discussed in **Chapter 1**, the main limiting factor of N-DMBI-H doping efficiency is its low miscibility in the conductive host, that causes its segregation from the semiconductor.

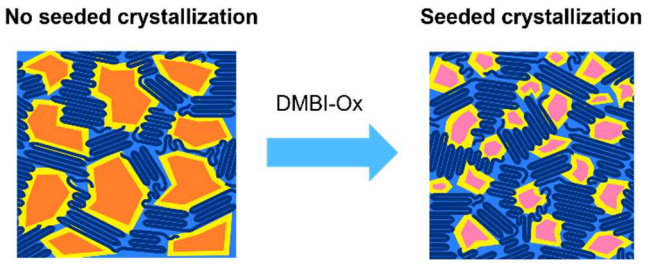

Figure 3.7 Hypothesized effect of DMBI-Ox. Left: N-DMBI-H (orange) forms domains within the polymeric matrix (blue). Doping happens only at the interfacial area between dopant and polymer (yellow). Right: the presence of DMBI-Ox triggers the nucleation of DMBI-H in smaller domains (pink)

Due to this phenomenon, only the dopant molecules at the interface between the segregated dopant domains and the conductive matrix are active during the doping process. While working with DMBI-Ox we noticed that it is less soluble than N-DMBI-H in chlorobenzene. We thus hypothesized that the presence of this impurity could trigger the heterogeneous nucleation of N-DMBI-H in domains of smaller dimensions during the polymer film formation, thus increasing the interfacial area between the dopant and the semiconductor and, as such, the doping efficiency. **Figure 3.7** shows a cartoon of the hypothesized phenomenon.

3.5 N-DMBI-H/DMBI-Ox blends characterization

3.5.1 Thermal characterization

To shed light on the nature of the interactions between N-DMBI-H and DMBI-Ox we decided to analyse their blends via Differential Scanning Calorimetry (DSC), a suitable technique for the study of nucleating agents.[14,15]

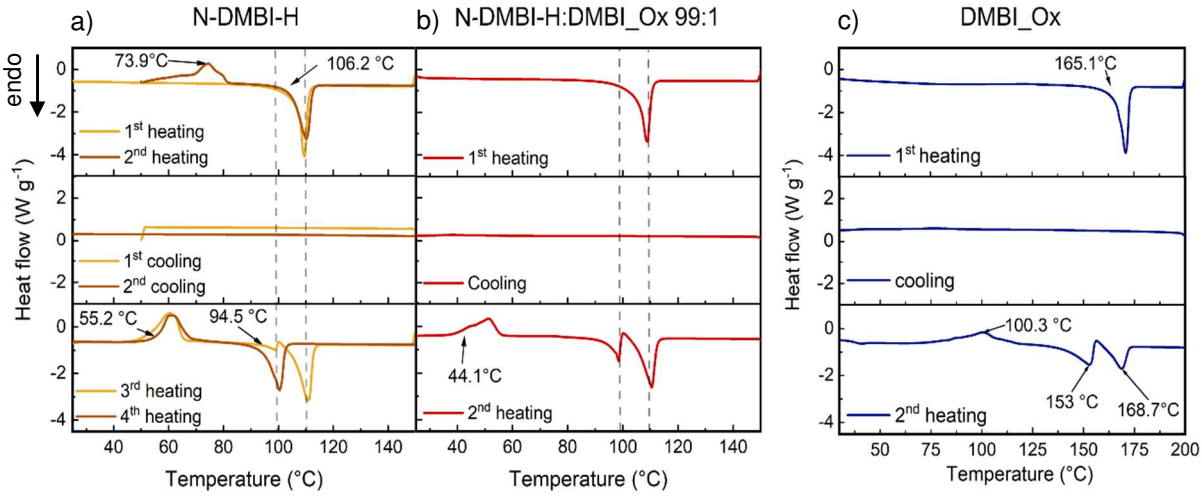

Figure 3.8 DSC thermograms related to successive heating and cooling cycles of pure N-DMBI-H sample (a), N-DMBI-H:DMBI_Ox 99:1 (mol:mol) blend (b) and pure DMBI_Ox sample (c). Arrows highlight onset of the main phase transitions or their peak temperature if a clear-cut determination of onset was not possible. In plots **a** and **b,** grey lines are placed at the main fusion peaks positions. In the case of graph **a**, 2nd cooling trace refers to the cooling cycle between the 3rd and 4th heating cycles. All measurements were carried out under N_2 flow. Further details are reported in the experimental section.

We firstly analysed a pure N-DMBI-H sample, to get insight on the phase transition of our pristine material. We performed all the thermal treatments between 25 and 150°C and under N_2 flow, to avoid any possible oxidation reaction triggered by heat. Under such conditions, we repeatedly heated and cool down the same N-DMBI-H sample. The obtained thermograms are reported in **Figure 3.8a**. In the first heating cycle a peak appears around 110°C, with an onset at 106.2°C. This feature is associated with N-DMBI-H melting.[7] No crystallization event is highlighted during the following cooling cycle, while the second heating scan shows a cold recrystallization peak around

74°C, again followed by the compound fusion. During the third heating cycle, cold recrystallization peak shifts to 60°C (onset 55.2°C) and a new fusion peak at around 98°C appears, followed again by the one associated with N-DMBI-H melting. In the fourth heating scan, the only endothermic feature present is that around 99°C, while cold crystallization remains unchanged, apart from a small shift of its onset to higher temperatures. We suspected that the appearance of the second melting peak could be triggered by formation of DMBI-Ox during the successive heating cycles due to presence of oxygen traces in the crucible. The DSC crucible was in fact punctured before the measurement, so oxygen might have penetrated it during the process. We thus repeated the same DSC treatments on three further samples of N-DMBI-H, stopping the measurement after two, three and four heating cycles respectively. We then analysed via NMR the crucible content of each sample. The obtained NMR spectra are collected in **Figure 3.9** and confirm that DMBI-Ox content in the sample increases with the number of thermal cycles.

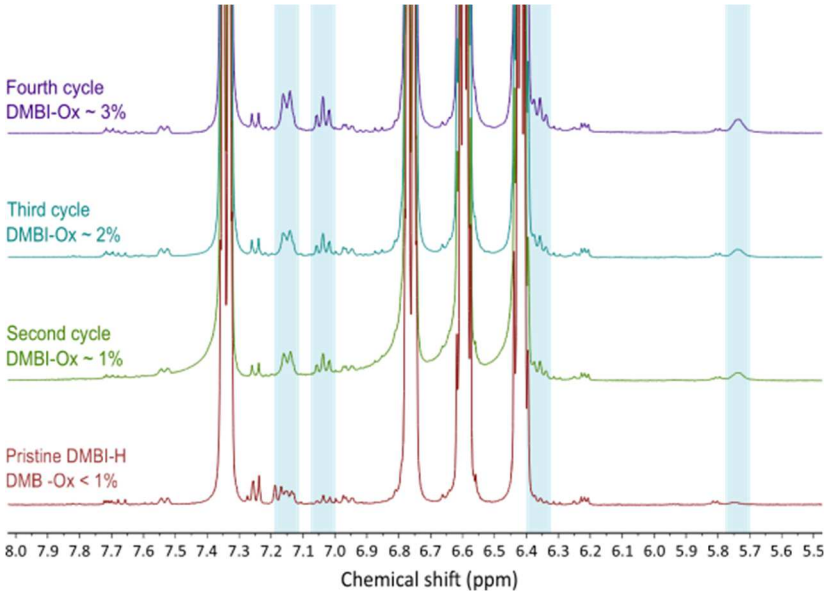

Figure 3.9 ^{1}H NMR spectra of N-DMBI-H in DMSO-d_6 after each DSC heating cycles. Peaks related to DMBI-Ox are highlighted in light blue.

We thus prepared a sample mechanically mixing N-DMBI-H and DMBI-Ox in a 99:1 molar ratio and compared the obtained DSC analysis (**Figure 3.8b**). In the first heating cycle only N-DMBI-H melting peak is present. This is expected, since DMBI-Ox melting point is higher than 150°C and located at 165-170°C, as highlighted by the DSC of pure DMBI-Ox reported in **Figure 3.8c**. Again, no feature was detected during the cooling cycle, in complete analogy to pure N-DMBI-H sample. The second heating scan then resembles the third heating cycle of pure N-DMBI-H DSC: a cold crystallization peak located around 52 °C appears (onset around 44°C), followed by two melting peaks at 99°C and 109°C respectively. The appearance of the second endothermic peak at 98-99°C cannot be ascribed to features of pure DMBI-Ox: the two endothermic peaks detected in the second scan of DMBI-Ox thermogram are in fact at far higher temperatures. It can instead be explained by the nucleation of a different crystalline phase of N-DMBI-H, initiated by the presence of the oxidation impurity. The obtained phase might correspond either to a eutectic peak, a specific composition of the two compounds that melts at lower temperatures with respect to the pure ones, or to a different N-DMBI-H polymorph.[16,17] However, the thermal characterization alone cannot give further insight on this phase transition nature.

3.5.2 XRD characterization

To confirm that the unexpected melting peak corresponds to a new N-DMBI-H crystalline phase, we performed XRD characterization of N-DMBI-H:DMBI-Ox 99:1 blends. We firstly characterized the crystalline nature of a pure N-DMBI-H sample and compared it to the calculated crystal pattern obtained by single crystal data published in Demadrille's group work (**Figure 3.10a**,**b**).[3] The two patterns are essentially the same, thus confirming that the material we isolated via solvent evaporation has the same crystal structure of the one previously described in the literature. We thus prepared a solid sample of N-DMBI-H containing 3 mol% of DMBI-Ox. We selected this composition since, according to the NMR analysis reported in **Figure 3.9**, this is the amount of DMBI-Ox necessary to trigger the complete nucleation of N-DMBI-H in the new phase with melting point of 98-99°C. We then melted the sample at 140°C under N_2, to reproduce the thermal treatment of the DSC analysis. We let the sample cool down to room temperature, obtaining the formation of an amorphous glass, and heated it again at 60°C to obtain a crystalline solid. We firstly performed NMR characterization of the

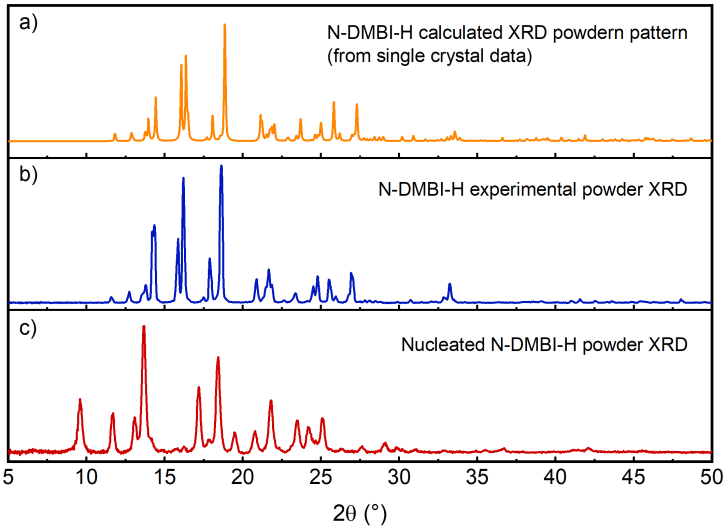

Figure 3.10 (a) calculated XRD powder pattern of N-DMBI-H obtained from single crystal data; (b) diffraction pattern of a pure N-DMBI-H sample; (c) powder XRD pattern of a sample of N-DMBI-H nucleated by DMBI-Ox.

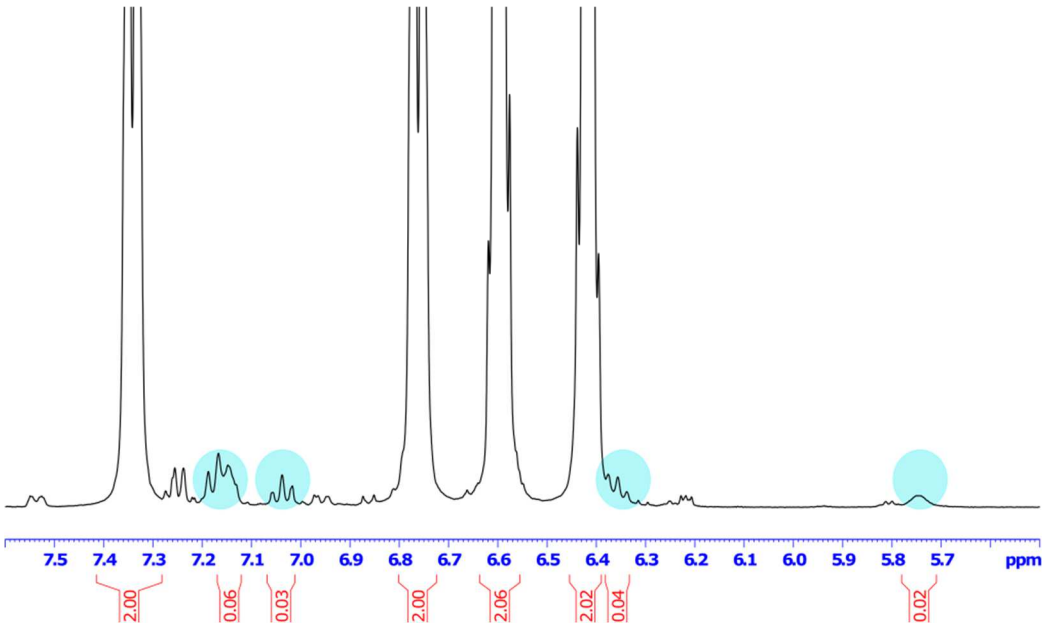

Figure 3.11 ^{1}H-NMR spectrum in DMSO-d_6 of the N-DMBI-H:DMBI-Ox blend analysed via XRD. Peaks related to DMBI-Ox are highlighted in light blue.

obtained powder to make sure that the performed treatment did not alter the composition of the blend. The obtained NMR spectrum, here reported in **Figure 3.11**, confirms the maintained sample composition. We subsequently performed XRD characterization of the powder (**Figure 3.10c).** The obtained pattern is sizably different from that of pure N-DMBI-H. Since a eutectic mixture should show a crystal pattern given by superimposition of those of the individual components,[18] data confirm that DMBI-Ox work as nucleating agent for the dopant and seeds the crystallization of a different N-DMBI-H polymorph.

3.6 Comparison with a different nucleating agent

To corroborate our results, we decided to extend our analysis to another nucleating agent. For the purpose, we selected and synthesized a branched o-phenylenediamine derivative (oPDA), whose structure is reported in **Figure 3.12**.

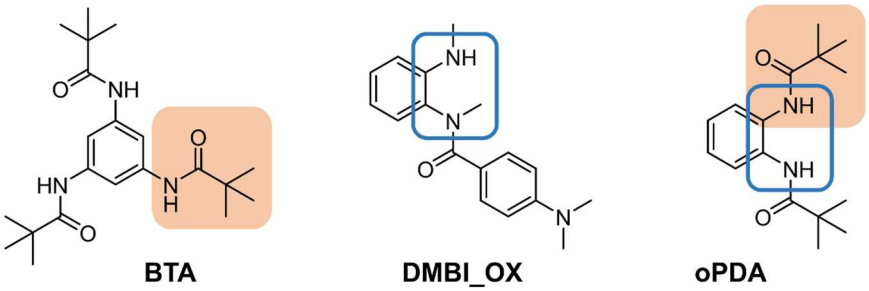

Figure 3.12 Molecular structure of the selected branched amide oPDA, the common industrial nucleating agent BTA and DMBI_Ox. The tert-butyl-amide group common to BTA and oPDA is highlighted in orange, while the o-substitution pattern shared by DMBI-Ox and oPDA is highlighted in blue.

This compound has never been specifically studied as nucleating agent. Its choice was however dictated by three factors:

- Branched amides are generally known to be good nucleating agents. They are for examples used with this purpose with isotactic polypropylene.[15]
- The structure of oPDA is designed to resembles that of tris-tert-butyl-1,3,5-benzenetrisamide (BTA; Irgaclear XT 386, **Figure 3.12**), which is a very common industrial nucleating agent.[14,19] Moreover, it also recalls the 1,2-substitution pattern of DMBI-Ox, which might induce the same behaviour with respect to N-DMBI-H.
- The solubility of oPDA in chlorobenzene is around 13 $mgmL^{-1}$, lower than that of N-DMBI-H (> 15 $mgmL^{-1}$), a property which suggest the possibility to induce heterogeneous crystallization during solution processing.

We then repeated the same DSC experiment previously reported on a N-DMBI-H:oPDA 99:1 (mol:mol) blend. The results are reported in **Figure 3.13a**. In analogy with the thermal characterization of DMBI-Ox containing blends, the first heating scan shows only the peak related to melting of N-DMBI-H, as expected by the high melting point of pure oPDA (~181-182°C, **Figure 3.13b**). Again, no crystallization peak was detected during the cooling cycle.

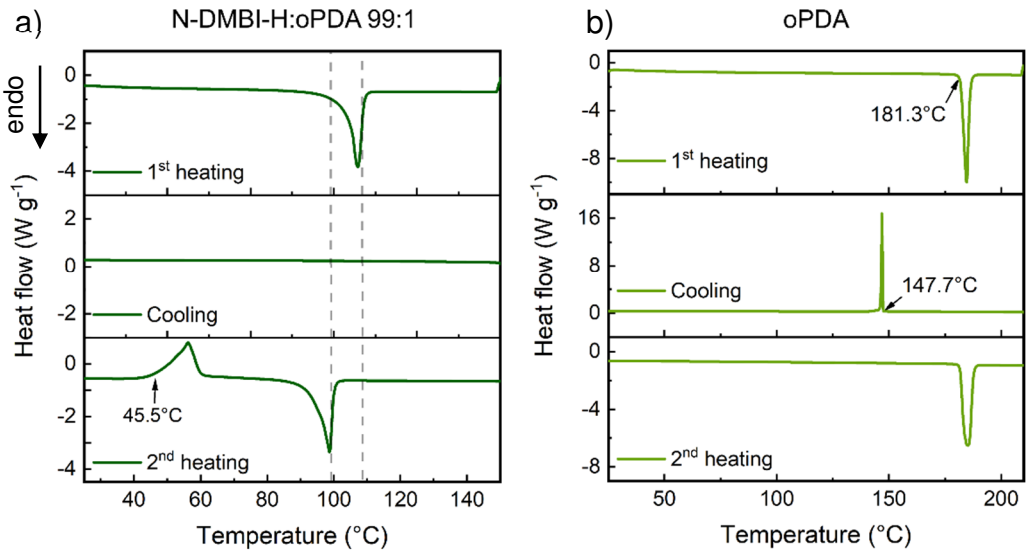

Figure 3.13 DSC thermograms related to successive heating and cooling cycles of a N-DMBI-H:oPDA 99:1 (mol:mol) blend (a) and pure oPDA (b). Arrows highlight onset of the main phase transitions. In plots **a**, grey lines are placed at temperatures corresponding to the previously detected melting peaks of the two N-DMBI-H polymorphs. All measurements were carried out under N_2 flow. For further details see the experimental section.

The second heat scan instead is essentially the same of the one we obtained during the fourth heating cycle of pure N-DMBI-H: we observe a cold crystallization peaked at 56 °C (onset at 45.5 °C), followed by a melting peak at 98°C. This second melting peak is at the same temperature of that of N-DMBI-H samples nucleated by DMBI-Ox, suggesting that oPDA nucleates the same N-DMBI-H phase. Apparently oPDA is even a more efficient nucleation seed than DMBI-Ox. With addition of only 1 mol% of oPDA, the complete nucleation of the dopant second phase is indeed obtained and no presence of the pristine N-DMBI-H phase is detected in the thermogram. Furthermore, the cold crystallization peak onset is here shifted to lower temperatures with respect to the fourth heating cycle of pure N-DMBI-H (from 55°C to around 44-45°C). This feature, more commonly observed in crystallizations happening during cooling scans, is generally attributed to improved seeded crystallization and further suggest a more efficient heterogeneous nucleation.[14,20]

3.7 Characterization of N-DMBI-H films containing nucleating agents

The performed thermal characterization demonstrates that both DMBI-Ox and oPDA can efficiently nucleate a different crystalline phase of N-DMBI-H in the case of blends recrystallized by melts. We decided to verify if this behaviour corresponds to formation of smaller N-DMBI-H domains in crystallization processes happening during solvent evaporation, a condition resembling the polymeric films preparation.

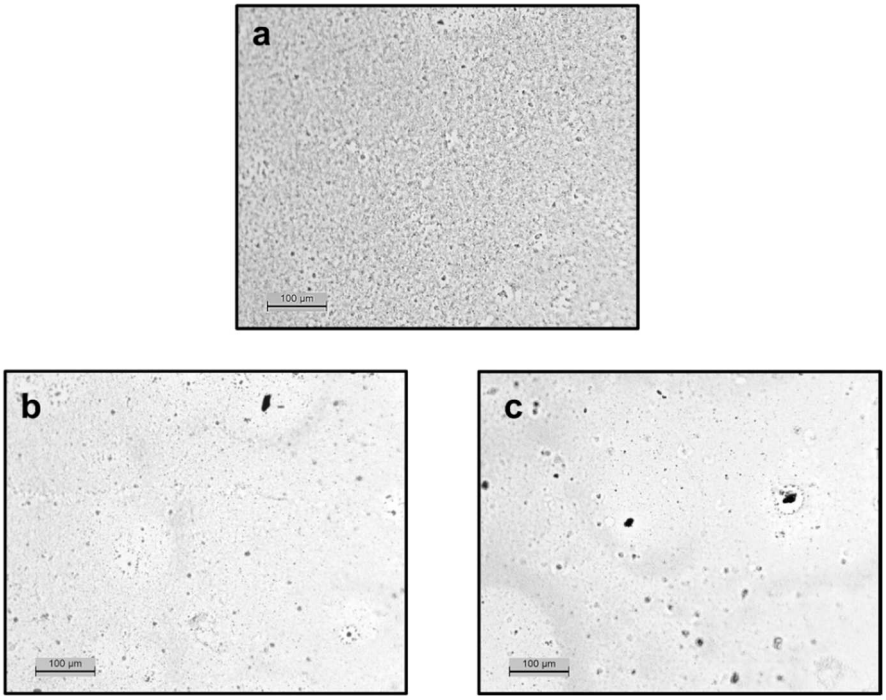

Figure 3.14 Optical microscope images of films spin coated from 10 mgmL^{-1} solutions of N-DMBI-H (a), N-DMBI-H:DMBI-Ox 99:1 (b) N-DMBI-H:oPDA 99:1(c) in chlorobenzene. Images were collected in transmission mode. Scale bar: 100 µm.

We thus prepared two films from chlorobenzene solution of N-DMBI-H containing 1 mol% of DMBI-Ox and oPDA respectively and compared their optical microscopy images to those obtained from solutions containing only N-DMBI-H. When no nucleating agent is present, N-DMBI-H crystallizes in coarser grains (**Figure 3.14a**). For both films containing DMBI-Ox and oPDA the obtained crystallites are finer and less easily detectable, a result generally associated with a seeded crystallization process (**Figure 3.14b,c**).[14,21] The data thus hints that both these nucleating agents could in principle reduce the dimension of N-DMBI-H domains within polymeric films obtained via spin coating.

3.8 Impact of oPDA on polymer/dopant blends

Since oPDA shows the same behaviour of N-DMBI-Ox when interacting with N-DMBI-H, we extended the analysis to the impact of this second nucleating agent on the electrical performances of P(NDI2OD-T2)/N-DMBI-H blends. The obtained results are collected in **Table 3.1**. We firstly measured the conductivity of P(NDI2OD-T2) films containing 30 wt% of oPDA, to investigate if this compound alone could improve the polymer performances, as it was for DMBI-Ox (entry 1). We measured a conductivity value of 1.5×10^{-6} Scm^{-1}, a value close to that here previously reported for P(NDI2OD-T2) blended with 30 wt% of DMBI-Ox. Also in this case, we performed an electrochemical characterization of oPDA to evaluate its HOMO level and electron donating capability (Experimental section, **Figure 3.23**). We were not able to detect any oxidation peak within the electrochemical stability range of the used solvent (acetonitrile), which confirm that this compound has a very deep HOMO level and cannot dope the polymer. The reason behind the conductivity enhancement is thus likely connected, in analogy to DMBI-Ox, to higher crystallinity and carrier mobility improvement. We then measured the conductivity of a film containing 10 wt% of a 80:20 molar mixture of N-DMBI-H and oPDA, obtaining a value of 1.1×10^{-3} Scm^{-1} (entry 2), again in good agreement with that obtained using a N-DMBI-H:DMBI-Ox 80:20 molar mixture (9×10^{-4} Scm^{-1}). These results thus confirm that oPDA behaves like DMBI-Ox also within P(NDI2OD-T2)/N-DMBI-H blends. Since our DSC data show that 1 mol% of oPDA is enough to give complete nucleation of N-DMBI-H second crystalline phase, we decided to use a 99:1 N-DMBI-H:oPDA mixture to dope P(NDI2OD-T2) (entry 3-6, **Table 3.1**). We then compared the obtained results to those of films doped using pure N-DMBI-H (**Figure 3.15**). The presence of oPDA evidently boost electrical performances, especially in films containing small dopant concentrations, and leads to a maximum conductivity of 5.0×10^{-3} Scm^{-1} in the case of films doped with 30 wt% of

Table 3.1 Electrical conductivity of P(NDI2OD-T2) films doped with oPDA:N-DMBI-H mixtures as a function of their composition.

entry	oPDA:N-DMBI-H (mol:mol)	wt%	σ (Scm^{-1})	enhancement[a]
1	Pure oPDA	30	1.5×10^{-6}	-
2	80:20	10	1.1×10^{-3}	-
3	1:99	3	8.3×10^{-5}	3.6
4	1:99	5	3.9×10^{-4}	4.7
5	1:99	10	3.1×10^{-3}	3.2
6	1:99	30	5.0×10^{-3}	2.5

[a]calculated as ratio with respect to values obtained from polymer films containing the same wt% of pure N-DMBI-H.

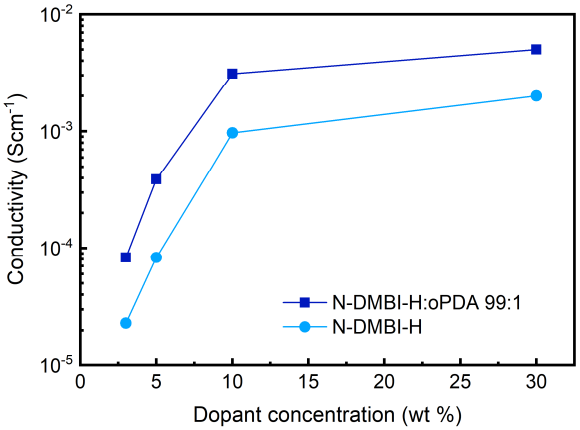

Figure 3.15 Conductivity values of N-DMBI-H doped P(NDI2OD-T2) films in the presence (blue squares) and absence (light blue circles) of oPDA.

N-DMBI-H, which is one of the highest conductivity values reported for P(NDI2OD-T2) films doped with N-DMBI-H under similar processing conditions (see **Figure 3.2** for commonly reported values).

The obtained results are in line with the hypothesis of a more efficient doping. However, the detected conductivity enhancement might again be correlated to an improved charge carrier mobility as well. We thus performed Grazing Incidence Wide Angle X-Ray Scattering (GIWAXS) on polymeric films containing 10 wt% of N-DMBI-H in the presence and in the absence of 1% mol of oPDA, to analyse any change in the polymer crystallinity or packing induced by this additive (**Figure 3.16**). In both films P(NDI2OD-T2) adopts a face-on orientation, as highlighted by the presence of In-Plane (IP) (h00) lamellar stacking peaks, IP (001) backbone repeat peaks and Out-Of-Plane (OOP) π-π stacking (0h0) peak in the sector-averaged profiles. Presence of very weak OOP (h00) lamellar stacking peaks indicates a minority edge-on orientation. No evident difference can be detected between the two diffraction patterns, which indicates that oPDA does not induce noticeable changes within the ordered phase of the polymer. This supports our hypothesis of a more efficient doping process induced by dopant heterogeneous nucleation rather than an improved charge carrier mobility.

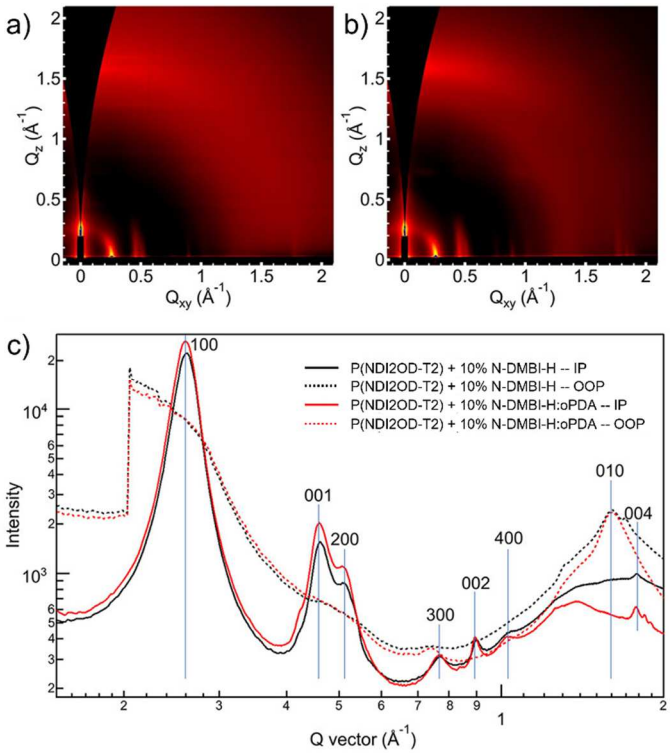

Figure 3.16 2D grazing-incidence wide-angle X-ray scattering (GIWAXS) patterns of the P(NDI2OD-T2) film doped with 10 wt % of N-DMBI-H (a) and 10 wt % of the N-DMBI-H:oPDA 99:1 mixture (b). (C) Sector averaged 1D profiles along OOP (dashed line) and IP (full lines). Reprinted from reference 25.

3.9 Conclusions

In conclusion, the obtained results demonstrate that the formation of N-DMBI-H oxidation impurities is not necessarily detrimental for electrical performances of doped semiconductors but, in the right conditions, can improve their conductivity. The obtained data show in fact that N-DMBI-H exists in two different crystalline phases, one melting at 98-99°C and the other melting at 108-110°C, and that the N-DMBI-H degradation product DMBI-Ox can efficiently seed the nucleation of the first one, with a beneficial impact on the doping process. The same effect can be obtained with different nucleating agents and the performed characterizations suggest that the reason behind the observed performance enhancement is a better distribution of the dopant in smaller

nucleated domains within the semiconductor matrix, which increases the amount of dopant interacting with the conductive host and, as a consequence, the doping efficiency.

If nucleating agents have already been reported to enhance transport properties via tuning of organic semiconductors crystallinity and morphology,[14,21] no example of the use of this approach to mitigate effect of dopants/semiconductor poor miscibility is, to the best of our knowledge, present in the literature. Our findings thus introduce the use of these additives as a novel strategy to increase doping efficiency, alternative to more common approaches aiming at improving semiconductor/dopant mutual solubility via structural modification, a process that can sometimes lead to improved doping efficiency at the expense of charge carrier's mobility. Moreover, the approach is potentially general and might lead to increased performances also in other dopant/semiconductors systems with the selection of the right nucleating agent.

3.10 Experimental methods

P(NDI2OD-T2) was purchased from Flexterra (M*n*=34.7 kDa, PDI=1.9). All other chemicals and solvents were purchased from J&K Scientific, Sigma-Aldrich, Alfa Aesar, Merck, Thermo Scientific and used as received.

3.10.1 Synthetic procedures

Chromatographic purifications were performed using Davisil LC 60A silica gel (pore size 60 Å, 70-200 μm). Composition of solvent mixtures used as eluents are indicated as volume/volume ratios. Melting points were determined using a Buchi M-560 apparatus. Solution Nuclear Magnetic Resonance (NMR) spectra were acquired with a Bruker Avance 400 NEO Spectrometer.

3.10.1.1 Synthesis of N-DMBI-H

N-DMBI-H was synthesized according to the procedure reported in **Chapter 4**, Experimental methods section.

^{1}H NMR (400 MHz, chlorobenzene-d_5) δ 7.41 (d, J=8.8 Hz, 2H), 6.77 (m, 2H), 6.61 (d, J=8.8 Hz, 2H), 6.36 (m, 2H), 4.67 (s, 1H), 2.66 (s, 6H), 2.40 (s, 6H).

3.10.1.2 Isolation of DMBI_Ox

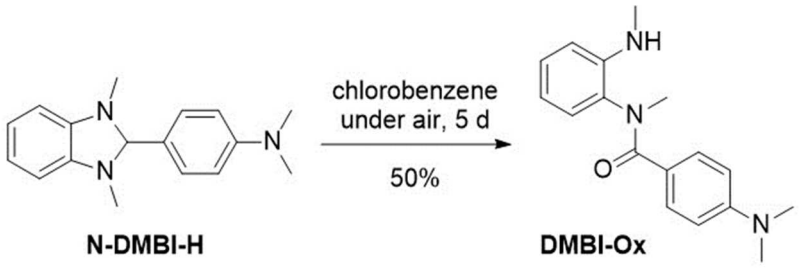

In a 25 mL roundbottom flask, **N-DMBI-H** (150 mg, 0.561 mmol) is dissolved in 10 mL of chlorobenzene. The solution is kept stirring at room temperature and under air for five days, monitoring **N-DMBI-H** degradation by TLC (eluent: DCM/AcOEt 1:1). After five days, no more **N-DMBI-H** is present in the mixture. Chlorobenzene is evaporated under vacuum, and the obtained powder is purified by column chromatography (eluent: DCM/AcOEt 9:1 gradient DCM/AcOEt 1:1). 80 mg of **DMBI-Ox** are recovered as an off-white solid (0.28 mmol, 50% yield). mp 169-170 °C. Anal. Calcd. for C17H21N3O: C, 72.06; H, 7.47; N, 14.83; O, 5.65. Found: C, 71.88; H, 7.54; N, 14.61.

^{1}H NMR (400 MHz, chlorobenzene-d_5) δ 7.47 (d, J=9.1, 2H), 7.02-6.98 (m, 1H), 6.71 (dd, J=7.7, 1.4 Hz, 1H), 6.51 (dd, J=8.1, 1.1 Hz, 1H), 6.39 (td, J=7.5, 1.3 Hz, 1H),

6.18 (d, J=9.1 Hz, 2H), 4.18 (q, J=5.2 Hz, 1H), 3.19 (s, 3H), 2.67 (d, J=5.2 Hz, 3H), 2.40 (s, 6H).

^{1}H NMR (400 MHz, benzene-d_6) δ 7.65 (d, J=8.9 Hz, 2H), 6.98 (t, J=7.8 Hz, 1H), 6.71 (dd, J=7.6, 1.3 Hz, 1H) 6.44 (d, J=8.1 Hz, 1H), 6.39 (td, J=7.6, 1.2 Hz, 1H), 6.21 (d, J=8.9 Hz, 2H), 3.94 (q, J=5.1 Hz, 1H), 3.21 (s, 3H), 2.42 (d, J=5.2 Hz, 3H) 2.24 (s, 6H).

^{13}C{^{1}H} NMR (100 MHz, benzene-d_6) δ 171.01, 151.21, 144.60, 132.16, 130.53, 128.67, 128.17, 122.88, 110.50, 110.30, 39.04, 36.29, 29.61.

3.10.1.3 Synthesis of oPDA

Synthesis was performed following a literature procedure.[22]
In a 250 mL flask, 1,2-phenylenediamine (1.59 g, 14.7 mmol) is dissolved in 90 mL of dry dichloromethane, then triethylamine (3.58 g, 35.4 mmol) is added. The solution is cooled to 0 °C with an ice bath, then pivaloyl chloride (3.90 g, 32.3 mmol) is slowly added dropwise. The solution is kept at room temperature for 21 hours, observing the formation of a white precipitate. Reaction progress is monitored by TLC (eluent: heptane/AcOEt 6:4). The mixture is diluted with dichloromethane to obtain a clear solution which is therefore washed with a 5% aqueous HCl solution (75 mL), a saturated $NaHCO_3$ solution (100 mL), brine (75 mL) and deionized water (75 mL). The organic phase is dried over Na_2SO_4, filtered and the dichloromethane is evaporated under reduced pressure. The product is taken up with heptane and filtered to recover 3.463 g of white crystals (12.5 mmol, 85% yield). mp 182-183 °C.

^{1}H NMR (400 MHz, $CDCl_3$) δ 8.08 (br, 2H), 7.41-7.37 (m, 2H), 7.21-7.17 (m, 2H), 1.31 (s, 18H).

3.10.1.4 NMR spectra

N-DMBI-H

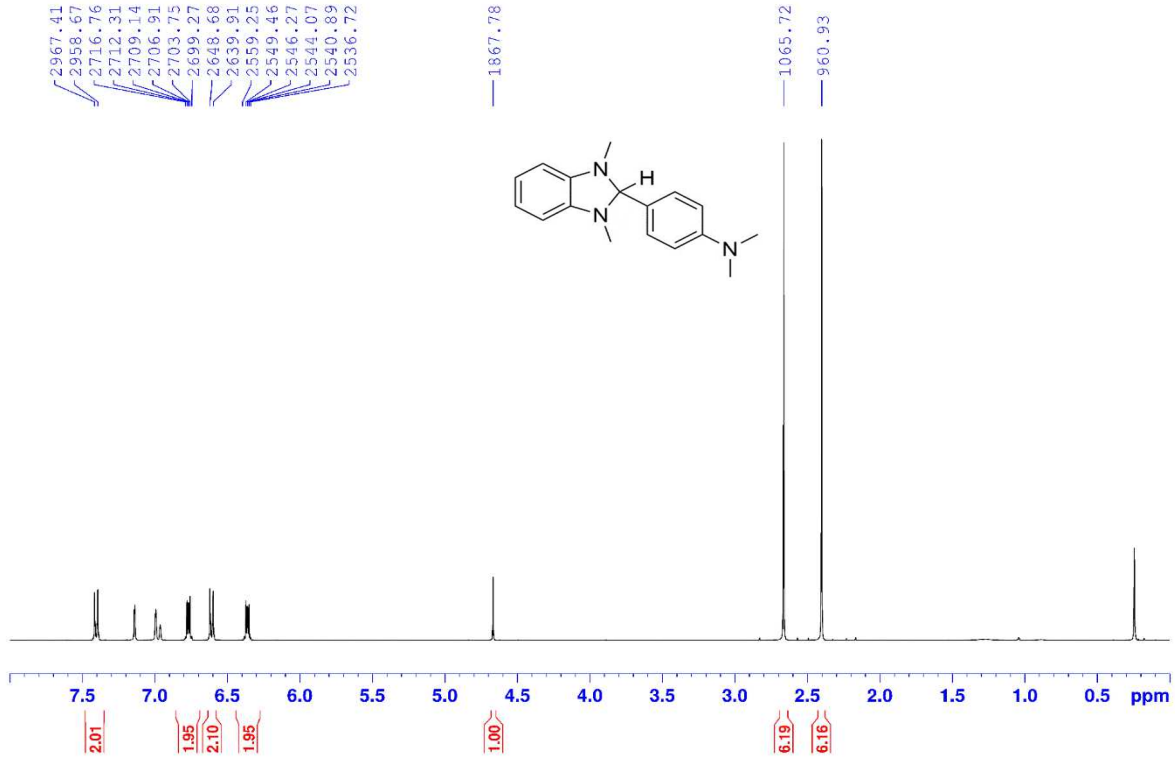

Figure 3.17: ^{1}H NMR of N-DMBI-H in Chlorobenzene-d_5.

DMBI_Ox

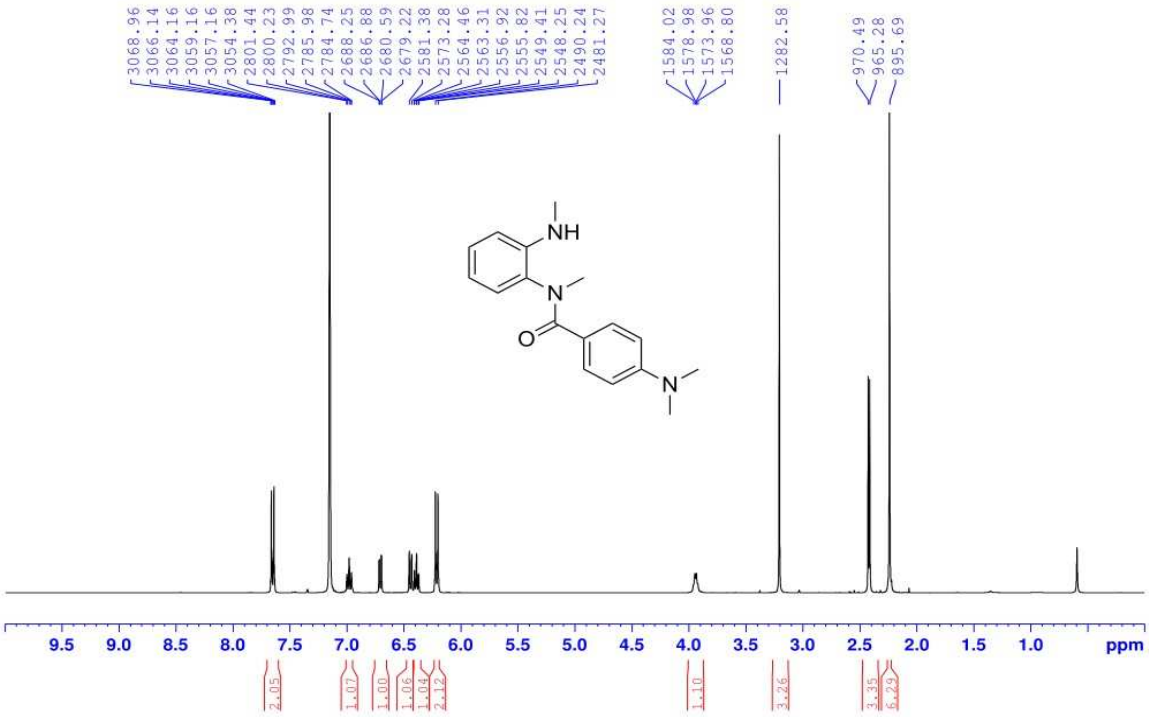

Figure 3.18: ^{1}H NMR of DMBI-Ox in Benzene-d_6.

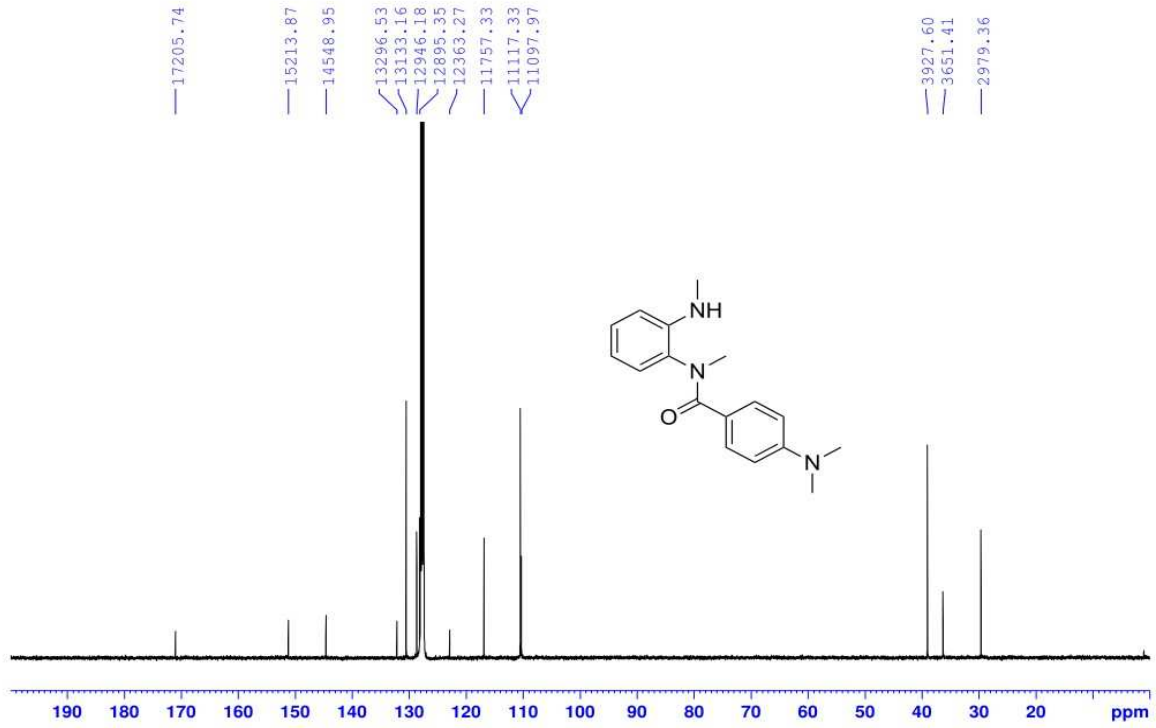

Figure 3.19: $^{13}C\{^{1}H\}$ NMR of DMBI_Ox in Benzene-d_6.

oPDA

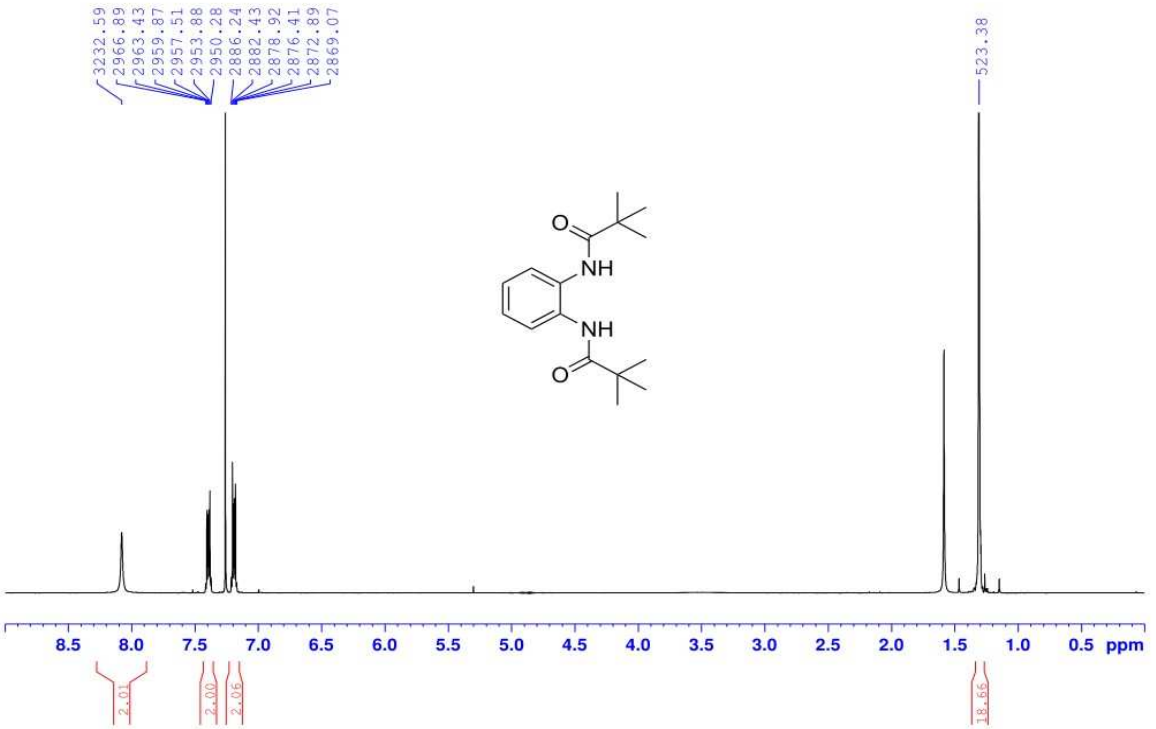

Figure 3.20: ^{1}H NMR of oPDA in $CDCl_3$.

3.10.2 N-DMBI-H oxidation in solid state

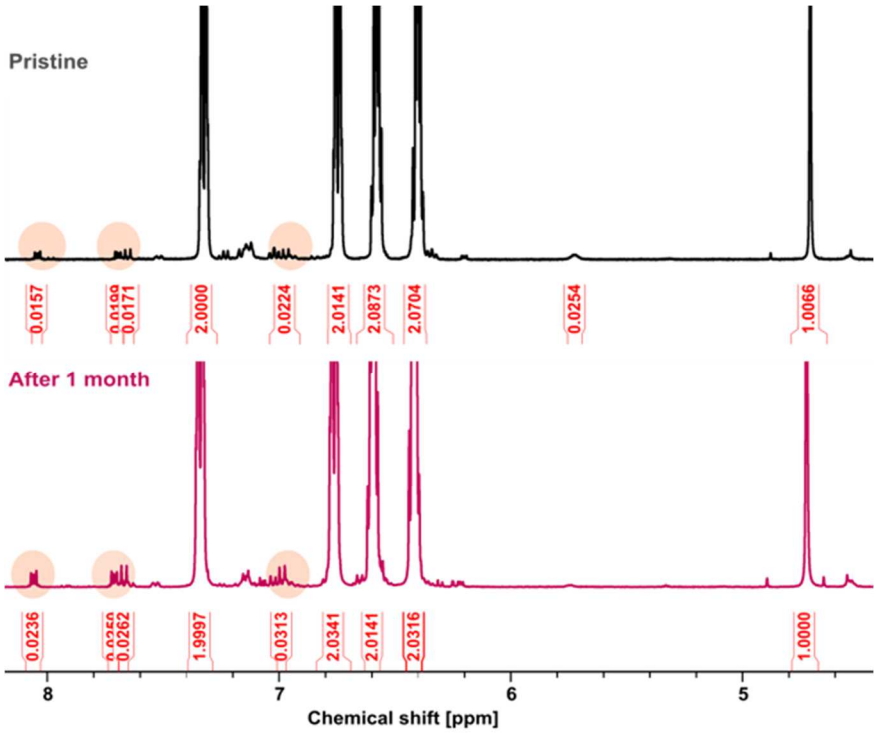

Figure 3.21 ^{1}H-NMR spectrum of pristine N-DMBI-H powder (black) and sample left under air for 1 month (purple) in DMSO-d_6. Peaks related to N-DMBI^{+} are highlighted with orange dots. Peak integration highlights around 1% of N-DMBI^{+} formation within the analysed time span.

3.10.3 N-DMBI-H oxidation in the presence of moisture

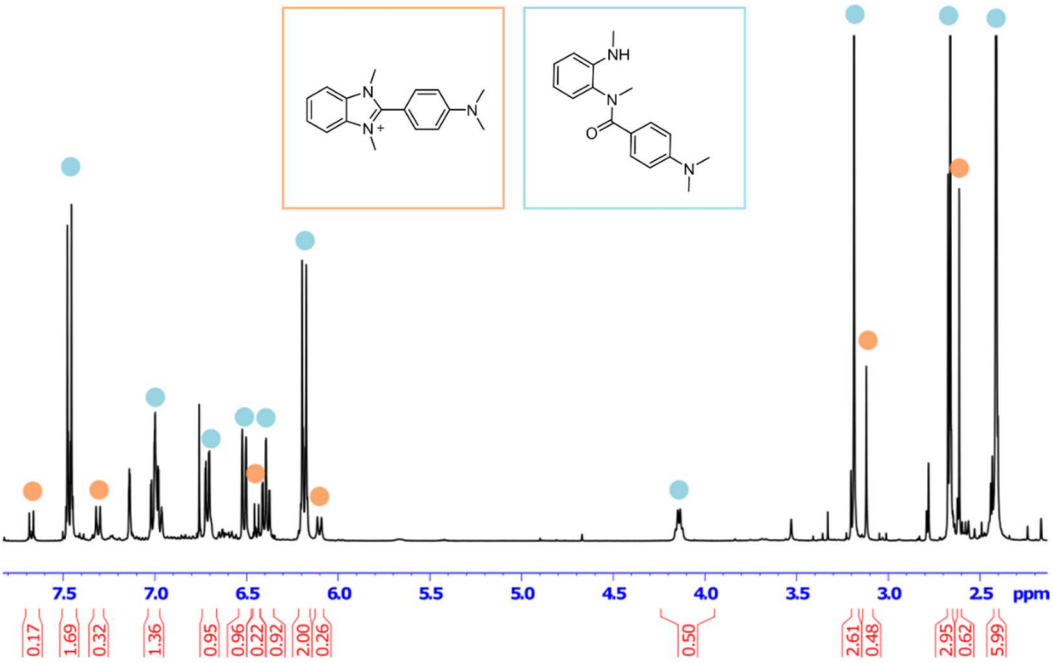

Figure 3.22 ^{1}H-NMR spectrum collected after 353 hours of evolution of a 10 mgmL^{-1} solution of N-DMBI-H in chlorobenzene-d^5 saturated with D_2O water and kept under air. Peaks related to N-DMBI^{+} and DMBI-Ox are highlighted with orange and light blue dots respectively.

Degradation of N-DMBI-H in chlorobenzene saturated with water leads to formation of a mixture of the dopant oxidation side-products DMBI-Ox and N-DMBI$^+$ of 9:1 molar composition. The behaviour is analogue to that obtained during the same experiment performed in the absence of water.

3.10.4 Preparation and Characterization of Films

3.10.4.1 Thin film preparation

P(NDI2OD-T2) polymer was dissolved at room temperature in chlorobenzene at a concentration of 5 gL^{-1} and used after 12 h of dissolution. **N-DMBI-H**, **N-DMBI-H**:**oPDA** and **N-DMBIH:N-DMBI-Ox** solutions were prepared at room temperature at concentration of 5 gL^{-1} each. Aliquots of polymer and dopant solutions were mixed at room temperature just before the deposition to reach the desired dopant concentration.

Low-alkali 1737F Corning glasses were used as substrate for electrical measurements and were cleaned in ultrasonic bath of Milli-Q water, acetone, and isopropyl alcohol (10 minutes of sonication in each solvent). By a shadow mask, electrodes of a 1.5 nm thick Cr adhesion layer and 25 nm thick Au film were deposited by thermal evaporation on the substrates. The solvent cleaning procedure was repeated and the substrates were then exposed to O_2 plasma at 100 W for 10 minutes. Thin polymer films were then spin-casted from solutions onto the substrates (1000 rpm for 60 seconds) and annealed at 150 °C for six hours under inert atmosphere.

Film thickness (average: 40±5nm) was measured with an alpha-step IQ profilometer from KLATencor.

3.10.4.2 Electrical Characterization

The I-V curves were measured at room temperature under nitrogen atmosphere in 2-point contact method with a Wentworth Laboratories probe station and using a semiconductor device analyser (Agilent B1500A). The electrical conductivity was then calculated through the linear fit of the I-V data, the thin films thickness and the geometry of the device active channel.

3.10.4.3 GIWAXS Characterization

Samples for GIWAXS measurements were obtained following the same procedure described in section **3.10.4.1** but using silicon substrates instead of glass. GIWAXS measurements were performed at the SAXS/WAXS beamline at the Australian Synchrotron.[23] 2D scattering patterns were recorded using a Pilatus 2M detector. Sample-to-detector distance was calibrated using a silver behenate reference standard. The sample and detector were enclosed in a vacuum chamber to suppress air scatter. Scattering patterns were measured as a function of angle of incidence, and data shown acquired with an angle of incidence near the critical angle maximizing scattering inten-

sity from the sample. Further details on the procedure can be found in previous publications.[24]

3.10.5 DSC characterization

DSC measurements were performed with a DSC 1 STAR^e System from Mettler Toledo, using aluminium crucibles. Calibration was performed with an Indium standard. All DSC measurements were conducted under N_2 flow (80 mLmin^{-1}).
DSC crucibles were prepared and closed inside a glovebox, under argon atmosphere ($O_2 < 0.1$ ppm, H_2O level < 0.1 ppm), apart from that containing only **oPDA**. DSC crucibles were punctured immediately before performing the analysis.

Sample containing pure N-DMBI-H

Two consecutive DSC treatments were performed on sample containing only pure **N-DMBI-H**. After the first DSC analysis, the sample was allowed to cool down to room temperature before undergoing the second thermal treatment. Sample weight: 11.27 mg

First DSC treatment method:
- 1st heating: from 25 °C to 150 °C, 10 °Cmin^{-1}
- isotherm at 150 °C for 3 minutes
- cooling: from 150 °C to 50 °C, 10 °Cmin^{-1}
- isotherm at 50 °C for 3 minutes
- 2nd heating from 50 °C to 150 °C, 10 °Cmin^{-1}

Second DSC treatment method:
- 1st heating: from 25 °C to 150 °C, 10 °Cmin^{-1}
- isotherm at 150 °C for 3 minutes
- cooling: from 150 °C to 20 °C, 5 °Cmin^{-1}
- isotherm at 20 °C for 5 minutes
- 2nd heating: from 20 °C to 150 °C, 10 °Cmin^{-1}

Sample containing pure DMBI-Ox

Sample weight: 8.50 mg.
DSC treatment method:
- 1st heating: from 25 °C to 200 °C, 10 °Cmin^{-1}
- isotherm at 200 °C for 2 minutes
- cooling: from 200 °C to 25 °C, 10 °Cmin^{-1}
- isotherm at 25 °C for 2 minutes
- 2nd heating: from 25 °C to 200 °C, 10 °Cmin^{-1}

N-DMBI-H/DMBI-Ox 99:1 blend

The N-DMBI-H and DMBI-Ox blend was prepared inside a glovebox under argon atmosphere. 0.51 mg of DMBI-Ox powder were mechanically mixed with 50.00 mg of N-

DMBI-H powder. DSC Sample weight: 13.84 mg.
The DSC method used is the same of N-DMBI-H second thermal treatment.

Sample containing pure oPDA
Sample weight: 6.86 mg.
DSC treatment method:

- 1st heating: from 25 °C to 210 °C, 10 °C min^{-1}
- isotherm at 210 °C for 3 minutes
- cooling: from 210 °C to 20 °C, 5 °Cmin^{-1}
- isotherm at 20 °C for 5 minutes
- 2nd heating: from 20 °C to 210 °C, 10 °Cmin^{-1}

N-DMBI-H/oPDA 99:1 blend
The N-DMBI-H and oPDA blend was prepared inside a glovebox under argon atmosphere. 0.31 mg of oPDA powder were mechanically mixed with 31.00 mg of N-DMBI-H. DSC sample weight: 8.39 mg.
The DSC method used is the same of N-DMBI-H second thermal treatment.

3.10.6 XRD powder characterization

Powder XRD characterization was performed with a benchtop Rigaku MiniFlex 600 diffractometer, equipped with an X-Ray source working with Cu-Kα wavelength of 1.54 Å. Detector parameters: 40 kV voltage, 15mA current.
All diffractograms were collected at room temperature, in air over a 2θ range going from 3.00 deg to 70.00 deg, with a step of 0.02 deg and a scan speed of 0.8 deg/min. Around 50 mg of sample were used for each measurement.

Preparation of sample containing N-DMBI-H and DMBI-Ox
70.4 mg of pure NDMBI-H powder were mixed with 2.2 mg of DMBI-Ox. The mixture was sealed in a 10 mL amber glass ampule under nitrogen atmosphere. The ampule was then heated up to 140°C to melt the mixture. After melting, the mixture was allowed to cool down to room temperature. The cooling process required about 20 minutes. A clear, glassy-like solid formed. The ampule was then heated up to 60 °C for 1 hour before breaking it to recover the N-DMBI-H/DMBI-Ox blend powder.

3.10.7 Optical microscope characterization

Optical microscope images were acquired in transmission mode using a Leica DM LM Microscope. Films were prepared according to the following procedure. **N-DMBI-H**, **N-DMBI-H:DMBI-Ox 99:1** and **N-DMBI-H:oPDA 99:1** solutions were prepared in chlorobenzene at a concentration of 10 $mgmL^{-1}$. Using these solutions, films were spin coated with a Laurell WS 650 spin coater in an N_2 glovebox (1000 rpm for 15 s)

onto glass substrates previously cleaned with ethanol and treated with UV-Ozone for 10 minutes.

3.10.8 Electrochemical characterization

Electrochemical measurements were carried out with a Parstat 2273 potentiostat (Princeton Applied Research). All measurements were performed inside a glove box, under argon atmosphere ($O_2 < 0.1$ ppm, $H_2O < 0.1$ ppm), using a three electrode cells with glassy carbon pin (AMEL, diameter = 3 mm) as working electrode, a platinum wire as counter electrode and Ag/AgCl as reference electrode. All the potentials were measured vs the Ag/AgCl electrode, and then reported against a reference ferrocene/ferrocenium (Fc/Fc^+) redox couple. 1.5 mM solutions of the compounds in anhydrous acetonitrile with 0.1 M of tetrabutylammonium perchlorate as supporting salt were selected as electrolyte. The compounds were first investigated in the stability range of the solvent (from −1.8 V to +1.5 V vs Ag/AgCl) via Differential Pulse Voltammetry (DPV) analysis with a 2 mVs^{-1} step and 25 mA as amplitude, to highlight oxidation and reduction peaks. Cyclic voltammetry (CV) analysis was then performed in correspondence of the peak of interest (if present) at 50 mVs^{-1} scan speed. In each case an internal resistance was applied to compensate the resistance of the system (~ 180 Ω).

HOMO levels were evaluated from both DPV and CV analysis considering, in the case of cyclic voltammetry the oxidation peaks onset, if the oxidation process is non reversible. In the case of HOMO level calculated from CV analysis, half of the scan speed, i.e. 0.025V, was subtracted from the oxidation potential value E_{FC}. The absolute value was then evaluated using the formula $E_{HOMO} = -(E_{FC}+4.8)$

.

Electrochemical characterization of oPDA

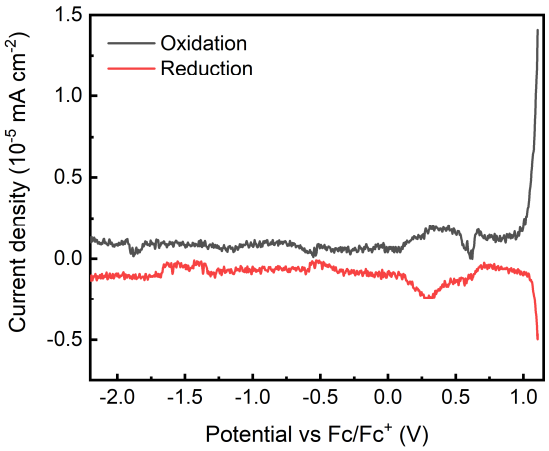

Figure 3.23 DPV analysis of oPDA solution in acetonitrile. Potentials are reported vs ferrocene ($E_{1/2}Fc/Fc^+ = +0.394$ V vs Ag/AgCl). No noticeable peak is present within the solvent stability range. Current density growth at potentials higher than 1.0 V vs Fc/Fc^+ is related to solvent degradation.

3.11 Bibliography

1 P. Wei, J. H. Oh, G. Dong and Z. Bao, *J. Am. Chem. Soc.*, 2010, **132**, 8852–8853.

2 C. Y. Yang, Y. F. Ding, D. Huang, J. Wang, Z. F. Yao, C. X. Huang, Y. Lu, H. I. Un, F. D. Zhuang, J. H. Dou, C. an Di, D. Zhu, J. Y. Wang, T. Lei and J. Pei, *Nat. Commun.*, 2020, **11**, 1–10.

3 O. Bardagot, C. Aumaître, A. Monmagnon, J. Pécaut, P. A. Bayle and R. Demadrille, *Appl. Phys. Lett.*, 2021, **118**, 1–6.

4 J. Liu, L. Qiu, R. Alessandri, X. Qiu, G. Portale, J. J. Dong, W. Talsma, G. Ye, A. A. Sengrian, P. C. T. Souza, M. A. Loi, R. C. Chiechi, S. J. Marrink, J. C. Hummelen and L. J. A. Koster, *Adv. Mater.*, 2018, **30**, 1–9.

5 B. Saglio, M. Mura, M. Massetti, F. Scuratti, D. Beretta, X. Jiao, C. R. McNeill, M. Sommer, A. Famulari, G. Lanzani, M. Caironi and C. Bertarelli, *J. Mater. Chem. A*, 2018, **6**, 15294–15302.

6 Y. M. Gross, D. Trefz, C. DIngler, D. Bauer, V. Vijayakumar, V. Untilova, L. Biniek, M. Brinkmann and S. Ludwigs, *Chem. Mater.*, 2019, **31**, 3542–3555.

7 S. Riera-Galindo, A. Orbelli Biroli, A. Forni, Y. Puttisong, F. Tessore, M. Pizzotti, E. Pavlopoulou, E. Solano, S. Wang, G. Wang, T. P. Ruoko, W. M. Chen, M. Kemerink, M. Berggren, G. Di Carlo and S. Fabiano, *ACS Appl. Mater. Interfaces*, 2019, **11**, 37981–37990.

8 Y. Shin, M. Massetti, H. Komber, T. Biskup, D. Nava, G. Lanzani, M. Caironi and M. Sommer, *Adv. Electron. Mater.*, 2018, **4**, 1–8.

9 B. D. Naab, S. Zhang, K. Vandewal, A. Salleo, S. Barlow, S. R. Marder and Z. Bao, *Adv. Mater.*, 2014, **26**, 4268–4272.

10 Z. Chen, Y. Zheng, H. Yan and A. Facchetti, *J. Am. Chem. Soc.*, 2009, **131**, 8–9.

11 R. Steyrleuthner, R. Di Pietro, B. A. Collins, F. Polzer, S. Himmelberger, M. Schubert, Z. Chen, S. Zhang, A. Salleo, H. Ade, A. Facchetti and D. Neher, *J. Am. Chem. Soc.*, 2014, **136**, 4245–4256.

12 A. Luzio, L. Criante, V. D'Innocenzo and M. Caironi, *Sci. Rep.*, 2013, **3**, 1–6.

13 M. M. Nahid, R. Matsidik, A. Welford, E. Gann, L. Thomsen, M. Sommer and C. R. McNeill, *Adv. Funct. Mater.*, 2017, **27**, 1–11.

14 N. D. Treat, J. A. Nekuda Malik, O. Reid, L. Yu, C. G. Shuttle, G. Rumbles, C. J. Hawker, M. L. Chabinyc, P. Smith and N. Stingelin, *Nat. Mater.*, 2013, **12**, 628–633.

15 M. Q. Xia and Y. F. Zhang, *J. Therm. Anal. Calorim.*, 2021, **145**, 3053–3066.

16 L. Rycerz, *J. Therm. Anal. Calorim.*, 2013, **113**, 231–238.

17 M. L. P. Leitao, M. S. C. C. Canotilho, J. C. Pereira, A. T. Sousa and J. S. Redinha, *J. Therm. Anal. Calorim.*, 2002, **68**, 397–412.

18 C. Macasoi, E. Pincu, B. Jurca, C. Romanitan and V. Meltzer, *Thermochim. Acta*, 2023, **724**, 179499.

19 M. Blomenhofer, S. Ganzleben, D. Hanft, H. W. Schmidt, M. Kristiansen, P. Smith, K. Stoll, D. Mäder and K. Hoffmann, *Macromolecules*, 2005, **38**, 3688–3695.

20 K. Shi, G. Liu, H. Sun, B. Yang and Y. Weng, *Polymers (Basel).*, 2022, **14**, 1–16.

21 C. Lindqvist, J. Bergqvist, C. C. Feng, S. Gustafsson, O. Bäcke, N. D. Treat, C. Bounioux, P. Henriksson, R. Kroon, E. Wang, A. Sanz-Velasco, P. M. Kristiansen, N. Stingelin, E. Olsson, O. Inganäs, M. R. Andersson and C. Müller, *Adv. Energy Mater.*, 2014, **4**, 1–10.

22 R. Harter, C. Weymuth, R. Sheffold, P. Engel and A. Linden, *Helv. Chim. Acta*, 1993, **76**, 353–371.

23 N. M. Kirby, S. T. Mudie, A. M. Hawley, D. J. Cookson, H. D. T. Mertens, N. Cowieson and V. Samardzic-Boban, *J. Appl. Crystallogr.*, 2013, **46**, 1670–1680.

24 E. Gann, M. Caironi, Y. Y. Noh, Y. H. Kim and C. R. McNeill, *Macromolecules*, 2018, **51**, 2979–2987.

25 F. Pallini, S. Mattiello, M. Cassinelli, P. Rossi, S. Mecca, W. L. Tan, M. Sassi, G. Lanzani, C. R. McNeill, M. Caironi and L. Beverina, *ACS Appl. Energy Mater.*, 2022, **5**, 2421–2429.

Chapter 4

4 New N-DMBI-H based n-type dopants: structural variations toward higher doping efficiencies

---

Part of the results reported in this chapter have been published in a paper: P. Rossi, F. Pallini, G. Coco, S. Mattiello, W. L. Tan, L. Mezzomo, M. Cassinelli, G. Lanzani, C. R. McNeill, L. Beverina and M. Caironi, "An iminostilbene functionalized benzoimidazoline for enhanced n-Type solution doping of semiconducting polymers for organic thermoelectrics".

Adv. Mater. Interfaces, **2023**, 10, 2202416

In the previous chapter, we discussed a strategy to increase N-DMBI-H doping efficiency without the need of any structural modifications of the dopant or the semiconductor host. The chemical modification of N-DMBI-H structure is however another highly valuable approach to tune the host/semiconductor interactions and increase the doping efficiency. In this chapter, the synthesis and characterization of a library of new benzimidazoline based dopants is thus discussed. Efficient and versatile protocols for the introduction of new variations on N-DMBI-H structure are firstly reported. Then, the structure-function-properties relationships of a selected set of original derivatives are studied, leading to the definition of guidelines for the design of new and more efficient n-type dopants.

This work was performed in collaboration with Mario Caironi's group at the Italian Institute of Technology (IIT), Nguyen's research group at the Center for Polymers and Organic Solids (University of California, Santa Barbara) and with Giuseppe Mattioli, affiliated to the Italian national Research Council (Instituto di Struttura della Materia ISM-CNR). Part of the dopants synthesis was performed by two formers students of the group: Giulia Garavaglia and Arianna Marassi.

4.1 Molecular structure modification: a strategy to tune semiconductor and dopant interaction

As already discussed in Chapter 1 and 3, one of the main factors limiting N-DMBI-H performances is its limited dispersibility in most polymeric semiconductors. This issue, firstly reported in a work by Schlitz, causes the phase separation between the undoped host matrix and N-DMBI-H, reducing the fraction of activated dopant and limiting the achievable doping efficiency.[1,2] Several studies were dedicated at improving the miscibility between this compound and the semiconductor host, to mitigate the impact of the segregation phenomenon and obtain higher perfromances[3–7].
Structural modifications of the semiconductor to increase the host-dopant mutual affinity are efficient in mitigating the issue. For example, introduction of polar side chains on Phenyl-C61-butyric acid methyl ester (PCBM) molecule significantly improves its compatibility with N-DMBI-H, with consequent higher doping efficiencies.[8] The functionalization of P(NDI2OD-T2) polymeric structure with polyethylene glycol chains led to the same effect.[1,9] Tuning of the aggregation and crystallization behaviour of polymeric materials via structural variation is then another approach that showed to increase N-DMBI-H miscibility in the host, since dopants are reported to preferentially accommodate in disordered regions of semiconductor matrixes.[3] The introduction of kinked monomers in P(NDI2OD-T2) polymer conjugated backbone, for example, demonstrated to cause the disruption of the polymer chains packing and crystallinity and to consequently improve dopant distribution in the host.[6] These structural modifications however in some cases also resulted in reduced carrier's mobilities, limiting the electrical performances obtainable with these materials.[6,10] In parallel to these strategies acting on the semiconductor structure and properties, tuning of N-DMBI-H molecular structure also represents a valuable alternative to reach the same goal.

4.1.1. Examples of variations on N-DMBI-H structure

The literature reports several N-DMBI-H derivatives, with structures functionalized to tune the dopant properties and direct improved interactions with different sites of the semiconductor counterpart. **Figure 4.1** collects some of them. One of the first reported N-DMBI-H derivatives is DPBI, in which two phenyl rings replace the methyl groups on the dopant amine functionality.[11] This structural variation was introduced to improve the dopant interactions with the conjugated semiconductor counterpart and to stabilize the dopant via charge delocalization on the aromatic substituents. DPBI however did not show any evident improvement in performance with respect to N-DMBI-H. In another work, Saglio and coworkers demonstrated that the introduction of longer and branched N-alkyl substituents on the dopant molecule increases the dopant affinity with semiconductor polymers alkyl side-chains.[12] All the dopants synthesized by the authors (DEtBI, DprBI, DbuBI, DiPrBI and DiBuBI) showed in fact improved miscibility with P(NDI2OD-T2) and consequent higher doping performances with respect

to N-DMBI-H. The very recently reported julolidine functionalized benzimidazoline derivative (JLBI-H) was designed to increase the dopant lipophilicity and miscibility with apolar semiconductors. Blended with $PC_{61}BM$, this compound led to almost a 36-fold doping efficiency enhancement with respect to the reference dopant, thanks to a reduced phase segregation.[13] Derivatives bearing glycol groups (TEG-DMBI) showed instead a better compatibility with semiconductor having polar side chains.[5]

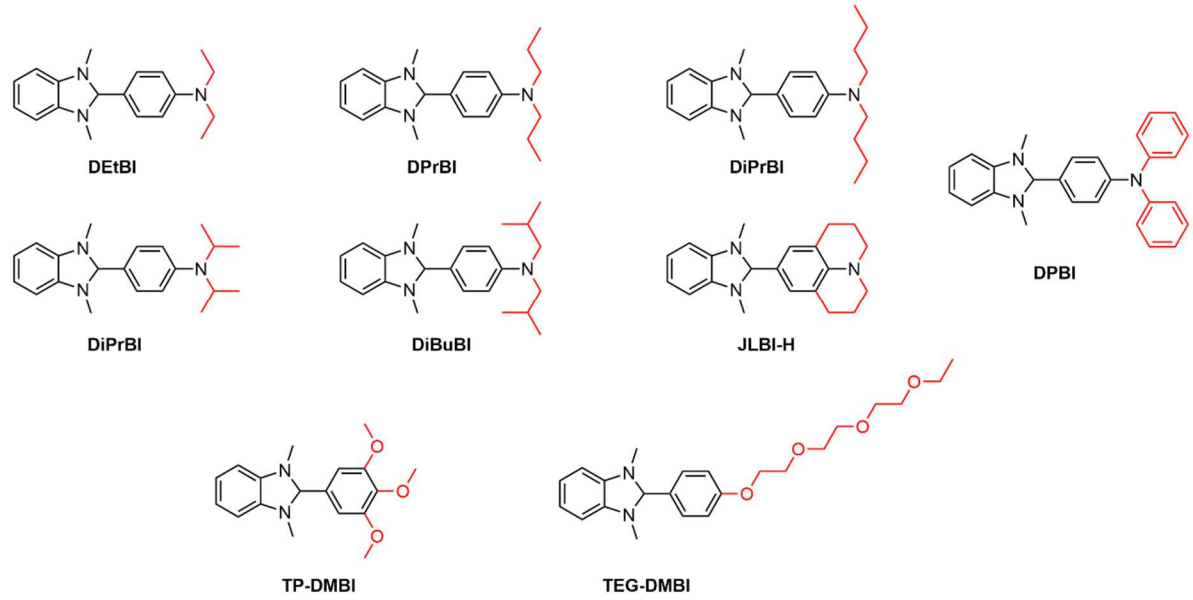

Figure 4.1 Examples of N-DMBI-H derivatives reported in the literature and specifically synthesized to improve dopant/host miscibility. The different substitution pattern with respect to N-DMBI-H is highlighted in red.

As a further example, the trimethoxyphenyl substituted benzimidazoline derivative TP-DMBI showed improved miscibility with the chains of benzodifurandione-based oligo(p-phenylene vinylene) (BDOPV) based polymers with respect to N-DMBI-H.[14] In this case, the introduction of electron donating methoxy substituents also influenced the energy levels of the dopant and increased its electron donating capability, which is another effective strategy to improve doping efficiency.[15]

The reported examples demonstrate that a tailored structural modification of the N-DMBI-H molecule can serve to highly improve the doping performances. Extending the approach to unexplored substitution patterns could thus lead to new and more efficient n-type dopants.

4.1.2. Literature approaches for the synthesis of N-DMBI-H derivatives

The possibility of highly modulate the properties of new N-DMBI-H based dopants goes along with the capability of introducing a wide number of substituents, in different positions, on the benzimidazoline structure. This necessarily requires versatile and efficient synthetic strategies.

Two main pathways are reported in the literature for the synthesis of N-DMBI-H,[12,15,16]

as shown in **Scheme 4.1.** Path A consists in the acetic acid catalysed condensation between N,N-dimethy-1,2-phenylendiamine (**B1)** and 4-(dimethylamino)-benzaldehyde (DMAB), a process sometimes assisted by ultrasounds. The reaction allows obtaining the dopant with a 26% yield. Both reagents are commercially available. If required, **B1** can be obtained via a three-step synthetic procedure in which the first step is the reaction between 1,2-phenylendiamine and tosylchloride in dichloromethane to give the corresponding bissulfonamide (**1**). Product **1** is then deprotonated in dimethylformamide and alkylated with methyl iodide to give product **2.** The hydrolysis of **2** in concentrated sulfuric acid, followed by neutralization, gives then **B1**. Considering these steps, the overall reaction yield for N-DMBI-H is 18%.

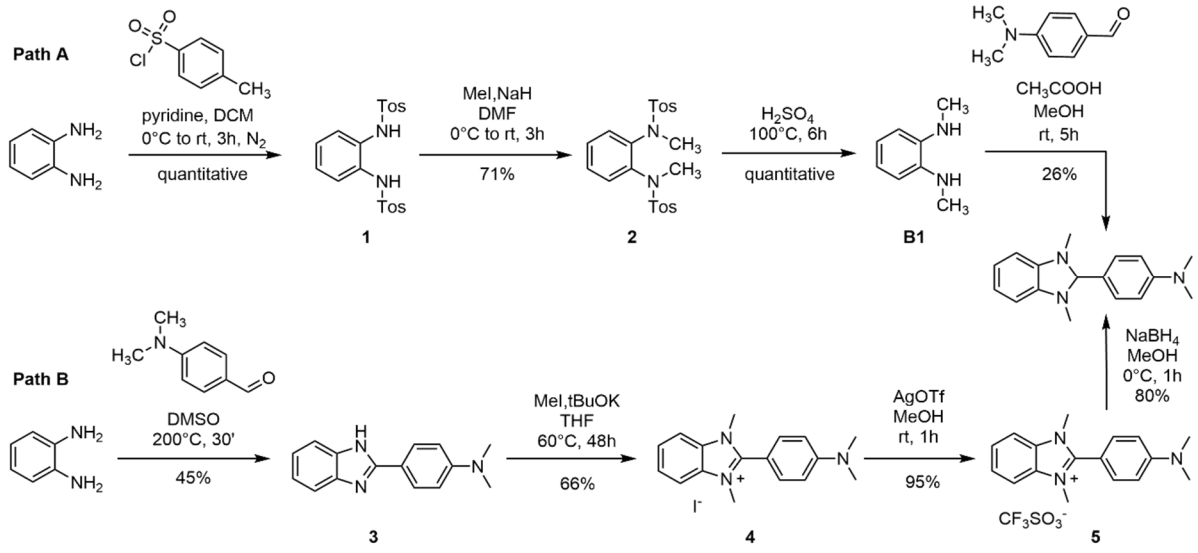

Scheme 4.1 Synthetic pathways reported in the literature for the synthesis of N-DMBI-H.

Path B instead consists in a first direct reaction between 1,2-phenylendiamine with 4-(dimethylamino)-benzaldehyde to give product **3**, which then undergoes a double alkylation by methyl iodide in alkaline conditions to give product **4**. Product **4** is then converted in the corresponding triflate salt (**5**) via metathesis with silver triflate and this intermediate is finally converted into N-DMBI-H via reduction reaction mediated by sodium borohydride ($NaBH_4$). The overall yield is 23%.

Both processes allow for a functionalization of the dopant dimethylaniline residue by selecting different aldehydes as starting reagents. For instance, all the derivatives reported in **Figure 4.1** were obtained following Path A and selecting the right reaction partner to **B1**. In both cases, it is in principle also possible to change the alkyl residue on the benzimidazole nitrogen atoms via selection of a different alkylating agent with respect to methyl iodide. These protocols present however some limitations. Path A has a limited generality. For example, it is not suitable for reactants not soluble in alcohols, like aldehydes bearing extended conjugation. Neither of the two allow the synthesis of asymmetric derivatives bearing different substituents on the benzimidazoline moiety.

To extend the number of possible variations on the structure of benzimidazoline based

n-type dopants and, consequently, further tune their properties, more versatile synthetic strategies are thus required.

4.2 Aim of the work

N-DMBI-H scarce miscibility within most semiconductors is probably one of the most relevant issues limiting its doping efficiency. The tuning of the substitution pattern of N-DMBI-H with both different solubilizing chains and electron releasing groups, proved to be an efficient approach to mitigate this issue and obtain performance improvements. A tailored design of new variations of N-DMBI-H structure could lead to further performances enhancement. This work thus focused on the design and synthesis of new and more efficient N-DMBI-H derivatives.

The known synthetic protocols for the preparation of benzimidazoline-based dopants are not suitable for the synthesis of possibly relevant derivatives, such as those possessing different alkyl chains at the benzimidazoline nitrogen atoms. We thus developed more general synthetic routes, compatible with such kind of derivatives. Then, we performed a detailed structure-function-properties relationship characterization of a selected set of original derivatives to define the factors determining their different performances.

4.3 Synthesis of new N-DMBI-H derivatives

When looking at new synthetic routes for the preparation of benzimidazoline based dopants, we aimed at finding procedures that could allow several variations on N-DMBI-H structure (**Figure 4.2**). In particular, we aimed at obtaining

- derivatives with extended conjugation on the N-DMBI-H dimethylaniline nitrogen;
- derivatives with alkyl or aryl substituents on the benzimidazole moiety;
- dimeric dopants.

These functionalization patterns were mainly designed to increase the dopant efficiency in different ways. Dopants functionalized with π-conjugated moieties should have stronger interactions with the semiconductors conjugated backbones. Alkyl substituents on the other hand, should improve affinity of the dopant with polymeric side chains, according to the reports by Saglio's group.[12] These substitution patterns thus aimed at controlling the doping efficiency by tuning the interactions between the host and the dopant.
Dimeric dopants were instead designed to increase the number of doping sites per molecule, another strategy that can improve the doping efficiency and reduce the dopant concentration required to reach high conductivities.
We finally aimed at obtaining derivatives with aryl substituents on the benzimidazole core. No example of N-DMBI-H based dopant bearing this type of functionalization is

in fact, to the best of our knowledge, present in the literature and this structural diversity might lead to valuable characteristics.

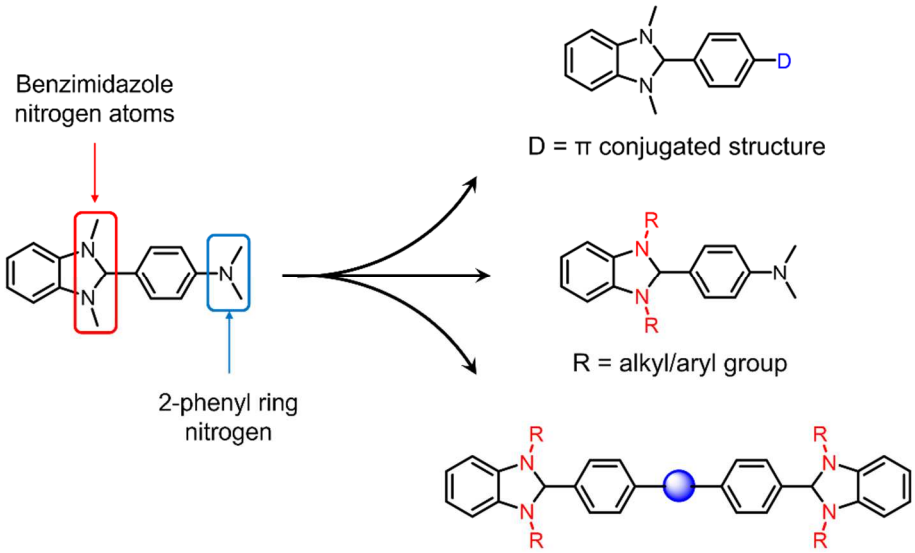

Figure 4.2 Designed structural variations of the N-DMBI-H structure. The pristine molecules sites interested by functionalization are highlighted in red and blue.

4.3.1. Acid-clay catalysed condensation protocol

As first synthetic approach, we adapted a solvent-free acid catalysed condensation reaction in heterogeneous phase. The protocol was previously reported by Bonacci et al. for the synthesis of benzimidazole derivatives.[17] The approach requires an acid Montmorillonite clay (Montmorillonite-K10), which works both as catalyst and as an efficient water adsorbent, this latter feature pushing condensation reactions equilibrium toward products.

The reaction conditions are here reported in **Scheme 4.2**. All the used diphenylamines (**B**) and non-commercial aldehydes (**A**) were synthesized by former members of the group. Few details on the synthesis of these derivatives are reported in the experimental method section (synthesis of derivatives **A1**-**A4** and **B1, B2**). Since, as we discussed in Chapter 3, N-DMBI-H derivatives are known to be prone to oxidation when heated under air, we performed all the reactions under inert atmosphere. As different works report that light can trigger the degradation of such compounds,[18,19] we also performed the reactions and the purification steps in the dark. It is also worth mentioning that, following the literature procedure, we initially activated the reaction through microwave heating. We however tested the same reaction by heating with conventional systems, always obtaining the same conversions yields.

As first attempt we tested the approach for the synthesis of N-DMBI-H dopant (derivative **C1**). Since the reaction happens in solventless conditions, we heated the reactant mixture at 120°C, to guarantee melting and homogeneous mixing of both the reagents used (DMAB and N,N-dimethy-1,2-phenylendiamine, melting points of 74°C[20] and 31°C[21] respectively). After one hour, the reaction reached complete conversion and the

product was isolated with a yield of 63.7% via solvent extraction from the solid mixture followed by chromatographic purification. It is worth noting that the obtained reaction yield is three times that of the previously reported common N-DMBI-H synthetic procedures.

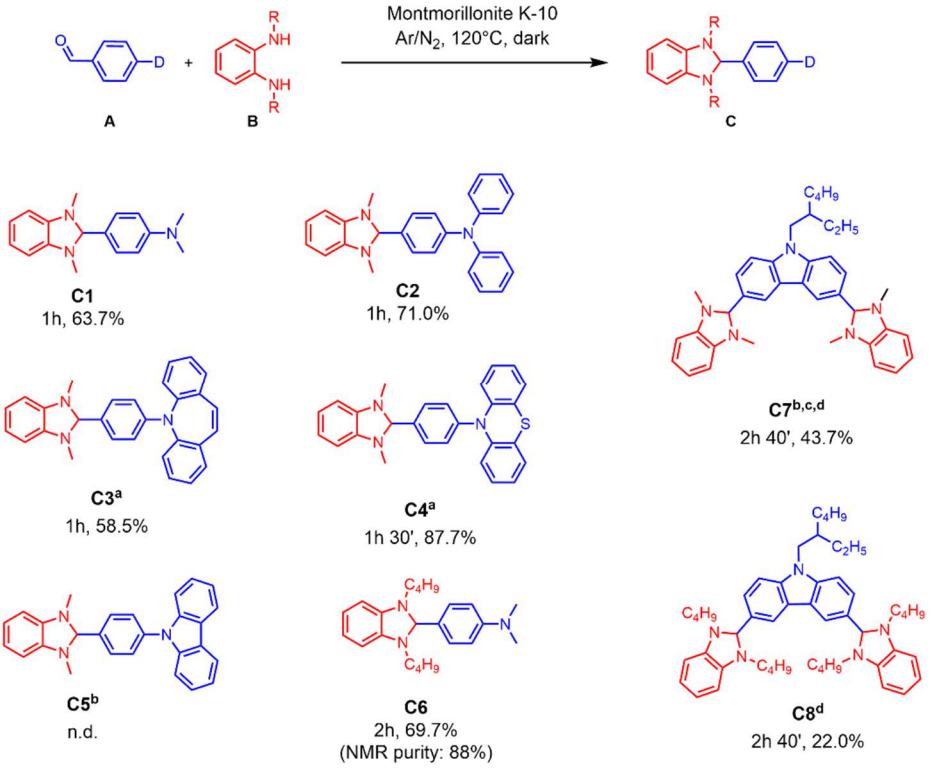

Scheme 4.2 Reaction scheme of the acid-clay catalysed condensation reaction, together with the obtained products. For each product the reaction time and the isolated yields are reported. General conditions used: aldehyde (A) and o-phenylendiamine (B) in 1:1 molar equivalents; Montmorillonite K-10: 100 wt% with respect to the used diamine. [a]after the first 30 minutes/1 hour of reaction, temperature was raised to 180°C. [b]Temperature was set to 150°C. [c]After 1 hour, temperature was set to 180°C and, after another hour, to 210°C. [d]The reaction was performed using 2.2 molar equivalents of diamine.

We then decided to test the reaction on another known dopant of the benzimidazoline family, the diphenyl functionalized DPBI (**C2**), to verify if the same synthetic route could be suitable for the synthesis of more complex derivatives bearing aryl substituents on the dimethylamine functionality. Despite the higher melting point of the starting 4-(diphenylamino)benzahldeyde (132-133°C),[22] the conversion was completed within 1 hour and the product was isolated with a 71.0% yield.

The protocol was then extended to original derivatives (**C3**-**C8**). In the case of products **C3** and **C4** the reaction temperature had to be adjusted to 180°C due to higher melting points of the forming products, leading to progressive solidification of the reaction mixture. In both cases the reaction proceeded smoothly, and the products were isolated with 58.5 % and 87.7 % yield respectively after chromatographic purification. For product **C5**, a temperature adjustment to 150°C was instead dictated by the higher melting point of the starting aldehyde (see experimental methods section, derivative **A3**, m.p: 156-158°C). No product was however detected within the reaction crude and the high temperature led to degradation of part of the reagents.

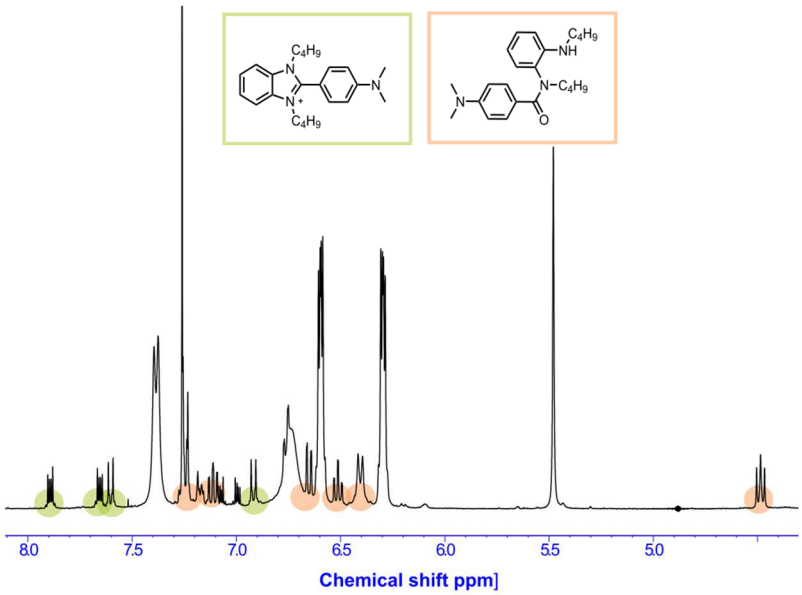

Figure 4.3 Details of the aromatic portion of the ^{1}H NMR spectrum ($CDCl_3$) of product **C6** contaminated by unknown impurities. Peaks are tentatively associated to the indicated oxidation side-product on the base of those of N-DMBI-H oxidation impurities (see reference 18 and Chapter 3).

In the case of product **C6**, we repeated the reaction three times. The conditions used for each test and the obtained yields are summarized in **Table 4.1**. We firstly tested the same conditions used for N-DMBI-H synthesis (entry 1). The product was recovered with a 53.6% yield. It however showed a 83% NMR purity, due to presence of impurities tentatively associated to oxidation side products (see NMR in **Figure 4.3**), and residual N,N-dibutyil-1,2-phenylendiamine (**B2**). The latter could not be separated from **C6** via column chromatography. We then repeated the reaction using an excess of DMAB (entry 2). This allowed to avoid presence of residual **B2** within the product. However, derivative **C6** resulted particularly prone to oxidation during purification from residual aldehyde via column chromatography, and again we obtained the compound with an 85% NMR purity. We repeated once more the reaction using 1.05 molar equivalent of N,N-dibutyil-1,2-phenylendiamine, to induce complete conversion of the aldehyde. In this case, we changed the purification to solvent extraction followed by a treatment of the obtained solution with anhyd. $MgSO_4$ powder. Metal ions are known to easily form coordination complexes with compounds containing aminic nitrogens.[23,24] By letting rest the solution on $MgSO_4$ powder under inert atmosphere, we thus aimed at removing the unreacted excess diamine while avoiding air exposure. This procedure allowed us to isolate product **C6** with a higher yield (69.7%) and with no presence of residual **B2**. The obtained compound still presented traces of DMAB (3%) and oxidation impurities (9%), which highlights the high oxygen sensitivity of this derivative.

Table 4.1 Conditions tested for the synthesis of derivative **C6**.

Test	DMAB (eq.)	B2 (eq.)	Yield % (NMR purity)
1	1	1	53.6 % (83%)
2	1.25	1	52.7 % (85%)
3[a]	1	1.05	69.7 % (88%)

[a]purification via treatment on $MgSO_4$

Finally, the protocol allowed us to obtain the dimeric derivatives **C7** and **C8** with yields of 43.7% and 22% respectively. As in the case of products **C3** and **C4**, synthesis of derivative **C7** required to progressively raise reaction temperature to 210°C, due to solidification of the reaction mixture after product formation. The reaction work-up for the isolation of derivative **C8** required instead the same treatment with $MgSO_4$ used for derivative **C6,** to remove excess of diamine before chromatographic purification.

4.3.2. Reductive cyclization protocol

The adapted acid-clay catalysed condensation protocol resulted particularly efficient for the synthesis of N-DMBI-H and for the preparation of different original derivatives with various functionalization patterns. However, we could not synthesize the target compounds **C5** using this protocol**,** and derivative **C6** was obtained with a purity inadequate for its use in devices application. Moreover, the developed route is still not suitable for an asymmetric functionalization of the dopant benzimidazole core, which might offer more possibilities in terms of tuning of properties. We thus decided to test a different synthetic route, here reported in **Scheme 4.3** to further extend our library of dopants.

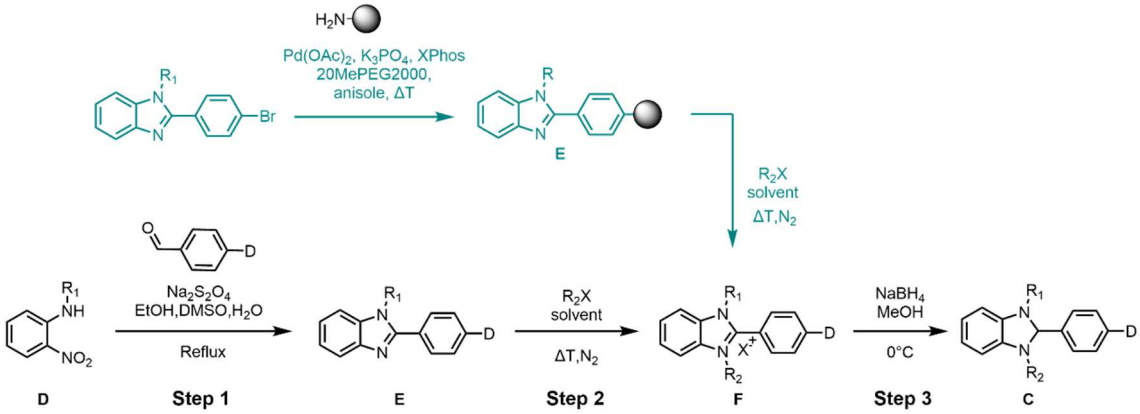

Scheme 4.3 Synthetic routes for the synthesis of N-DMBI-H starting from a reductive cyclisation reaction (**step 1**). Derivatives **E** can be obtained also via Buchwald-Hartwig amination on 2-(4-bromophenyl)-benzimidazole.

The protocol is adapted from a procedure previously reported by Yang group for the synthesis of alkyl and aryl substituted benzimidazoles.[25] The synthetic procedure consists in a three-step pathway. The first step is a one-pot condensation and reductive cyclization reaction between an alkylated o-nitroaniline (**D**) and an aldehyde in the presence of the reducing agent sodium dithionite ($Na_2S_2O_4$) (**step 1**). Via alkylation of the obtained 2-arylbenzimidazoles **E** (**step 2**) and subsequent reduction of the isolated arylbenzimidazolium salts **F** mediated by $NaBH_4$ (**step 3**), it is then possible to obtain benzimidazoline derivatives.

With respect to the previously reported synthetic routes, this protocol potentially allows to prepare N-DMBI-H derivatives bearing asymmetric substitution patterns, since the alkylation of the two benzimidazole nitrogen atoms happens in different steps. The approach in principle is also suitable for a divergent functionalization of the 2-phenyl

ring of the N-DMBI-H structure, which could further extend the possibility of structural diversification. By using 4-bromobenzhaldeyde as starting reagent, it is for example possible to prepare 2-(4-bromophenyl)-benzimidazole. This compound can then be functionalized with different amine groups via Buchwald Hartwig amination (**Scheme 4.3**, blue path). The following sections will be dedicated to the study of each reaction step.

4.3.2.1. Synthesis of 2-arylbenzimidazoles via reductive cyclization

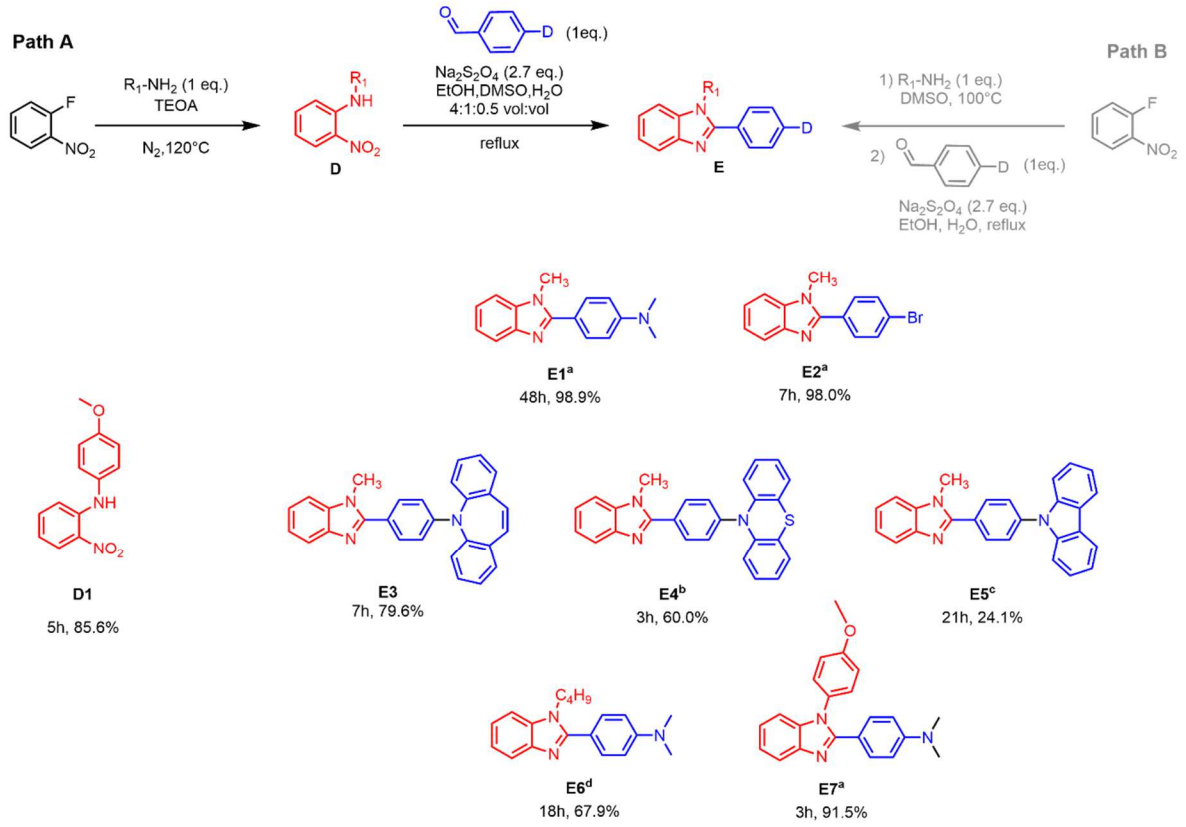

Scheme 4.4 General conditions for the preparation of 2-arylbenzimidazoles (**E**) via reductive cyclization reaction. The obtained products are reported, together with the required reaction time and isolated yields. The synthesis of the required o-nitroaniline (**D**) and the following reductive cyclization can happen either in a two-step process (Path A) or one-pot (Path B). [a]On the scale of this reaction, the amount of water naturally present in DMSO was enough to promote the reaction; [b]further 0.5 mL of water were required to promote the reaction; [c]Reaction was performed using only EtOH and H_2O as solvent; [d]product obtained following Path B;

The first step of this second synthetic route consists in the preparation of 2-arylbenzimidazoles (**E**) via a one-pot reductive condensation and cyclization reaction between the required N-alkyl-1,2-nitroaniline (**D**) and aldehyde in the presence of $Na_2S_2O_4$. The reaction conditions used are reported in **Scheme 4.4**. The reaction happens in a refluxing mixture of ethanol, dimethylsulfoxide (DMSO) and water. Addition of water in the mixture accelerates the reaction, as reported by Oda and coworkers.[26]

If not commercial, the starting 1,2-nitroaniline (**D**) can be obtained by reacting 1-fluoro-2-nitrobenzene with a selected amine.[25] Following this route, we prepared the N-

(4-methoxyphenyl)-2-nitroaniline (**D1**) required for the synthesis of derivative **E7** via reaction of 2-fluoronitrobenzene with p-anisidine, performed at 120°C under inert atmosphere and in the presence of triethanolamine (TEOA). TEOA works as solvent in this reaction and is also necessary to deprotonate the p-anisidine and to neutralize the hydrofluoric acid formed during the reaction. N-butyl-2-nitroaniline, required for the synthesis of derivative **E6**, was instead prepared via reaction of 2-fluoronitrobenzene with butylamine in DMSO at 100°C. The obtained product was not isolated and was directly used for the preparation of derivative **E6** according to the reaction reported in **Scheme 4.4**, **Path B**. In all the other cases, commercial N-methyl-nitroaniline was used as starting reagent.

The protocol allowed us to obtain derivatives **E1**, **E2** and **E7** with excellent yields of 98.8%, 98.0% and 91.5% respectively. In all the other cases, products were obtained with good yields between 60% and 80%, apart from product **E5**, that was isolated with a poorer yield of 24% due to difficulties in the product purification.

4.3.2.2. Functionalization of 2-arylbenzimidazoles via Buchwald-Hartwig amination

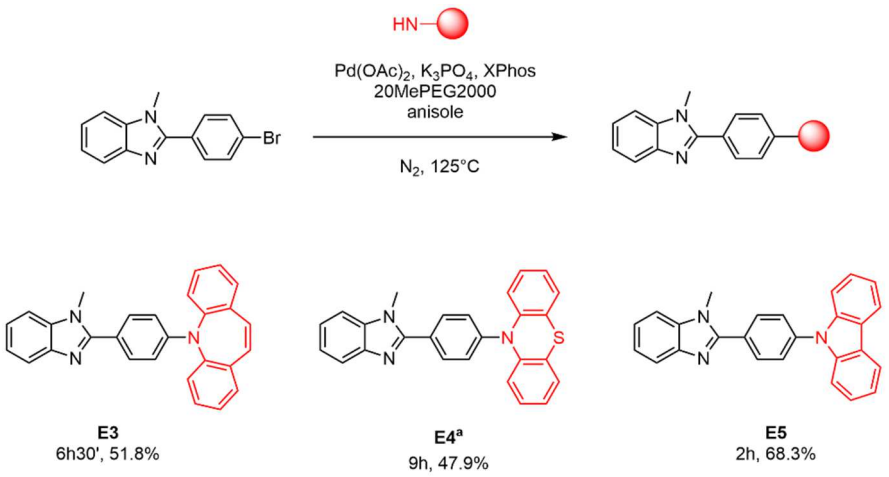

Scheme 4.5 Reaction scheme for the synthesis of derivatives **E3-E5** via Buchwald Hartwig amination. General reaction conditions: **E2** (1 eq.), coupling partner (1.1 eq.), $Pd(OAc)_2$ (0.01 eq.), XPhos (0.02 eq.), K_3PO_4 (1.5 eq.), 20MePEG2000 (9 wt% with respect to base). [a]The reaction temperature was set to 135°C for the first 7 hours and then at 150°C for the following 2 hours and the reaction was performed with 1.25 eq. of coupling partner.

As aforementioned, we specifically prepared derivative **E2** to allow a subsequent versatile functionalization of the para position of the benzimidazoline core 2-phenyl ring via Buchwald Hartwig amination reaction. We then tested this approach for the synthesis of products **E3-E5**. For the purpose, we adapted the reaction conditions from a previous work by our group.[27] The amination was performed using 1% mol of $Pd(OAc)_2$ as catalyst in the presence of XPhos as phosphine ligand, K_3PO_4 as the base and PEG2000 dimethylether as phase transfer catalyst. Small amounts of anisole (30-40 wt

% with respect to the overall reaction mass) were added as mixing aid. The general reaction conditions and the obtained products are reported in **Scheme 4.5**.

The desired product **E2**-**E5** were obtained selecting the commercially available dibenzoazepine, phenothiazine and carbazole as coupling partners for **E2**. In the case of derivative **E4,** the reaction was performed with a higher excess of coupling partner and temperature was adjusted to 135°C for the first 7 hours and then to 150°C for the following 2 hours to push the reagent conversion. The products were recovered via suspension of the crude in an acid aqueous solution followed by filtration of the obtained solid. The recovered powders were then further purified by washing with the appropriate solvents to give products **E3**, **E4** and **E5** with a fair yield of 51.8%, 47.9% and 68.3% respectively. This second protocol results then preferable to the previous one for the synthesis of derivative **E5.**

4.3.2.3. Alkylation of 2-arylbenzimidazoles

The following step in the synthesis of the benzimidazoline based dopants is the alkylation of the obtained 2-arylbenzimidazoles to give the corresponding 2-arylbenzimidazolium salt. Depending on the selected alkylating agent, it is possible, at this step of the protocol, to obtain asymmetric derivatives.
The general synthetic pathway and the obtained product are reported in **Scheme 4.6**. Unless otherwise specified, all the reaction were performed under inert atmosphere. The specific reaction conditions and yields are collected in **Table 4.2** for each product.

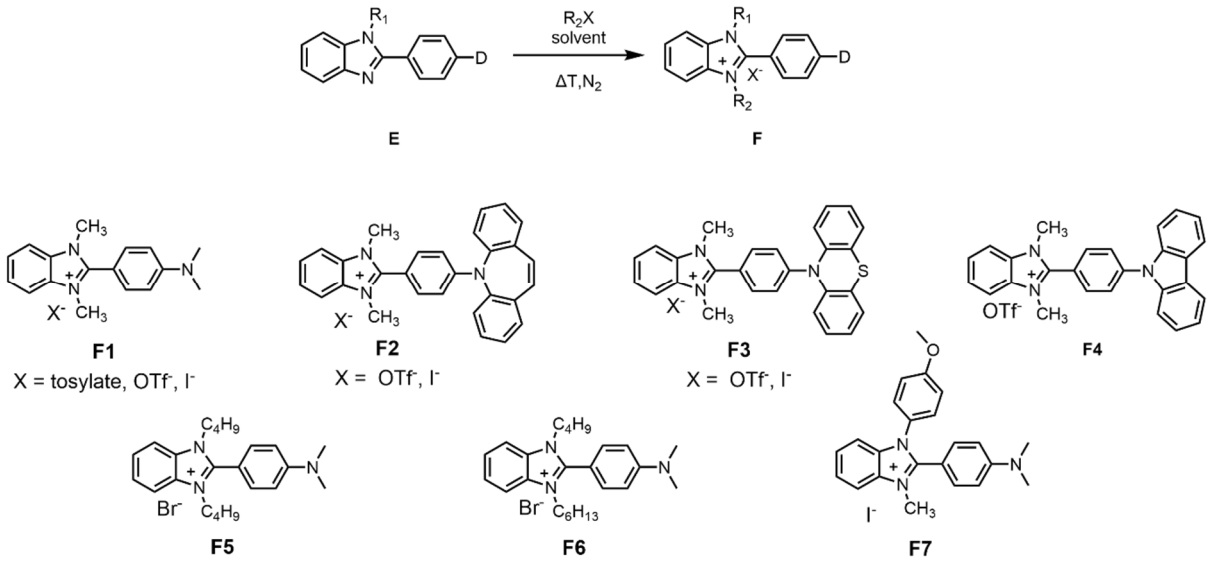

Scheme 4.6 General scheme for the synthesis of 2-arylbenzimidazolium salts via alkylation reaction of 2-arylbenzimidazoles. The obtained products are reported as well.

Table 4.2 Reaction conditions followed for the synthesis of derivatives **F1**-**F7**. The same derivative was, in some cases, obtained with different counteranions.

Entry	Product	R_2X[a]	Temperature	Solvent	Time	Yield % (NMR purity)
1	**F1**	Methyl tosylate[b]	reflux	MeCN	24 h	-
2	**F1**	MeOtf	rt	Toluene		79.0%[d](80%)
3	**F2**	MeI	reflux	MeCN	5h	80.3%
4	**F2**	MeOtf	rt	MeCN	1h 30'	88.5%
5	**F3**	MeI	reflux	MeCN	23h	84.5%
6	**F3**	MeOtf	rt	MeCn	3h	68.7%
7	**F4**	MeOtf	rt	MeCN	2h	90.3%
8	**F5**	1-bromobutane	90°C	Toluene[c]	4h 45'	70.9%
9	**F6**	1-bromohexane	110°C	Toluene[c]	5h	76.1%
10	**F7**	MeI	reflux	MeCN	5h	54.2%
11	**F7**	MeI	reflux	AcOEt	12h	74.0%

[a] alkylating agents were used in 1.1-2.1 eq. with respect to the starting reagent depending on the specific reaction. More details are reported in the Experimental Methods section; [b]This reaction was not performed under N_2 atmosphere, but in the presence of a calcium chloride trap for humidity. [c]Toluene was added after 4 hours (**F5**) or 1 hour (**F6**). [d] the product was recovered in a mixture with the starting reagent **E1.**

The reaction was tested with different alkylating agents and conditions depending on the specific target product. We firstly tested the methylation of derivative **E1** to the corresponding benzimidazolium salt **F1**, precursor for the synthesis of N-DMBI-H dopant (**Table 4.2**, entry 1-2). We tried the reaction using acetonitrile as medium and methyl p-toluenesulfonate as alkylating agent, used in excess (1.5 eq.) with respect to the starting reagent (entry 1). The reaction was stopped after 24 hours, and the product was recovered via precipitation induced by diethyl ether addition followed by filtration. The NMR analysis of the isolated solid, revealed it to be a mixture of three different species: the target product, the residual reagent **E1** and an unknown impurity in a 1:0.34:1 molar ratio. The obtained ^{1}H-NMR spectrum suggests the impurity to be the derivative obtained via second alkylation of **F1** on the nitrogen of the aniline residue (see **Figure 4.4**). This product likely forms after the first methylation of the more nucleophilic benzimidazole nitrogen, due to partial solubility of the obtained derivative **F1** in acetonitrile, that makes it prone to interact a second time with the methylating agent. This hypothesis is supported by the fact that no product obtained via monoalkylation of the aniline nitrogen could be identified within the reaction mixture.
The undesired side-product was efficiently removed via crystallization in water saturated with sodium p-toluenesulfonate. Due to the high amount of residual reagent, we did not further purify the crude. We then repeated the reaction using a stronger alkylating agent, methyl triflate, to promote complete conversion of **E1** in shorter times.

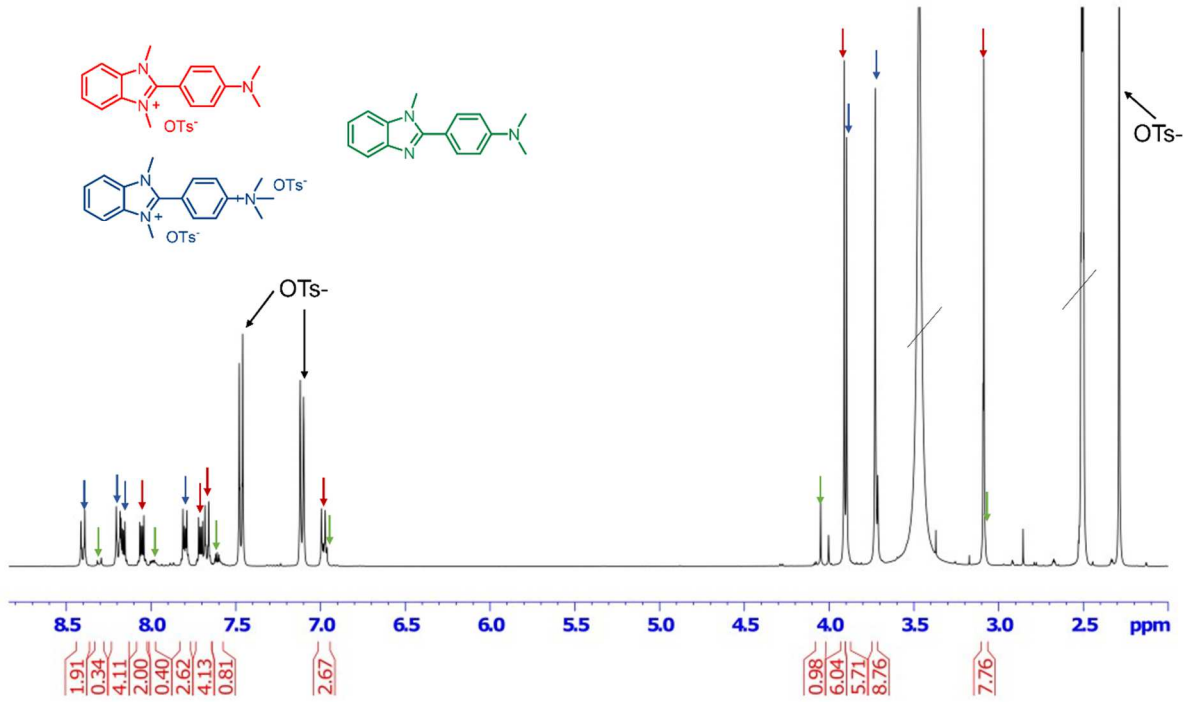

Figure 4.4 ^{1}H solution NMR spectrum in DMSO-d6 of the solid isolated from reaction between **E1** and p-toluensulfonate. Peaks associated to the product **F1**, the dialkylated impurity and the reagent **E1** are highlighted in red, blue, and green respectively.

We also changed the reaction solvent to toluene, in which the solubility of product **F1** is suppressed. In this way, we aimed at inducing the precipitation of **F1** to avoid the formation of the dialkylated side-product even in the presence of excess methylating agent. The strategy successfully allowed to reduce the presence of the unwanted impurity within the reaction crude to 4 mol% and to increase the obtained yield to 79%. The crude showed however again presence of 20% of unreacted reagent, due to poor solubility of the aryl benzimidazole **E1** in toluene, suppressing its complete conversion to product. The right purification procedure for the removal of the residual reagent is still under investigation. Even if we did not isolate product **F1** with the required purity for the following reduction step, the obtained result suggests that via appropriate solvent selection it should be possible to induce complete reagent conversion, while avoiding formation of undesired side-products.
The alkylation reaction was then tested for the synthesis of derivatives **F2-F7.** In the case of derivatives **F2-F4**, the reaction proceeded with no detection of undesired side-product using methylating agents of different strength (MeI and MeOTf). This is likely due to the reduced nucleophilicity of the nitrogen in para position to the 2-phenyl ring of these derivatives, which is incorporated in conjugated moieties. All these products were isolated with good yields higher than 68%.

Products **F5** and **F6** were obtained by reacting derivative **E5** with two different alkylating agents, 1-bromobutane and 1-bromohexane. We selected these two alkylating agents to obtain the benzimidazolium salt precursors for the synthesis of two alkylated dopants, one with a symmetric functionalization pattern (**F5**) and the other with an

asymmetric one (**F6**). Despite the presence of an aniline residue susceptible to second alkylation, no dialkylation side product was detected in both reactions, probably because these alkylating agents are weaker with respect to those used for the synthesis of derivative **F1.** We then isolated the target derivatives **F5** and **F6** with yields of 70.9% and 76.1% respectively.

In the case of derivative **F7**, the reaction was firstly tested using methyl iodide as methylating agent in acetonitrile. In such conditions the undesired cationic side-product formed. We managed however to isolate the target product via crystallization in n-pentanol with a yield of 54.2%. To completely avoid formation of this side-product, we repeated the reaction using ethyl acetate as medium, since product **F7** is poorly soluble in this solvent. This approach allowed to induce **F7** precipitation after its formation. By doing this we avoided the formation of the unwanted impurity and recovered the product via simple filtration, increasing the isolated yield of the reaction to 74.0%.

4.3.2.4. Reduction of benzimidazolium salts

The last step of the tested protocol for the synthesis of benzimidazoline derivatives is the reduction of the obtained benzimidazolium salts via reaction with $NaBH_4$ in methanol at 0°C.

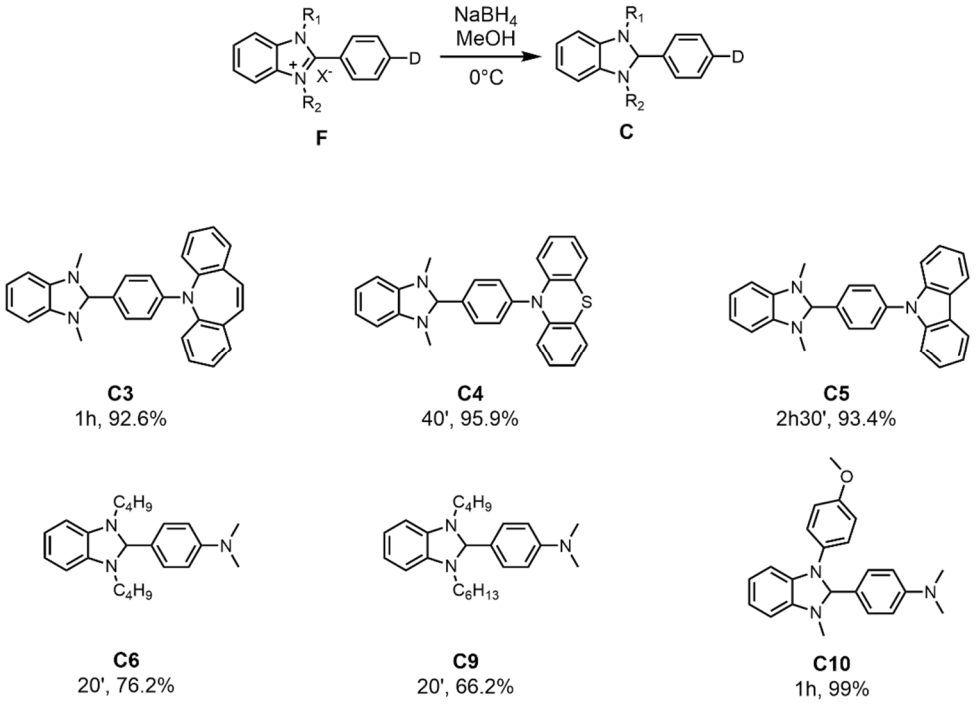

Scheme 4.7 General protocol for the synthesis of benzimidazoline derivatives (**C**) via reduction reaction of benzimidazolium salts (**F**). The obtained products are reported together with reaction yields and times. 2 to 11 molar equivalents of $NaBH_4$ were used with respect to **F,** depending on the selected derivative.

The reduction reaction conditions used are the same of the previously reported N-DMBI-H synthetic protocol shown in **Scheme 4.1, Path B** and are here reported in **Scheme 4.7**, together with the obtained products. In the case of derivative **C3** and **C4**, the reaction was performed on the corresponding iodide salts. The equivalents of

reducing agent used had to be adjusted depending on the specific derivative solubility in the used solvent and on the reaction rate.

The reaction proceeded successfully for all the reacted benzimidazolium salts. Apart from derivatives **C6** and **C9**, all the products precipitated out of the reaction medium and were isolated via simple filtration, with excellent yields higher than 90%. In the case of derivatives **C6** and **C9**, the products are obtained as liquids soluble in methanol. As such, a different purification procedure based on evaporation of methanol followed by solvent extraction had to be performed. While studying the synthesis of derivative **C6** via acid-clay catalysed condensation reaction, we noticed that these alkylated dopants are very prone to oxidation. For this reason, we carried out these purification procedures rigorously under inert atmosphere. The approach allowed us to obtain the two derivatives with yields of 76.2% and 66.2% respectively, and with the level of purity (NMR purity $> 98\%$) required for application in devices.

Table 4.3 Overall reaction yields of the synthesis of dopant via reductive cyclization protocol. In the case of derivatives **C3-C5**, yields are reported for the synthetic route mediated via Buchwald-Hartwig (BH) amination as well.

Product	Overall Yield (%)[a]	
		BH amination
C3	59.2%	37.7 %
C4	48.6%	38.0%
C5	20.3%	60.5%
C6	36.6%	-
C9	34.2%	-
C10	57.4%	-

[a] yield of synthesis of the starting aldehydes are not included in the evaluation.

Table 4.3 collects the overall reaction yields for the synthesis of dopant performed via the reductive cyclization route. In the case of derivatives **C3-C5,** we also calculated the yields for the protocol involving the Buchwald Hartwig amination step. Except for derivatives **C6** and **C9**, all products could be obtained with fair yields higher than 48%. Considering the yields of the reactions reported in the literature for the synthesis of N-DMBI-H (23-26%), these results are enough satisfactory.

Through the approach we could successfully obtain two original asymmetric derivatives, product **C9** and **C10**, and we could also synthesize derivative **C4**, not obtainable via the previously tested heterogeneous condensation reaction.

It is worth mentioning that all the products were generally recovered with higher NMR purity when synthesized through this second protocol. These benzimidazoline derivatives are in fact sensitive to oxidation when in solution, in analogy to N-DMBI-H (see Chapter 3), but, since most of them precipitates in methanol during the reduction reaction with $NaBH_4$, it is easier to avoid their degradation with this second synthetic route. The work-up procedure following the acid-clay catalysed condensation reactions requires instead solvent extraction and column chromatography, which makes hard to

avoid partial (1-3 % in mol) product degradation during its recovery. This is not an irrelevant consideration for the selection of a synthetic route for such derivatives since, as we mentioned in Chapter 3, even such amounts of degradation products might affect the dopant performances in devices applications.

4.3.3. Conclusion

With this work, we developed two versatile synthetic strategies suitable for the synthesis of a wide library of N-DMBI-H based n-type dopants, functionalized with different substitution patterns and on different positions of the benzimidazoline moiety. The two protocols, respectively based on an acid-clay catalysed condensation reaction and on a reductive cyclization reaction, are adapted from literature reported procedures for the synthesis of benzimidazoles. They were however previously never reported for the synthesis of benzimidazoline based dopants.

The two synthetic routes were successfully applied for the preparation of known derivatives (N-DMBI-H, DPBI) and 8 original benzimidazoline derivatives. The developed montmorillonite-clay catalysed condensation protocol resulted particularly suitable for the synthesis of a series of N-DMBI-H derivatives with extended conjugation, even if it showed some limits with substrates characterized by high melting points. The protocol was also successfully extended to the synthesis of two dimeric dopants and of a derivative functionalized with longer alkyl chains. The same route then resulted more efficient in terms of reaction yields for the synthesis of N-DMBI-H with respect to the synthetic routes reported in the literature.

The developed reductive cyclization-based protocol allowed a further extension of the library of benzimidazoline based dopants to other derivatives with extended conjugation and compounds with asymmetric structures. The route also proved to be suitable for a divergent functionalization of the benzimidazole core of the dopant via Buchwald Hartwig amination reaction, which makes it ideal for a further extension of the library of benzimidazoline derivatives. With respect to the acid-clay catalysed condensation reaction, the protocol results preferable for the synthesis of derivatives highly sensitive toward oxidation, that, through this route, can successfully be prepared with the required purity for application in devices.

4.4. Structure-function-properties relationships of the new dopants

In the previous section of this Chapter, I discussed the synthesis of a wide library of new benzimidazoline based dopants. In this second section, I will instead show the results of the characterization of a selected set among these new N-DMBI-H derivatives, with the aim of describing the impact of the different substitution pattern on their doping performances. **Figure 4.5** collects the studied dopants. For this work we selected the three derivatives functionalized with conjugated moieties (**C3**-**C5**), a derivative characterized by long alkyl chains (**C6)** and the aryl functionalized asymmetric dopant (**C10**). From now on, I will refer to these compounds with names recalling the main structural variations with respect to N-DMBI-H, so to make their recognition easier. The three derivatives with extended conjugation will be called IStBI, PThBI and CBzBI, as they were obtained via functionalization of the benzimidazoline core with an iminostilbene, a phenothiazine and a carbazole unit respectively. Derivatives **C6** will be named $2C_4$-DMBI, recalling the butyl substituents used to functionalize the dopant benzimidazole moiety. I will call then derivative **C10** AnDMBI, as its structure is functionalized with an anisyl moiety.

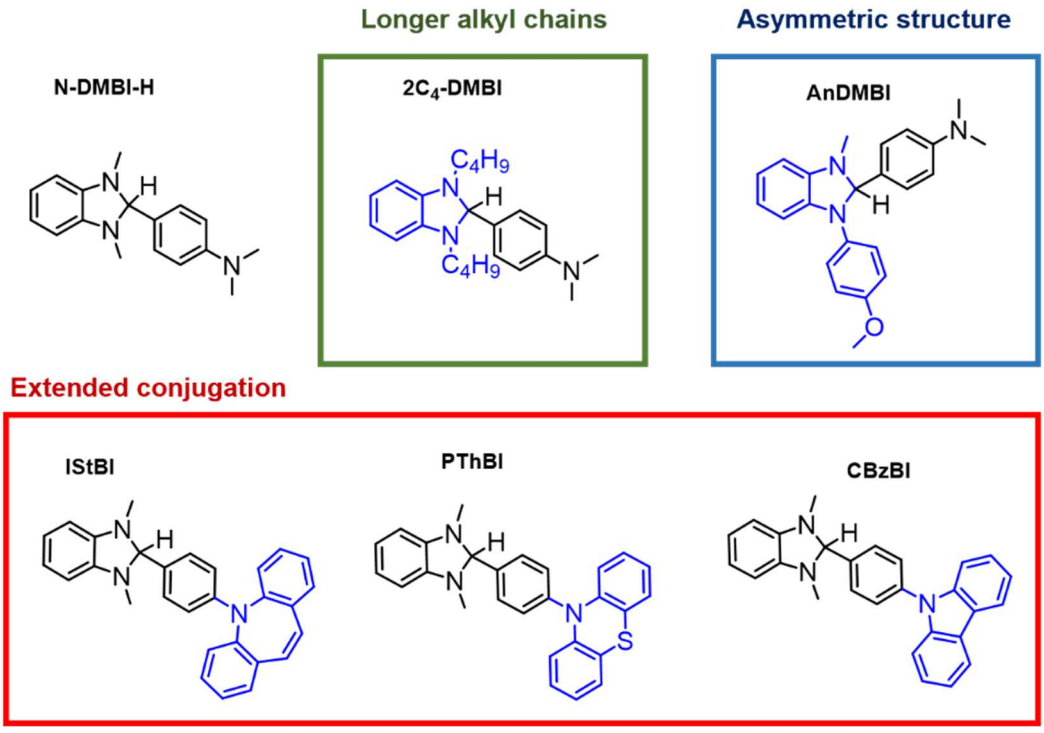

Figure 4.5 Molecular structure of N-DMBI-H and of the selected derivatives. The molecule portion interested by structural modification (with respect to N-DMBI-H) is highlighted in blue. Derivatives with extended conjugation on the aniline moiety, derivatives with longer alkyl chains on the benzimidazole nitrogen atoms and asymmetric derivatives are highlighted in red, green, and blue respectively.

4.4.1. Thermal Characterization of new dopants

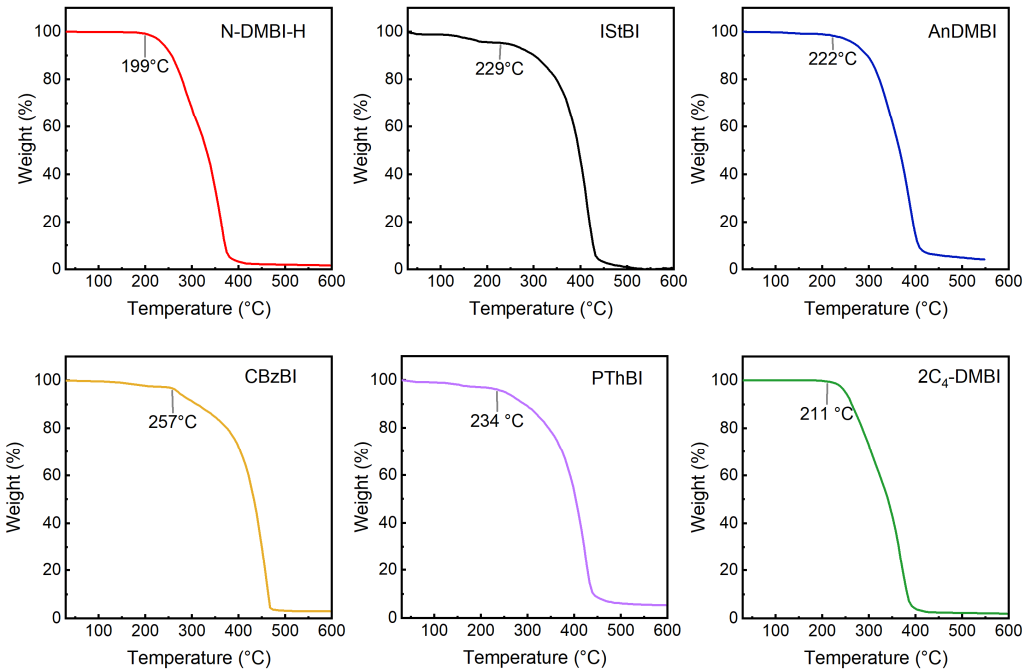

Figure 4.6 Thermograms related to TGA analysis of N-DMBI-H (red), IStBI (black), AnDMBI (blue), CBzBI (yellow), PThBI (purple) and $2C_4$-DMBI (green). Temperature at which degradation/sublimation starts is indicated on each graph. All measurements were performed under N_2 flow(50mLmin^{-1}) at a heating rate of 10 °Cmin^{-1}.

We performed a complete thermal characterization of the selected new derivatives via Thermogravimetric analysis (TGA) and Differential Scanning Calorimetry (DSC). Since the doping process is generally activated via thermal annealing of the polymer/dopant blends, this characterization is essential to understand the limit temperature for such treatment and its effect on the blend microstructure. We firstly analysed the thermal stability of the compounds via TGA and compared it to that of N-DMBI-H (**Figure 4.6**).The films annealing procedures are generally performed under inert atmosphere, so we carried out the TGA analysis under N_2 flow. All compounds start degrading at temperature higher than 200°C and show improved thermal stability with respect to N-DMBI-H. Via DSC measurements, we then analysed the melting points of the solid derivatives (**Figure 4.7**). Again, we performed the analysis under N_2 atmosphere. In the case of $2C_4$-DMBI, the melting point is below room temperature (the compound is stored as an oil) and, as such, it was

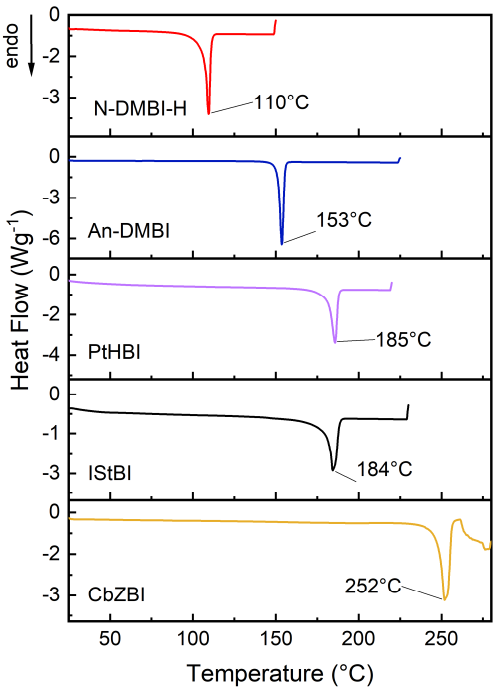

Figure 4.7 DSC thermograms of the obtained N-DMBI-H derivatives compared to that of the reference dopant. For each compound, melting peak temperature is indicated. Measurements were performed under N_2 flow(80mLmin^{-1}) at a heating rate of 10 °Cmin^{-1}.

not characterized. All the analysed compounds have melting points (T_m) higher with respect to that of N-DMBI-H (110°C), varying between 150 and 250°C. Among the three derivatives functionalized with more planar conjugated moieties, IStBI and PThBI show a similar melting point of ~180°C, while the T_m of CBzBI is located at around 250°C. This difference is probably related to stronger intermolecular interactions induced by the higher planarity of the carbazole unit with respect to the iminostilbene and the phenothiazine one.

4.4.2. Electrochemical Characterization of new dopants

We then performed an electrochemical characterization of the benzimidazoline derivatives to analyse the impact of the introduced structural modification on their electronic structure and thus doping capabilities. As discussed in Chapter 2, doping mediated by N-DMBI-H like derivatives (DH) happens either via hydride transfer or via formation of the corresponding $D^{\bullet}$ radicals, that then work as electron donor. We thus evaluated both the HOMO of the selected derivatives and the LUMO of the corresponding benzimidazolium triflate salts D^+ (hexafluorophosphate salt only in the case of $2C_4$-DMBI, see experimental methods for the synthesis). The latter corresponds in fact to the SOMO of the dopants radical $D^{\bullet}$. We analysed the literature references N-DMBI-H and DPBI (derivative **C2**) as well for comparison.

The energy levels were firstly calculated via Density Functional Theory (DFT-B3LPY) and then evaluated via Cyclic Voltammetry (CV). Differential Pulse Voltammetry (DPV) was also performed to support the CV data showing non reversible oxidation or reduction peaks. **Figure 4.8** shows the obtained CV plots. The plots are similar for all the compounds. The first oxidation event, relevant for the evaluation of the HOMO

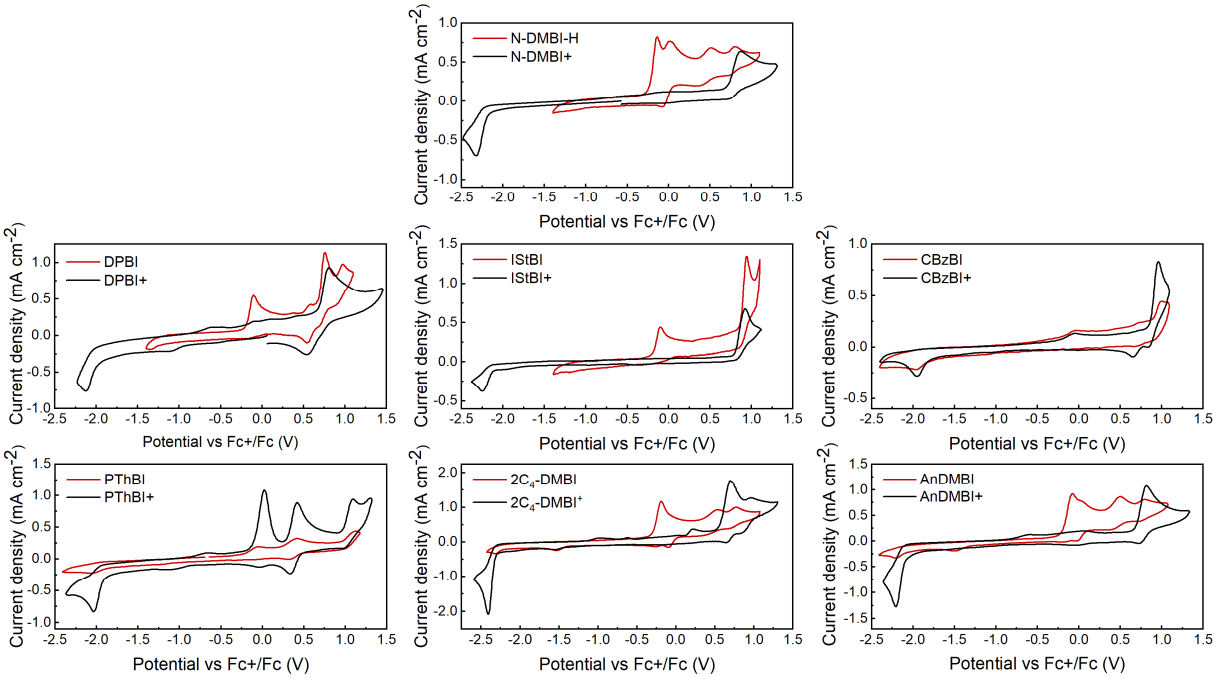

Figure 4.8 Cyclic voltammetry measurements of the neutral dopants (red lines) and the corresponding benzimidazolium salts (black lines). Measurements were performed using a 0.1 M solution of tetrabutylammonium perchlorate in acetonitrile as electrolyte. Potentials are reported against the ferrocene/ferrocinium redox couple.

level, is non reversible for all the neutral dopants. Several oxidation events are then visible at more positive potentials. Most of these are only partially reversible. The only exceptions are the second oxidation peaks present in CV plots of N-DMBI-H, AnDMBI and $2C_4$-DMBI. These are reversible and, according to previous electrochemical characterizations of benzimidazoline derivatives, can be associated to oxidation events involving the N-dimethyl group on the 2-phenyl ring of these compounds. In line with this interpretation, the same peak is not visible in CV plots of derivatives not functionalized with such group.[15] For the neutral dopants analysed in a potential window between -2.5 V and +1.25 V (vs Fc/Fc^+), a not very intense non-reversible reduction peak is then observed when going to more negative potentials after the occurrence of the oxidation events. This peak is located at the same potentials observed for the reduction of the corresponding benzimidazolium salts. This suggests formation of the dopants' cations following the oxidation process. The reduction processes observed in the CV plots of the analysed benzimidazolium salts D^+ are all non-reversible as well. Since these events are associated to formation of the radicals $D^{\bullet}$, the poor reversibility of these reactions can be correlated to a low stability of such species. A series of oxidation peaks can then be observed in all the plots related to these salts, going to more positive potentials. All these oxidation events are only partially reversible, except for the oxidation peak located at +0.68 V Fc/Fc^+ in the CV plot of $DPBI^+$ and the second oxidation peak located at +0.89 vs Fc/Fc^+ in the CV plot of $2C_4$-$DMBI^+$, that are reversible. These peaks might be in part be associated to oxidation of species forming after the salts' reduction. For these derivatives, we in fact performed the measurements going firstly toward negative potentials. The redox potentials relevant for the evaluation of the HOMO and SOMO levels of the dopants are collected in **Table 4.4**. The measured energy levels are reported as well, together with those calculated via DFT. **Table 4.4** also collects the energy levels evaluated via DPV. The corresponding plots and redox potentials are instead reported in the experimental methods sections.

Table 4.4 calculated (DFT) and measured (CV and DPV) HOMO and SOMO energy levels of N-DMBI-H and its derivatives. Oxidation (E_{ox}) and reduction (E_{red}) potentials evaluated from CV measurements are reported as well.

Dopant (DH)	E_{ox} (V) ($DH^{\bullet+}/DH$)	HOMO (eV)			E_{red} (V) ($D^+/D^{\bullet}$)	SOMO (eV)		
		CV	DPV	DFT[a]		CV	DPV	DFT[a]
N-DMBI-H	-0.19	-4.61	-4.58	-4.86	-2.26	-2.54	-2.52	-2.65
DPBI	-0.20	-4.60	-4.59	-4.92	-1.99	-2.81	-2.80	-2.95
IStBI	-0.19	-4.61	-4.59	-4.88	-2.17	-2.63	-2.60	-2.68
PThBI	-0.09	-4.71	-4.70	-4.98	-1.98	-2.82	-2.81	-3.11
CBzBI	-0.11	-4.69	-4.71	-4.97	-1.90	-2.90	-2.87	-3.07
AnDMBI	-0.09	-4.71	-4.69	-4.65	-2.13	-2.67	-2.65	-2.75
$2C_4$-DMBI	-0.22	-4.58	-4.58	-4.64	-2.32	-2.48	-2.42	-2.64

[a] B3LYP

The energy levels measured via DPV and CV are in good agreement. The DFT calculated values are generally lower with respect to the measured ones but, except for AnDMBI and DPBI HOMO levels, their trend agrees well with that of the electrochemical measurements. The HOMO level of N-DMBI-H is located around -4.61 eV according to CV analysis, while its SOMO is located around -2.54 eV. These values are in line with those previously reported for the same derivative.[15,18] In the case of $2C_4$-DMBI, the obtained HOMO and SOMO levels are only at slightly higher energy (-4.58 eV and -2.48 eV). This agrees with the fact that substitution of methyl functionalities with longer alkyl chains on the benzimidazole nitrogen atoms should not significantly impact on the electron donating capability of the derivative. In the case of AnDMBI, both the HOMO and the SOMO levels are instead stabilized with respect to the parent dopant. This might be due to a charge delocalization effect from the benzimidazole nitrogen to the anisyl group.

DPBI was characterized as literature example of dopant with extended conjugation. Its HOMO level results located at -4.60 eV, almost identical to that of N-DMBI-H, which suggests that the introduction of two aromatic rings on the aniline residue of the dopant does not influence much its HOMO. This is in agreement with a previous report by Fabiano and coworkers showing that the HOMO level of N-DMBI-H-like derivatives is mainly localized on the benzimidazole core.[15] In line with this behaviour, the functionalization of the same aminic residue on N-DMBI-H structure with π-conjugated moieties does not affect much the position of this energy level. In the case of IStBI, the HOMO is essentially the same of that of DPBI and N-DMBI-H. PThBI and CBzBI show instead only slightly lower HOMO levels, located at -4.71 and -4.69 eV respectively. The introduction of π-conjugated groups on the dopant structure stabilizes instead in all cases the SOMO level, that reaches values of -2.63 eV, -2.81 eV, -2.82 eV and -2.90 eV for IStBI, DPBI, PThBI and CBzBI respectively. Again, this is in line with Fabiano's group work suggesting that the functionalization of the 2-phenyl ring of the benzimidazoline can impacts the SOMO level of the compound.[15] The stabilization effect might be explained with a less electron-donor character of the aminic nitrogen incorporated in such conjugated structures. The higher SOMO observed for IStBI might be connected to the iminostilbene moiety antiaromatic character.[28] This antiaromaticity might favour the delocalization of the unpaired electrons of the iminostilbene nitrogen toward the benzimidazoline core compared to the phenothiazine, the carbazole, or the diphenyl aromatic moieties.

In all cases, the dopants have a HOMO level close or lower with respect to that of N-DMBI-H, which suggest that, thermodynamically speaking, they cannot donate electrons via direct electron transfer to a semiconductor. Most compounds have deeper SOMO levels. The differences with respect to N-DMBI-H are however limited, and all the derivatives should be capable of working as dopants once activated with the suitable treatments, even in the case of a doping mechanism mediated by formation of the corresponding radicals ($D^{\bullet}$).

4.4.3. Preliminary study on IStBI performances

We firstly tested the doping efficacy of IStBI. For the purpose, we again selected P(NDI2OD-T2) polymer as semiconductor counterpart since this material is one of the benchmark polymers for doping studies. We prepared P(NDI2OD-T2) films containing molar concentration of IStBI between 0-50% with respect to the polymer repeating unit. Films were spin coated from toluene and thermally annealed at 180°C for 2 hours. We then measured the films conductivity (σ) and compared the obtained values with those of samples prepared according to the same procedure but using different concentrations of the two references dopant N-DMBI-H and DPBI (**Figure 4.9a**).

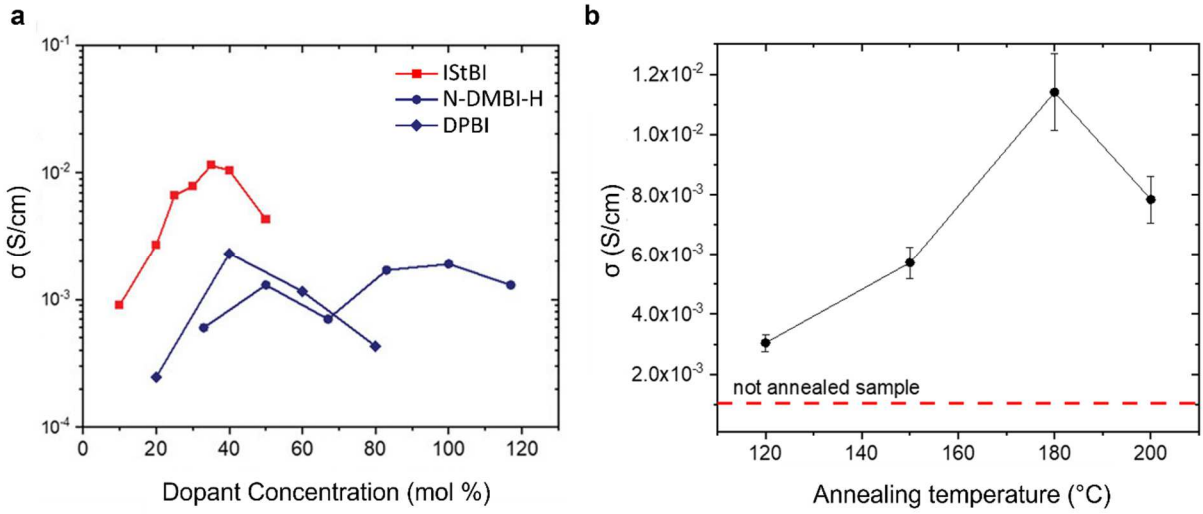

Figure 4.9 a) Conductivity values of P(NDI2OD-T2) films doped with different molar concentration of IStBI (red squares), N-DMBI-H (blue circles) and DPBI (blue diamonds); b) conductivity values of films doped with a 35 mol% concentration of IStBI in the function of thermal annealing temperature. The value obtained for a not annealed film is reported as well with a red dashed line. Adapted from reference 69.

The maximum σ values of films doped with N-DMBI-H and DPBI are in the order of 2×10^{-3} Scm^{-1}, in line with those previously reported in the literature for such derivatives.[12,15,29] P(NDI2OD-T2) doped with IStBI achieve instead a maximum conductivity of $(1.14 \pm 0.13) \times 10^{-2}$ Scm^{-1} at a dopant molar concentration of 35%. This value is five order of magnitude higher with respect to the conductivity of pristine P(NDI2OD-T2), reported to be in the order of 10^{-7} Scm^{-1}.[12] The electrical performances then drop at higher dopant concentrations. This trend might be correlated either to a decreased doping efficiency due to dopant segregation or to a reduced charge carrier's mobility associated to higher microstructural disorder.[2,30]

We also tested the effect of the thermal annealing temperature on the electrical performances obtained using this dopant, with the aim of optimizing the doping activation conditions (**Figure 4.9b**). The measurement was performed at a dopant molar concentration of 35 %, i.e. the one giving the maximum electrical conductivity in our experiments. Interestingly, the not annealed films already shows a conductivity of $\sim1\times10^{-3}$ Scm^{-1}, in the same order of magnitude of that of annealed films doped with N-DMBI-H. This suggest that this dopant is also active at room temperature. Conduc-

tivity then progressively increases with annealing temperature, reaching a maximum value at 180°C followed by a drop when the process is carried out at higher temperatures. We explain the performance growth with more efficient thermal activation of the dopant and thus increased charge carrier density. Mobility can also be influenced but no conclusive argument can be given on this respect as the performances depends on the charge carrier density and mobility product. Having said that, thermal treatments can increase crystallinity and packing order of the polymeric chains.[31] According to the previously shown thermal characterization (**Figure 4.7**) then, IStBI melts at around 180°C. The fact that the film conductivity reaches the maximum value at this temperature, might also be associated to melting of dopant crystallites in the film and improved diffusivity of the dopant in the polymeric matrix, in agreement with the observation of Fabiano and co-worker in their work on sequential doping of poly(benzimidazobenzophenanthroline) (BBL) with N-DMBI-H.[32] Explaining the drop in conductivity observed for films annealed at 200°C is instead not straightforward. The phenomenon might be rationalized either in terms of partial degradation of the dopant or, considering previous reports on thermally accelerated dopants diffusion,[32,33] with a partial de-doping associated with out-diffusion of IStBI from the film at such high temperature. According to our TGA characterization (**Figure 4.6**), this compound should be stable at temperatures below 230°C. As such we propend for the second hypothesis. Further characterizations are however required to give a clear-cut explanation.

The electrical conductivity obtained using IStBI is one order of magnitude higher with respect to that of films doped with the literature references dopants. To the best of our knowledge, it is also the highest σ reported for P(NDI2OD-T2) polymeric films solution-doped with benzimidazoline-based dopants.[2,12,34,35] According to our electrochemical characterization, the different performances obtained with IStBI with respect to the reference dopants cannot be ascribed to a stronger electron donating capability. The HOMO levels of the three analysed derivatives are in fact almost identical ($\sim$-4.60 eV) and the SOMO level of our derivative is located at -2.63 eV, deeper with respect to that of N-DMBI-H (-2.54 eV). The results then hint at a different interaction between the semiconductor matrix and this compound.

4.4.4. A comprehensive study of the effect of different functionalization patterns on doping performances

The preliminary characterization of the P(NDI2OD-T2) films doped with IStBI already gives some insight on the effect of the functionalization pattern of this derivative on its efficacy. As a following step of our work, we carried out a deeper structure-function properties relationship characterization on the whole selected set of dopants, with the aim of comparing the effect of their different molecular structure on the doping performances.

For the purpose, we prepared and characterized P(NDI2OD-T2)/dopant blends, all processed from the same solvent and treated at the same annealing temperature, so to compare the properties of the different compounds under the same operating condi-

tions. We thus selected toluene as processing solvent and activated the doping via thermal annealing at 180°C for 2 hours, to reproduce the conditions giving the best performances in the case of IStBI. According to the performed TGA analysis, all the dopants are thermally stable at such temperature (see **Figure 4.6**).

More data on characterization of doped films processed from different solvents can be found in **Appendix B**.

4.4.4.1. Electrical characterization of doped polymeric films

We firstly characterized the electrical properties of P(NDI2OD-T2) films containing the analysed dopants in concentration between 10 and 100 mol% with respect to the polymer repeating unit. Doping was performed via solution mixing. Since we carried out this experiment with non-commercial batches of polymer, different from those used for the previously reported studies, we repeated the electrical characterization for IStBI and N-DMBI-H as well. The measured conductivity values are reported in **Figure 4.10**. In the case of CBzBI, we had to reduce the maximum analysed dopant concentration to 55 mol%. The scarce solubility in toluene of this dopant (1.7 gL^{-1}) led in fact to very diluted polymeric solutions with addition of higher dopant amounts, giving very defective and thin films (thickness < 20 nm), not suitable for a proper characterization.[†††]

The conductivity of N-DMBI-H doped films shows an initial growth of three order of magnitude with respect to that of the pristine polymer (~1×10^{-7} Scm^{-1}) at low doping levels (10 mol%). The conductivity then progressively reaches a plateau at higher concentrations, the maximum value being of (1.3 ± 0.3) × 10^{-3} Scm^{-1} at 70 mol% of dopant. The obtained values and their trend are again in line with those reported for the same dopant.[12,30] We could not measure the conductivity of CBzBI doped polymeric films at dopant concentrations higher than 55 mol%. However, this compound shows a behaviour like the parent dopant, reaching a maximum conductivity of (5 ± 1) × 10^{-4} Scm^{-1} at a dopant concentration of 40 mol%, close to that obtained using the same amount of N-DMBI-H. In the

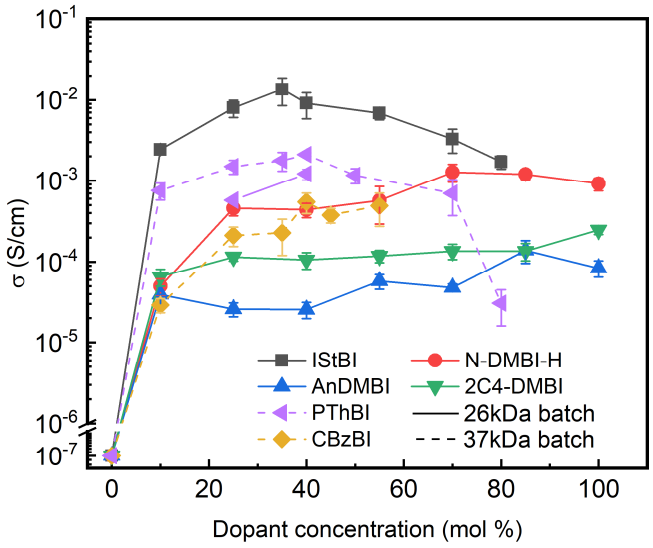

Figure 4.10 Conductivity of P(NDI2OD-T2) films doped with different DMBI derivatives. Values obtained using the 26kDa and 37kDa P(NDI2OD-T2) batches are highlighted in solid and dashed lines respectively.

[†††] This dopant is slightly more soluble in o-dichlorobenzene (oDCB). We thus also tested oDCB as processing solvent. However, due to the higher boiling point of oDCB with respect to toluene, a feature known to lead to thinner films in spin coating procedures,[68] we still obtained very thin films. We thus sticked to the first solvent used.

case of the other dopants, the results highlight that the structural modifications introduced on the N-DMBI-H molecule highly impacts the electrical performances. Two different trends can be recognized. For AnDMBI and $2C_4$-DMBI, the doped P(NDI2OD-T2) films achieve the same electrical performances of N-DMBI-H at low dopant concentrations (10 mol%), but the conductivity shows a very limited growth at higher dopant amounts. For both dopants, the measured σ does not overcome values of 1-2 × 10^{-4} Scm^{-1} and results almost constant in the case of $2C_4$-DMBI. AnDMBI is the worst performing derivative of the whole set: films doped with this derivative achieve a maximum conductivity of (1.4 ± 0.4) × 10^{-4} Scm^{-1} at 85 mol% dopant concentration.

P(NDI2OD-T2) films doped with PThBI and IStBI show instead the best performances, with conductivities reaching a maximum value at dopant concentration between 35-40 mol%, followed by a drop. This trend agrees with our previous observations on IStBI. IStBI results the best performing dopant among the analysed set. P(NDI2OD-T2) polymer doped with this compound shows a maximum conductivity of (1.3 ± 0.5) × 10^{-2} Scm^{-1} at 35 mol% of dopant content, in perfect agreement with the data shown in **Figure 4.9**. PThBI doped films reach instead a maximum σ of (2.1 ± 0.1) × 10^{-3} Scm^{-1} at 40% mol of dopant content. The value is in the same order of magnitude with respect to the maximum σ achieved using N-DMBI-H but is observed at lower dopant amounts, which hints at a higher doping efficiency.

For films doped with PThBI and CBzBI, we used a different P(NDI2OD-T2) batch, with a number average molecular weight M_n of 37kDa (polydispersity index PDI: 3.46), higher than that of the polymer used for the characterization of the other derivatives (M_n = 26 kDa, PDI = 2.65). We moved to this second batch for practical reasons. The use of this second higher M_n polymer allowed us to spin coat less defective and slightly thicker films (thickness ≥ 20 nm) even from diluted polymer solutions containing high concentrations of these dopants poorly soluble in toluene (PThBI solubility in toluene: 2.8 gL^{-1}).

Molecular weight of semiconductor polymers is a factor that can impact both charge carrier mobility and the doping efficiency. Polymer with different M_n are in fact generally characterized by a different level of crystallinity,[36] a feature reported to influence carriers transport[37] but also miscibility with dopants.[7] To analyse any difference in performance induced by the features of this second polymer batch, we measured the conductivity of films obtained with the 26 kDa P(NDI2OD-T2) batch and doped with 25mol% and 40 mol% of PThBI. We then compared the obtained values with those of films prepared using the 37kDa polymer batch (see **Figure 4.10**). The obtained conductivities are of (5.7 ± 0.5) × 10^{-4} Scm^{-1} and (1.2 ± 0.2) × 10^{-3} Scm^{-1} respectively. These values are around half those obtained using the polymer with higher M_n. To deepen the reasons behind this difference we evaluated the field-effect mobility μ_{FET} of both P(NDI2OD-T2) batches in Top-Gate-Bottom-Contact architecture. The polymer μ_{FET} was evaluated to be 0.17 $cm^2V^{-1}s^{-1}$ in linear regime (μ_{linear}) and 0.24 $cm^2V^{-1}s^{-1}$ in saturation regime (μ_{sat}) for the 37kDa batch, around twice that of the 26kDa batch

(μ_{linear} = 0.09 $cm^2V^{-1}s^{-1}$, μ_{sat} = 0.15 $cm^2V^{-1}s^{-1}$). This could explain the different electrical performance, even if a concomitant effect on doping efficiency cannot be completely ruled out. The observed conductivity difference does not change much our observations on this dopant behaviour: films doped with PThBI reach conductivities in the same order of magnitude of those doped with N-DMBI-H, but at lower dopant concentrations. We do not have a comparison between the two batches for CBzBI. It is however reasonable to expect the difference to be of the same entity of that detected for PThBI.

4.4.4.2. Optical characterization

To shed light on the reasons behind the different electrical performances, we carried out a UV-Vis-NIR characterization of the doped films, with the aim of analysing the P(NDI2OD-T2) polarons formation and, therefore, the charge-injection efficiency of the studied dopants. The obtained absorption spectra are collected in **Figure 4.11**. The intrinsic, undoped P(NDI2OD-T2) polymer film UV-Vis-NIR spectrum is characterized by an absorption peak located at 394 nm, associated to the π-π* transition, and a intrachain charge-transfer absorption band peaked around 710 nm. This is in line with previously reported optical characterization of this polymer.[30,38] The introduction of charges in the semiconductor, is accompanied by the neutral polymer charge-transfer band bleaching and by the appearance of the negative polaron absorption features (peak around 510 nm and absorption tail above 800 nm). This behaviour is in agreement with previous reports on the doping of P(NDI2OD-T2) and on its polaron optical properties.[15,30,38] A comparison of the polaronic peak intensity growth in function of the dopant concentration in the different spectra highlights a clear correlation between the

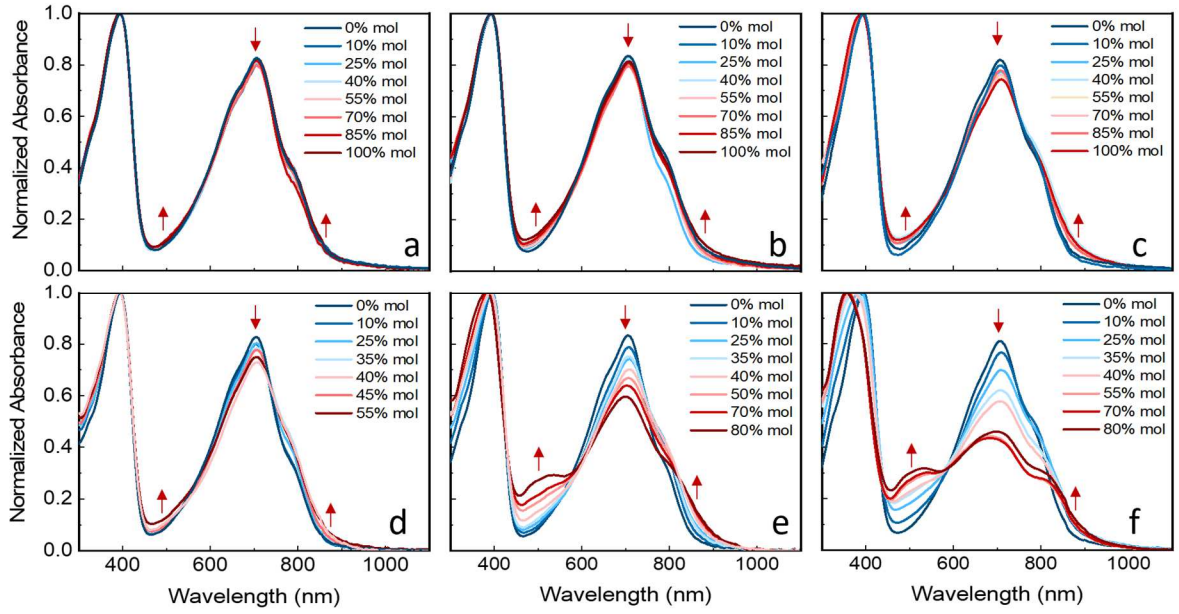

Figure 4.11 UV-Vis-NIR absorption spectra of P(NDI2OD-T2) polymer films doped with different molar concentrations of AnDMBI (a), $2C_4$-DMBI (b), N-DMBI-H (c), CBzBI (d), PThBI (e) and IStBI (f). Spectra were normalized with respect to the π-π* transition related peak (λ~394 nm). Bleaching of the polymer charge transfer band and appearance of polaron related absorption features are indicated with red arrows.

charge-injection efficiency and the electrical conductivities obtained with the analysed dopants.

For those dopants showing the poorer electrical performances, the intensity of the polaron absorption and, as such, the charge carrier density does not grow much with dopant concentrations. For films doped with AnDMBI, the derivative associated to the worst electrical performances, almost no polaronic feature is detected in the UV-Vis-NIR spectra. This is sign of very inefficient doping. A clear-cut differentiation of $2C_4$-DMBI and CBzBI doping efficacy based solely on the optical characterization is not straightforward. In agreement to the electrical characterization data, the polaron formation efficiency of these dopants seems however intermediate between that of AnDMBI and N-DMBI-H. Films doped with the most performing dopants, i.e. PThBI and IStBI, show instead much more intense polaronic absorption bands, whose intensity evidently grows in function of the dopant concentration. A progressive blue-shift of the π-π* absorption peak located at 394 nm, is also visible in the absorption spectra related to polymeric films containing these dopants, this phenomenon again reported as associated to polarons formation.[38] In agreement with the electrical conductivities trend, IStBI displays the highest charge injection efficiency.
These results demonstrate that charge carrier density of P(NDI2OD-T2) films doped with PThBI and IStBI progressively increases with dopant concentration. Therefore, the conductivity drops shown by polymeric films blended with these compounds at dopant concentration above 40 mol% cannot be ascribed to a reduced doping efficiency but is likely connected to a lower charge carrier mobility. This might be correlated with either coulomb scattering induced by the presence of dopant counterions in the conductive matrix or with higher microstructural disorder due to consistent amounts of dopant added to the host.[2,30,39]

4.4.4.3. AFM characterization of P(NDI2OD-T2)/dopants blends

The different efficiency of the analysed dopants cannot be explained exclusively based on their electron donating capability. According to the electrochemical data reported in **Table 4.4**, both IStBI and PThBI have SOMO levels lower with respect to N-DMBI-H. Nonetheless, they are more efficient dopants. The electron-transfer reaction should instead be more efficient for $2C_4$-DMBI, this derivative having the shallowest SOMO energy level among all those characterized. Still, its performances as dopant are very poor.
We thus performed a morphological characterization of the doped films to verify if the observed different behaviours could be associated to a different microstructure of the semiconductor/dopant blends and different solid-state interactions between the analysed derivatives and the polymer.

We firstly characterized the P(NDI2OD-T2) doped films via Atomic Force Microscopy (AFM). For the purpose, we prepared P(NDI2OD-T2) films containing a dopant concentration of 40 mol%, corresponding to the dopant/repeating unit ratio giving an

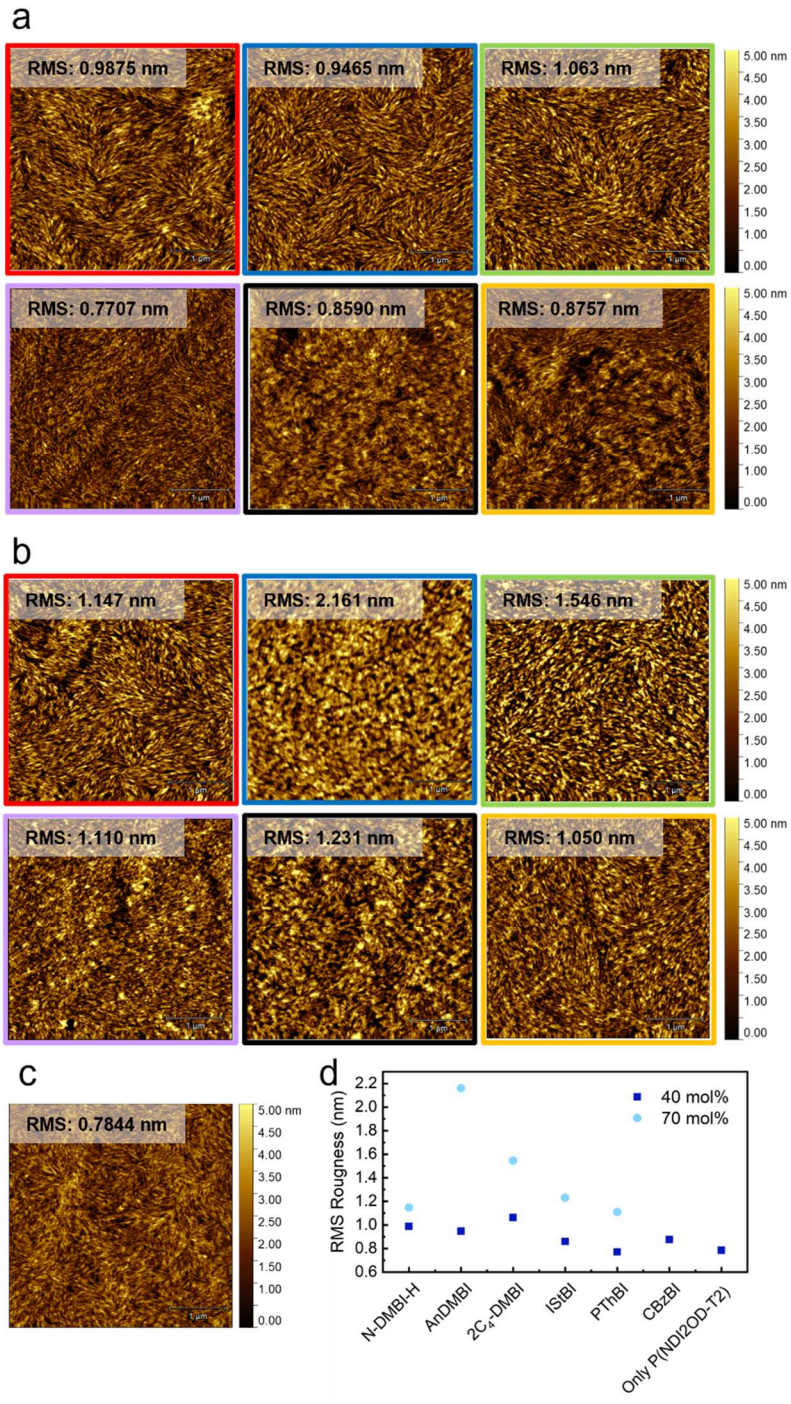

Figure 4.12 4×4 µm AFM images (scale bar: 1 µm) of P(NDI2OD-T2) doped with of N-DMBI-H (red), AnDMBI (blue), $2C_4$-DMBI (green), PThBI (purple), IStBI (black) and CBzBI (yellow) at a concentration of 40mol% (a) and 70mol% (55% in the case of CBzBI) (b). Image of a pristine polymeric film (c). RMS roughness of the obtained analysed films (d).

evident diversification of the electrical performances. We also prepared a neat polymer film as reference. **Figure 4.12a** collects the obtained AFM images and a comparison of their Root Mean Square (RMS) surface roughness (**Figure 4.12c**). All the films show the typical topography of P(NDI2OD-T2) pristine film casted from toluene, characterized by elongated fibrillar structure[40]. Films doped with derivatives bearing extended conjugation (PThBI, IStBI and CBzBI) are characterized by smoother surfaces. Films containing N-DMBI-H, AnDMBI and $2C_4$-DMBI, are instead rougher and characterized by higher presence of surface aggregates. This feature is generally associated with low micibility between the polymer and the dopant, leading to segregation of the latter.[2,12,13] Interestingly, we could not observe the striking level of segregation previously reported for N-DMBI-H,[2,12] possibly due to different processing conditions. We could however see coarser aggregates in some spot of the films when scanning wider surface areas, which suggest local segregates agglomeration (**See Appendix C** for images).

We also analysed films containing higher dopant concentrations of 70 mol% (55% in the case of CBzBI). **Figure 4.12b** shows the collected images**.** All these films are characterized by higher surface roughness and microstructural variation with respect

to blends containing lower dopant concentrations, which is explained by the very high amount of dopant added to the polymeric matrix. Nonetheless, a comparison of the RMS roughness of these second set of samples shows that the two dopants featuring the worst doping efficiency, i.e. AnDMBI and $2C_4$-DMBI, are also those with the most evident surface segregation. On the overall, these data reveal a correlation between the doping efficiency and the dopant segregation level and suggest that a functionalization of N-DMBI-H structure with bulky π-conjugated moieties leads to stronger interaction and a better intermixing between the dopant and the semiconductor host.

Dopant segregation can happen both before and after thermal annealing of the polymer/dopant blend, as recently observed by Demadrille and coworkers.[41] It was also observed that dopants tend to diffuse within the semiconductor host, the process being accelerated under thermal treatment.[32,33] We thus decided to further investigate the nature of the observed segregation phenomenon to understand if it happens before or after the doping thermal activation. For the purpose, we prepared a second set of P(NDI2OD-T2) films containing a dopant concentration of 70 mol%, with the same solutions used for the preparation of those reported in **Figure 4.12b**. In this case, we did not anneal the films, but dried them under vacuum before AFM analysis. For this experiment, we analysed only three representative samples. We selected P(NDI2ODT2) films doped with N-DMBI-H, IStBI and $2C_4$-DMBI, i.e. the literature reference dopant, the one giving the best performances and one of the worst performing derivatives of

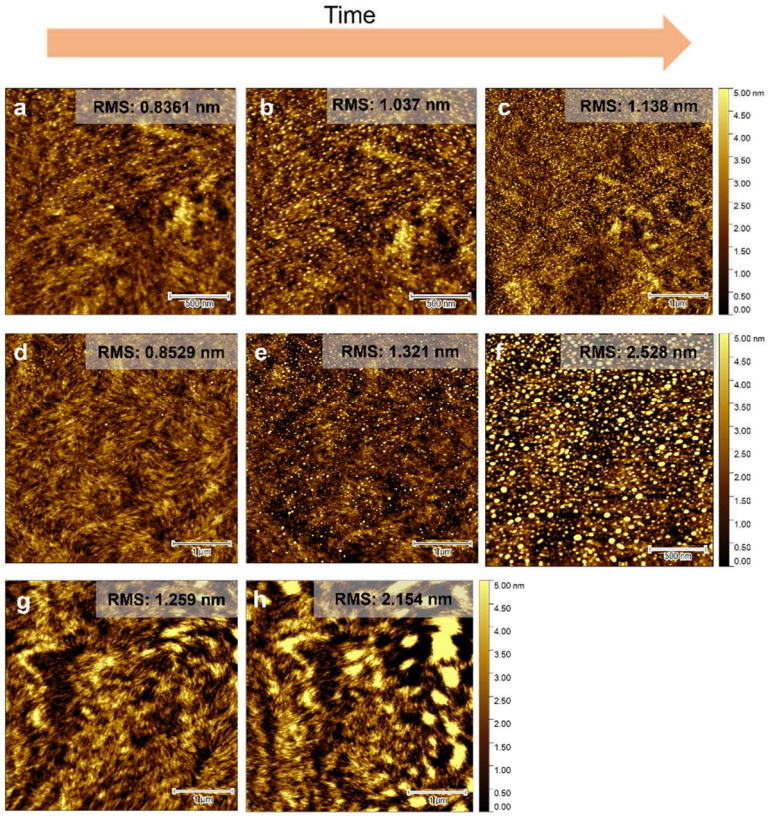

Figure 4.13 AFM images of P(NDI2OD-T2) films containing 70mol% of IStBI (a-c), N-DMBI-H (d-f) and $2C_4$-DMBI (g,h) and dried under vacuum before measurements. Images of the same spot were progressively collected for each sample within an hour of time. Scale bar: 500 nm in the case of images a,b and f, 1 µm in all other cases.

the analysed set. **Figure 4.13** collects the obtained images.

Unexpectedly, all the dried films resulted stable while kept under N_2 atmosphere but showed sizeable surface segregation of the dopant with time, once exposed to air for AFM analysis. We speculate that this phenomenon could be associated either with the formation of domains of oxidized dopant on the film surface or, based on our results on nucleating agents (Chapter 3), to a seeded surface nucleation promoted by the formation of tiny amounts of oxidized dopant.

Further studies supporting this second hypothesis are reported in **Appendix C**. Due to this fast film surface evolution, it was not possible to obtain AFM images of the pristine dried films. AFM scans require in fact at least 15-20 minutes to be completed. Nonetheless, a comparison of the RMS roughness of the first images of dried films with those of annealed films (see **Figure 4.14**) highlights that annealing procedures enhance the level of segregation and microstructural variation. These observations suggest that the dopants mainly segregate from the polymeric matrix during the film thermal treatment.

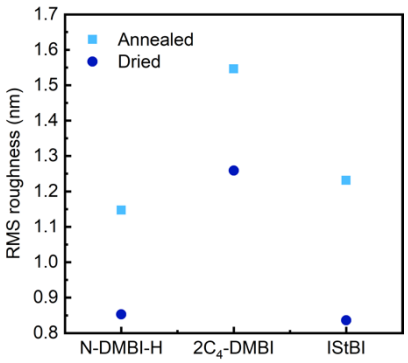

Figure 4.14 RMS roughness of dried and annealed P(NDI2OD-T2) films doped with 70 mol% of N-DMBI-H, $2C_4$-DMBI and IStBI

Considering the higher smoothness of films doped with derivatives with extended π-conjugation, the obtained results thus hint at a slower out-diffusion of these dopants from the film during thermal annealing. Again, this behaviour suggests stronger interactions between these derivatives and the polymer. A concomitant effect of the dopants molecular size and geometry cannot be ruled out, since bulkier dopants are reported to be less prone to diffusion.[33,42,43]

It is finally worth mentioning that, when collecting AFM images of annealed films, we could not notice the same fast surface evolution we observed for dried samples. We rationalize this phenomenon considering that, after thermal annealing, the non-activated dopant is either already segregated or has been activated during the process and remains as a counterion in the blend bulk.

4.4.4.4. GIWAXS characterization of P(NDI2OD-T2)/dopant blends

To corroborate the AFM analysis results and to further deepen the effect of the different compounds molecular structure on the dopant/polymer interactions, we analysed the microstructure of the P(NDI2OD-T2) annealed films via Grazing Incidence Wide-Angle X-ray Scattering (GIWAXS). In this case, we only characterized films containing dopant concentrations of 40 mol%. The obtained GIWAXS patterns are collected in **Figure 4.14**, together with the corresponding sector averaged profiles.

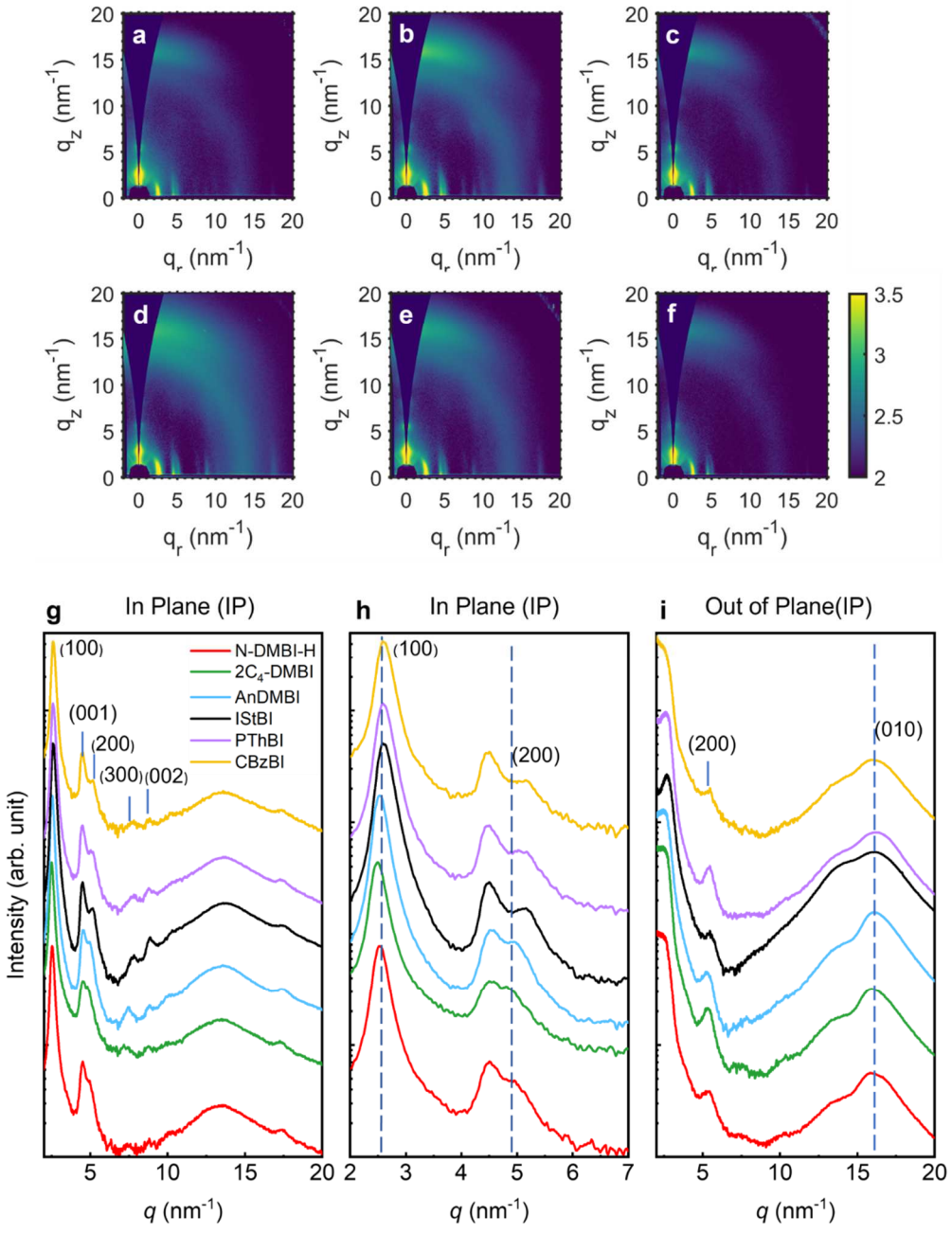

Figure 4.15 2D GIWAXS patterns of the P(NDI2OD-T2) films doped with 40% mol of N-DMBI-H (a), AnDMBI (b), 2C4-DMBI (c), IStBI (d), PThBI (e) and CBzBI (f). Sector averaged 1D profiles along the IP (g) and along the OOP (i) direction. The IP profile is reported together with a magnification between 2 (nm^{-1}) and 7 (nm^{-1}) q vector values (h). Peaks associated to the most evident changes are highlighted with dashed blue lines.

For all the samples, GIWAXS patterns show diffraction peaks related to both face-on and edge on molecular conformation with respect to the substrate, a features already

reported for doped P(NDI2OD-T2) films.[12,44] In all cases the face-on component is predominant, as highlighted by the marked In Plane (IP) lamellar stacking (h00) and backbone stacking (00h) replicas and by the Out-Of-Plane (OOP) π-π peak (010). The minority edge-on oriented regions are instead evidenced by the OOP (h00) lamellar stacking peak.[45,46] In all the cases, the replicas related to backbone stacking are not affected by dopant introduction in the film, which suggests that order is preserved on the local scale. Interestingly, while AnDMBI and $2C_4$-DMBI show similar peak positions with respect to N-DMBI-H, the in plane (h00) lamellar replicas are shifted toward higher q vector values in the case of derivatives functionalized with a π-conjugated moiety (PthBI and IStBI and CbZBI), this feature corresponding to a shrinkage of the lamellar d spacing in the real space. This behaviour has been previously rationalized with an improved intercalation of the dopant between the P(NDI2OD-T2) backbones, leading to an increase in the polymer backbones average distance and, therefore, to the generation of additional space for the alkyl chain layer and contraction along the (h00) direction.[12] This hypothesis is also supported by the reduced intensity of the (010) OOP π-π stacking peak visible in the diffraction patterns related to these compounds, which is possible to explain as dopant penetration between the polymer crystalline regions with disruption of the interchain π-π interactions. This features hints also at a reduced long-range order in polymeric films doped with DMBI-derivatives bearing extended conjugation. In semicrystalline copolymers like P(NDI2OD-T2), charge transport is however reported to be mainly determined by local interconnectivity between aggregates. Maintaining short range order in such materials is thus sufficient to guarantee percolative pathways for charge carriers and good electrical performances.[47]
These results are in line with those of our AFM characterization and corroborate the hypothesis that the observed PThBI and IStBI higher efficiency is due to stronger interactions with the polymeric chains that mitigate their out-diffusion and segregation during thermal annealing.

4.4.5 Theoretical simulation of dopants out-diffusion

The obtained results suggest that the efficiency of a dopant is dictated by the competition of two thermally activated processes within the metastable dopant/semiconductor matrix: the diffusion of the dopant - eventually causing surface segregation - and the doping reaction. If the affinity between the dopant and the polymer is strong and, consequently, the diffusion process is slow, a bigger fraction of dopant molecules is activated before the formation of coarse segregates, and the doping is efficient. If the dopant diffusion is instead fast due to weak interactions with the host, most of the dopant molecules segregate at the surface prior to actual doping events. To substantiate this hypothesis, we studied the diffusion behaviour of the analysed dopants from the P(NDI2OD-T2) matrix via classic molecular dynamic simulation based on GFN-FF (Geometries-Frequencies-Non-Covalent interaction Force-Field).[48] This work was performed and conceptualized by Giuseppe Mattioli of the ISM-CNR. The study was restricted to the two most performing dopants, PThBI and IStBI, the model dopant N-

DMBI-H and the worst performing dopant AnDMBI. For the purpose, we created random spheroidal distributions (radius > 3 nm) of P(NDI2OD-T2) dimers and dopants in 1:1 molar ratio. We then simulated the evolution of the systems on a 3 ns time span at a temperature of 500K. **Figure 4.16** shows the evolution of the average radial distance between the centre of mass of the P(NDI2OD-T2) dimers and of the dopants from the centre of mass of the entire cluster. We underline that the diffusion processes within a real polymeric film are likely hampered with respect to this system composed of dimers. As such, the diffusion time scales of our simulation do not correspond to those of the real system, and the results must be considered as relative trends.

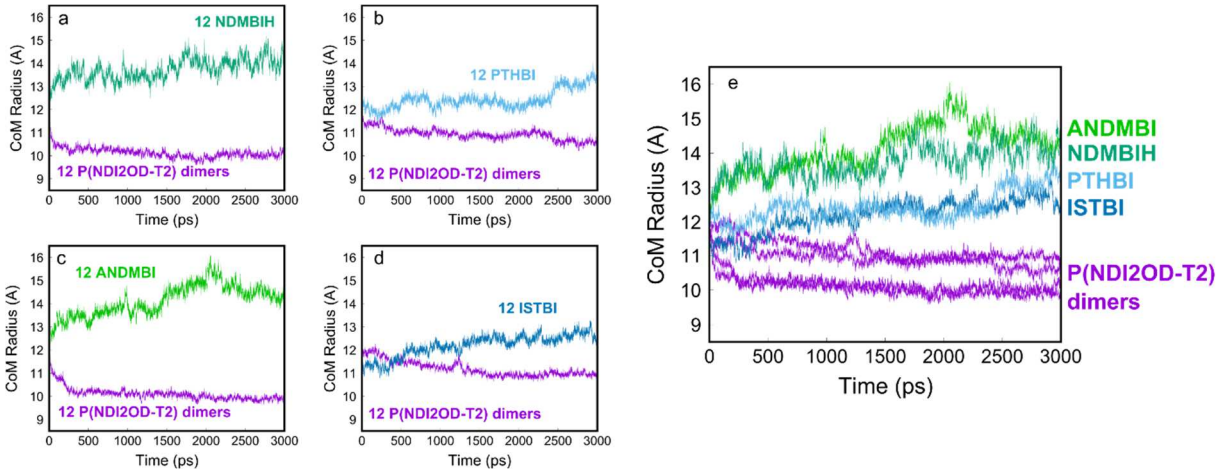

Figure 4.16 Evolution of the average radial distance of the Centre of Mass (CoM) of the P(NDI2OD-T2) dimers and the centre of mass of dopants from the entire cluster centre of mass. Data are reported for cluster containing N-DMBI-H (a), PThBI (b), AnDMBI (c) and IStBI (d). Graph **(e)** collects compares the obtained results.

The obtained graphs show that the different dopants possess a different tendency to diffuse away from the polymer. AnDMBI is the dopant showing the more pronounced tendency to phase segregation, followed by N-DMBI-H. PThBI and IStBI do not significantly segregate from the model polymer within the timespan of the simulation. Such trends are in good agreement with the experimental data of our electrical, optical, and morphological characterization. These results thus corroborate our data interpretation and further confirm that, with a suitable molecular structure modification, it is possible to modulate the dopant/semiconductor solid state interactions and thus performances. Such phenomenon is independent from any consideration of the position of the characteristic energy levels, although dopants could be designed featuring both reduced tendency to phase segregation and improved thermodynamic driving force for the doping process.

4.4.6 Effect of electronic structure on doping efficiency

Despite having a similar chemical structure and displaying the same morphological features in blend with P(NDI2OD-T2) polymer, CBzBI shows a very poor doping efficiency with respect to PThBI and IStBI. A possible explanation of the three derivatives different efficacy is the different position of their Singly Occupied Molecular Orbitals. Shallower SOMO levels have indeed been reported to improve doping efficiencies of

benzimidazoline based derivatives.[15] A computational study by Wang's group shows that the ionization energy of the benzimidazoline radicals (the results of the heterolytic cleavage process) represents the driving force for the doping reaction. The same holds true even in the case of a doping mechanism mediated by hydride transfer.[49] The SOMO levels of CBzBI, PThBI and IStBI are of -2.90, -2.82 and -2.63 eV respectively, according to our electrochemical characterization. The values are perfectly in line with the electrical performances obtained for the three derivatives and the corresponding efficiency of charge injection detected via optical characterization. This consideration suggests then that, in the research for more efficient benzimidazoline-based n-type dopants, the best candidates are those having both the right affinity and compatibility with the semiconductor and a high SOMO energy level.

The same consideration might explain in part the relatively poorer performances of AnDMBI with respect to N-DMBI-H, since its SOMO level (-2.67 eV) has a lower energy with respect to that of the parent dopant (-2.54 eV).

4.4.7 Thermoelectric properties of films doped with IStBI

As we mentioned in the first chapter, doping of organic semiconductors is critical for the development of efficient Organic Thermoelectric generators (OTEGs), requiring both p- and n- type materials with high conductivities[‡‡‡]. Since commercially available p-type materials achieving σ greater than 1000 Scm^{-1} through doping exist, the main bottleneck for the development of efficient OTEGs is the lack of n-type materials with comparable charge transport properties.[50] The research community is thus striving for the synthesis of both new n-type materials and more efficient n-type dopants capable of inducing the conductivity enhancements required to reach thermoelectric properties suitable for applications in devices.[3,12,50,51] IStBI is the most performing dopant we developed, we thus decided to explore its blends with P(NDI2OD-T2) in Organic Thermoelectric Generators. For the purpose, we prepared P(NDI2OD-T2) films doped with IStBI in a dopant concentration range between 20 and 50 mol%. We then characterized the blends thermoelectric properties by measuring the in-plane Seebeck coefficient (S) at room temperature using a custom-built setup.[52] Results are collected in **Figure 4.17**.

All the characterized samples show a negative S value as expected for n-type doped materials.[53] The S absolute values range from -129 ± 3 to -9.3 ± 0.8 μVK^{-1}. For doped organic semiconductors, charge transport can be described as thermally activated hopping between the Fermi energy (E_F) and the Transport energy (E_{tr}) levels. In such systems the Seebeck coefficient is proportional to the difference between these two levels and can be expressed as[50,54]

[‡‡‡] We recall that the thermoelectric properties of organic semiconductors are mainly associated to their power factor, which is defined as $PF=\sigma S^2$, where S is the Seebeck coefficient.

$$S = \frac{E_F - E_{tr}}{T}$$

The observed trend of the Seebeck coefficient as a function of increasing dopant concentration suggests then a progressive shift of the semiconductor Fermi level closer to the $E_{tr.}$[50] The results thus further confirms that the addition of IStBI efficiently increases the number of carriers in the semiconductor blend, as we previously observed through UV–vis spectroscopy. The highest power factor PF is achieved at a dopant concentration of 20 mol% and is estimated to be $(4.2 \pm 0.3) \times 10^{-3}$ $\mu Wm^{-1}K^{-2}$. This value is in line with that evaluated by other authors for P(NDI2OD-T2) polymer doped with benzimidazoline based dopants.[12] The PF measured for the sample containing 35% mol of IStBI is very close to the maximum recorded value, which confirms the validity of the σ maximization approach.

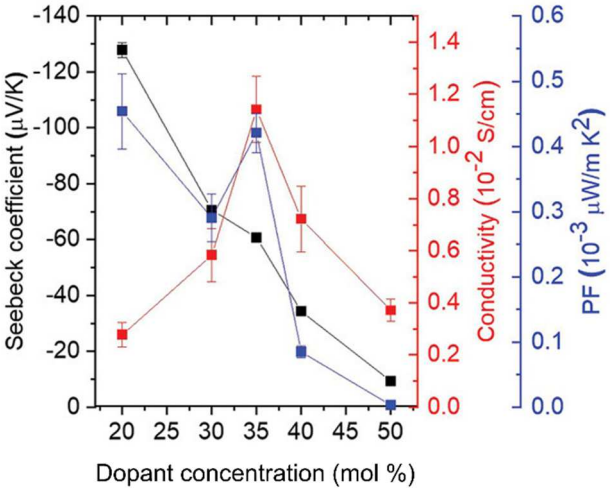

Figure 4.17 Seebeck coefficient (black line), electrical conductivity (red line), and power factor (blue line) of doped P(NDI2OD-T2) samples at increasing IStBI concentration (mol%), measured at room temperature. The blends were prepared with the same materials used for IStBI preliminary study. Adapted from reference 69.

For applications as power generator for low-power consumption sensors and electronics, a thermoelectric device should ideally deliver electrical powers > 1 μW over few cm^2 area and under small thermal gradient.[50,55] p-type organic semiconductors can reach power factors of tens $\mu Wm^{-1}K^{-2}$. The most promising n-type organic semiconductors materials for thermoelectric applications display power factors greater than 10 $\mu Wm^{-1}K^{-2}$.[7,50,56] The performances we obtained using P(NDI2OD-T2)/IStBI blends are still very limiting for a practical use in thermoelectric devices. This is mainly to attribute to the intrinsic limitations of P(NDI2OD-T2) in achieving sufficiently high conductivities, owing to the backbone torsion of this polymer structure leading to strongly localized charge carriers.[57] Nevertheless, recently, OTEGs reaching power output densities of tens of $nWcm^{-2}$ have been fabricated using materials with σ in the range of 1-2 S cm^{-1}, thanks to optimization of the device architecture.[55] Therefore, it cannot be excluded that, by combining further improvements on the doping process with the right device geometry optimization, the use of P(NDI2OD-T2) will allow to reach thermoelectric properties relevant for applications. Moreover, the remarkable doping properties shown by IStBI with P(NDI2OD-T2) suggest the possibility of exploiting this benzimidazoline-based dopant with other n-type organic semiconductors, not affected by the same intrinsic limitations of P(NDI2OD-T2).

4.4.8 Conclusions

In this work, we characterized the structure-property relationships of a series of original benzimidazoline derivatives bearing different molecular functionalization patterns with respect to the reference dopant N-DMBI-H. Via a combination of optical and electrical characterization of P(NDI2OD-T2) polymer/dopants blends, we showed that the introduced structural modifications highly impact the dopants efficacy. Our results reveal that the functionalization of N-DMBI-H aniline nitrogen with bulky substituents having extended π-conjugation can lead to striking performances enhancement. The introduction of aryl and alkyl substituents on the benzimidazole core makes instead the doping less effective.
Via AFM and GIWAXS analysis, we demonstrated a correlation between these dopants' efficiency and their solid-state interactions with the semiconductor host. The results of this morphological characterization reveal indeed that the thermal activation of N-DMBI-H derivatives competes with their thermally driven phase segregation from the semiconductor matrix and suggest that stronger compatibility between the dopant and the host can slow down this process, leading to higher doping efficiency. The hypothesis, in agreement with the observation of other groups, is well supported by computational studies. With a further comparison of the doping performances and the energy levels of the analysed derivatives, we also showed that, within dopants displaying similar affinity with the semiconductor, those having the shallowest SOMO levels are the most efficient.

Among all the characterized dopants, we presented an iminostilbene functionalized benzimidazoline derivative, IStBI, that shows promising doping performances. This compound combines a SOMO level close to that of N-DMBI-H with stronger interactions with the semiconductor backbones. Thanks to these features, the use of this dopant in blends with P(NDI2OD-T2) polymer allowed to achieve a maximum conductivity value of $(1.3 \pm 0.5) \times 10^{-2}$ Scm^{-1}, almost one order of magnitude higher with respect to those reported for the reference benzimidazoline derivatives. If not in combination with P(NDI2OD-T2) polymer, the remarkable doping efficacy shown by this dopant suggest its possible efficient use for thermoelectric applications as well.

On the overall, this work confirms that a tailored structural modification of benzimidazoline based dopants is an effective strategy to tune their doping efficiency. The obtained results also help in defining design guidelines for more performing N-DMBI-H based n-type dopants, directing the synthesis of new derivatives toward compounds bearing both strong interactions with the host and high SOMO energy levels.

4.5. Experimental methods

4.5.1. Synthetic procedures

Reagents were purchased from TCI, BLD pharm, Sigma-Aldrich and Fluorochem. Solvents were bought from Merck, Carlo-Erba and Acros, and used as received unless otherwise stated. Palladium catalysts were purchased from Apollo Scientific. Montmorillonite K-10 clay was purchased from Sigma-Aldrich and oven-dried at 130 °C for 24 hours before use. $MgSO_4$ powder used during dopant synthesis work-up was dried with the same procedure. $Na_2S_2O_4$ at 85% wt. was used for synthesis of 2-arylbenzimidazoles. Chromatographic purifications were performed using Davisil LC 60A silica gel (pore size 60 Å, 70-200 μm). Composition of solvent mixtures are indicated as volume/volume ratios. Melting points were determined using a Buchi M-560 apparatus. Microwave activated reaction were performed with a Discover-S CEM apparatus. Solution Nuclear Magnetic Resonance (NMR) spectra were acquired with a Bruker Avance 400 NEO Spectrometer. For ^{1}H and ^{13}C NMR of known derivatives, only chemical shifts are indicated. All NMR tubes of dopants were prepared and closed inside an argon filled glovebox to avoid compound oxidation during spectra acquisition.

4.5.1.1. Previously obtained aldehydes and 1,2-phenylendiamines

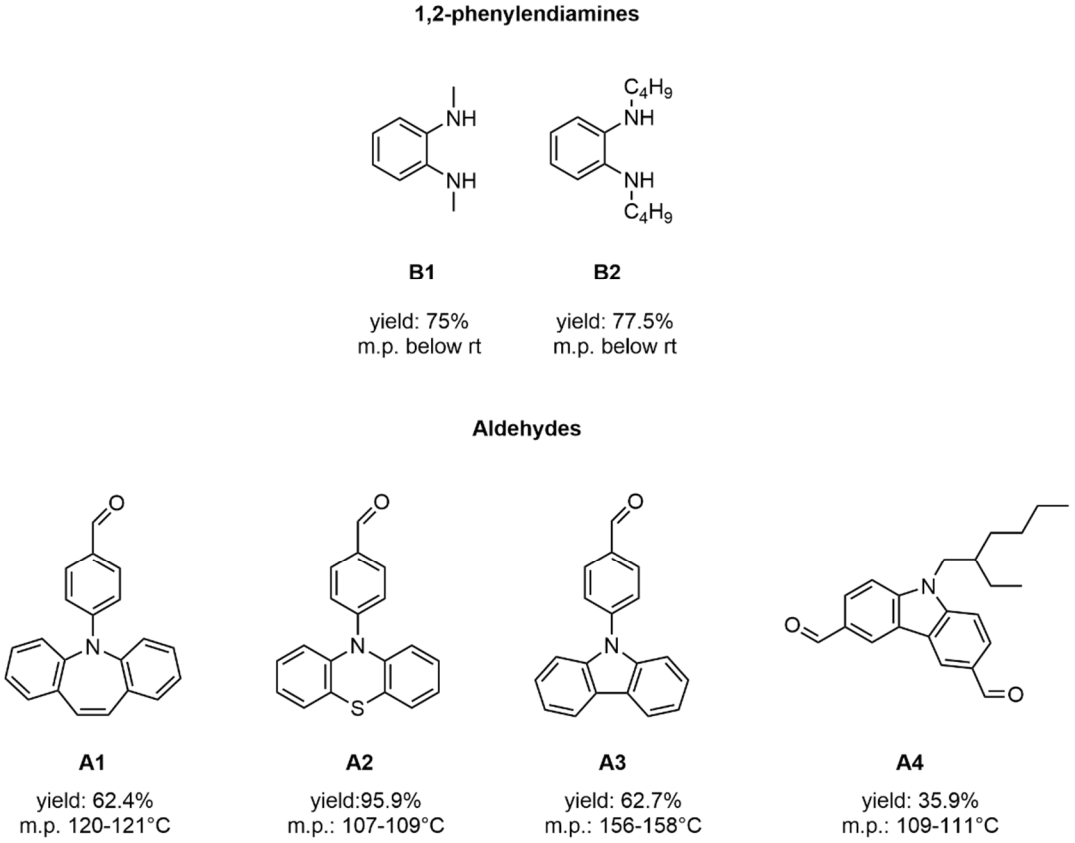

Figure 4.18 Aldehydes (**A1**-**A4**) and 1,2-phenylendiamines (**B1**,**B2**) used for the synthesis of N-DMBI-H derivatives and here reported with the relative melting point and reaction yield.

A library of aldehydes and 1,2-phenylendiamines were synthesized by previous members of our group to be used in the synthesis of benzimidazoline based dopants. The obtained derivatives are collected in **Figure 4.18,** together with their overall synthetic yield and the melting point (m.p.)**.**

A detailed description of the synthesis of these derivatives goes beyond the scope of this work and only the essential information will be thus given.
Derivative **A1**, **A2** and **A3** were synthesized via Buchwald-Hartwig amination on 4-bromobenzaldehyde adapting a procedure previously reported by our group,[58] while derivative **A4** was obtained via Vilsmeier-Haack reaction on commercial 9-(2-ethylhexyl)carbazole, followed by purification via column chromatography.

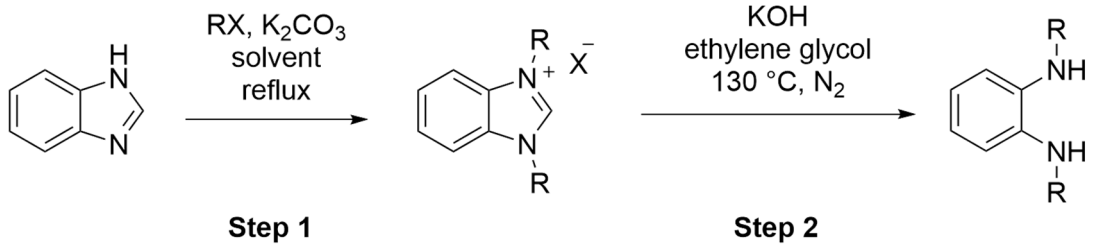

Scheme 4.8 synthetic route to derivatives **B1** and **B2**.

Derivative **B1** and **B2** were obtained according to the procedure reported in **scheme 4.8**. **B1** and **B2** benzimidazoles salt precursors were obtained starting from commercial benzimidazole via an alkylation reaction (**Step 1),** adapting a literature synthetic procedure by Roberts et al.[59] In the case of derivative **B1**, methyl iodide was used as alkylating agent in acetonitrile. 1-bromobutane was instead used for the synthesis of the precursor salt of derivative **B2.** The alkylation reaction was obtained in a two-step process in the case of **B2**, the first performed in acetonitrile (6h) and the second performed in toluene (26h). The following alkaline hydrolysis reaction (**Step 2)** was adapted from another literature procedure by Zimmer group[60] and allowed to obtain derivatives **B1** and **B2**.

4.5.1.2. Synthesis of 1,2-nitroamines (derivative D1)

1,2–nitroamine **D1** was synthetized according to the following synthetic procedure (**Scheme 4.9)**. Details on the procedure will be given in the next paragraph.

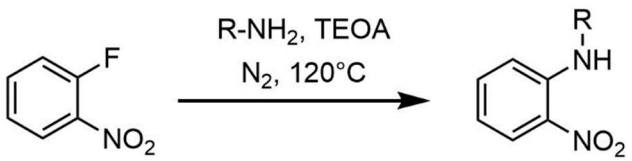

Scheme 4.9 Synthetic route for the preparation of 1,2-nitroamines.

Synthesis of derivative D1

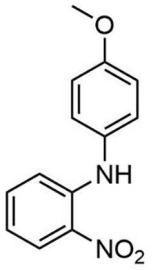

2-fluoronitrobenzene (4.000 g, 28.35 mmol) and p-anisidine (3.492 g, 28.36 mmol) are added to a 100 mL roundbottom flask and are put under nitrogen atmosphere. Triethanolamine (4.229 g, 28.35 mmol) is added, and the mixture is heated at 120 °C for 5 hours. The reaction is cooled down to room temperature, then water (30 mL) is added, and the mixture is acidified by addition of 5% HCl (final pH~2). After 2 hours stirring at room temperature, the mixture is filtered on a Büchner funnel. The collected solid is dried until weight stabilization. 5.930 g of pure product (24.28 mmol, 85.6% yield) are recovered as a red-purple powder. mp 88-90 °C.

^{1}H NMR (400 MHz, $CDCl_3$) δ[ppm] 9.40 (br, 1H), 8.19 (dd, J = 8.7, 1.5 Hz, 1H), 7.32 (ddd, J = 8.6, 7.0, 1.5 Hz, 1H), 7.20 (d, J = 8.9 Hz, 2H), 7.00 (dd, J = 8.7, 1.0 Hz, 1H), 6.96 (d, J = 8.9 Hz, 2H), 6.71 (ddd, J = 8.6, 7.0, 1.2 Hz, 1H), 3.84 (s, 3H)[61].

4.5.1.3. Synthesis of 2-arylbenzimidazoles (derivatives E1-6)

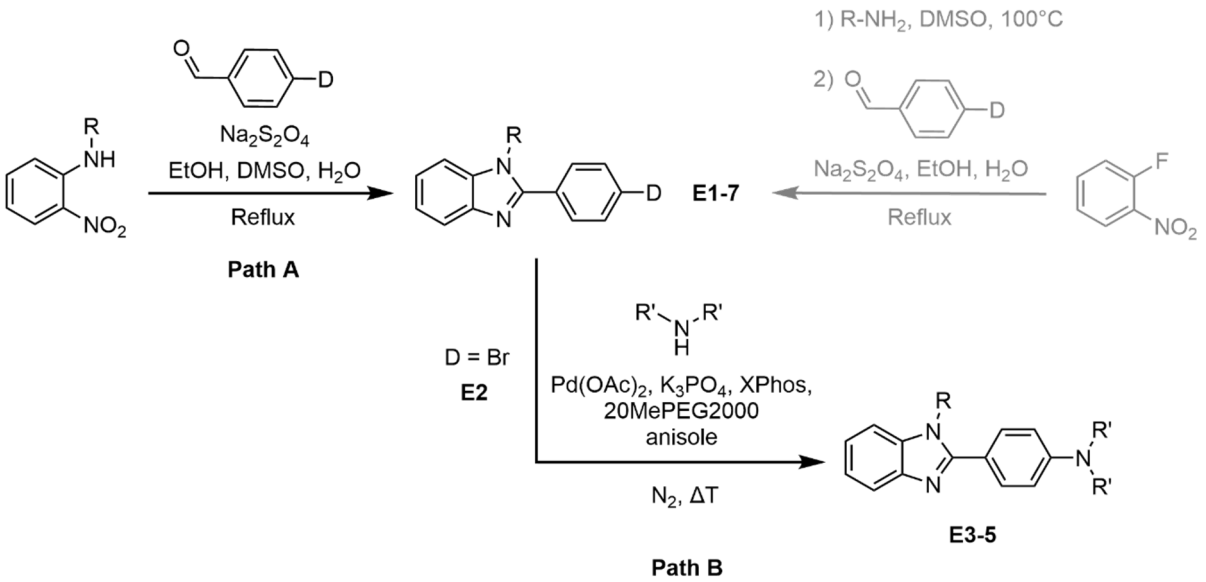

Scheme 4.10 Synthetic routes for the preparation of 2-arylbenzimidazoles.

2-arylbenzoimidazoles were synthetized according to the synthetic procedure reported in (**Scheme 4.10)**. Two different protocols were used to obtain the desired product: a direct reductive cyclization reaction between the required 1,2-nitroamine and aldehyde (**Path A**) or a Buchwald-Hartwig amination reaction on the as obtained **Derivative E2** (**Path B**).

General procedure for Path A

1,2-nitroamine (1 eq.), aldehyde (1 eq.) and $Na_2S_2O_4$ (85%, 2.7 eq.) are added to a round bottom flask. Ethanol, DMSO and water are added to the flask in 4:1:0.5 volume ratio. The mixture is put under reflux. After the reagents complete conversion is reached, the reaction is stopped and let cool down to room temperature. The crude is

moved to a beaker, 3% NH_3 solution is added (between 10 mL and 50 mL depending on the recation scale) and the mixture is let stirring for 30 minutes. The solid is filtered on a Hirsh funnel and washed with water. The recovered powder is then dried in vacuum at 65°C until weight stabilization.

In the case of derivative **E6**, it was possible to obtain the synthesis of the required 1,2-nitroamine and the following reductive cyclization step via a one pot reaction (see **Scheme 4.10,** gray path).

General procedure for Path B

Before the reaction beginning, anisole is carefully degassed by freeze-pump-thaw. In a 50 mL roundbottom flask, derivative **E2 (**1 eq.**)**, the required coupling partner (1.1 eq.), K_3PO_4 (1.5 eq.) and poly(ethylene glycol) dimethyl ether (MW = 2000, 9 wt. % with respect to the base) are put under N_2 atmosphere. In a second flask, $Pd(OAc)_2$ (0.01 eq.) and XPhos (0.02 eq.) are dissolved under N_2 atmosphere in 1.0 mL of anisole at 60 °C. The as obtained solution is transferred in the flask containing all the other reagents, and the mixture is heated at 125 °C. After reaching complete reagent conversion, the reaction is stopped and cooled down to room temperature. The crude is then purified with the required treatment.

Details on reagents, thermal treatments and solvent used will be given for each product in the next sections, together with reaction times, purification procedures and obtained yields or with any variation in the synthetic procedure.

Synthesis of derivative E1 via Path A

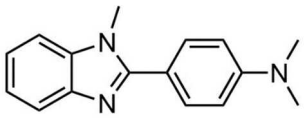

From N-methyl-2-nitroaniline (4.000 g, 25.29 mmol), 4-dimethylaminobenzaldehyde (3.775 g, 25.30 mmol) and $Na_2S_2O_4$ (85%, 13.989 g, 68.294 mmol) in Ethanol (20 mL) and DMSO (5 mL). 5 mL of DMSO are added after 24 hours of reaction. Overall reaction time: 48 hours. Product obtained as off-white solid (6.289 g, 25.02 mmol, 98.9% yield). mp 144-156 °C.

^{1}H NMR (400 MHz, $CDCl_3$) δ[ppm] 7.83-7.77 (m, 1H), 7.68 (d, J= 8.9 Hz, 2H), 7.38-7.31 (m, 1H), 7.31-7.24 (m, 2H), 6.80 (d, J = 8.9 Hz, 2H), 3.86 (s, 3H), 3.04 (s, 6H)[62].

Note: on this small scale, the amount of water naturally present in EtOH and DMSO was enough to bring the reaction to completion.

Synthesis of derivative E2 via Path A

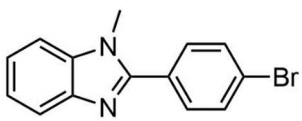

From N-methyl-2-nitroaniline (4.000 g, 25.29 mmol), 4-bromobenzaldehyde (4.681 g, 25.30 mmol) and $Na_2S_2O_4$ (85%, 13.989 g, 68.294 mmol), in ethanol (20 mL) and DMSO (5 mL). A yellow precipitate forms during the reaction. Overall reaction time: 7 hours. Product obtained as off-white solid (7.116 g, 24.78 mmol, 98.0% yield). mp 108-111 °C.

^{1}H NMR (400 MHz, $CDCl_3$) δ[ppm] 7.85-7.79 (m, 1H), 7.70-7.62 (m, 4H), 7.43-7.29 (m,3H), 3.86 (s, 3H)[63].

Note: on this small scale, the amount of water naturally present in EtOH and DMSO was enough to bring the reaction to completion.

Synthesis of derivative E3 via Path A

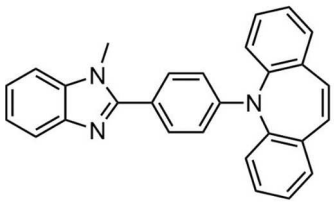

From N-methyl-2-nitroaniline (158 mg, 1.00 mmol), derivative **A1** (297 mg, 1.00 mmol), and $Na_2S_2O_4$ (85%, 615 mg, 3.00 mmol) in ethanol (4 mL), water (0.1 mL) and DMSO (1 mL). A yellow precipitate forms. Overall reaction time: 7 hours. Product is obtained as off-white solid (318 g, 0.796 mmol, 79.6% yield). mp 240-242 °C.

^{1}H NMR (400 MHz, DMSO−d_6): δ[ppm] 7.65-7.57 (m, 7H), 7.54-7.47 (m, 5H), 7.24-7.16 (m, 2H), 6.99 (s, 2H), 6.28 (d, J = 9.0 Hz, 2H), 3.78 (s, 3H).

^{13}C{^{1}H} NMR (100 MHz, DMSO−d_6): δ[ppm] 153.33, 149.39, 142.52, 141.76, 136.60, 135.74, 130.61, 130.41, 130.21, 129.93, 129.90, 127.67, 121.72, 121.59, 119.43, 118.46, 111.07, 110.14, 31.67.

Synthesis of derivative E3 via Path B

From derivative **E2** (1,000 g, 3.482 mmol), iminostilbene (740 mg, 3.83 mmol), K_3PO_4 (1.119 g, 5.223 mmol) and poly(ethylene glycol) dimethyl ether (MW = 2000, 150 mg), $Pd(OAc)_2$ (7.82 mg, 0.0348 mmol) and XPhos (33.2 mg, 0.0696 mmol). 1.5 mL of anisole are in this case added to the flask.
Overall reaction time: 6.5 hours. After cooling down to room temperature, 30 mL of water are added to the flask and the mixture is acidified by addition of citric acid. The solid is filtered on a Hirsh funnel, and subsequently refluxed in 50 mL of EtOH. The solid is filtered, then refluxed in 2 mL of Et_2O, and filtered again. The obtained off-white solid is dried in vacuum at 65 °C until weight stabilization (720 g, 1.802 mmol, 51.8% yield).

Synthesis of derivative E4 via Path A

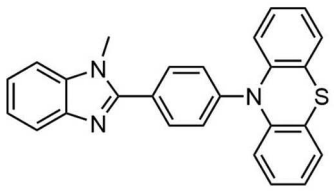

From N-methyl-2-nitroaniline (161 mg, 1.02 mmol), derivative **A2** (302 mg, 0.995 mmol), and $Na_2S_2O_4$ (85%, 547 mg, 2.67 mmol) in ethanol (4 mL), water (0.5 mL) and DMSO (1 mL). Further 0.5 mL of water are added to the flask after 1 hour of reaction time. A yellow precipitate forms during the reaction. Reaction progress is monitored via TLC using a mixture of Heptane/AcOEt 7:3 as eluent. Overall reaction time: 3 hours.
After filtration on Hirsh funnel, the powder obtained is taken up with methanol (5 mL) and filtered again. The yellowish solid is dried in vacuum at 65 °C until weight stabi-

lization (242 g, 0.597 mmol, 60.0% yield). mp 207-215 °C (darkening followed by fusion).

^{1}H NMR (400 MHz, DMSO−d_6): δ[ppm] 8.06 (d, J = 8.5 Hz, 2H), 7.70 (d, J = 7.4, Hz, 1H), 7.64 (d, J = 7.4 Hz, 1H), 7.51 (d, J = 8.4 Hz, 2H), 7.36 - 7.26 (m, 2H), 7.23 (d, J = 7.7 Hz, 2H), 7.10 (t, J = 7.7 Hz, 2H), 7.00 (t, J = 7.4 Hz, 2H), 6.95 (d, J = 8.0 Hz, 2H), 3.96 (s, 3H).

^{13}C{^{1}H} NMR (100 MHz, DMSO−d_6): δ[ppm] 152.32, 142.87, 142.60,142.50, 136.68, 131.60, 128.40, 127.49, 127.23, 127.14, 123.74, 122.63, 122.43, 121.99, 119.01, 118.71, 110.61, 31.81.

Synthesis of derivative E4 via Path B

From derivative **E2** (745 mg, 2.59 mmol), phenothiazine (659 mg, 3.31 mmol), K_3PO_4 (858 mg, 4.04 mmol), poly(ethylene glycol) dimethyl ether (MW = 2000, 71 mg), $Pd(OAc)_2$ (5.86 mg, 0.0261 mmol) and XPhos (25.0 mg, 0.0524 mmol). In this case, the mixture is heated at 135 °C. 0.5 mL of anisole are then added, and the mixture is kept at 135 °C for 7 h, and subsequently temperature is raised to 150 °C for 2 h. Overall reaction time: 9 hours. 50 mL of water are added and the mixture is acidified by addition of citric acid. The as obtained suspension is filtered on a Hirsh funnel, and the recovered solid is subsequently refluxed in 10 mL of AcOEt and filtered again. The obtained off-white solid is dried in vacuum at 65 °C until weight stabilization (503 g, 1.24 mmol, 47.9% yield).

Synthesis of derivative E5 via Path A

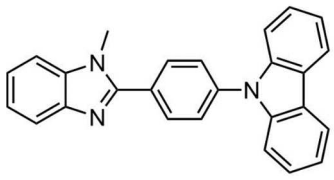

From N-methyl-2-nitroaniline (152 mg, 1.00 mmol), derivative **A3** (272 mg, 1.00 mmol), $Na_2S_2O_4$ (85%, 557 mg, 2.72 mmol) in H_2O (0.10 mL) and ethanol (1.19 mL). A yellow precipitate forms during the reaction. The reaction is monitored via TLC using dichloromethane as eluent. Overall reaction time: 21 hours. After filtration on a Hirsh funnel, the product is extracted from the obtained solid using isopropanol (10 mL). The isopropanol is evaporated under reduced pressure to give the product as a grey powder, which is then dried under vacuum at 65 °C until weight stabilization (90 mg, 0.241 mmol, 24.1 % yield). mp 174-176 °C, darkening followed by fusion.

^{1}H NMR (400 MHz, DMSO-d_6): δ[ppm] 8.29 (d, J = 7.7 Hz, 2H), 8.17 (d, J=8.4 Hz, 2H), 7.86 (d, J = 8.4 Hz, 2H), 7.74 (d, J = 7.6 Hz, 1H), 7.67 (d, J = 7.8 Hz, 1H), 7.55 (d, J = 8.2 Hz, 2H), 7.51-7.45 (m, 2H), 7.38-7.25 (m, 4H), 4.02 (s, 3H)[62].

Synthesis of derivative E5 via Path B

From derivative **E2** (800 mg, 2.78 mmol), carbazole (513 mg, 3.06 mmol), K_3PO_4 (887 mg, 4.18 mmol), poly(ethylene glycol) dimethyl ether (MW = 2000, 80 mg), $Pd(OAc)_2$

(6.20 mg, 0.0278 mmol) and XPhos (26.5 mg, 0.0557 mmol). The reaction progress is monitored via TLC using a mixture of heptane/AcOEt 8:2. Overall reaction time: 2 hours. The residual solvent is evaporated under reduced pressure. 25 mL of water are added to the crude and the mixture is acidified by addition of citric acid. After 30 minutes of sonication in an ultrasonic bath, the suspension is filtered on a Hirsh funnel. The recovered solid is suspended again in ethanol, sonicated in an ultrasonic bath and the suspension is again filtered to give a beige solid which is dried in vacuum at 65°C until weight stabilization (710 mg, 1.90 mmol, 68.3% yield).

Synthesis of derivative E6

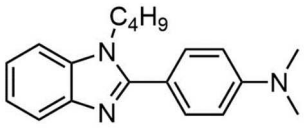

Derivative **E6** was obtained performing the synthesizing of 2-butyl-1-nitrobenzene and the following reductive cyclization reaction with 4-dimethylamminobenzaldehyde one-pot.

In a 2 neck 100 mL roundbottom flask, 2-fluoronitrobenzene (2.137 g, 15.14 mmol), and butylamine (1.153 g, 15.76 mmol) are added, followed by DMSO (4 mL). The mixture is heated at 100°C for 1 hour to reach complete conversion. The reaction is then let cool down to room temperature. 4-dimethylaminobenzaldehyde (2.248 g, 15.07 mmol) is dissolved in ethanol (16 mL) and the as obtained solution is added to the reaction, followed by $Na_2S_2O_4$ (7.875 g, 45.23 mmol) and water (0.5 mL). The reaction is heated under reflux and a yellow suspension forms. The reaction progress is monitored via TLC using a mixture of heptane/acetate 1:1 as eluent. After 17 hours conversion of the reagents is complete and the reaction is stopped. The mixture is moved in a 250 mL beaker and 70 mL of a 3% NH_3 solution are added. The mixture is let stirring for 30 minutes. A waxy solid separates from the aqueous phase. The solid is recovered via filtration and is redispersed in a AcOEt/heptane 1:1 mixture. A suspension of a white solid is obtained and filtered on a Hirsh funnel to give a first product fraction. The residual solvent is evaporated under reduced pressure and the obtained solid is redispersed in 4 mL of Et_2O. The dispersion is let resting at -18 °C for 15 hours and the solid is recovered by filtration. The obtained powder is refluxed in a 5% NH_3 solution for 15 minutes, and the dispersion is let cooling down to room temperature. The white solid is recovered via filtration to give a second product fraction. Both fractions are dried in vacuum at 65°C until weight stabilization to afford 3.000 g of product (10.23 mmol, 67.9% yield). mp 80-82 °C.

^{1}H NMR (400 MHz, $CDCl_3$): δ[ppm] 7.86-7.77 (m, 1H), 7.64 (d, J = 8.9 Hz, 2H), 7.42-7.35 (m, 1H), 7.31-7.24 (m, 2H), 6.81 (d, J = 8.9 Hz, 2H), 4.24 (t, J = 7.7 Hz, 2H), 3.04 (s, 6H), 1.85 (qnt, J = 7.7 Hz, 2H), 1.34 (sex, J = 7.4 Hz, 2H), 0.91 (t, J = 7.40, 3H).

^{13}C{^{1}H} NMR (100 MHz, $CDCl_3$): δ[ppm] 154.69, 151.22, 143.44, 135.97, 130.38, 122.05, 119.60, 118.02, 111.94, 109.92, 44.75, 40.38, 32.04, 20.20, 13.79.

Synthesis of derivative E7

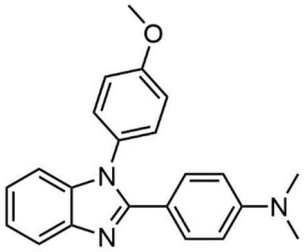

From derivative **D1** (2.000 g, 8.188 mmol), 4-dimethylaminobenzaldehyde (1.222 g, 8.190 mmol) and $Na_2S_2O_4$ (85%, 4.530 g, 22.11 mmol) in ethanol (10 mL) and DMSO (2.5 mL). A precipitate forms during the reaction. Overall reaction time: 3 hours.
Product is obtained as a white solid (2.574 g, 7.494 mmol, 91.5% yield). mp 158-160 °C.

^{1}H NMR (400 MHz, DMSO-d_6): δ [ppm] 7.68 (d, J = 7.6 Hz, 1H), 7.38 (d, J = 9.1 Hz, 2H), 7.34 (d, J = 8.9 Hz, 2H), 7.23 (td, J = 7.5 Hz, 1.2 Hz, 1H), 7.17 (td, J = 7.6, 1.2 Hz, 1H), 7.12 (d, J=8.9 Hz, 2H), 7.04 (d, J = 7.9 Hz, 1H), 6.64 (d, J = 9.1 Hz, 2H), 3.85 (s, 3H), 2.92 (s, 6H).

^{13}C{^{1}H} NMR (100 MHz, DMSO-d_6): δ [ppm] 150.07, 152.67, 150.69, 142.63, 137.64, 129.85, 129.63, 128.83, 122.24, 122.16, 118.51, 116.61, 115.14, 111.30, 109.94, 55.44, 39.65.

4.5.1.4. Synthesis of 2-aryl benzimidazolium salts (derivatives F1-7)

Alkylation of 2-arylbenzoimidazoles to obtain the dopants 2-aryl benzimidazolium salts precursors (derivatives **F1-7**) was performed according to the reaction reported in **Scheme 4.11.** Various alkylating agents and solvents were used, depending on the reactivity of the substrates and on the solubility of reagents and obtained products.

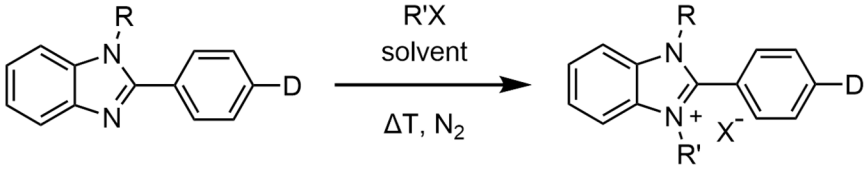

Scheme 4.11 General synthetic procedure for the preparation of 2-aryl benzimidazolium salts.

Synthesis of derivative F1 (tosylate salt)

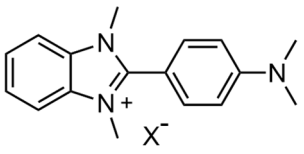

Derivative **E1** (1.000 g, 3.98 mmol) and methyl p-toluenesulfonate (1.111 g, 5.967 mmol) are added to a two neck, 100 mL roundbottom flask, provided with a calcium chloride trap. Acetonitrile (5 mL) is added. A suspension forms and the reaction is stirred under reflux for 24 hours. The reaction is let cool down to room temperature. 10 mL of Et_2O are added to the flask and the mixture is let stirring for 24 hours obtaining a suspension. The solid is recovered by filtration on a Hirsh funnel and washed with Et_2O. The obtained solid is purified via crystallization in deionized water saturated with sodium p-toluenesulfonate (5 mL). The as obtained white crystals are

filtered on a Hirsh funnel and dried in vacuum until weight stabilization. 461 mg of white powder are obtained, but presence of residual reagent lowers the purity to 66%.

Synthesis of derivative F1 (triflate salt)

Derivative **E1** (307 mg, 1.22 mmol) is added to a two neck, 50 mL roundbottom flask. The system is put under N_2. Anhydrous toluene (18 mL) is added. A yellow suspension forms. A first aliquot of methyl triflate (197 mg, 1.46 mmol) is added to the flask and the reaction is stirred at room temperature. A white precipitate forms. After 2 hours a second aliquot of methyl triflate (145 mg, 0.883 mmol) is added to the flask. The reaction is stopped after an overall time of 3 hours. The solid is recovered by filtration on a Hirsh funnel and dried under vacuum at 65°C until weight stabilization. 401 mg of a white powder are obtained, but presence of residual reagent lowers the purity to 80%.

Synthesis of derivative F2 (iodide salt)

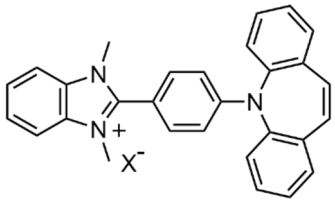

Derivative **E3** (193 mg, 0.483 mmol) is added to a two neck, 50 mL roundbottom flask. The system is put under N_2 and anhydrous acetonitrile (5 mL) is added. A white suspension forms. Methyl iodide (82.29 mg, 0.580 mmol) is added to the flask and the reaction is refluxed to obtain a solution. The reaction is stopped after 5 hours and let cool down to room temperature. A fraction of the product crystallizes in brownish crystals which are filtered on a Hirsh funnel. The recovered acetonitrile is then evaporated under reduced pressure and the obtained solid is redispersed in toluene and subsequently filtered. Both solid fractions are collected and dried under vacuum at 65 °C to give 210 mg of product as brownish solid (0.388 mmol, 80.3 % yield). mp: 260-301 (darkening followed by fusion).

^{1}H NMR (400 MHz, DMSO−d_6): δ[ppm] 8.03 (dd, J = 6.2, 3.1 Hz, 2H), 7.68 (dd, J =6.2, 3.1 Hz, 2H), 7.67-7.61 (m, 6H), 7.57-7.49 (m, 4H), 7.03 (s, 2H), 6.42 (d, J = 9.1 Hz, 2H), 3.84 (s, 6H).

^{13}C{^{1}H} NMR (100 MHz, DMSO-d_6): δ[ppm] 151.48, 150.89, 140.76, 135.33, 131.96, 131.69, 130.64, 130.37, 129.40, 128.02, 126.27, 113.04, 111.25, 108.79, 32.83.

Synthesis of derivative F2 (triflate salt)

Derivative **F2** was synthesized as triflate salt for electrochemical characterization. In a two neck 50 mL roundbottom flask, derivative **E3** (209 mg, 0.523 mmol) is added and the system is put under N_2 atmosphere. Anhydrous acetonitrile (10 mL) is added to the flask to obtain a suspension. Methyl triflate (113 mg, 0.689 mmol) is then added to the mixture and a solution is obtained. The reaction is stopped after 1 hour and 30 minutes. The solvent is evaporated under reduced pressure and the obtained solid is

redispersed in toluene and filtered and then redispersed in water and filtered again. The obtain off-white powder is then dried under vacuum at 65 °C until weight stabilization (261 mg, 0.463 mmol, 88.5 % yield). mp: darkening from T >210 °C followed by fusion in the interval 230-237 °C.

^{1}H and ^{13}C NMR spectra are the same of derivative **F2** obtained as iodide salt.

^{19}F NMR (400 MHz, DMSO-d_6): δ - 77.74 ppm.

Synthesis of derivative F3 (iodide salt)

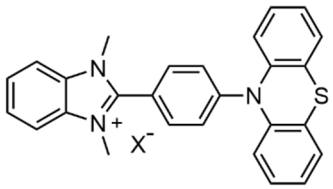

Derivative **E4** (240 mg, 0.592 mmol) is added to a 2 neck, 50 mL roundbottom flask. The system is put under N_2 and anhydrous acetonitrile (5 mL) is added, followed by methyl iodide (161.3 mg, 1.136 mmol). The reaction is refluxed and a yellow precipitate forms. After 23 hours, the reaction is stopped and the precipitate is filtered on a Hirsh funnel and washed with toluene. The recovered solution is evaporated under reduced pressure to obtain a second solid fraction which is redispersed in toluene and then filtered on a Hirsh funnel. Both solid fractions are recovered and dried under vacuum at 65 °C to afford the product as a yellowish powder (275 mg, 0.502 mmol, 84.7% yield). mp: darkening at T > 260 °C followed by fusion at 288-301 °C.

^{1}H NMR (400 MHz, DMSO−d_6): δ[ppm] 8.10 (dd, J = 6.2, 3.1 Hz, 2H), 7.84 (d, J = 8.8 Hz, 2H), 7.74 (dd, J = 6.2, 3.1 Hz, 2H), 7.52 (dd, J = 7.8, 1.2 Hz, 2H), 7.42-7.34 (m, 4H), 7.33-7.22 (m, 4H), 3.92 (s, 6H).

^{13}C{^{1}H} NMR (100 MHz, DMSO−d_6): δ[ppm] 150.31, 147.71, 140.96, 132.77, 131.76, 129.76, 128.44, 127.83, 126.50, 125.96, 124.54, 119.00, 114.33, 113.25, 32.8.

Synthesis of derivative F3 (triflate salt)

Derivative **F3** was synthesized as triflate salt for electrochemical characterization. Derivative **E4** (251 mg, 0.616 mmol) is added to a 2 neck, 50 mL roundbottom flask. The system is put under N_2 atmosphere and anhydrous acetonitrile (10 mL) is added, followed by methyl triflate (161.3 mg, 0.676 mmol). The obtained solution is left stirring at room temperature. A precipitate forms. After 3 hours the reaction is stopped and quenched with 0.3 mL of methanol and the suspension is filtered on a Hirsh funnel. The recovered solvent is evaporated under reduced pressure and the obtained solid is taken up with 5 mL of a 4:1 mixture of methanol and toluene, filtered and then redispersed in 5 mL of toluene and filtered again. Both solid fractions are then dried under vacuum at 65 °C to afford the product as a gray powder (241 mg, 0.423 mmol, 68.7% yield). mp 260-268 °C (darkening followed by fusion).

^{1}H and ^{13}C NMR spectra are the same of derivative **F3** obtained as iodide salt.

^{19}F NMR (400 MHz, DMSO-d_6): δ - 77.82 ppm.

Synthesis of derivative F4

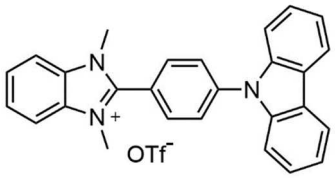

Derivative **F4** was synthesized as triflate salt and used both as reagent for following reaction steps and for electrochemical characterization. Derivative **E5** (314 mg, 0.840 mmol) is added to a 2 neck, 100 mL roundbottom flask. The system is put under N_2 and anhydrous acetonitrile (20 mL) is added, followed by methyl triflate (300 mg, 1.83 mmol). The obtained solution is left stirring at room temperature and is stopped after 2 hours by quenching with 1 mL of ethanol. The solvent is evaporated under reduced pressure. The obtained solid is taken up with toluene and is filtered on a Hirsh funnel, then is again taken up with water and filtered. The obtained grey powder is dried under vacuum at 65 °C (408 mg, 0.759 mmol, 90.3 % yield). mp: 272-291 °C (darkening followed by fusion).

^{1}H NMR (400 MHz, DMSO−d_6): δ[ppm] 8.31 (d, J = 7.8 Hz, 2H), 8.22-8.15 (m, 4H), 8.10 (d, J = 8.6 Hz, 2H), 7.80 (dd, J = 6.2, 3.1 Hz, 2H), 7.64 (d, J = 8.24, 2H), 7.56-7.47 (m, 2H), 7.41-7.33 (m, 2H), 4.04 (s, 6H).

^{13}C{^{1}H} NMR (100 MHz, DMSO−d6): δ[ppm] 149.84, 140.90, 139.58, 132.90, 131.84, 127.22, 126.71, 126.45, 123.20, 120.78, 120.69, 119.38, 113.43, 109.89, 32.90.

^{19}F NMR (400 MHz, DMSO-d_6): δ – 77.72 ppm.

Synthesis of derivative F5

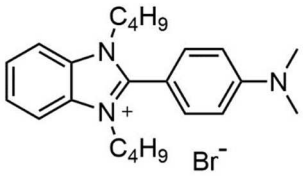

In a 2 neck 50 mL roundbottom flask, derivative **E6** (2.000g, 6.816 mmol) is added and the system is put under N_2. 1-bromobutane (1.168 g, 8.52 mmol) is added and the mixture is heated at 90°C, obtaining a homogeneous solution. The mixture is left stirring and a precipitate forms. After 3 hours and 45 minutes, 6 mL of toluene are added to the mixture, which is left stirring for 1 more hour. The reaction is then stopped and let cool down to room temperature. The obtained white precipitate is filtered on a Hirsh funnel and washed with Et_2O. The obtained solid is dried in vacuum and then purified via crystallization in anisole (7 mL). The obtained product is filtered, washed with Et_2O and toluene and dried in vacuum at 65°C until weight stabilization (2.080 g, 4.832 mmol, 70.9% yield). mp 223-225 °C.

^{1}H NMR (400 MHz, $CDCl_3$): δ[ppm] 7.88 (dd, J = 6.3, 3.1 Hz, 2H), 7.64 (dd, J = 6.2, 3.1 Hz, 2H), 7.60 (d, J = 8.9 Hz, 2H), 6.92 (d, J = 8.9, 2H), 4.46 (t, J = 7.6 Hz, 4H), 3.12 (s, 6H), 1.80 (qnt, J = 7.6 Hz, 4H), 1.26 (sex, J = 7.5 Hz, 4H), 0.83 (t, J = 7.4 Hz, 6H).

^{13}C{^{1}H} NMR (100 MHz, $CDCl_3$): δ[ppm] 152.71, 151.43, 131.47, 131.38, 127.48, 127.21, 113.71, 112.86, 46.92, 40.50, 31.44, 19.94, 13.59.

Synthesis of derivative F6

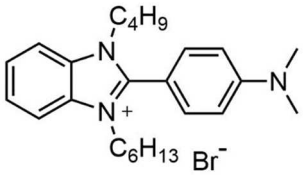

In a 2 neck 50 mL roundbottom flask, derivative **E6 (**1.200 **g,** 4.082 mmol**)** is added and the system is put under N_2 atmosphere. 1-bromohexhane (742.6 g, 4.498 mmol) is added to the flask and the mixture is heated at 110 °C. After 1 hour, 1 mL of toluene is added. After 4 hours, the reaction is stopped and let cool down to room temperature. Toluene (8 mL) is added and a white solid precipitate. The solid is filtered and washed with toluene and Et_2O. The filtrated solid is deliquescent. The recovered product is refluxed in AcOEt. The as obtained suspension is let cool down and the solid is filtered. The procedure is repeated once more. The recovered solid is dried under vacuum at 65°C to afford 1.422g of product (3.101 mmol, 76.0% yield). mp 134-137 °C.

^{1}H NMR (400 MHz, $CDCl_3$): δ[ppm] 7.93-7.83 (m, 2H), 7.68-7.62 (m, 2H), 7.60 (d, J = 8.9 Hz, 2H), 6.97 (d, J = 8.7 Hz, 2H), 4.51-4.40 (m, 4H), 3.13 (s, 6H), 1.86-1.73 (m, 4H), 1.32-1.09 (m, 8H), 0.83 (t, J = 7.3 Hz, 3H), 0.80 (t, J = 7.0 Hz, 3H).

^{13}C{^{1}H} NMR (100 MHz, $CDCl_3$): δ[ppm] 152.63, 151.33, 131.39, 127.23, 113.74, 113.60, 112.94, 47.00, 46.87, 40.53, 31.42, 31.05, 29.34, 26.27, 22.45, 19.92, 14.01, 13.59.

Synthesis of derivative F7

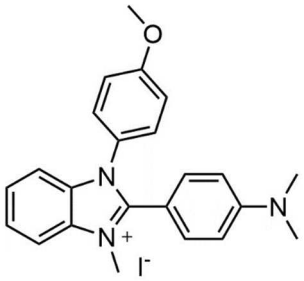

Derivative **E7** is added to a two neck, 100 mL roundbottom flask. The system is put under N_2 and the solvent is added. The mixture is heated up under reflux and a solution forms. Methyl iodide is then added. The mixture is kept stirring and the reaction progress is monitored via TLC using a mixture of heptane/AcOEt 7:3 as eluent. A white precipitate forms. After complete conversion, the reaction is stopped.

The reaction is repeated twice.

Test	E7	MeI	Solvent	Time
1	6.000 g (17.47 mmol)	2.727 g (19.22 mmol)	MeCN (20 mL)	5 h
2	2.000 g (5.823 mmol)	0.970 g (6.834 mml)	AcOEt (50 mL)	12 h

Work-up test 1: the precipitate is filtered on a Hirsh funnel. Acetonitrile is evaporated from the filtered solution under reduced pressure, to give a second powder fraction. This second solid fraction is refluxed in AcOEt for 30 minutes and then filtered again. The obtained solid (5.402 g) is purified via crystallization in n-pentanol (20 mL) to give the product as a white solid, which is then dried under vacuum at 65 °C (4.600 g, 9.477 mmol, 54.2 % yield)

Work-up test 2: the precipitate is filtered on a Hirsh funnel and washed with 20 mL of AcOEt. The collected solid is dried under vacuum at 65 °C to afford 2.081 g of product as a white powder (4.309 mmol, 74.0% yield). mp: 260-301 (darkening followed by fusion).

^{1}H NMR (400 MHz, DMSO−d_6): 8.17 (d, J=8.2 Hz, 1H), 7.75 (t, J = 7.8 HZ, 1H), 7,65 (t, J = 7.8 Hz, 1H), 7.49 (d, J = 9.0 Hz, 2H), 7.45-7.39 (m, 1H), 7.43 (d, J = 9.1 Hz, 2H), 7.14 (d, J = 9.0 Hz, 2H), 6.78 (d, J = 9.1 Hz, 2H), 4.02 (s, 3H), 3.82 (s, 3H), 2.99 (s, 6H).

^{13}C{^{1}H} NMR (100 MHz, DMSO−d_6): 160.11, 152.13, 151.77, 132.78, 132.22, 131.81, 129.01, 126.82, 126.39, 125.71, 115.25, 113.33, 112.64, 111.17, 105.86, 55.61, 39.49, 33.11.

4.5.1.5. Synthesis of dopants (derivatives C1-9)

Benzoimidazoline based dopants were synthetized either via acid catalysed condensation reaction (here described as **Route A**) or via reduction of the corresponding 2-aryl benzoimidazolium salts (here described as **Route B**).The reaction pathway for the two routes is reported in **Scheme 4.12.**

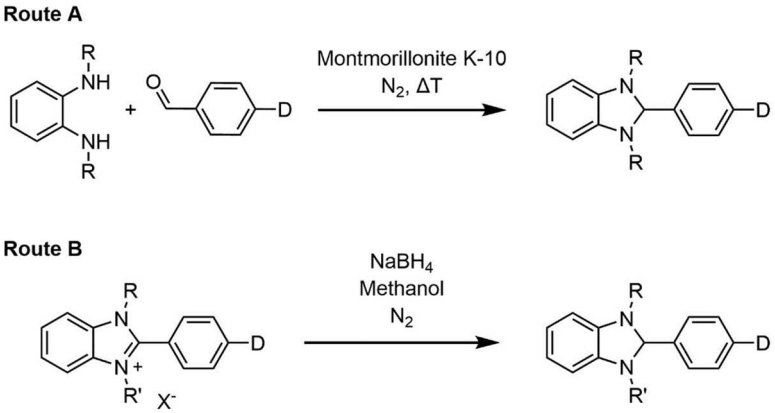

Scheme 4.12 Acid catalyzed condensation reaction pathway (Route A) and reduction reaction step for the preparation of DMBI based dopants.

General procedure for Route A

The reaction mixture is prepared inside a glove box, under argon atmosphere. All purification steps are performed in the dark. In a typical procedure, diamine, aldehyde, and Montmorillonite clay K10 are added to a 10 mL microwave vessel. The mixture is put under magnetic stirring, in the dark, and heated at the required temperature observing formation of a yellow mud (when indicated, heating was obtained by using microwaves MW). Every 30 minutes/1 hour of time, the reaction is let cool down to room temperature and the test tube is opened to remove condensed water from the vessel walls and to monitor the reaction progress via TLC using the appropriate eluent. After this procedure the reaction is always put under N_2 atmosphere before being heated up again. Once complete conversion is reached, the crude is taken up with

toluene (10-15 mL) and product extraction is helped with the use of an ultrasonic bath. The obtained suspension is filtered on a Teflon 0.45 μm syringe filter and the recovered solvent is evaporated under reduced pressure. The obtained solid is diluted with 5 mL of toluene and is filtered on a pad of silica using the appropriate eluent. Fractions containing the product are collected and the solvent is evaporated under reduced pressure to afford the product, which is then dried under vacuum.

Derivatives **C1-6** were synthesized using aldehyde and diamine in 1:1 molar ratio, while a 1:2.2 molar ratio was used for derivatives **C7** and **C8.** In the case of derivative **C2**, **C6** and **C8**, different reaction work-up were used and are deeply described in the section dedicated to the synthesis of these derivatives.

General procedure for Route B

In a 50 ml round bottom flask, 2-aryl benzimidazolium salt is added followed by methanol. The flask is placed at 0 °C in an ice bath and $NaBH_4$ is slowly added. The reaction is stopped after complete conversion.

Reactions are worked-up according to one of the following procedure.

Work-up A: a precipitate forms during the reaction; the precipitate is filtered on an Hirsh funnel and then dried under vacuum.

Work-up B: the product is soluble in methanol; methanol is evaporated under reduced pressure. The product is extracted with the appropriate solvent under N_2 atmosphere and the obtained solution is dried on $MgSO_4$, keeping the system under N_2. The organic phase is then recovered and filtered on a 0.45 μm syringe filter and the solvent is evaporated under reduced pressure. The obtained solid is dried under vacuum to afford the product.

Whichever the preparation procedure, the obtained product is stored under argon atmosphere at 4 °C to avoid oxidation from atmosphere. Details on reagents, thermal treatments and solvent used will be given for single in the next sections, together with reaction times and obtained yields.

Synthesis of derivative C1 (N-DMBI-H)

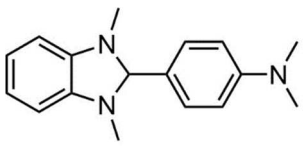

Derivative C1 was obtained only via route A.

From derivative **B1** (136 mg, 0.998 mmol), 4-(dimethylamino)benzaldehyde (153.1 mg, 1.026 mmol) and Montmorillonite clay K10 (118 mg). Reaction temperature is set at 120°C. Reaction completion is reached in 1 hour. Toluene: Et_2O 9:1 is used as eluent for TLC monitoring and for purification on SiO_2 pad.

Yellowish powder, 170 mg (0.636 mmol), 63.7 % yield.

^{1}H NMR (400 MHz, benzene–d_6): δ [ppm] 7.50 (d, J = 8.7 Hz, 2H), 6.88 (dd, J = 5.4, 3.2 Hz, 2H), 6.60 (d, J = 8.7 Hz, 2H), 6.41 (dd, J = 5.4, 3.2 Hz, 2H), 4.68 (s, 1H), 2.49 (s, 6H), 2.38 (s, 6H).

Synthesis of derivative C2 (DPBI)

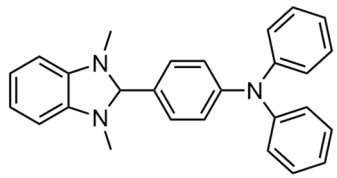

Derivative **C2** was obtained only via route A.
From derivative B1 (103.7 mg, 0.7614 mmol), 4-(N,N-diphenylamino)-benzaldehyde (201.7 mg, 0.7379 mmol), and Montmorillonite K10 clay (90.6 mg). Reaction temperature is set at 120°C. Reaction completion is reached in 1 hour. The reaction is stopped and taken up with dichlorometane to dissolve the crude and the obtained suspension is filtered on a 0.45 µm syringe filter. The obtained solution is evaporated under reduced pressure to give a waxy crude. The crude is taken up with heptane and the obtained suspension is filtered on a Hirsh funnel. The recovered powder is dried under vacuum to give 205 mg of product (0.524 mmol, 71.0% yield).

^{1}H NMR (400 MHz, $CDCl_3$): δ[ppm] 7.42 (d, J = 8.5 Hz, 2H), 7.32-7.22 (m, 4H), 7.16 -7.07 (m, 6H), 7.04 (t, J = 7.4 Hz, 2H), 6.72 (dd, J = 5.4, 3.2 Hz, 2H), 6.44 (dd, J = 3.2 Hz, 2H), 4.82 (s, 1H), 2.61 (s, 6H).

^{13}C{^{1}H} NMR (100 MHz, $CDCl_3$): δ[ppm] 148.91, 147.78, 142.29, 132.58, 129.65, 129.44, 124.79, 123.26, 123.12, 119.42, 105.94, 93.80, 33.46

Synthesis of derivative C3 (IstBI) via Route A

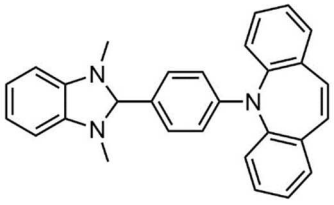

From derivative **B1** (149 mg, 1.09 mmol) and derivative **A1** (270 mg, 1.00 mmol) and montmorillonite K-10 (132 mg). Reaction temperature is initially set at 120°C for 30 minutes and the raised to 180°C. Reaction completion is reached after 1 hour. Toluene:Et_2O 9:1 is used as eluent for TLC monitoring and for purification on SiO_2 pad.
White powder, 243 mg (0.585 mmol), 58.5 % yield.

^{1}H NMR (400 MHz, benzene−d_6): δ[ppm] 7.38 (dd, J = 7.9, 1.1 Hz, 2H), 7.23 (d, J = 8.8 Hz, 2H), 7.15 – 7.11 (m, 2H), 7.09 (dd, J = 7.8, 1.6 Hz, 2H), 7.01 (td, J = 7.5, 1.3 Hz, 2H), 6.81 (dd, J = 5.4, 3.2 Hz, 2H), 6.52 (d, J = 8.8 Hz, 2H), 6.51 (s, 2H), 6.32 (dd, J = 5.4, 3.2 Hz, 2H), 4.50 (s, 1H), 2.24 (s, 6H).

^{13}C{1H} NMR (100 MHz, benzene−d_6): δ[ppm] 150.30, 143.55, 142.83, 136.88, 130.89, 130.76, 130.73, 129.95, 129.75, 128.92, 127.30 119.63, 112.23, 105.98, 94.27, 32.92.

Synthesis of derivative C3 (IstBI) via Route B

From iodide salt of derivative **F2** (200 mg, 0.369 mmol) and $NaBH_4$ (58.0 mg, 1.53 mmol) in 15 mL of methanol. Starting reagents form a solution. Reaction is complete in 1 hour. Purification via **Work-up A**.

White powder, 142 mg (0.342 mmol) 92.6% yield.

Synthesis of derivative C4 (PthBI) via Route A

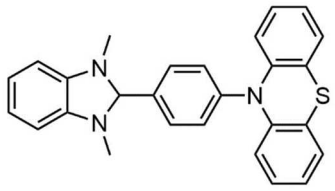

From derivative **B1** (136 mg, 0.998 mmol) and derivative **A2** (309.6 mg, 1.004 mmol) and montmorillonite K-10 (155.8 mg). Reaction temperature is set at 120°C for 1 hour and then at 180°C for 30 minutes (MW). Overall reaction time: 1 hour and 30 minutes. Toluene:Et_2O 9:1 is used as eluent for TLC monitoring and for purification on SiO_2 pad.
Yellowish powder, 369 mg (0.877 mmol), 87.7 % yield.

^{1}H NMR (400 MHz, benzene–d_6): δ[ppm] 7.42 (d, J = 8.2 Hz, 2H), 7.03 (d, J = 8.4 Hz, 2H), 6.98 (dd, J = 7.3, 1.8 Hz, 2H), 6.87 (dd, J = 5.4, 3.1 Hz, 2H), 6.67-6.58 (m , 4H), 6.38 (dd, J = 5.4, 3.1 Hz, 2H), 6.26 (dd, J = 7.8, 1.6 Hz), 4.55 (s, 1H), 2.23 (s, 1H).

^{13}C{1H} NMR (100 MHz, benzene−d_6): δ[ppm] 144.75, 142.48, 139.55, 131.36, 130.61, 127.32, 127.08, 123.10, 121.53, 120.08, 116.92, 106.33, 93.81, 33.31.

Synthesis of derivative C4 (PthBI) via Route B

From iodide salt of derivative **F2** (161 mg, 0.294 mmol) and $NaBH_4$ (66.58 mg, 1.760 mmol) in 3 mL of methanol. Starting reagents form a suspension. Reaction is complete in 40 minutes. Purification via **Work-up A**. White powder, 119 mg (0.282 mmol) 95.9% yield.

Synthesis of derivative C5 (CbzBI)

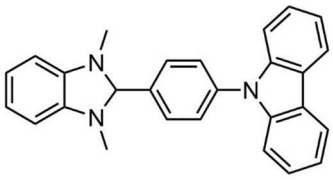

Derivative **C5** was obtained only via **route B**.

From derivative **F4** (282 mg, 0.492 mmol) and $NaBH_4$ (185 mg, 5.47 mmol) in 25 mL of methanol. Starting reagents form a suspension. $NaBH_4$ is added in two aliquots: 86 mg are firstly added and further 99 mg are added after 1 hour and 30 minutes. Overall reaction time: 2 hour and 30 minutes. Purification via **Work-up A.** Grey powder, 179 mg (0.460 mmol), 93.4% yield.

^{1}H NMR (400 MHz, $CDCl_3$): δ[ppm] 8.16 (d, J = 7.6 Hz, 2H), 7.83 (d, J = 8.32 Hz, 2H), 7.64 (d, J = 8.3 Hz, 2H), 7.51-7.46 (m, 2H), 7.46-7.40 (m, 2H), 7.34-7.28 (m, 2H), 6.77 (dd, J = 5.4, 3.1 Hz, 2H), 6.51 (dd, J = 5.4, 3.2 Hz, 2H), 5.02 (s, 1H), 2.69 (s, 6H).

^{13}C{^{1}H} NMR (100 MHz, $CDCl_3$): δ[ppm] 142.15, 140.89, 138.82, 138.48, 130.38, 127.10, 126.11, 123.63, 120.49, 120.22, 119.67, 109.95, 106.11, 93.76, 33.61.

Synthesis of derivative C6 (2C4-DMBI) via route A

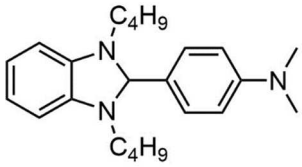

From derivative **B2**, 4-(dimethylamino)benzaldehyde and montmorillonite K-10. Reaction temperature is set at 120°C (MW). Overall reaction time: 2 hours. The reaction is repeated three times.

Reaction	B2 (mmol)	DMAB (mmol)	MK10 (mg)	Product (mmol)	Yield % (NMR puritiy)
1	225 mg (1.02)	150.6 mg (1.009)	226	190 mg (0.541)	53.6% (83%)
2	227 mg (1.03)	184.9 mg (1.233)	222	191 mg (0.543)	52.7% (85%)
3	230 mg (1.05)	149.7 mg (1.003)	240	246 mg (0.699)	69.7% (88%)

For the first two attempts, Toluene:Et_2O 95:15 is used as eluent for TLC monitoring and for purification on SiO_2 pad.
For the third attempt, a different purification procedure is followed: the crude mixture is extracted using 15 mL of petroleum ether. The obtained solution is filtered on a 0.45 µm syringe filter directly inside a two neck 50 mL roundbottom flask containing around 2 g of anhydrified $MgSO_4$ and previously put under N_2 atmosphere. After 30 minutes, the solution is again filtered on a 0.45 µm syringe filter in a second roundbottom flask and the solvent is evaporated under reduced pressure. The obtained oil is dried under high vacuum to give the product.

Synthesis of derivative C6 (2C$_4$-DMBI) via route B

From derivative **F5** (998 mg, 2.32 mmol) and $NaBH_4$ (175.60 mg, 4.64 mmol) in methanol (8 mL). Starting reagents form a solution. Reaction is complete in 20 minutes. Purification via **Work-up B** using petroleum ether as solvent for extraction (15 mL + 3 × 10 mL).

Colourless oil, 622 mg (1.77 mmol), 76.2 % yield.

^{1}H NMR (400 MHz, DMSO-d_6): δ[ppm] 7.39 (d, J = 8.8 Hz, 2H), 6.73 (d, J = 8.8 Hz, 2H), 6.61 (dd, J = 5.4, 3.2 Hz, 2H), 6.31 (dd, J = 5.4, 3.2 Hz, 2H), 5.49 (s, 1H), 3.00 (s, 6H), 2.98-2.85 (m, 4H), 1.40 (qnt, J = 7.5 Hz, 4H), 1.30-1.15 (m, 4H), 0.83 (t, J = 7.3 Hz, 6H).

^{13}C{^{1}H} NMR (100 MHz, DMSO-d_6): δ[ppm] 150.89, 140.86, 129.12, 126.47, 117.70, 111.74, 103.81, 87.91, 44.97, 40.02, 28.11, 19.62, 13.67.

Synthesis of derivative C7

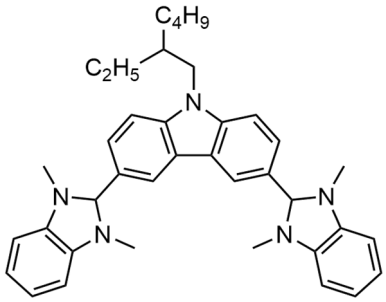

Derivative **C7** was obtained only via **route A.**

From derivative **B1** (149 mg, 1.09 mmol), derivative **A4** (162.9 mg, 0.4856 mmol), and Montmorillonite clay K10 (96.0 mg). Reaction temperature is set at 150°C for 1 hour, then at 180°C for 1 hour and finally at 210°C. Overall reaction time: 2 hour and 40 minutes. Toluene:Et_2O 95:15 is used as eluent for TLC monitoring and for purification on SiO_2 pad. Yellowish powder, 120 mg (0.210 mmol), 43.7% yield. m.p. 209-213 °C

^{1}H NMR (400 MHz, benzene-d_6): δ [ppm] 8.33 (d, J = 1.5 Hz, 2H), 7.87 (dd, J = 8.4, 1.5 Hz, 2H), 7.31 (d, J = 8.6 Hz, 2H), 6.92 (dd, J = 5.4, 3.2 Hz, 4H), 6.46 (dd, J = 5.4, 3.2, 4H), 4.94 (s, 2H), 3.85-3.72 (m, 2H), 2.41 (s,12H), 1.91 (spt, J = 6.1 Hz, 1H), 1.19-1.01 (m, 8H), 0.79 (t, J = 6.9 Hz, 3H), 0.68 (t, J = 7.4 Hz, 3H).

^{13}C{^{1}H} NMR (100 MHz, benzene−d_6): δ [ppm] 142.80, 142.53, 130.73, 127.01, 123.18, 122.01, 119.95, 109.45, 106.19, 95.19, 47.64, 39.58, 33.16, 31.18, 28.96, 24.61, 23.29, 14.18, 10.91.

Synthesis of derivative C8

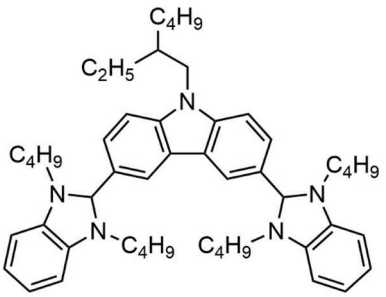

Derivative **C8** was obtained only via **route A**

From derivative **B2** (244 mg, 1.11 mmol), derivative **A4** (167.8 mg, 0.5002 mmol), and Montmorillonite clay K10 (244 mg). Reaction temperature is set at 120°C. Overall reaction time: 2 hour.

Reaction work-up: anhydrous $MgSO_4$ (3 g) is added to a previously anhydrified 2 neck roundbottom flask and the system is put under N_2 atmosphere. The reaction crude is extracted with degassed petroleum ether (20 mL) and the obtained solution is filtered through a 0.45 μm syringe filter directly in this flask. The solution is let rest on $MgSO_4$ for 1 hour, to remove residual diamine. The solution is then recovered and filtered again on a 0.45 μm syringe filter to remove solid residues and the solvent is evaporated under reduced pressure. The obtained solid is then diluted in 3 mL of toluene and filtered on a pad of silica using Toluene:Et_2O 95:15 is used as eluent. Fractions containing the product are collected and the solvent is evaporated under reduced pressure to afford the product.
Yellowish oil, 85 mg (0.11 mmol), 22.0% yield.

^{1}H NMR (400 MHz, benzene-d_6): δ [ppm] 8.35 (s, 2H), 7.83 (dd, J = 8.5, 1.5 Hz, 2H), 7.27 (d, J = 8.5 Hz, 2H), 6.94-6.89, (m, 4H), 6.55-6.47 (m, 4H), 3.75 (s, 2H), 3.72 (d, J = 7.3, 2H), 3.03-2.85 (m, 8H), 1.88 (spt, J = 6.2 Hz, 1H), 1.46-1.26 (m, 16H), 1.15-0.99 (m, 8H), 0.78 (t, J = 7.1 Hz, 3H), 0.69-0.62 (m, 15H).

$^{13}C\{^{1}H\}$ NMR (100 MHz, benzene-d_6): δ [ppm] 142.37, 141.85, 132.11, 129.33, 128.56, 127.08, 125.70, 123.02, 121.49, 119.10, 109.47, 105.02, 90.70, 47.51, 46.51, 39.47, 31.20, 30.22, 29.47, 29.45, 28.91, 24.63, 23.26, 21.43, 20.56, 14.16, 13.96, 10.92.

Synthesis of derivative C9

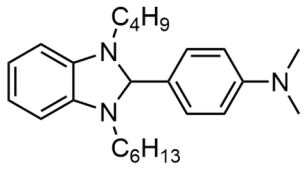

Derivative **C9** was obtained only via **route B.**

From derivative **F6** (460 mg, 1.00 mmol) and $NaBH_4$ (76 mg, 2.0 mmol) in methanol (4 mL). Starting reagents form a solution. Reaction is complete in 20 minutes. Purification via **Work-up B** using petroleum ether as solvent for extraction (15 mL × 3).

Colourless oil, 262 mg (0.664 mmol), 66.2% yield.

1H NMR (400 MHz, $CDCl_3$): δ [ppm] 7.37 (d, J = 8.7 Hz, 2H), 6.72 (d, J = 8.6 Hz, 2H), 6.59 (dd, J = 5.4, 3.2, 2H), 6.32-6.26 (m, 2H), 5.46 (s, 1H), 2.98 (s, 6H), 2.94-2.85 (m, 4H), 1.38 (qnt, J=7.5 Hz, 4H), 1.27-1.09 (m, 8H), 0.82 (t, J = 7.0 Hz, 3H), 0.81 (t, J = 7.4 Hz, 3H).

^{13}C $\{^{1}H\}$ NMR (100 MHz, $CDCl_3$): δ [ppm] 151.29, 141.41, 141.39, 129.76, 127.61, 117.91, 112.08, 103.87, 103.85, 88.99, 46.03, 45.70, 40.68, 31.68, 28.92, 26.93, 26.75, 22.74, 20.49, 14.17, 14.00.

Synthesis of derivative C10

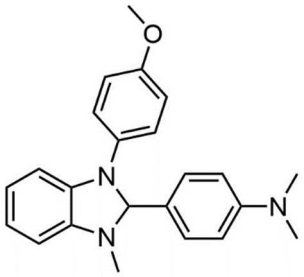

Derivative **C10** was obtained only via **route B.**

From derivative **F7** (1.340 g, 2.761 mmol) and $NaBH_4$ (424 mg, 11.2 mmol) in methanol (11mL). Starting reagents form a solution. Overall reaction time: 1 hour.
Purification via **Work-up A**.
Brownish powder, 985 mg (2.74 mmol), 99% Yield.

^{1}H NMR (400 MHz, DMSO−d_6): δ[ppm] 7.31 (d, J = 8.8 Hz, 2H), 7.07 (d, J = 9.0 Hz, 2H), 6.84 (d, J = 9.0 Hz, 2H), 6.66 (d, J = 8.8 Hz, 2H), 6.62 (td, J = 7.5, 1.0, 1H), 6.51 (td, J = 7.5, 1.0 Hz, 1H), 6.49-6.40 (m, 2H), 5.79 (s, 1H), 3.68 (s, 3H), 2.87 (2, 6H), 2.52 (s, 3H).

$^{13}C\{^{1}H\}$ NMR (100 MHz, DMSO−d6): δ[ppm] 155.49, 150.69, 141.73, 138.94, 134.76, 129.23, 125.46, 123.86, 119.16, 118.24, 114.32, 111.70, 105.38, 104.65, 89.36, 55.09, 32.34.

4.5.1.6. Preparation of 2-aryl benzimidazolum salt for electrochemical characterization

Triflate or hexafluorophosphate salt of 2-arylbenzimidazolium were prepared for electrochemical characterization, since these are stable in the thermodynamic potential window of the solvent used as electrolyte in such measurements (acetonitrile). As reported in **section 4.5.1.3**, for derivative **F2-4** it was possible to obtain the triflate salts via direct methylation of the 2-arylbenzoimidazol precursor. Whenever this was not possible, the required derivative was obtained either via ionic exchange reaction on the already obtained benzimidazolium salts (derivative **F5**) or via oxidation reaction of the dopant with AgOTf (derivative **C1**, **C2**, **C10**). The two procedures are here briefly described.

Preparation of hexafluorophosphate salts via ionic exchange

F5 (50 mg) is added to a 4 mL vial and 3 g of a NH_4PF_6 solution (33% wt. in water) are added. The obtained dispersion is let stirring for 24 hours at room temperature. The solid is filtered and the procedure is repeated once again. The obtained solid is dried in vacuum at 65°C until weight stabilization.

Preparation of triflate salts via oxidation with AgOTf

Dopant (1.00 mmol) is added to a test tube. AgOTf (1.10 mmol) is dissolved in methanol (2 mL) and the obtained solution is added to the test tube. A dark grey powder forms immediately. The mixture is kept stirring in the dark and the reaction progress is monitored via TLC using a mixture of toluene and Et_2O (9:1) as eluent. After 2 hours, the reaction is stopped. The mixture is filtered and the recovered solvent is evaporated under reduced pressure. The solid is dissolved in methanol and filtered on celite. The recovered solvent is then evaporated under reduced pressure to give the product, which is then dried under vacuum at 65°C until weight stabilization.

NMR of N-DMBI$^+$ OTf$^-$

^{1}H NMR (400 MHz, DMSO-d6): δ 8.06 (dd, J = 6.2, 3.2 Hz, 2H), 7.71 (dd, J= 6.2, 3.2 Hz, 2H), 7.67 (d, J = 9.1 Hz, 2H), 6.99 (d, J = 9.0 Hz, 2H), 3.91 (s, 6H), 3.09 (s, 6H) ppm. (see reference 15 for comparison)

^{19}F NMR (400 MHz, DMSO-d6): δ -77.75 ppm.

NMR of DPBI+ OTf-

^{1}H NMR (400 MHz, DMSO-d_6): δ 8.08 (dd, J = 6.2, 3.1 Hz, 2H), 7.73 (dd, J= 6.2, 3.1 Hz, 2H), 7.69 (d, J=8.9 Hz, 2H), 7.50-7.43 (m, 4H), 7.30-7.24 (m ,6H), 7.06 (d, J=8.9 Hz, 2H), 3.93 (s, 6H) ppm.

^{13}C NMR (100 MHz, DMSO-d6): δ 151.10, 150.64, 145.50, 132.16, 131.76, 130.11, 126.41, 126.36, 125.51, 118.43, 113.18, 111.00, 32.86 ppm.

^{19}F NMR (400 MHz, DMSO-d6): δ - 77.75 ppm.

4.5.2. NMR spectra

Derivative E3

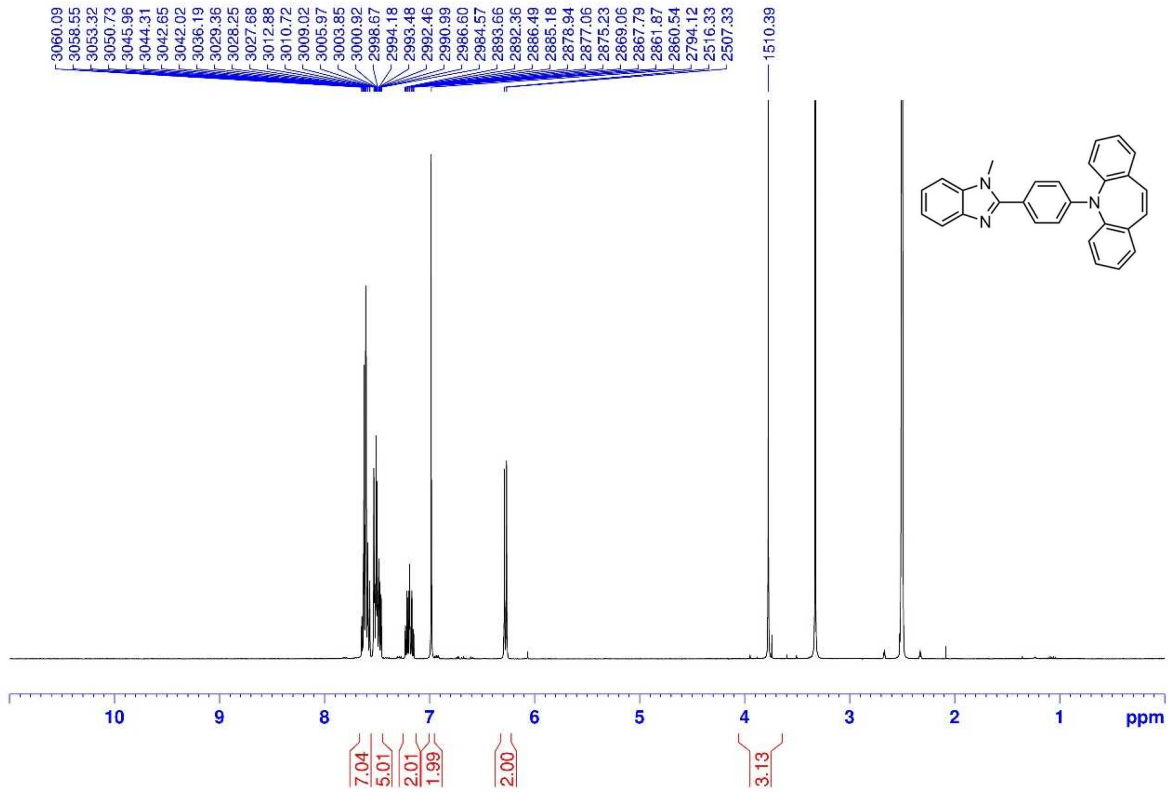

Figure 4.19 ^{1}H NMR of Derivative **E3** in DMSO-d$_6$.

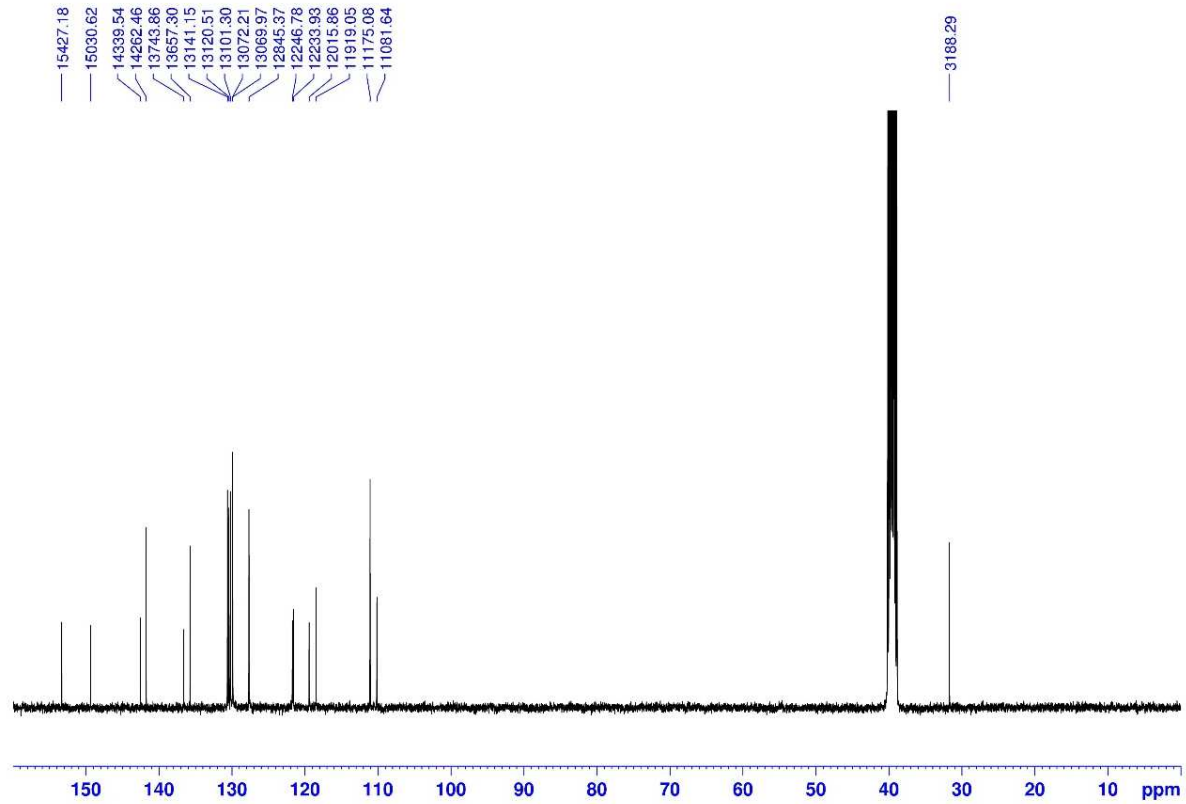

Figure 4.20 ^{13}C NMR of derivative **E3** in DMSO-d$_6$.

Derivative E4

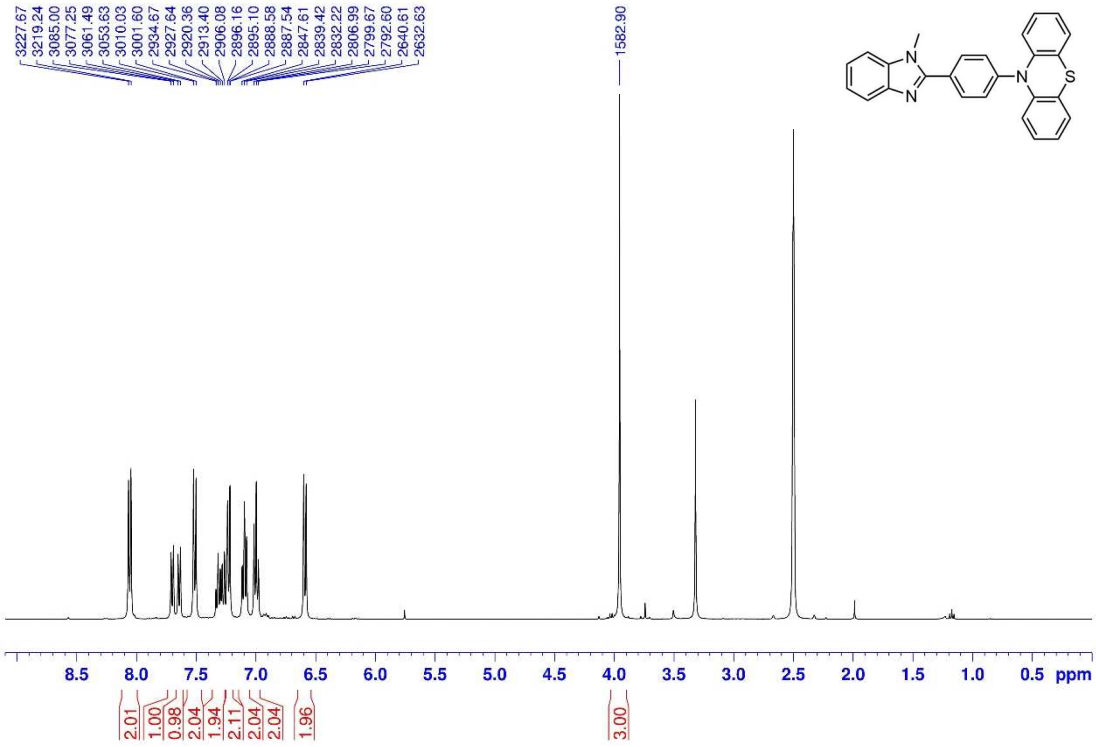

Figure 4.21 ^{1}H NMR of Derivative **E4** in DMSO-d$_6$ **Figure 4.12**

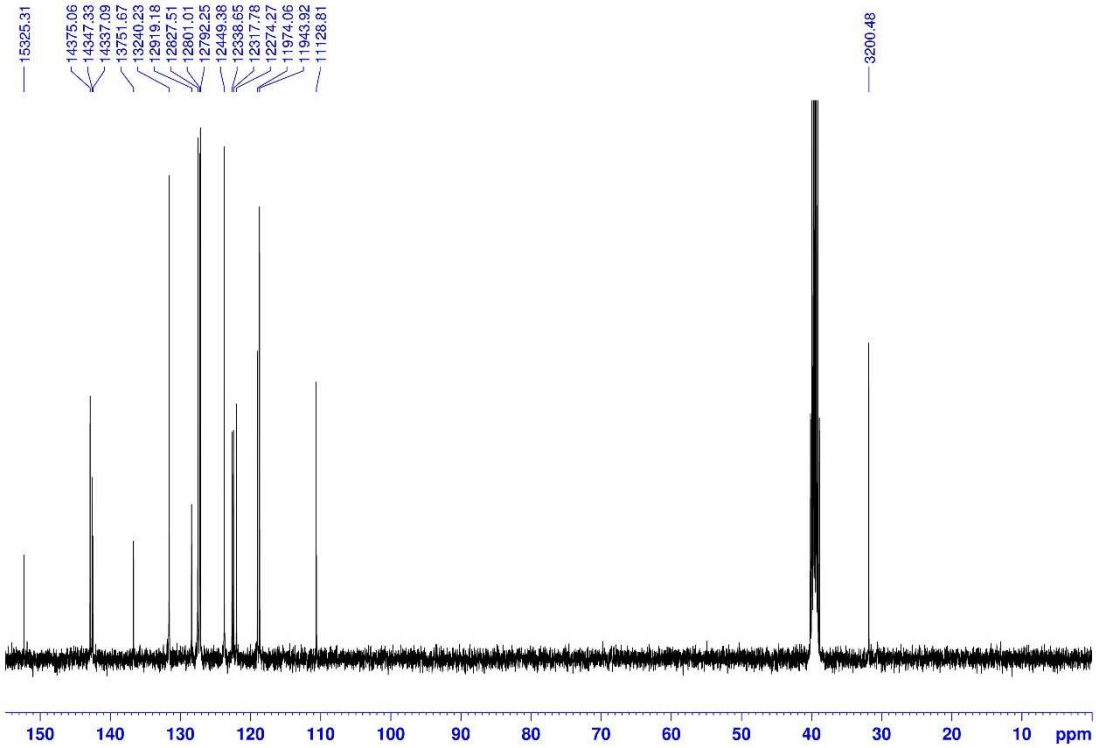

Figure 4.22 ^{13}C NMR of derivative E4 in DMSO-d$_6$.

Derivative E5

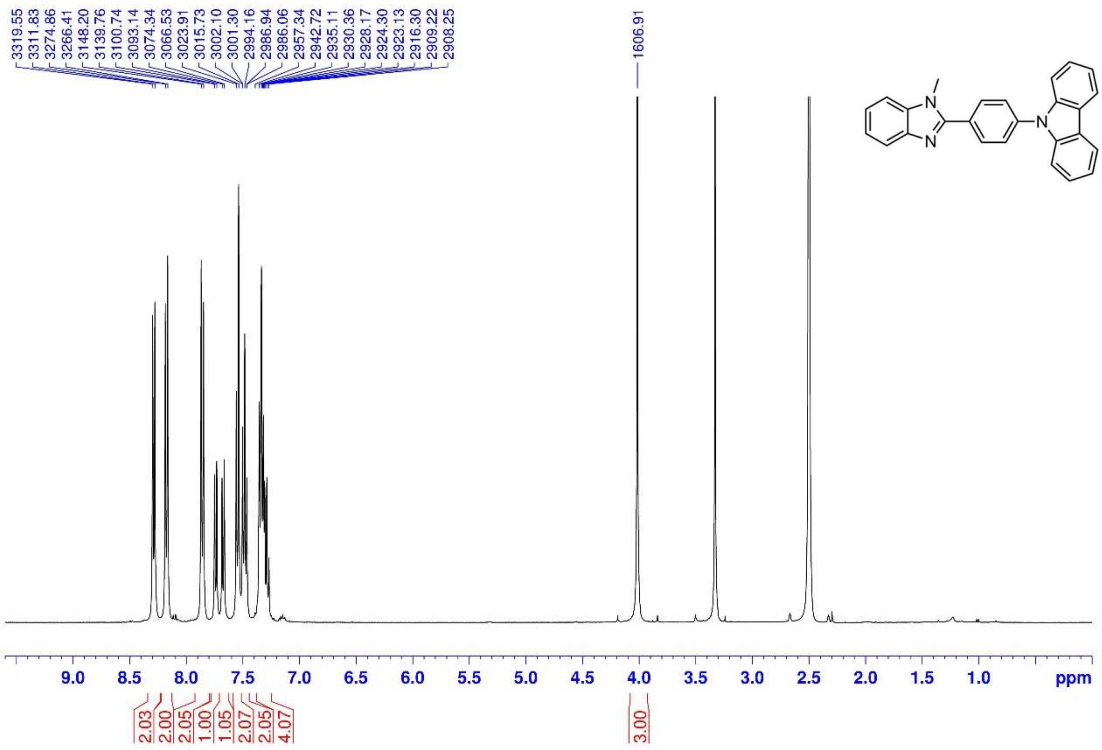

Figure 4.23 ^{1}H NMR of derivative **E5** in DMSO-d_6.

Derivative E6

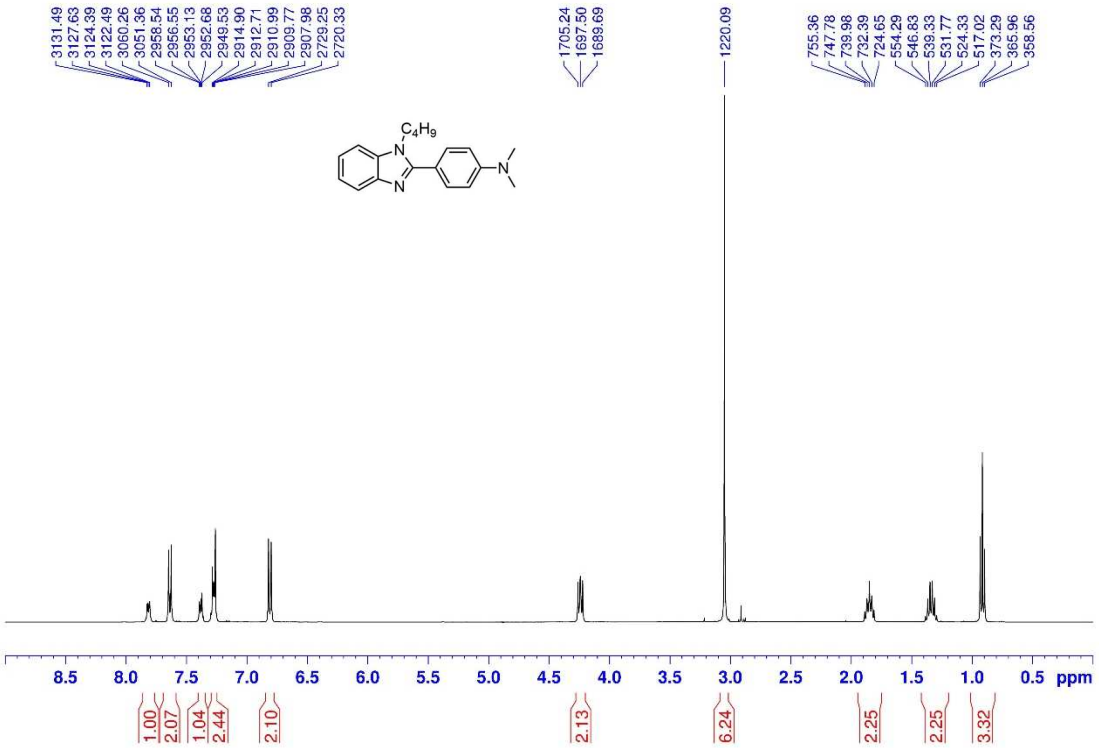

Figura 4.24: ^{1}H NMR of derivative **E6** in $CDCl_3$.

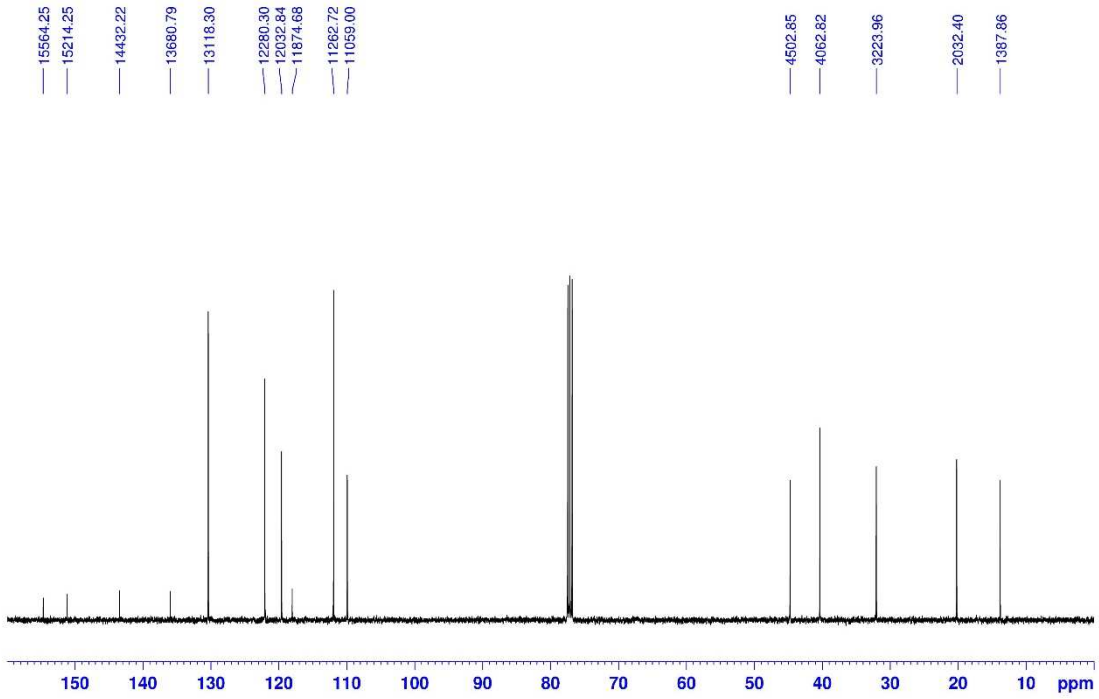

Figura 4.25: ^{13}C NMR of derivative **E6** in $CDCl_3$.

Derivative E7

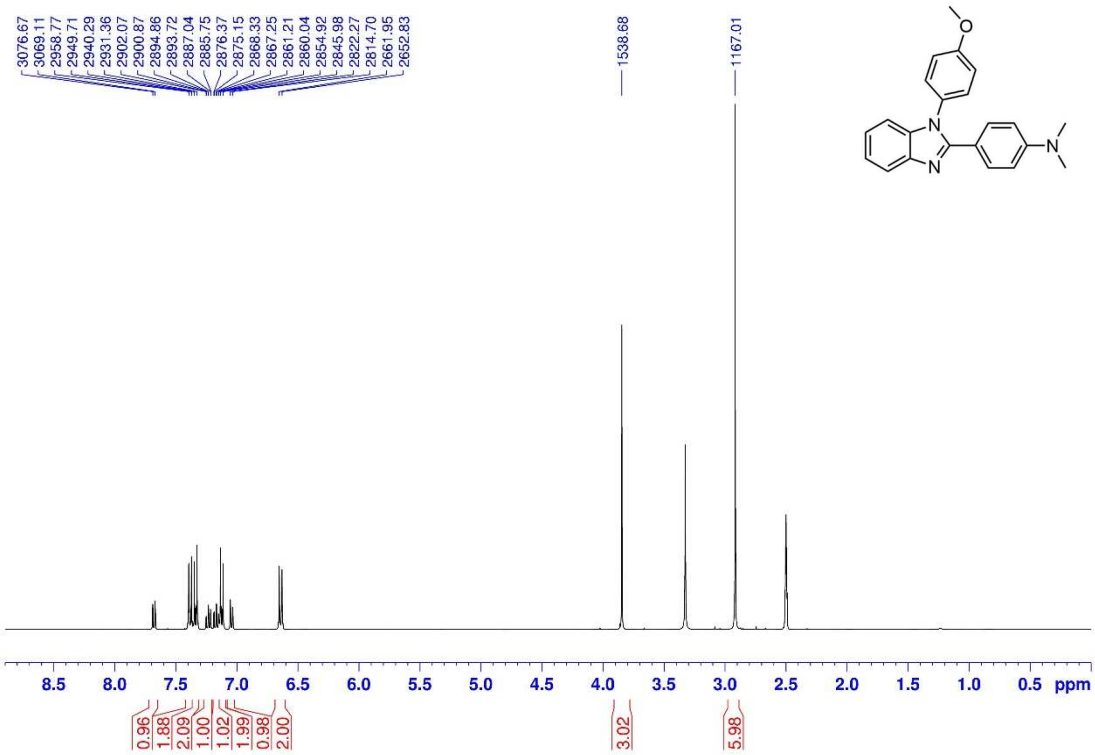

Figure 4.26 ^{1}H NMR of derivative **E7** in DMSO-d$_6$.

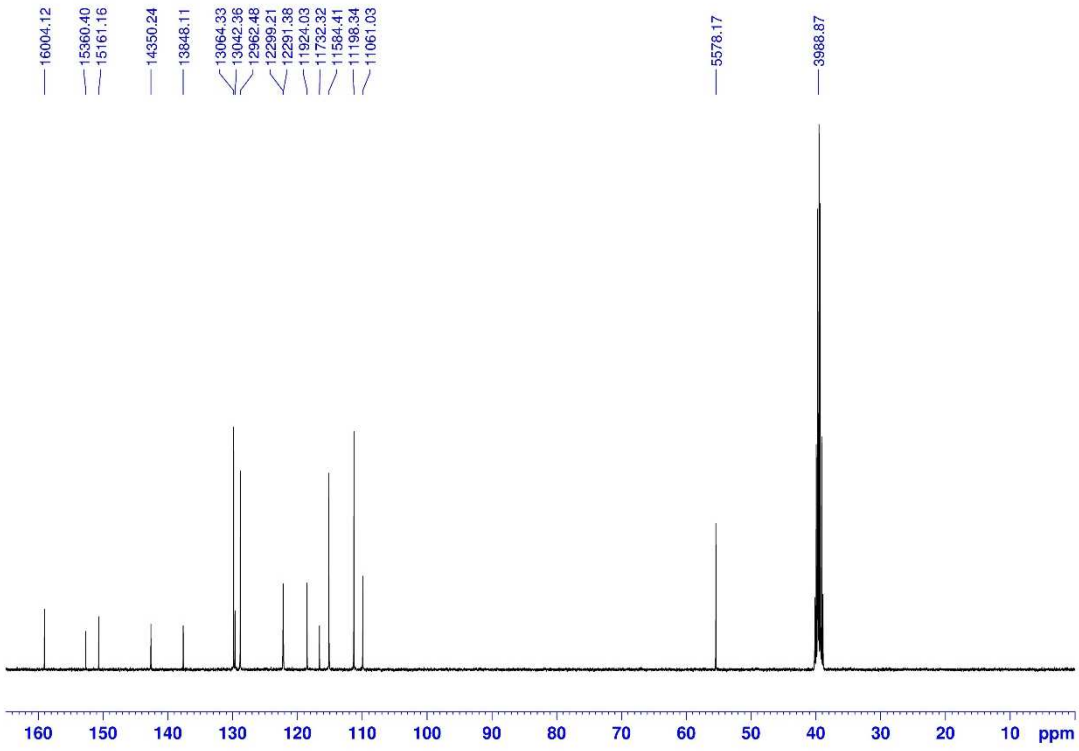

Figure 4.27 ^{13}C NMR of derivative **E7** in DMSO-d$_6$.

Derivative F2 (iodide salt)

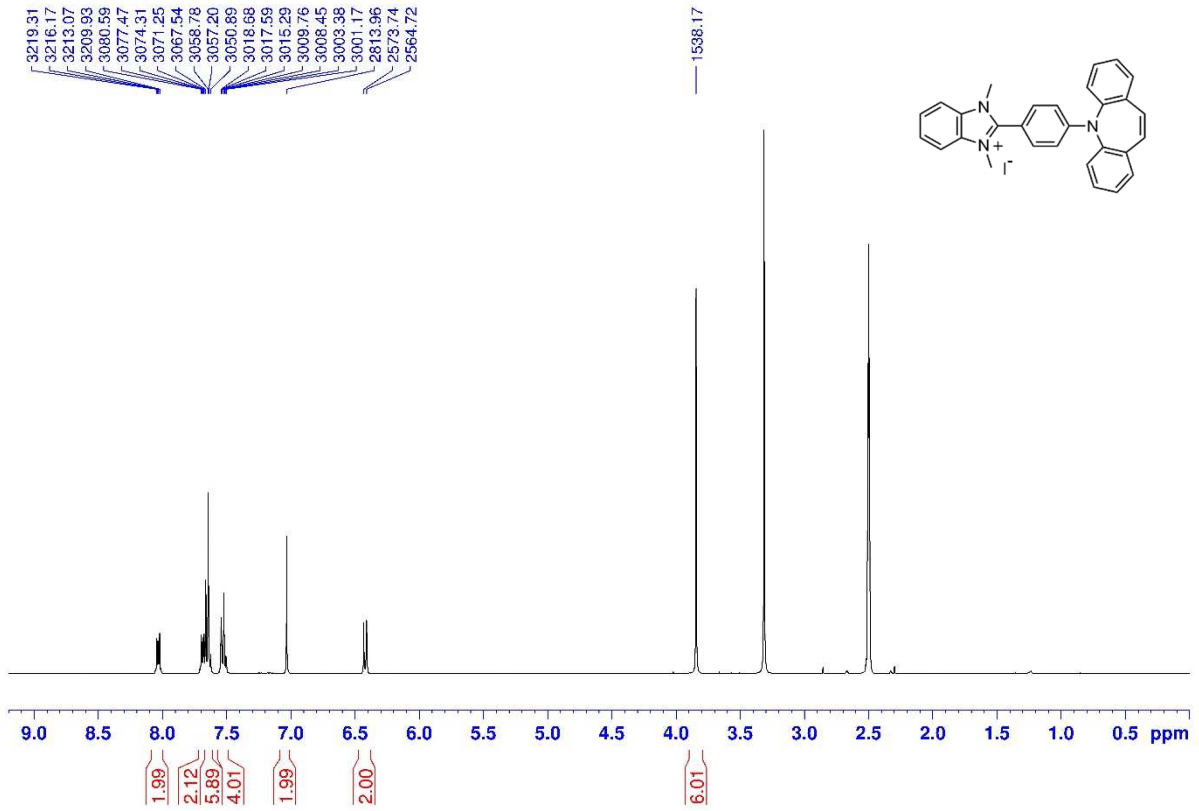

Figure 4.28 ^{1}H NMR of derivative **F2** in DMSO-d$_6$.

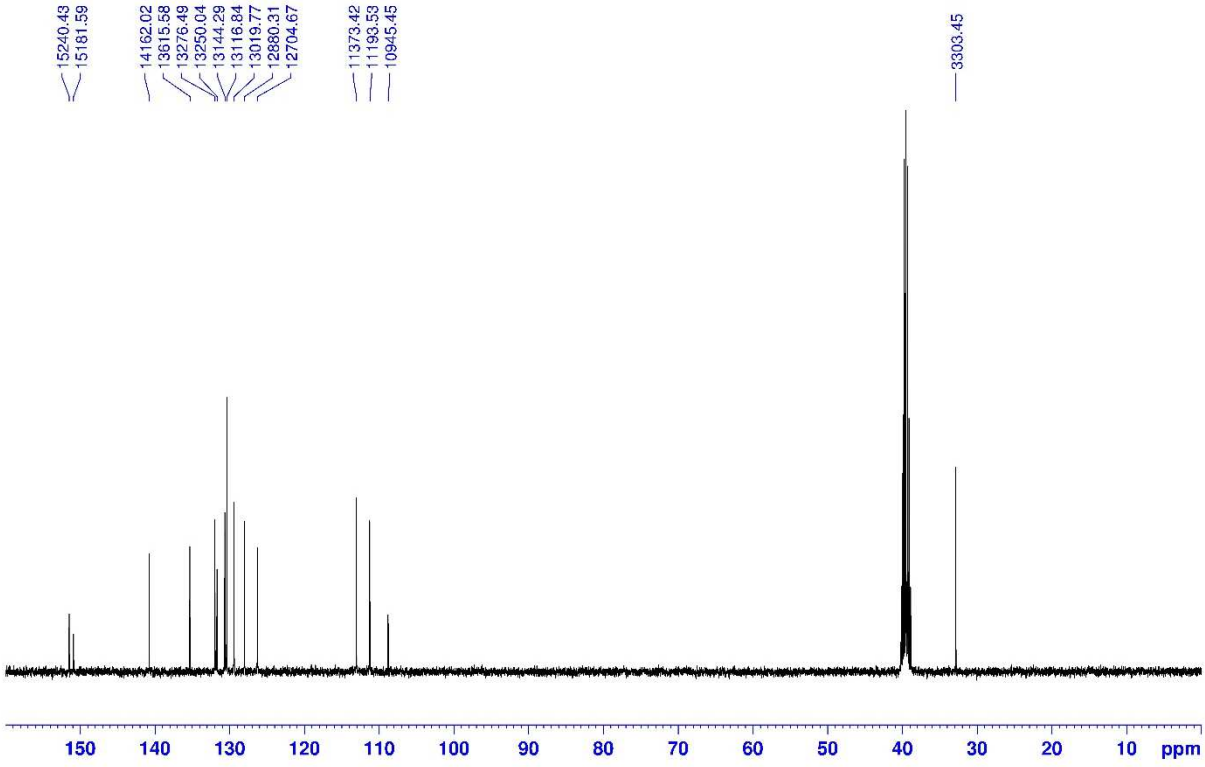

Figure 4.29 ^{13}C NMR of derivative **F2** in DMSO-d$_6$.

Derivative F2 (triflate salt)

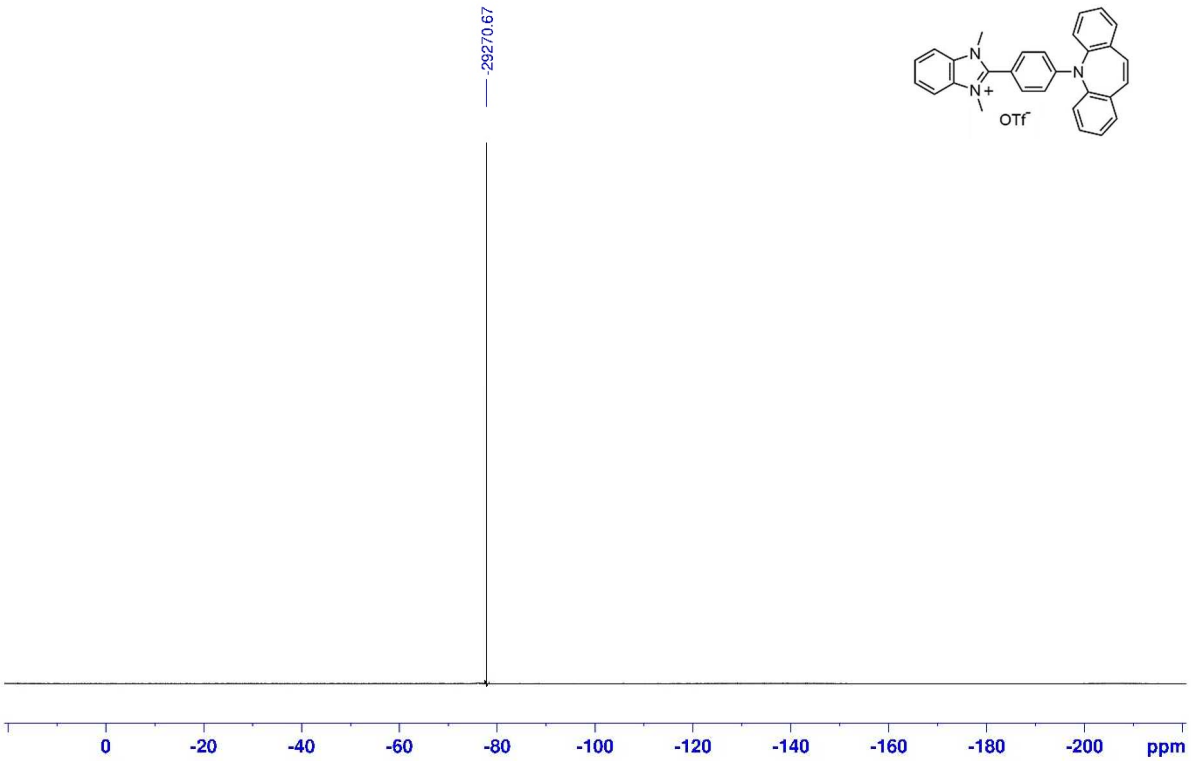

Figure 4.30 ^{19}F NMR of derivative **F2** in DMSO-d_6.

Derivative F3 (iodide salt)

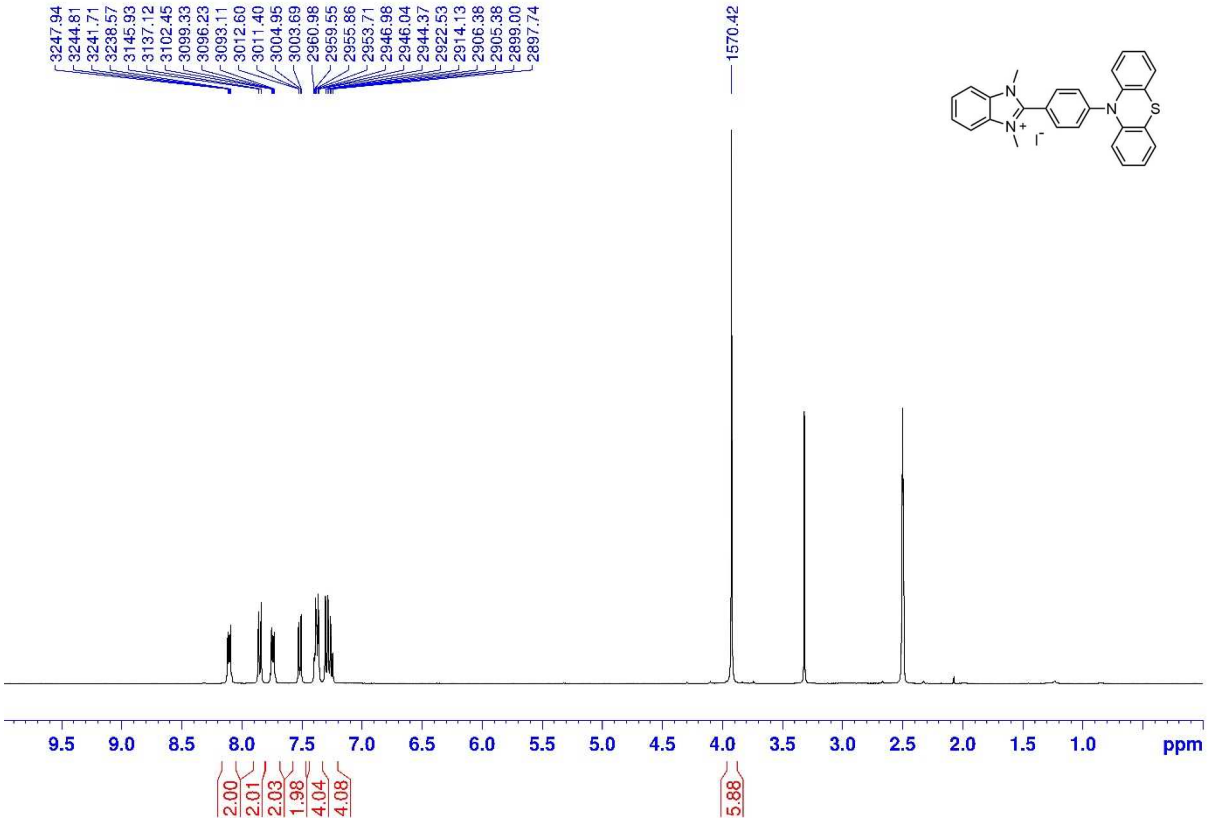

Figure 4.31 ^{1}H NMR of derivative **F3** in DMSO-d$_6$.

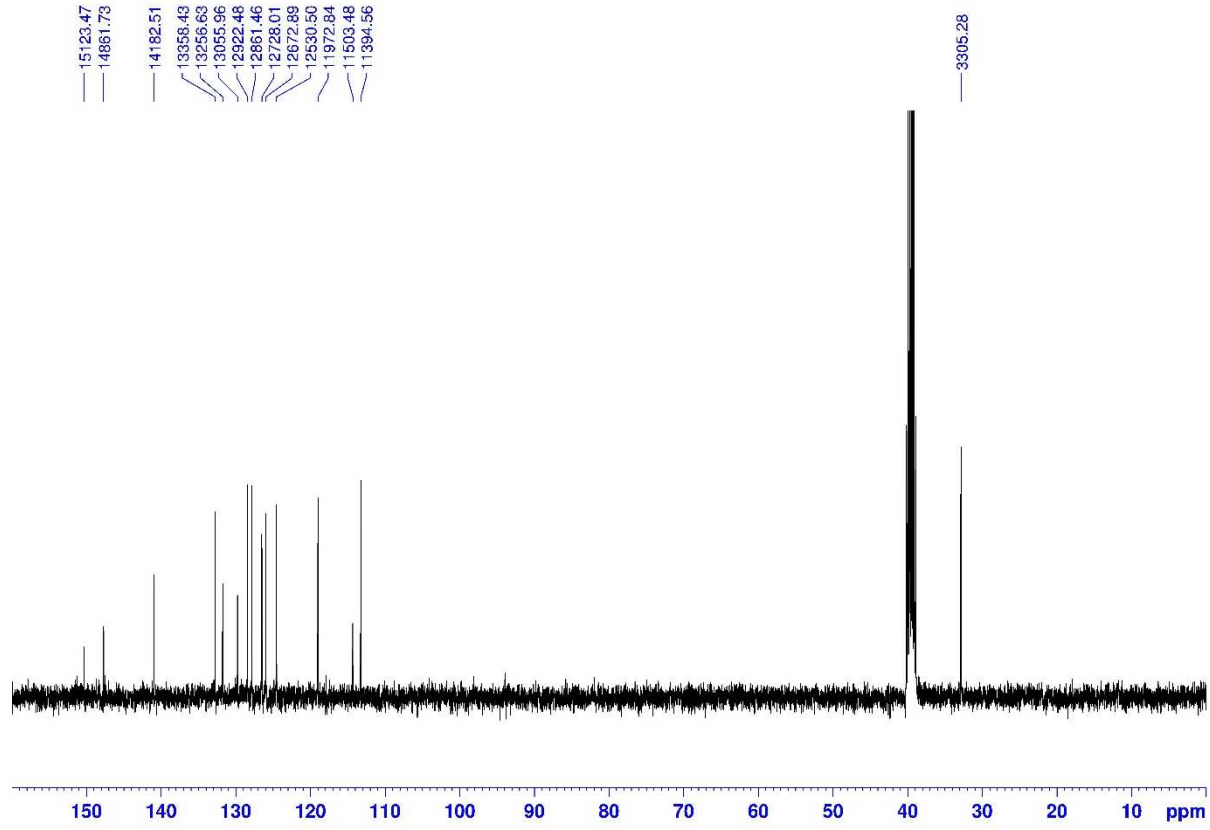

Figure 4.32 ^{13}C NMR of derivative **F3** in DMSO-d$_6$.

Derivative F3 (triflate salt)

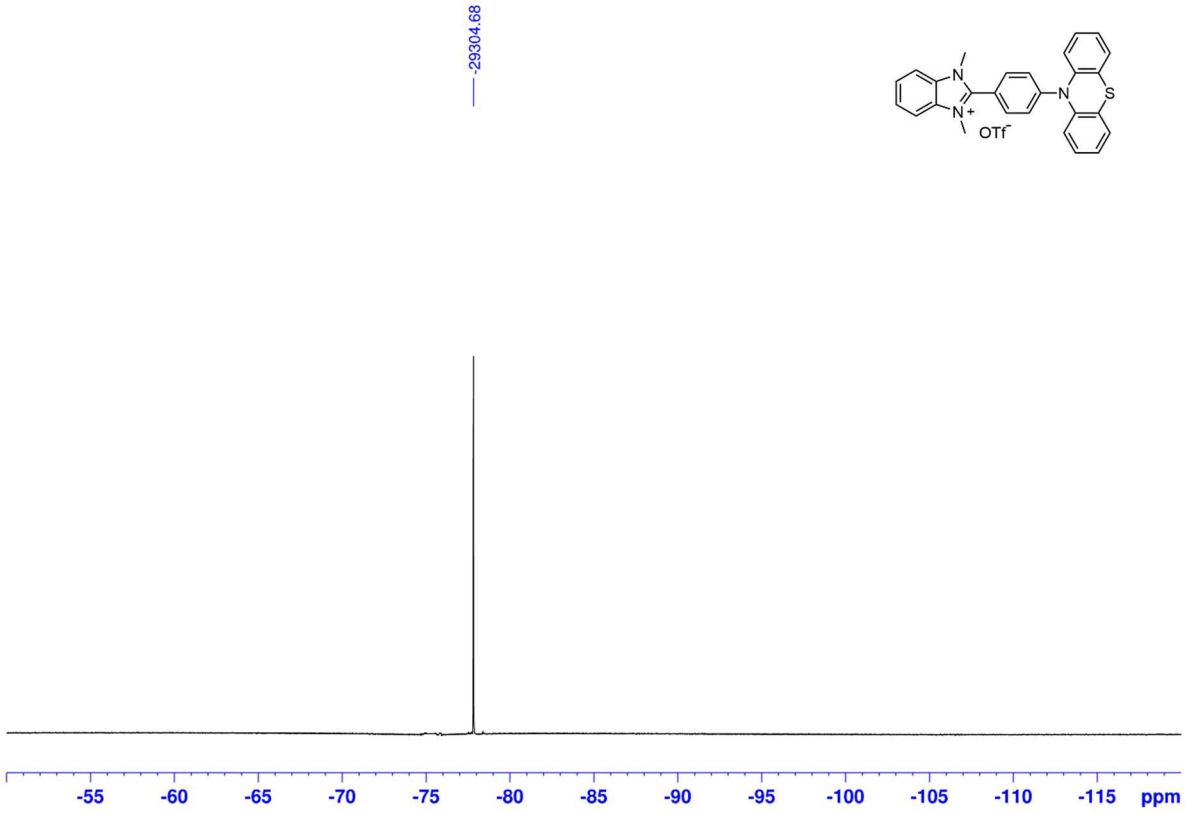

Figure 4.33 ^{19}F NMR of derivative **F3** in DMSO-d_6.

Derivative F4

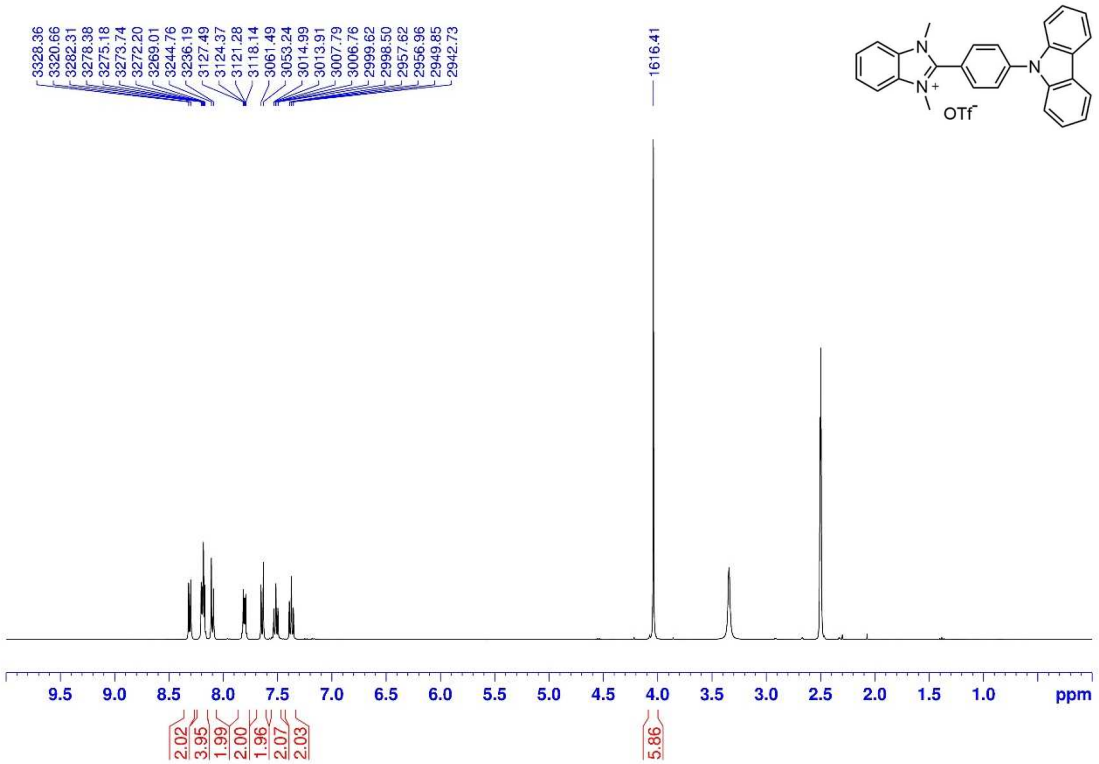

Figure 4.34 ^{1}H NMR of derivative **F4** in DMSO-d_6.

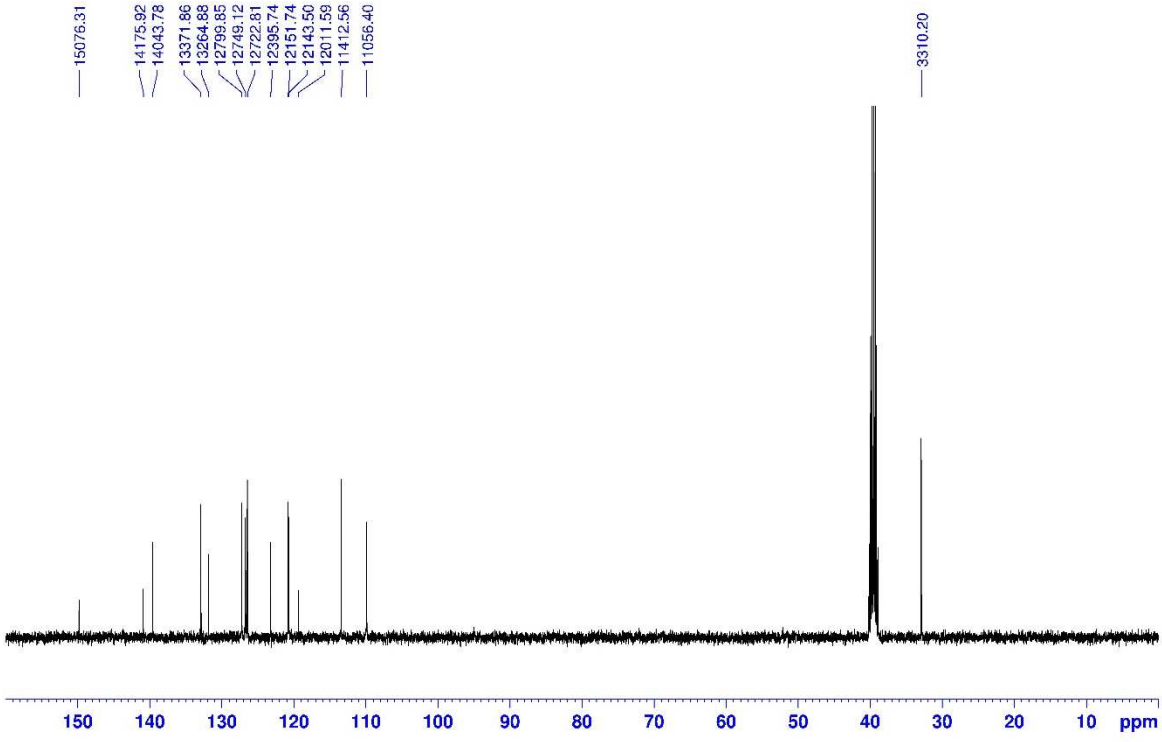

Figure 4.35 ^{13}C NMR of derivative **F4** in DMSO-d_6.

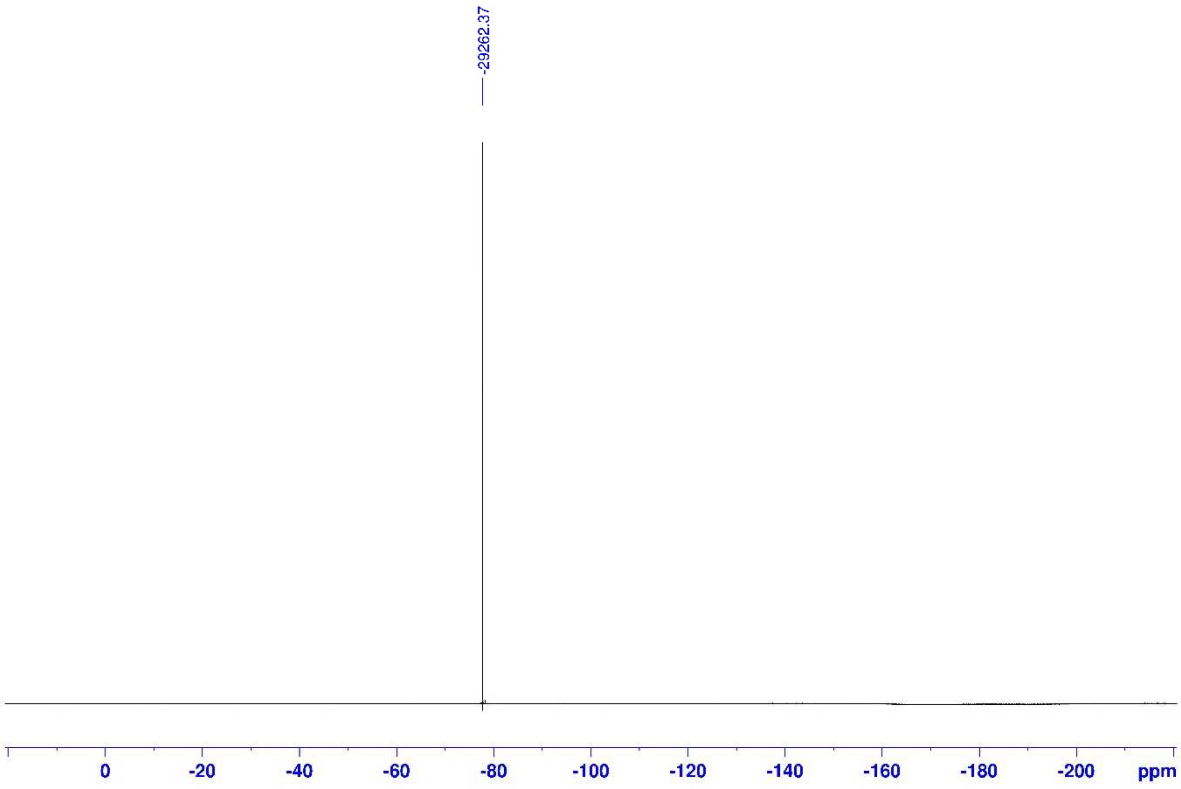

Figure 4.36 ^{19}F NMR of derivative **F4** in DMSO-d_6

Derivative F5

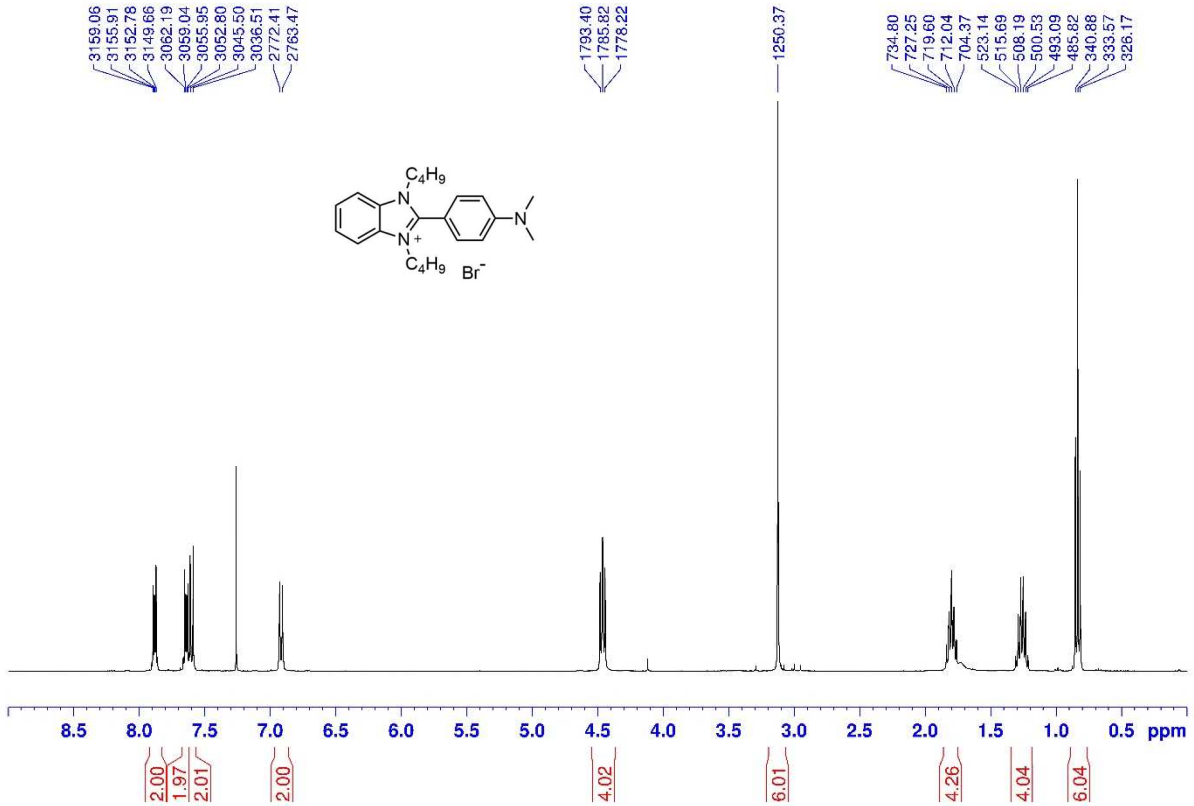

Figura 4.37 ^{1}H NMR of derivative **F5** in $CDCl_3$.

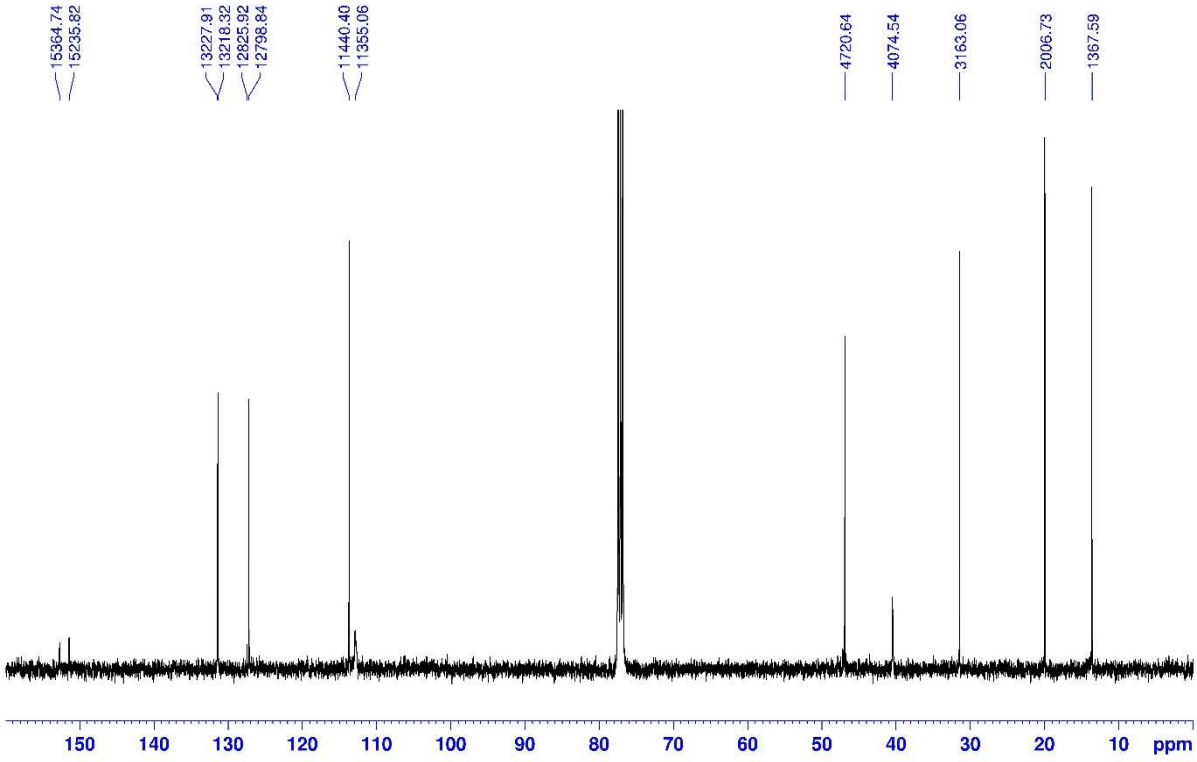

Figura 4.38 ^{13}C NMR of derivative F5 in $CDCl_3$.

Derivative F6

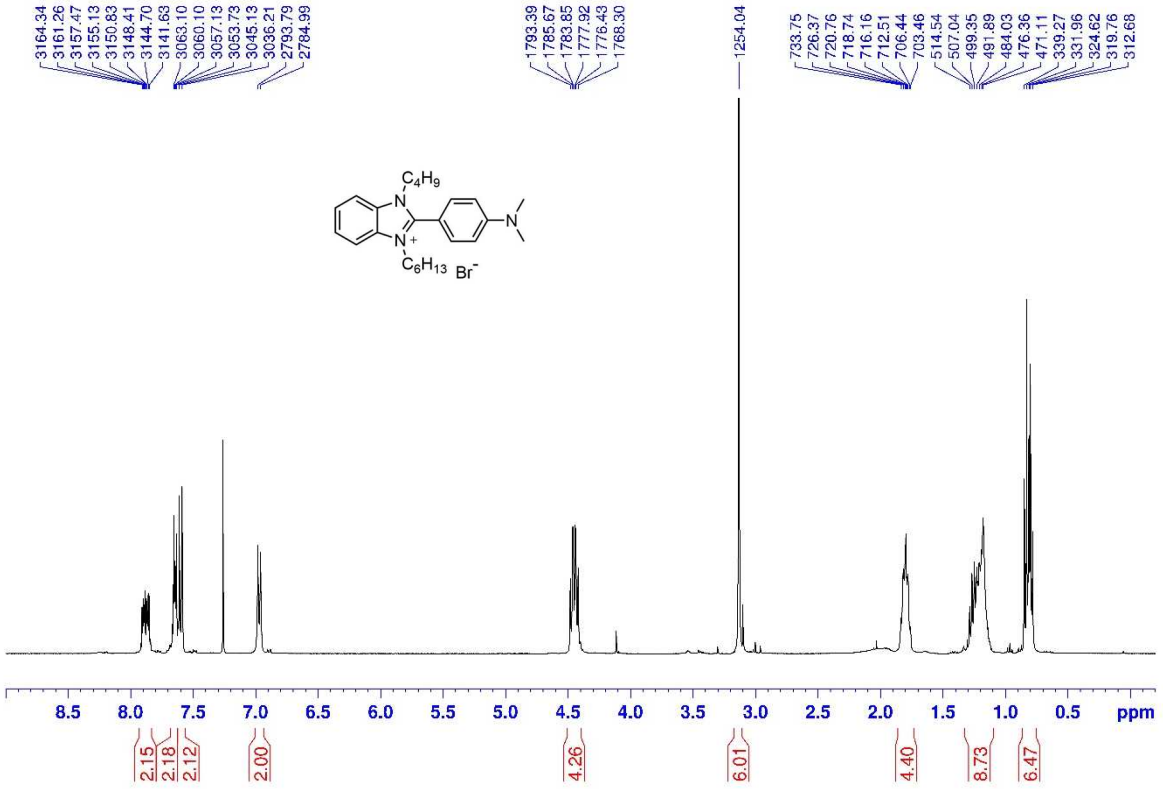

Figura 4.39 ^{1}H NMR of derivative **F6** in $CDCl_3$.

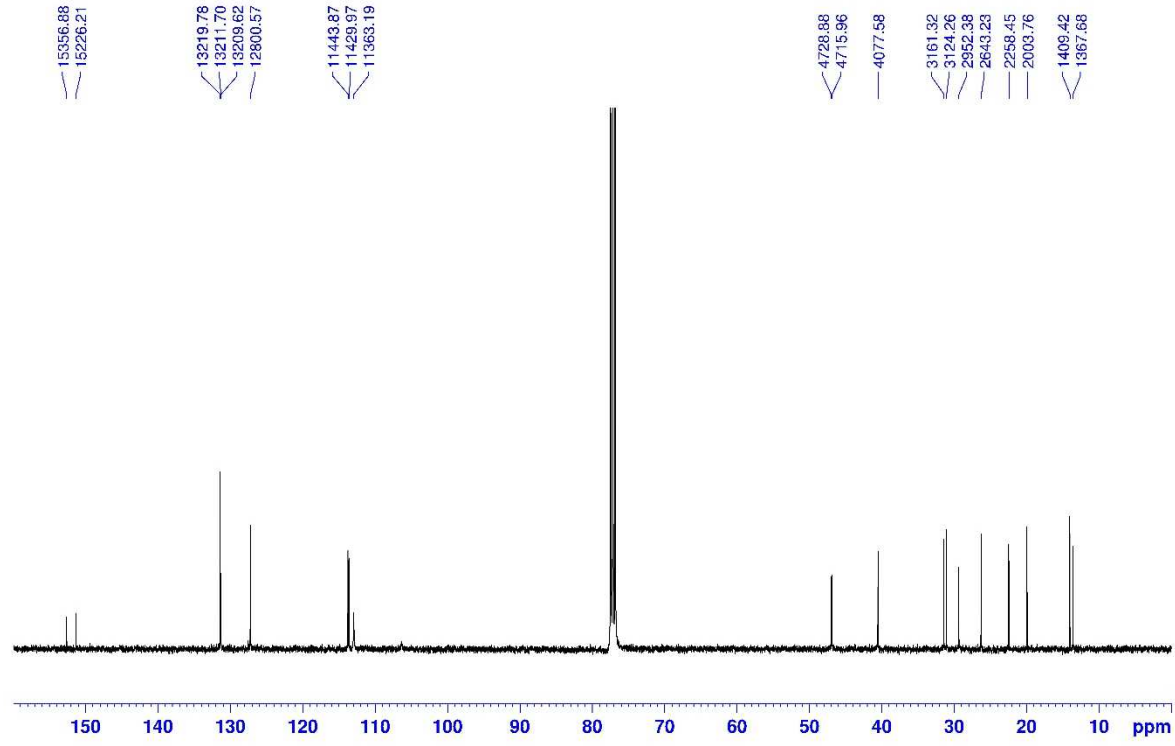

Figura 4.40 ^{13}C NMR of derivative **F6** in $CDCl_3$.

Derivative F7

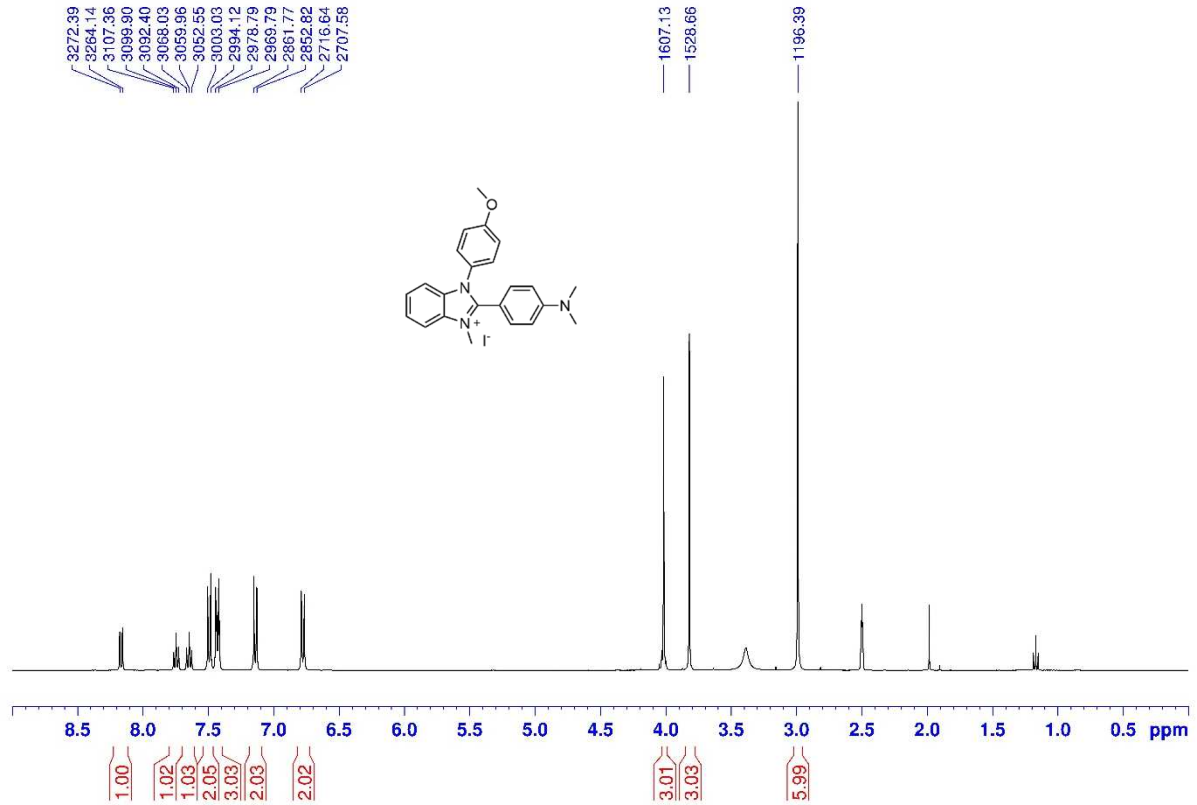

Figure 4.41 ^{1}H NMR of derivative **F7** in DMSO-d_6.

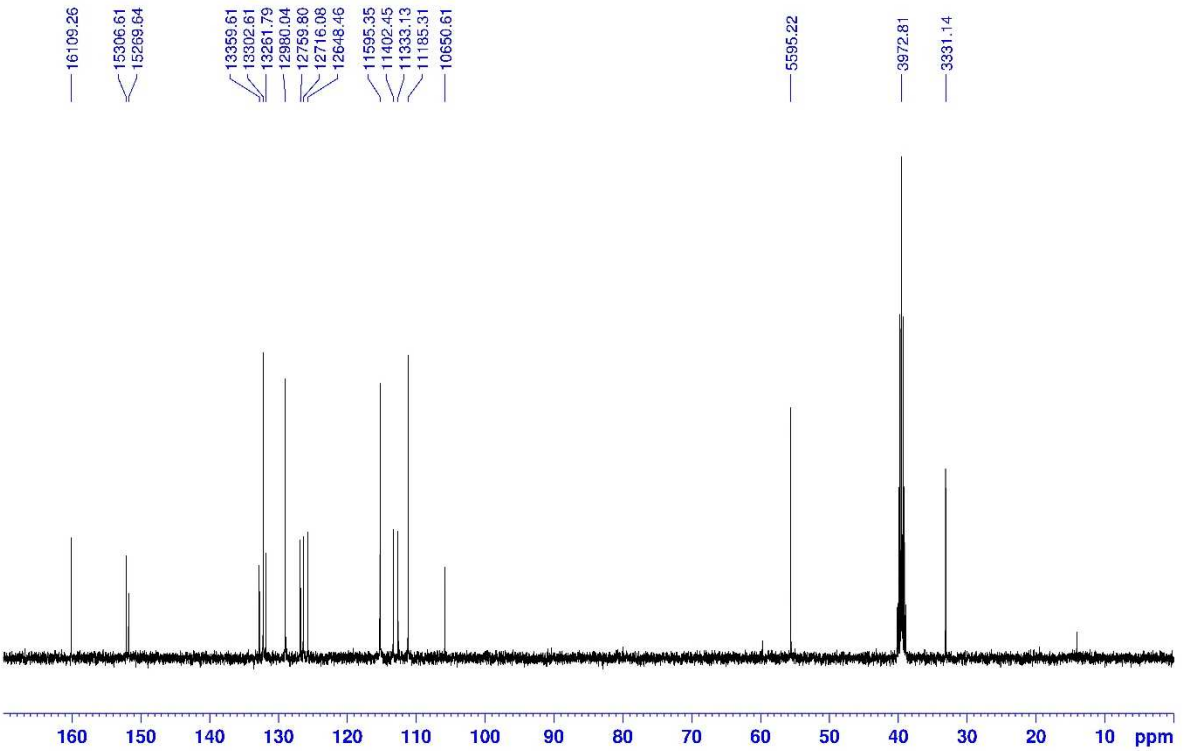

Figure 4.42 ^{13}C NMR of derivative **F7** in DMSO-d_6.

Derivative C1

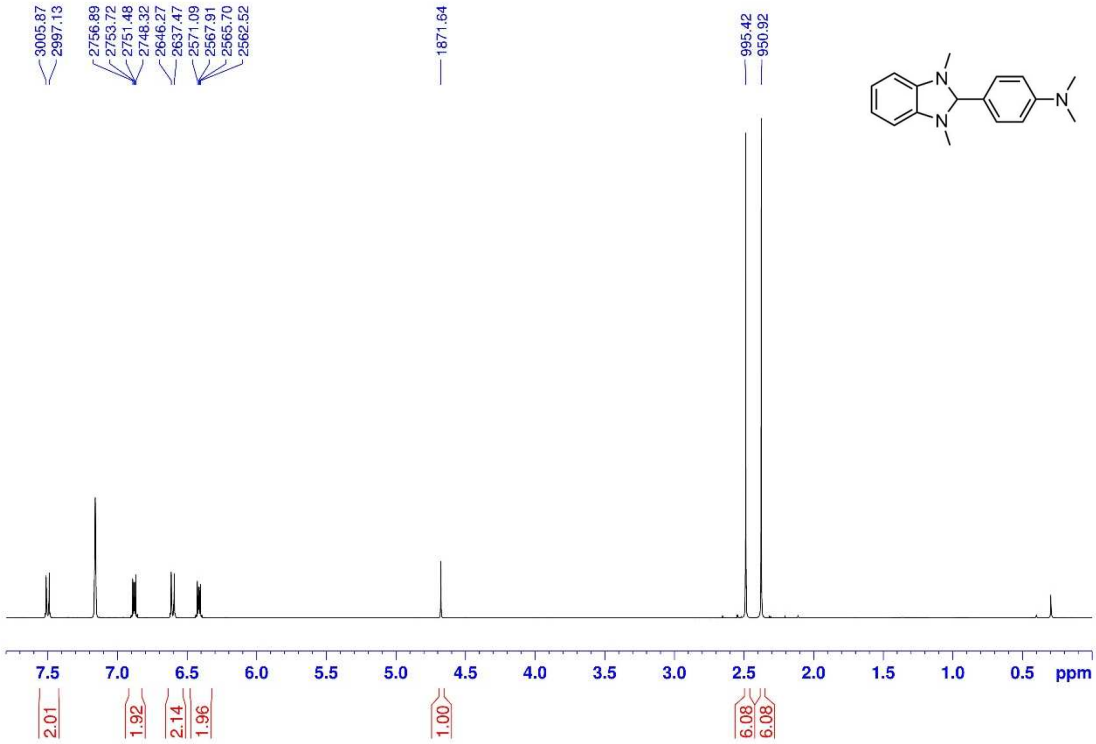

Figure 4.43 ^{1}H NMR of derivative **C1** in benzene-d_6.

Derivative C2

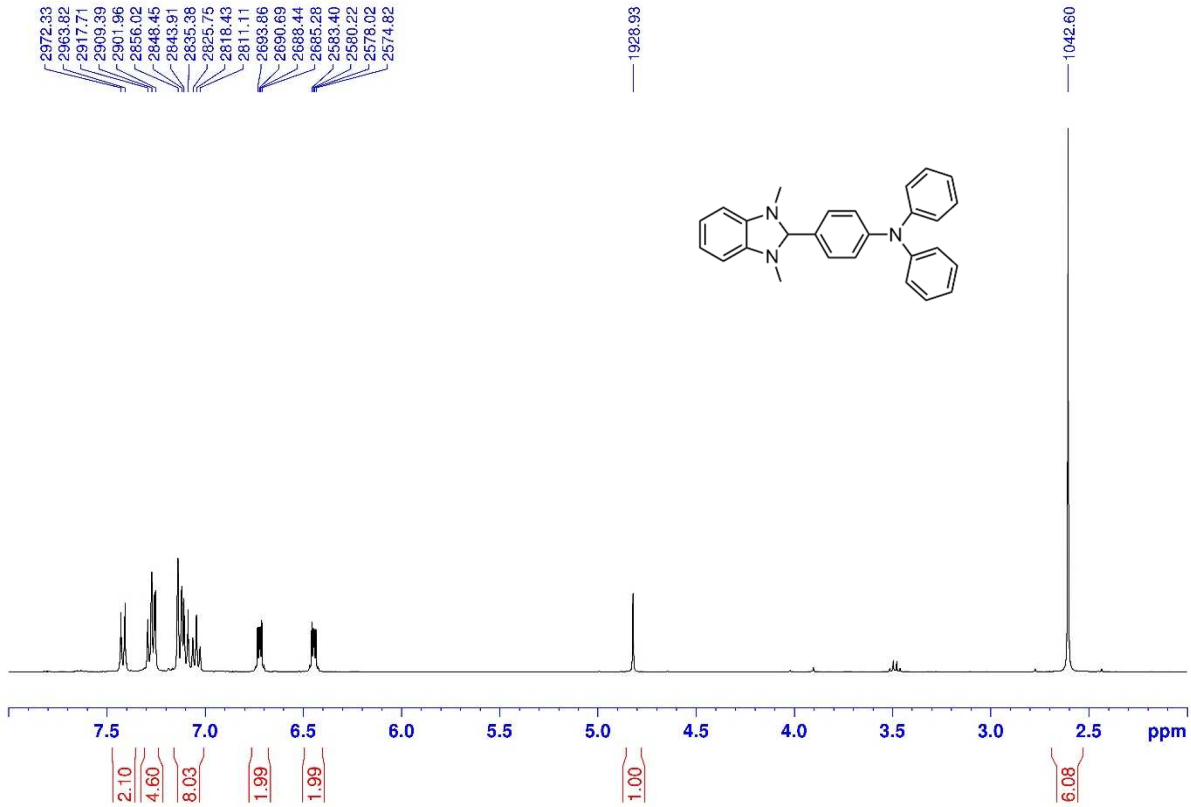

Figure 4.44 ^{1}H NMR of derivative **C2** in$CDCl_3$.

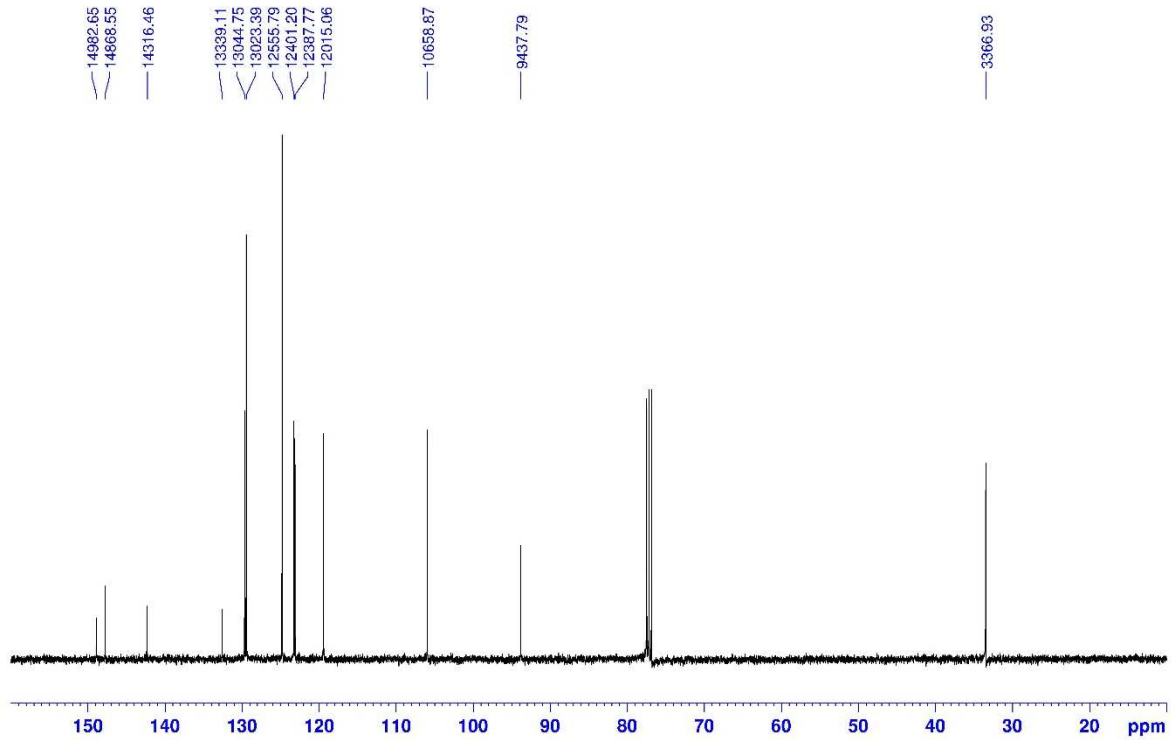

Figure 4.45 ^{13}C NMR of derivative **C2** in$CDCl_3$.

Derivative C3

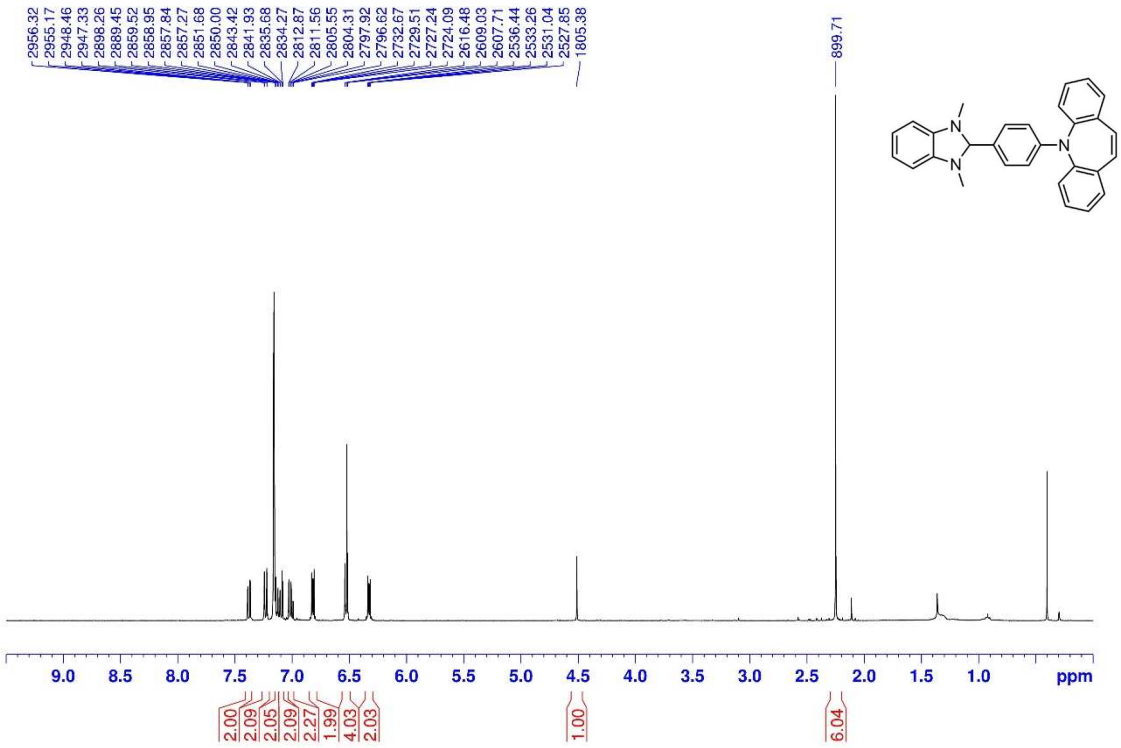

Figure 4.46 ^{1}H NMR of derivative **C3** in benzene-d_6.

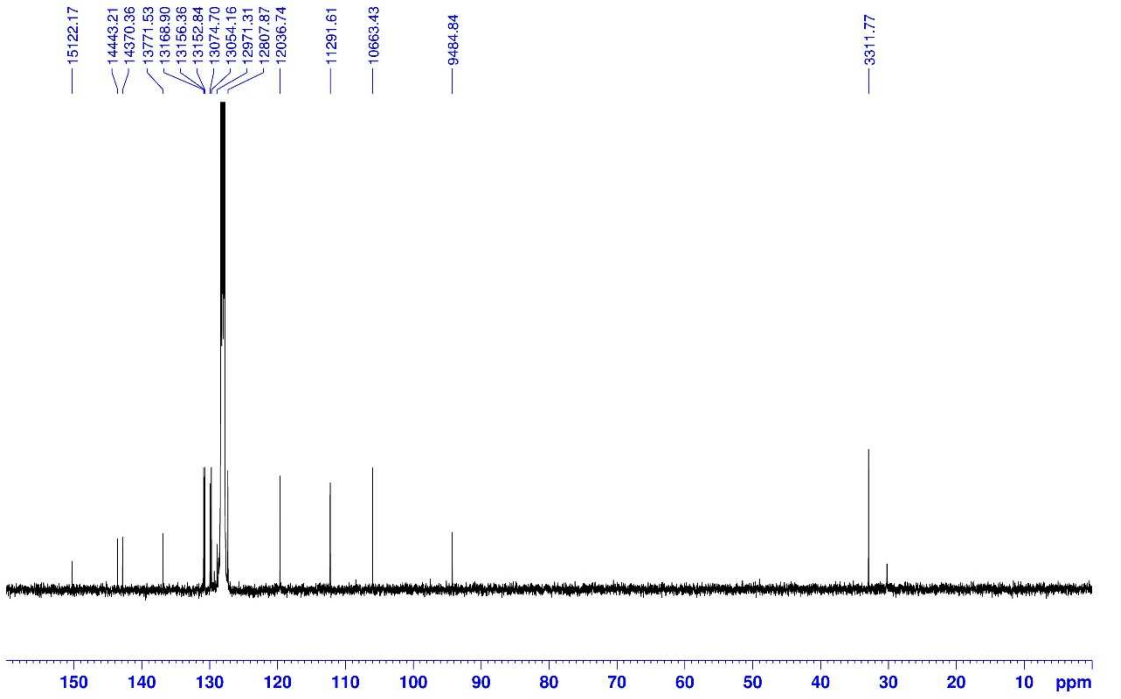

Figure 4.47 ^{13}C NMR of derivative **C3** in benzene-d_6.

Derivative C4

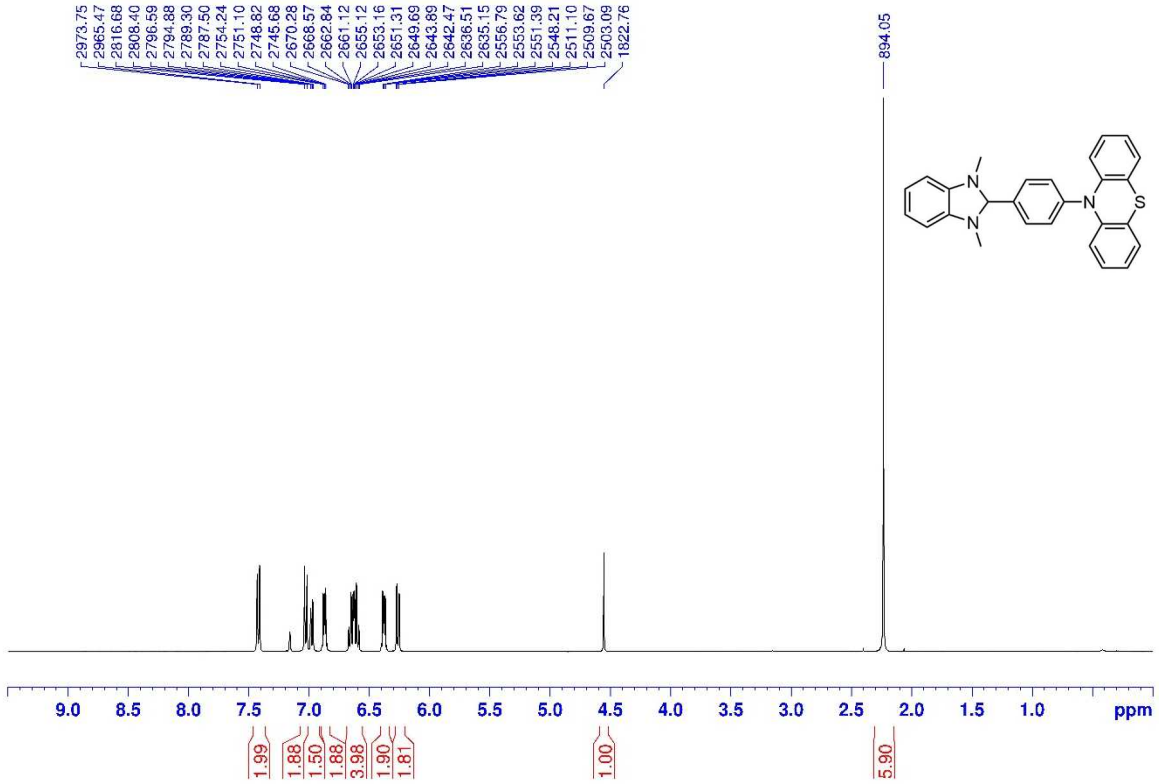

Figure 4.48 ^{1}H NMR of derivative **C4** in benzene-d_6

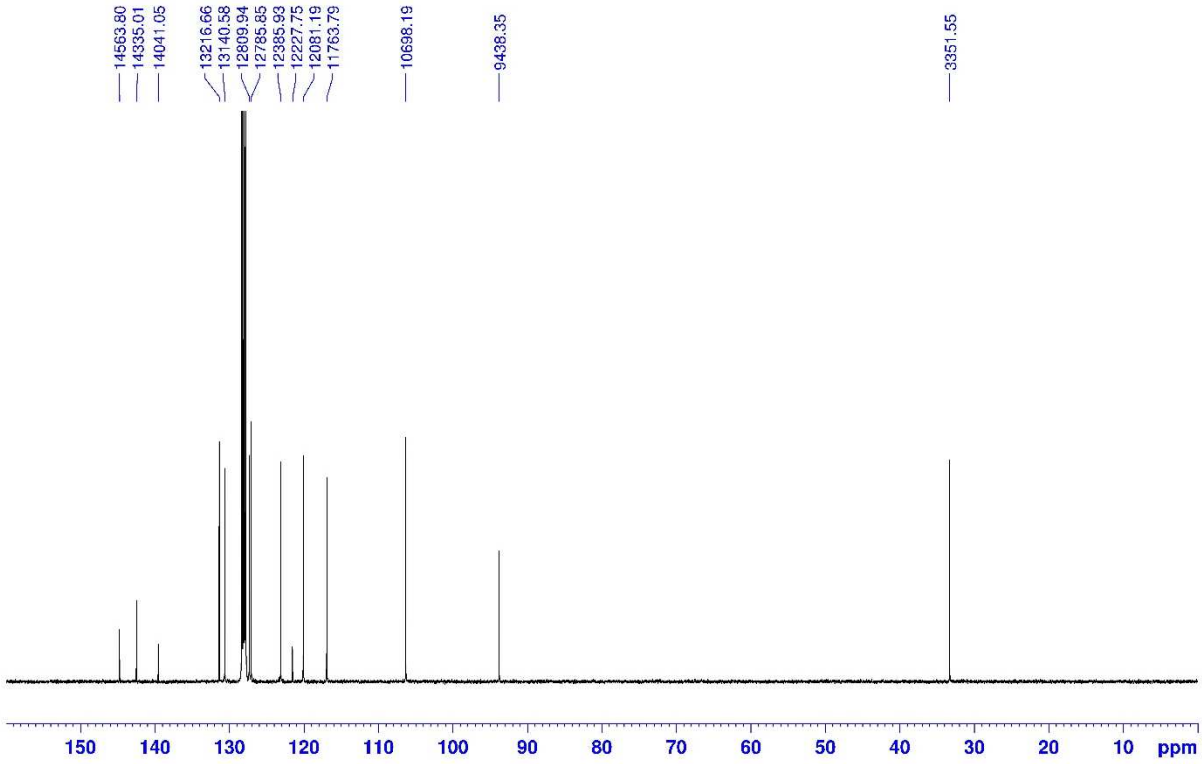

Figure 4.49 ^{13}C NMR of derivative **C4** in benzene-d_6.

Derivative C5

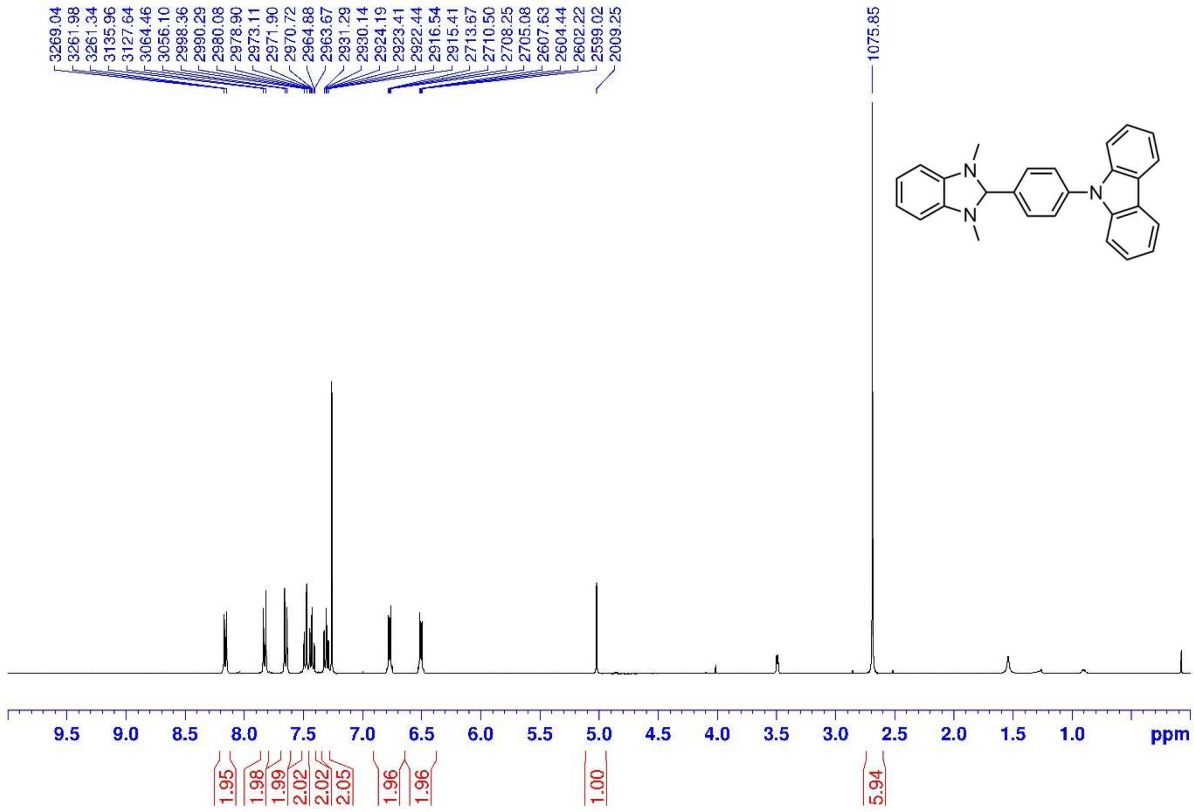

Figure 4.50 ^{1}H NMR of derivative **C5** in $CDCl_3$.

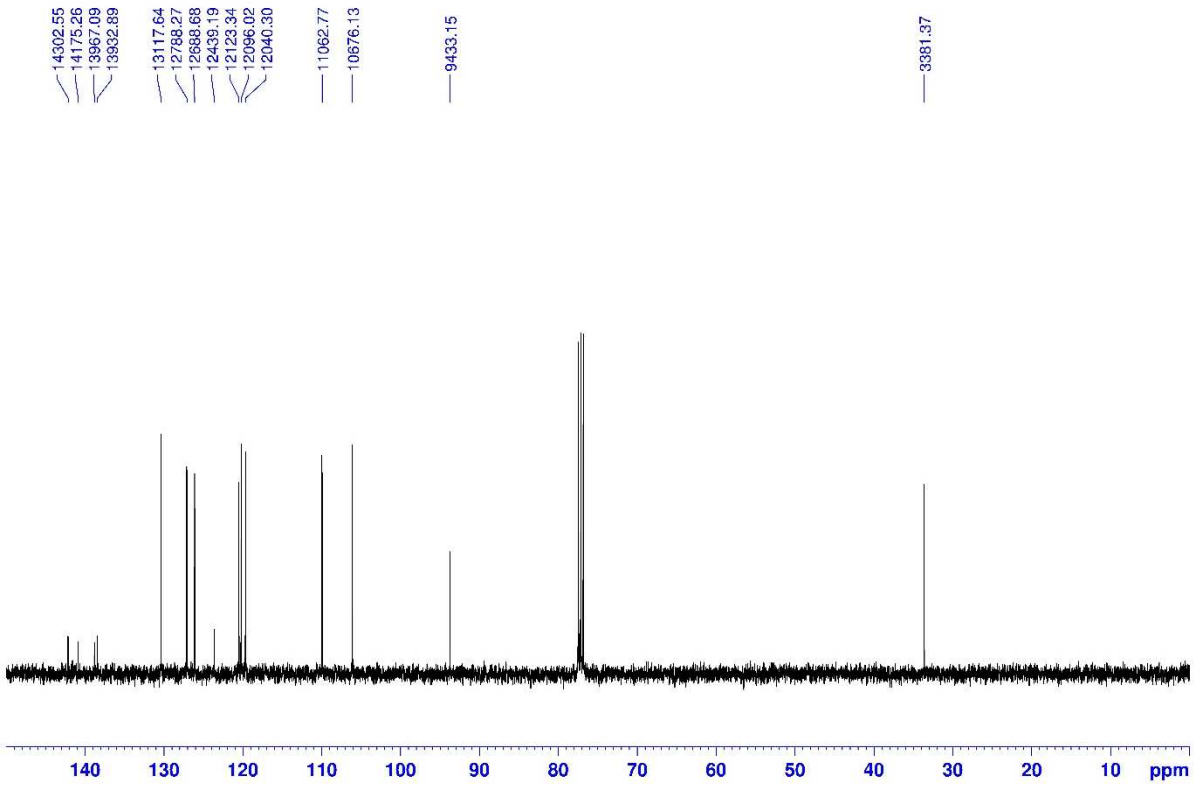

Figure 4.51 ^{13}C NMR of derivative **C5** in $CDCl_3$.

Derivative C6

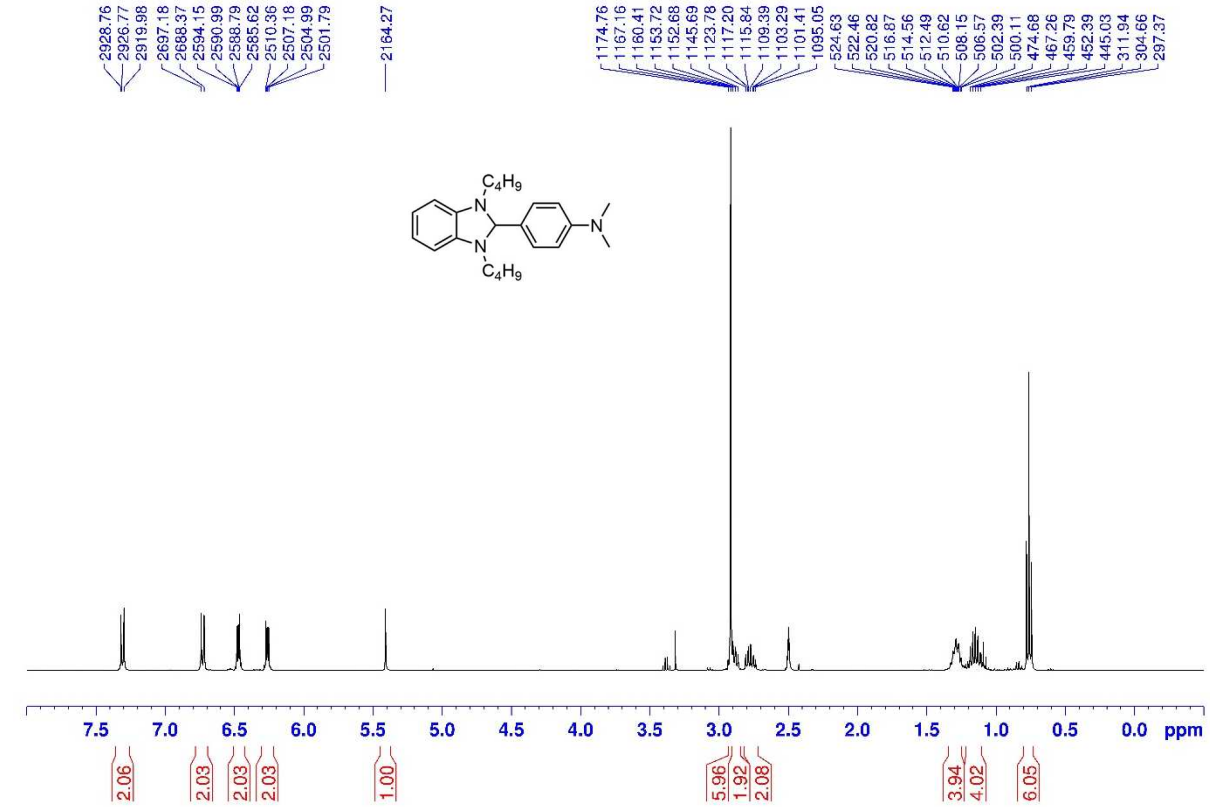

Figure 4.52 ^{1}H NMR of derivative **C6** in DMSO-d$_6$.

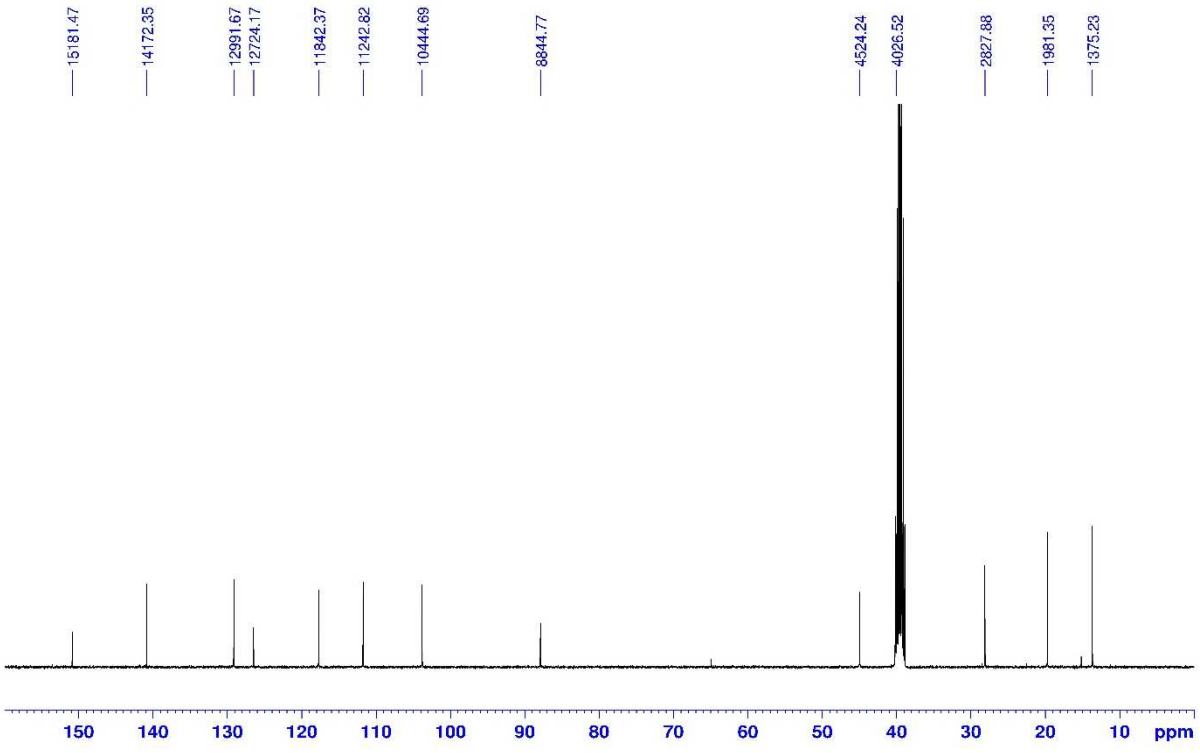

Figura 4.53 ^{13}C NMR of derivative **C6** in DMSO-d$_6$.

Derivative C7

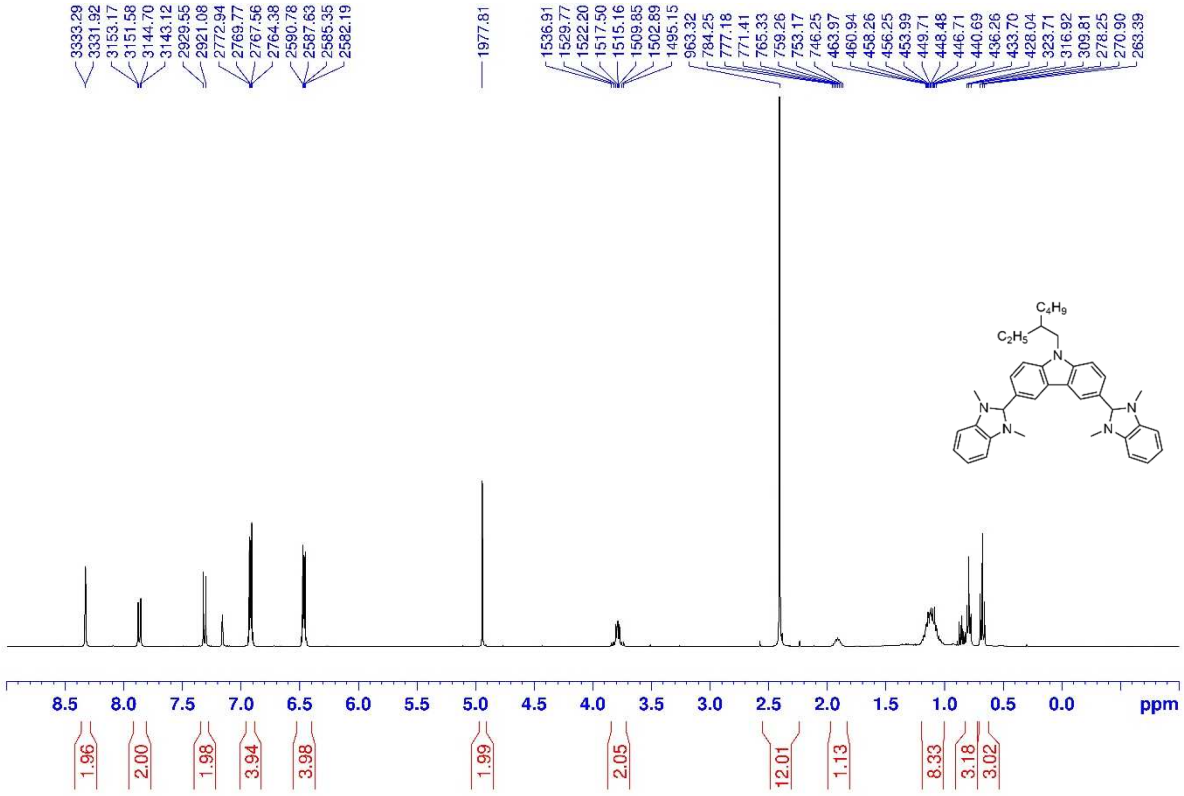

Figure 4.54 ^{1}H NMR of derivative **C7** in benzene-d_6.

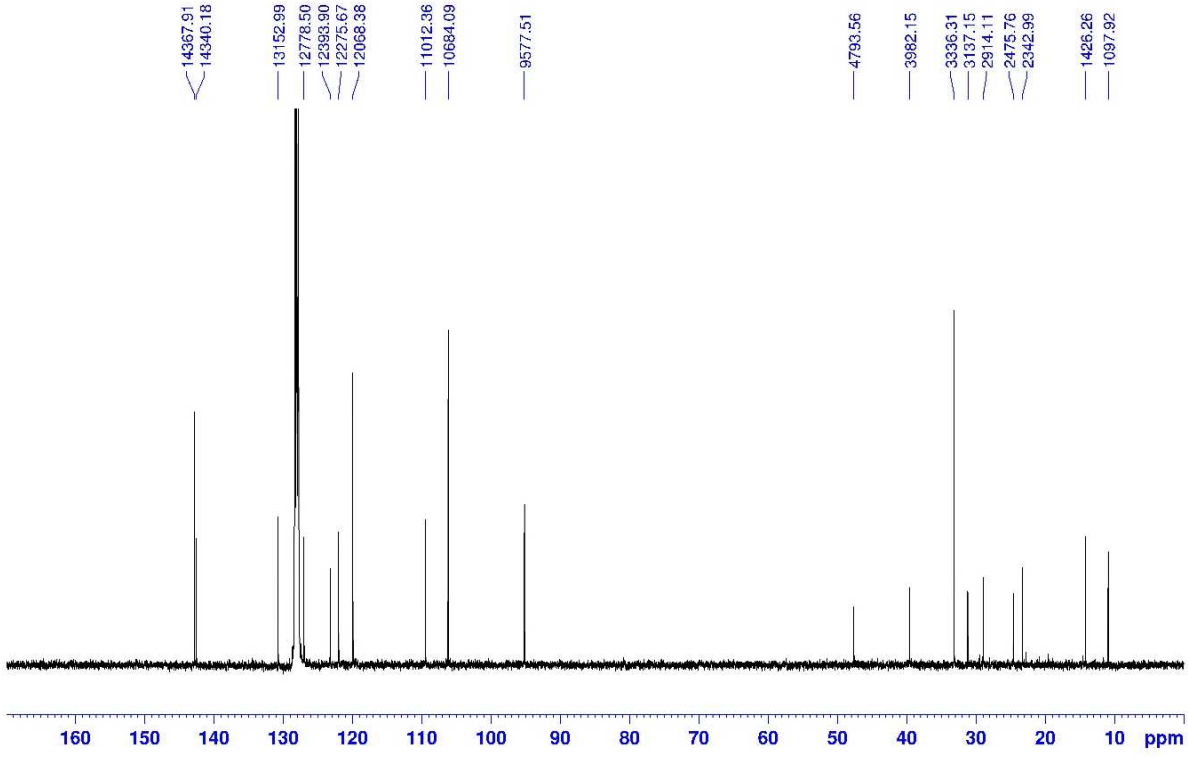

Figure 4.55 ^{13}C NMR of derivative **C7** in benzene-d_6.

Derivative C8

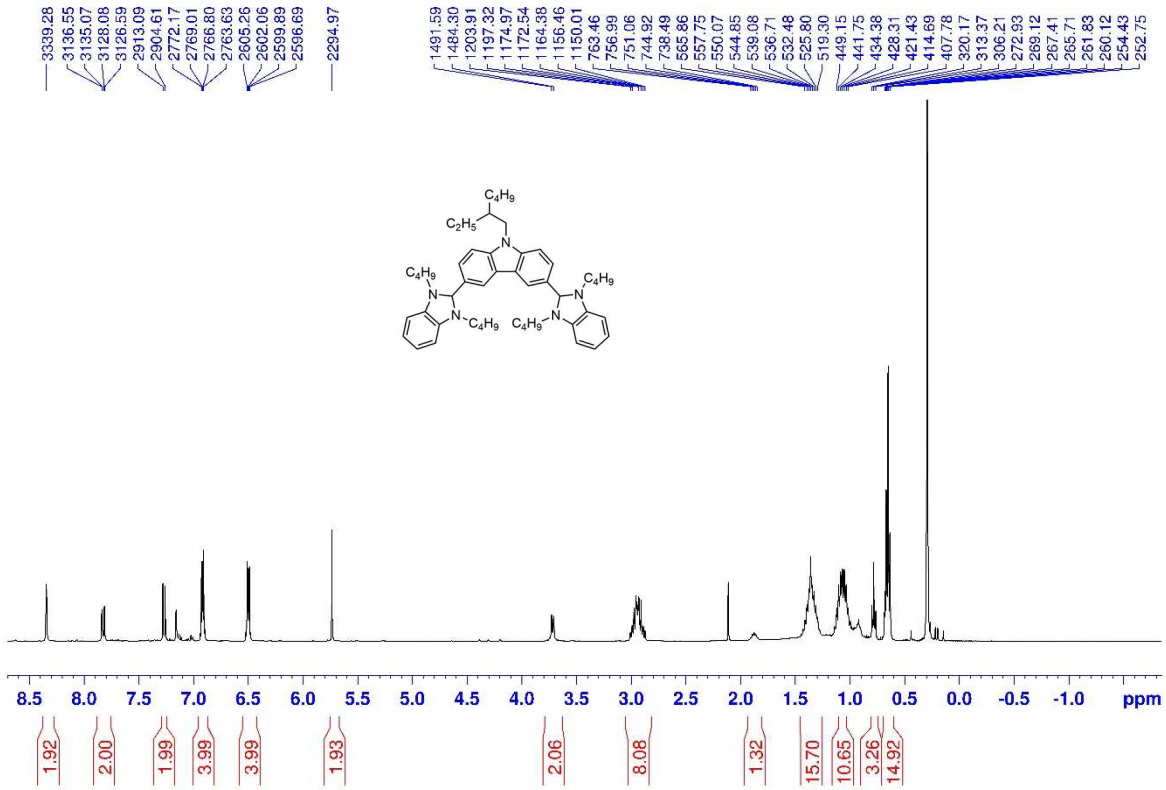

Figure 4.56 ^{1}H NMR of derivative **C8** in benzene-d$_6$. Integral of multiplet at 1.15-0.99 ppm exceed the expected value (8H) due to residual petroleum ether.

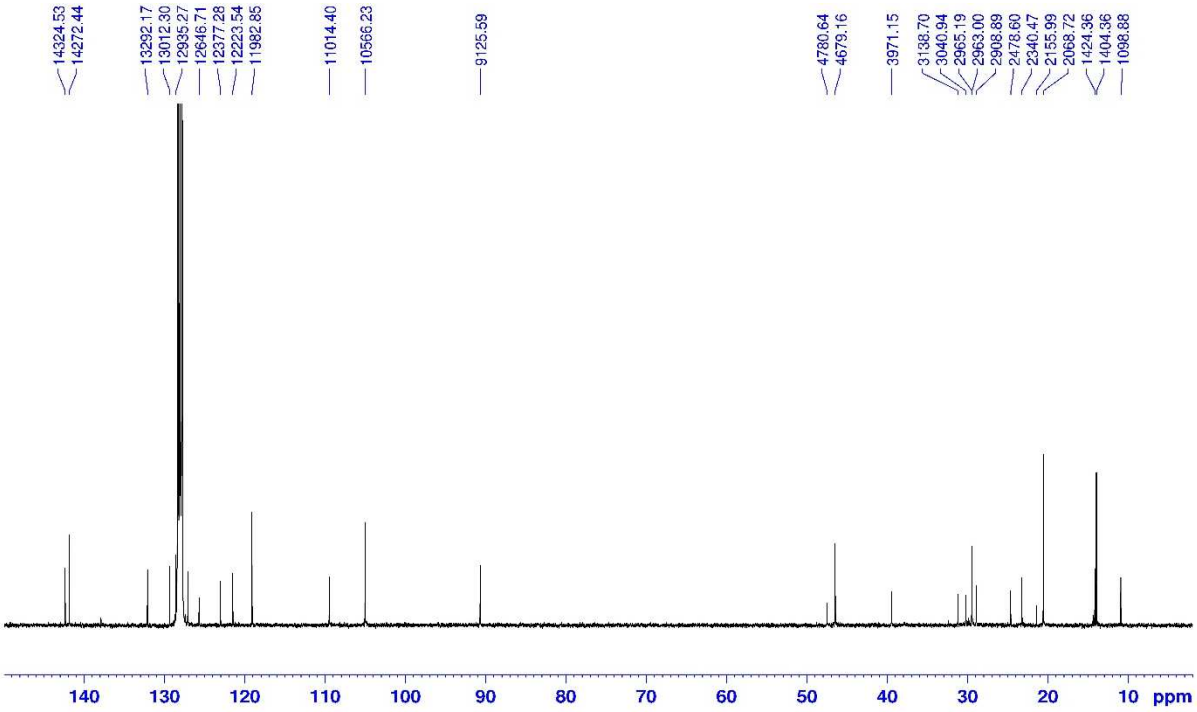

Figure 4.57 ^{13}C NMR of derivative **C8** in benzene-d$_6$.

Derivative C9

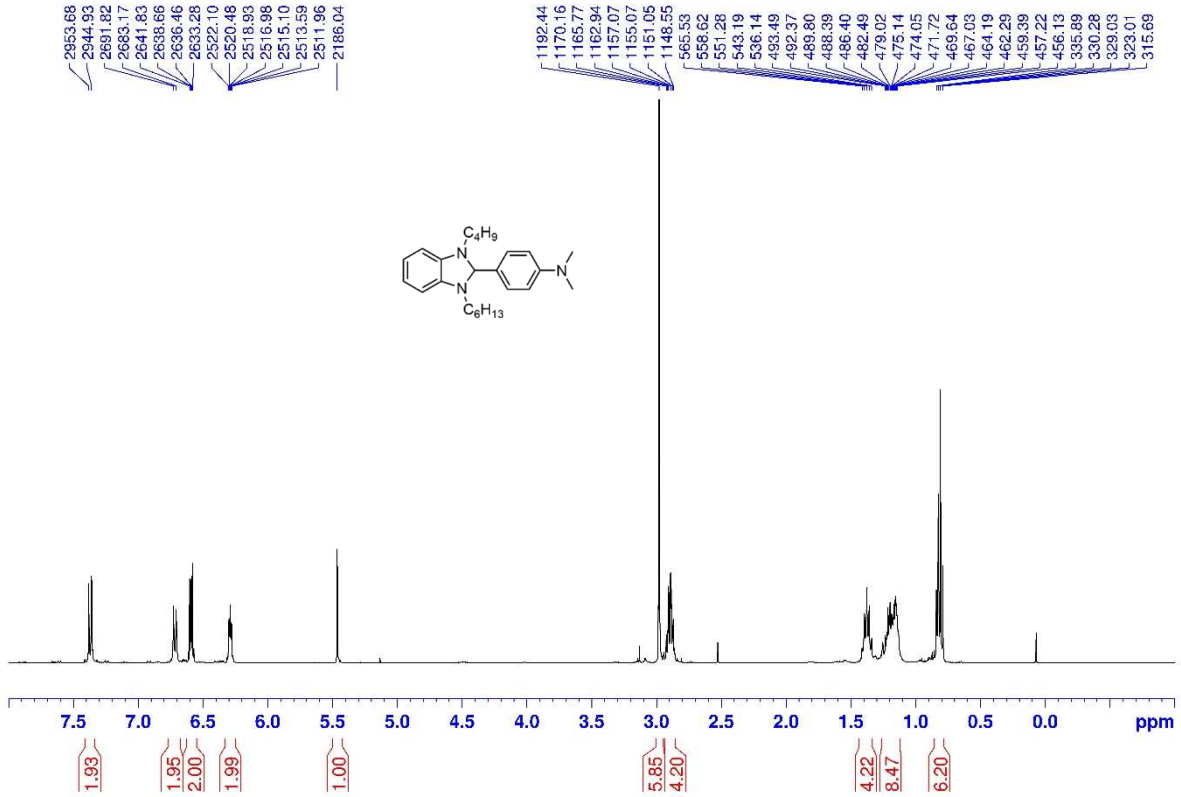

Figure 4.58 ^{1}H NMR of derivative **C9** in $CDCl_3$.

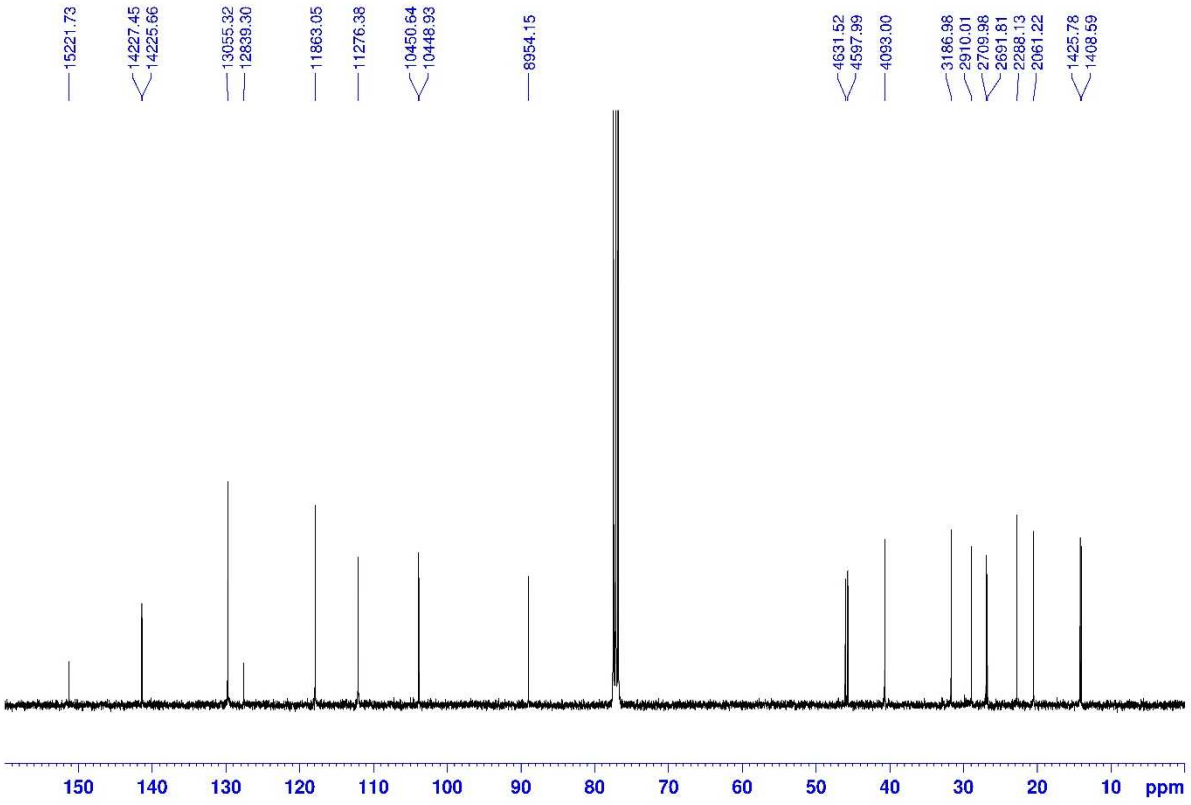

Figure 4.59 ^{13}C NMR of derivative **C9** in $CDCl_3$.

Derivative C10

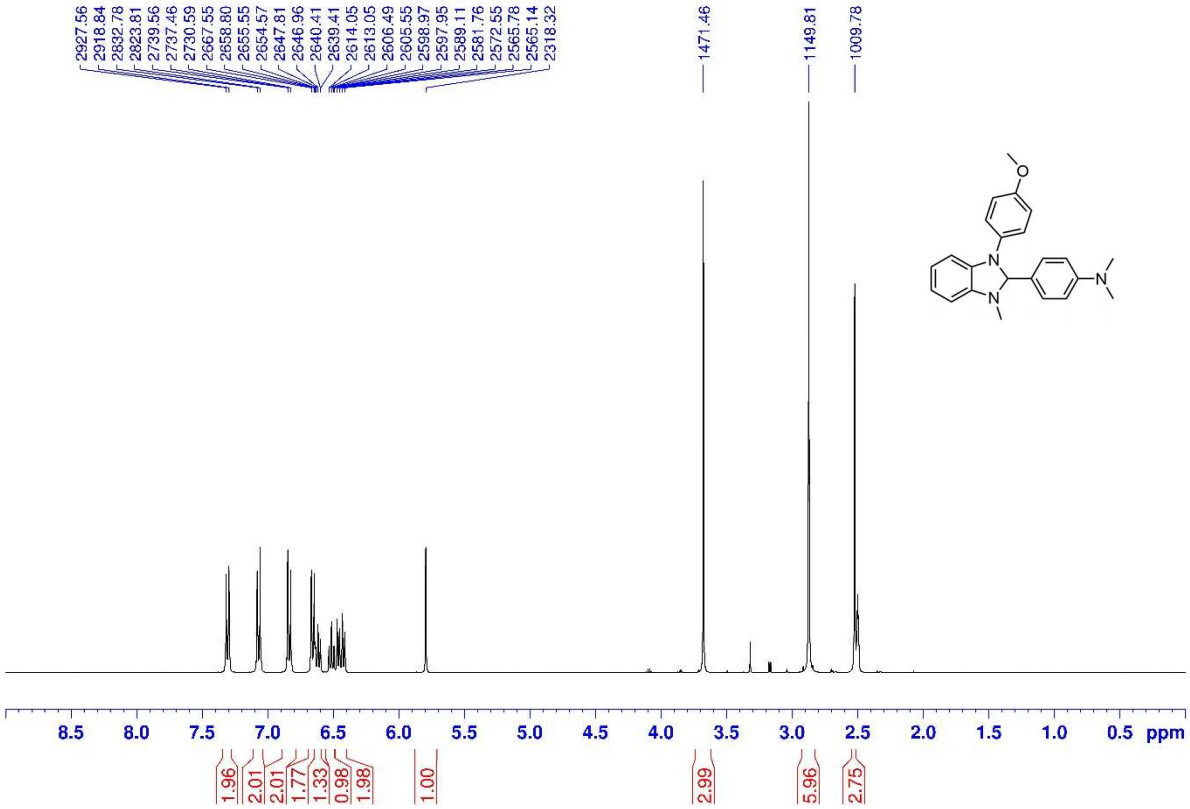

Figure 4.60 [1]H NMR of derivative **C10** in DMSO-d$_6$.

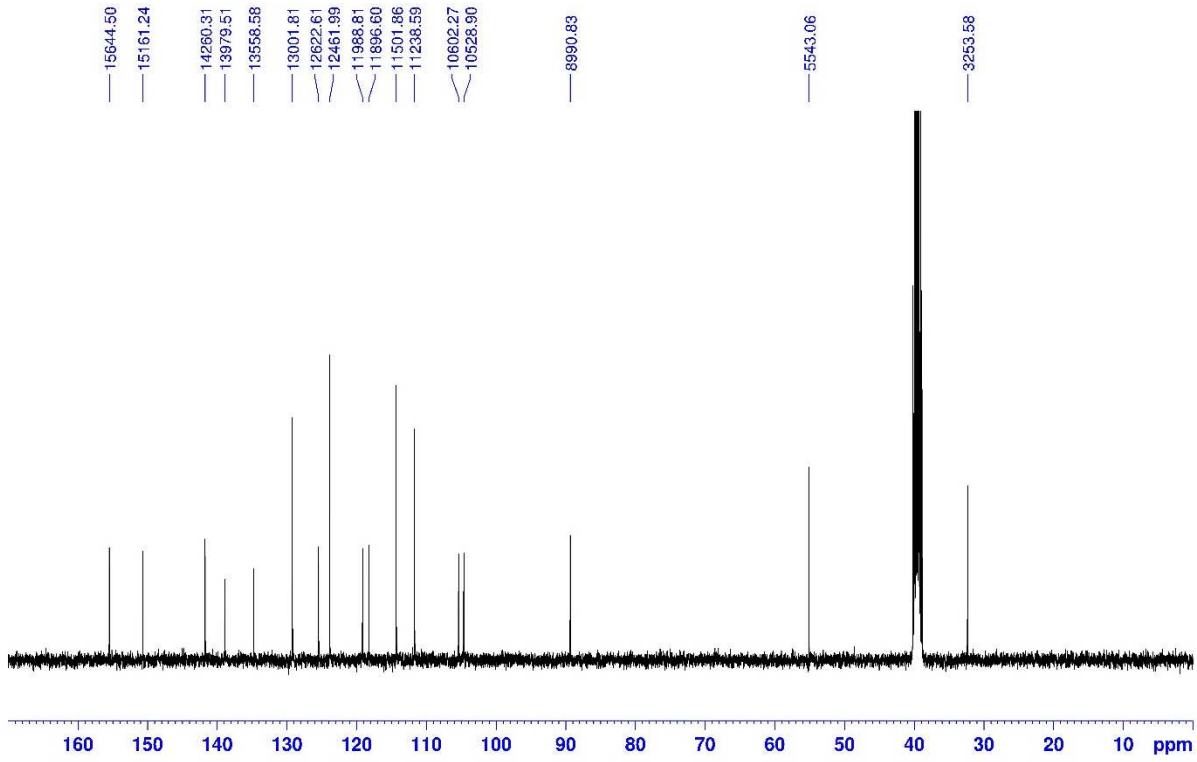

Figure 4.61 [13]C NMR of derivative **C10** in DMSO-d6.

NMR of DPBI$^+$ OTf$^-$

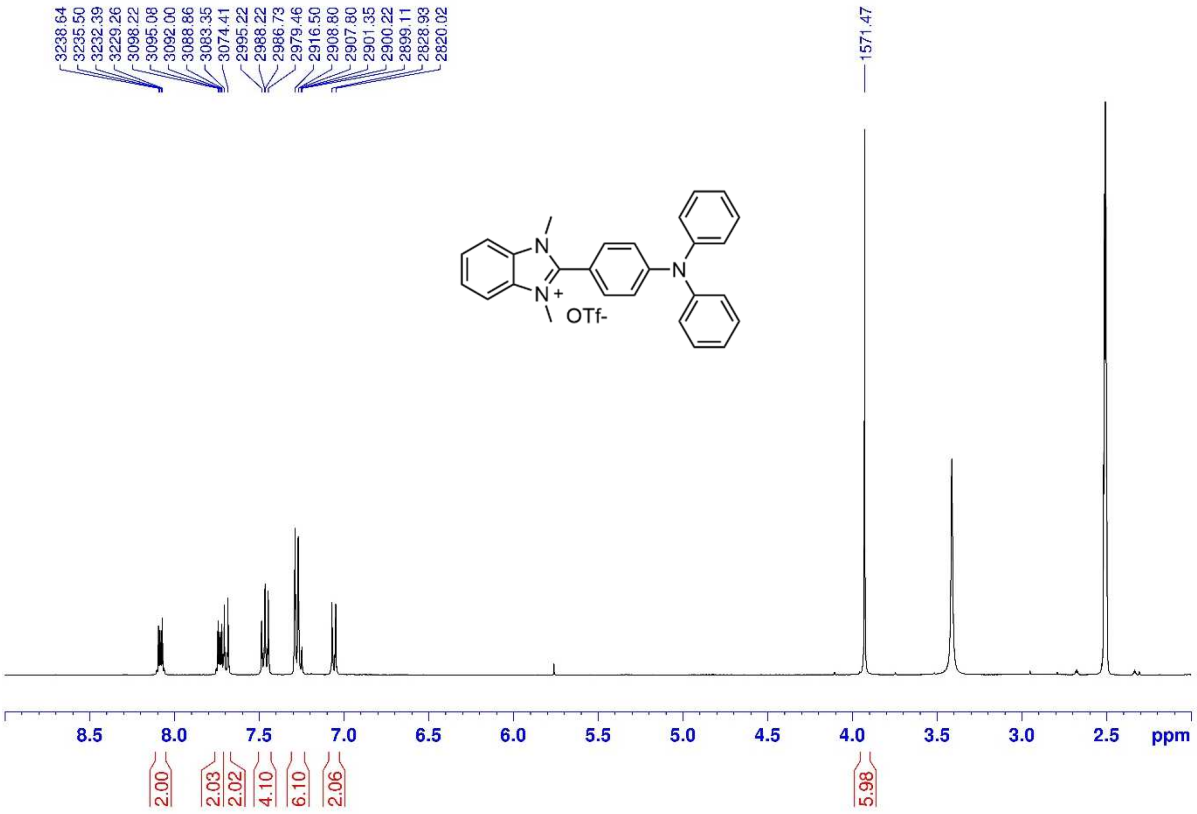

Figure 4.62 ^{1}H NMR of DPBI$^+$ OTf$^-$ in DMSO-d$_6$.

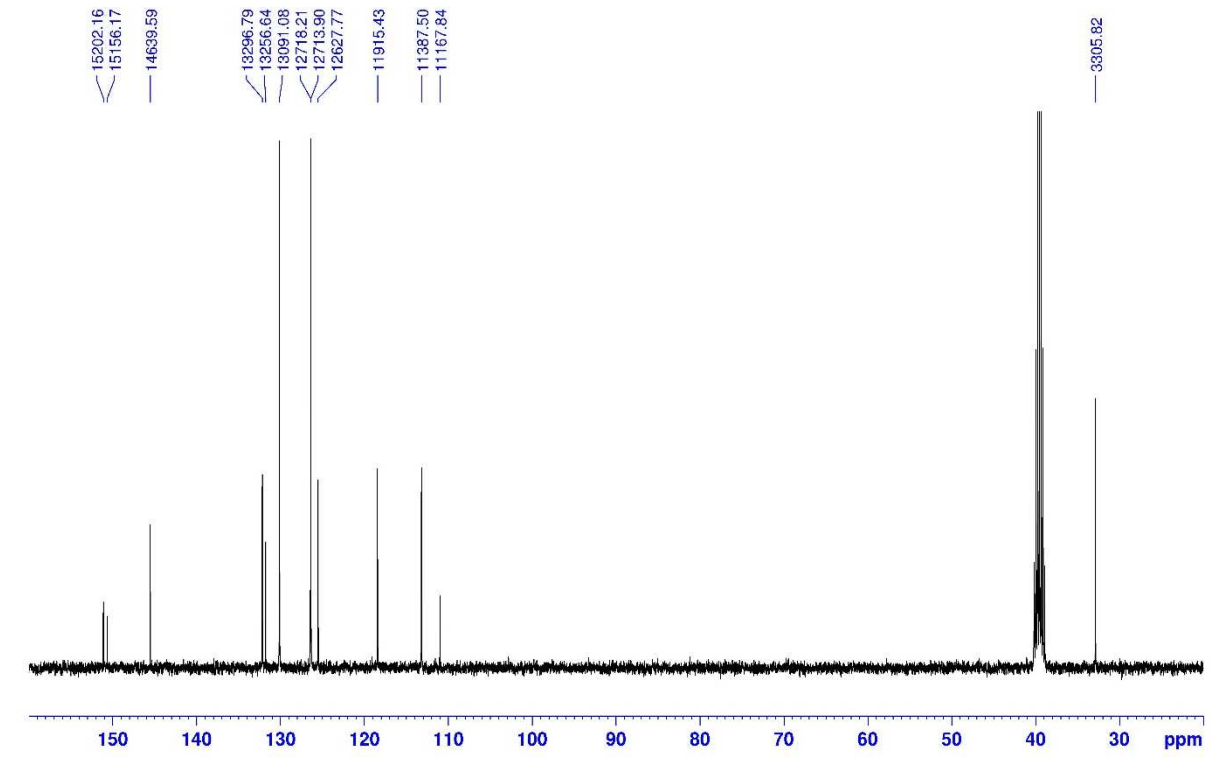

Figure 4.63 ^{13}C NMR of DPBI$^+$ OTf$^-$ in DMSO-d$_6$

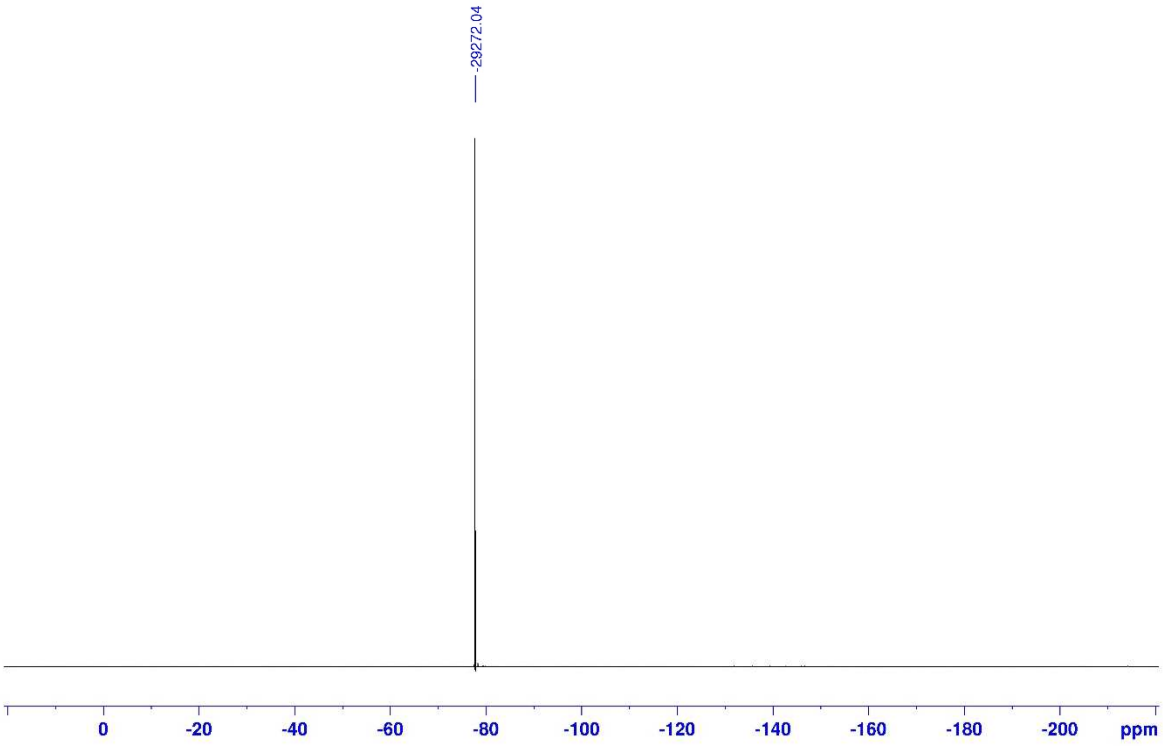

Figure 4.64 ^{19}F NMR of $DPBI^{+}$ OTf^{-} in DMSO-d_6

4.5.3. Thermal characterization

4.5.3.1. Differential Scanning Calorimetry

Melting point of dopants was evaluated via DSC analysis. Measurements were performed with a DSC 1 STAR^e System from Mettler Toledo, using aluminium crucibles. Calibration was performed with an Indium standard. All DSC measurements were conducted under N_2 flow (80 $mLmin^{-1}$) and with a rate of 10°$Cmin^{-1}$.
DSC crucibles were prepared and closed inside a glovebox, under argon atmosphere (O_2 < 0.1 ppm, H_2O level < 0.1 ppm). DSC crucibles were punctured immediately before performing the analysis.
DSC methods:

- AnDMBI: heating from 25°C to 225°C (sample weight: 6.29 mg)
- PThBI: heating from 25°C to 220°C (sample weight: 8.50 mg)
- IStBI: heating from 25°C to 230°C (sample weight: 6.87 mg)
- CBzBI: heating from 25°C to 280°C (sample weight: 8.05 mg)

In the case of N-DMBI-H, we considered the first heating cycle of DSC characterization reported in Chapter 3.

4.5.3.2. Thermogravimetric analysis

TGA measurements were performed with a TGA/DSC 1 STARe System from Mettler Toledo, using alumina crucibles. The analyses were performed with the following TGA method: heating from 35°C to 600 °C with a 10°C/min rate, under 50 mL/min N_2 flow.

- AnDMBI: sample weight 12.8300 mg
- PThBI: sample weight 3.2215 mg
- IStBI: sample weight 3.3310 mg
- CBzBI: sample weight 15.2095 mg
- N-DMBI-H: sample weight 19.9832 mg
- $2C_4$-DMBI: sample weight 34.3096 mg

In the case of $2C_4$-DMBI, the crucible was prepared inside the glove box, under argon, and exposed to air only for few seconds before TGA analysis under N_2 flow to avoid oxidation of the product.

4.5.4. Electrochemical characterization

Electrochemical characterization of the synthesised dopants was performed inside an argon filled glove box (O_2 <0.1 ppm, H_2O <0.1 ppm) using a three-electrode cell. An AMEL glassy carbon pin electrode (3 mm diameter) mirror polished with deagglomerated alumina paste (0.3 μm, purchased from Buelher) and milliq H_2O was used as working electrode, a platinum wire was used as counter electrode and an Ag/AgCl wire

was used as quasi-reference electrode. The obtained potentials were then referred to the Fc/Fc^+ redox couple. Anhydrous acetonitrile (99.8% Alfa Aesar) containing around 2.0 mM of substrate and 0.1 M of tetrabutylammonium perchlorate (99% Thermo Scientific) as supporting salt was used as electrolyte.

Cyclic voltammetry (CV) analysis was performed at 50 mV/s, while Differential Pulse Voltammetry (DPV) was performed using either steps of 5mV/s and modulation amplitude of 50 mV or step of 2mV/s and modulation amplitude of 25 mV. Since the systems showed high resistance, an Ohmic drop compensation between 160-200 Ω was applied. Oxidation and reduction potentials (E_0) were evaluated from DPV analysis using the following formula[15]

$$E_0 = E_p \pm \frac{\Delta E}{2}$$

were ∆E is the modulation amplitude (∆E >0 for oxidation processes and ∆E <0 for reduction processes) and E_p is the DPV peak value. Oxidation and reduction potentials were extrapolated from Cyclic Voltammetry curves as mean value between reduction and oxidation peaks, if present, otherwise the peak onset was considered a good estimation.

Once the oxidation and reduction potentials were evaluated, HOMO and LUMO energy levels of the compounds were calculated with respect to Fc/Fc^+ couple using the formula

$$E_{vac} = -e(E_0 + 4.8V)$$

Differential Pulse Voltammetry measurements

	E_{ox} (V)		E_{red}(V)
N-DMBI-H	-0.22	N-DMBI$^+$ OTf$^-$	-2.28
DPBI	-0.21	DPBI$^+$ OTf$^-$	-2.00
AnDMBI	-0.11	AnDMBI$^+$ OTf$^-$	-2.15
IStBI	-0.21	IStBI$^+$ OTf$^-$	-2.20
CBzBI	-0.11	CBzBI$^+$ OTf$^-$	-1.93
PThBI	-0.10	PThBI$^+$ OTf$^-$	-1.99
$2C_4$-DMBI	-0.22	$2C_4$-DMBI$^+$ PF_6^-	-2.38

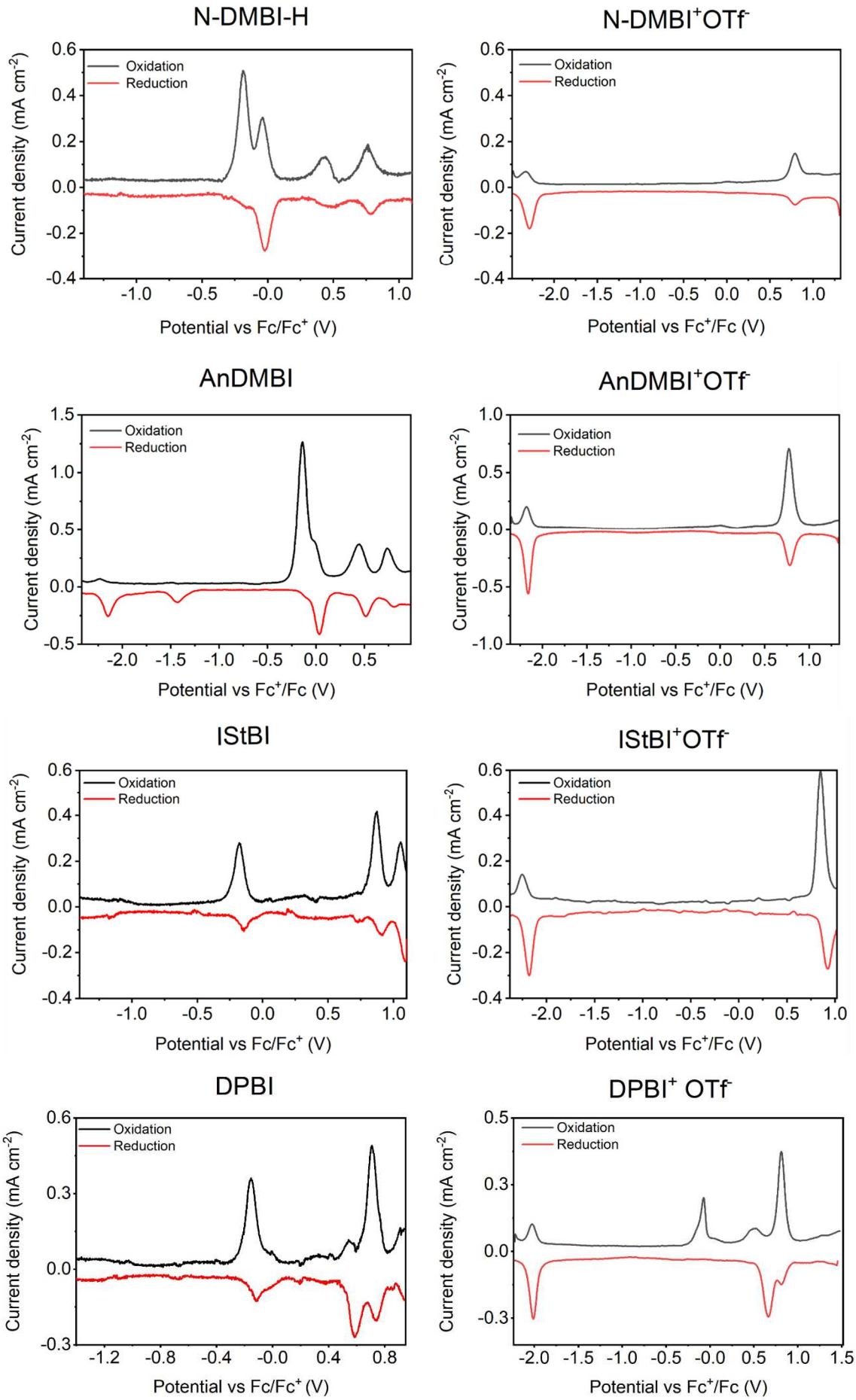
N-DMBI-H
Oxidation
Reduction
Current density (mA cm-2)
Potential vs Fc/Fc+ (V)
N-DMBI+OTf-
Oxidation
Reduction
Current density (mA cm-2)
Potential vs Fc+/Fc (V)
AnDMBI
Oxidation
Reduction
Current density (mA cm-2)
Potential vs Fc+/Fc (V)
AnDMBI+OTf-
Oxidation
Reduction
Current density (mA cm-2)
Potential vs Fc+/Fc (V)
IStBI
Oxidation
Reduction
Current density (mA cm-2)
Potential vs Fc/Fc+ (V)
IStBI+OTf-
Oxidation
Reduction
Current density (mA cm-2)
Potential vs Fc+/Fc (V)
DPBI
Oxidation
Reduction
Current density (mA cm-2)
Potential vs Fc/Fc+ (V)
DPBI+ OTf-
Oxidation
Reduction
Current density (mA cm-2)
Potential vs Fc+/Fc (V)

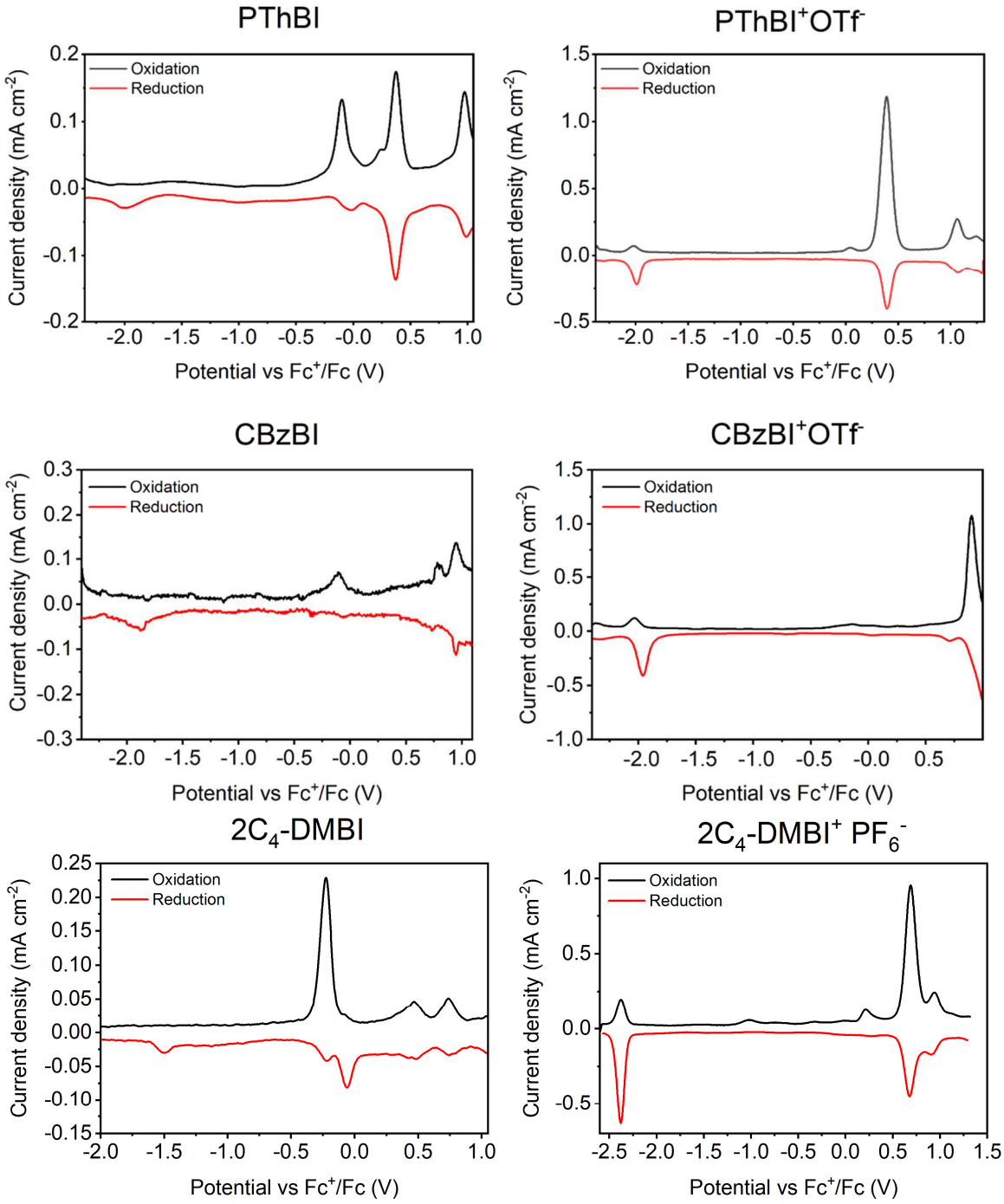

4.5.5. Preparation and characterization of films analysed in preliminary studies on IStBI

Film preparation and characterization was performed by Pietro Rossi and Giulia Coco (Italian Institute of Technology IIT).

4.5.5.1. Substrates Preparation for Conductivity Measurements

Corning glass (low alkali, 1737F) slides were cut into 15 mm × 15 mm pieces. Metallic contacts were patterned on the substrates through a shadow mask by thermal evap-

oration (MB-ProVap-3) depositing a 3 nm Cr adhesion layer and a thick 50 nm Au layer. Each electrode was 3 mm × 15 mm and the interelectrode distance was 5 mm.

4.5.5.2. Thin Films Deposition

A stock solution of P(NDI2OD-T2) (Polyera ActivInk N2200 M_n = 37.4 kDa, polydispersity index PDI of 2.1) in toluene (Sigma-Aldrich) was prepared with a concentration of 10 gL^{-1} and was kept stirring at 60 °C overnight to ensure complete dissolution. Using the same solvent, solutions of IStBI were prepared at a concentration of 5 g L^{-1}. Only fresh-made (<2 h) dopant solutions were used. To perform solution doping, aliquots of dopant and polymer stock solutions were mixed at corresponding amounts to reach the selected doping concentration. Finally, toluene was added to adjust all the aliquots to the same polymer concentration. The glass substrates were cleaned sequentially in deionized water, acetone and 2-propanol (Sigma-Aldrich) submerged in an ultrasonic bath for 10 min each. Following, the substrates were exposed to a O_2 plasma (Femto Diener electronic) at 100 W for 10 min. The thin films were cast via spin-coating technique inside a N_2-filled glovebox, the deposition parameters were 1000 rpm for 60 s followed by 3000 rpm for 10 s. The samples were then thermally annealed on a hotplate for 2 hours at a temperature comprised in the 120–200 °C range. A thickness in the range of 65 ± 5 nm for all the films was determined using a mechanical profilometer (Alpha-step IQ, KLA Tencor). The same protocol was applied with samples containing N-DMBI-H and DPBI.

4.5.5.3. Electrical conductivity measurements

The I–V characteristics were collected in the current saturation regime employing a two-point contact configuration by means of a probe-station (Wentworth Laboratories) connected to a semiconductor device parameter analyser (Agilent B1500A). Measurements were performed at room temperature (RT) in a N_2-filled glovebox. Forward and backward scans were performed to exclude the presence of hysteresis. The electrical conductivity values were subsequently calculated, considering the geometrical parameters, from the resistance values extrapolated from the I–V curves.

4.5.5.4. Seeback coefficient measurements

The in-plane Seebeck coefficient measurements were performed using a custom setup built for thin films characterization and described in detail in the work of Beretta et al.[52] Measurements were conducted at RT and under vacuum conditions (10^{-4} mbar) to reduce convection phenomena and to avoid samples oxidation. Due to the instrumentation limitations only samples with an electrical resistance below 10 MΩ could be measured.

4.5.6. Preparation and characterization of films doped with different DMBI derivatives

P(NDI2OD-T2) polymer used for the preparation of films containing different DMBI based dopants was synthesized via direct arylation reaction according to a literature procedure.[64] A first batch with M_n of 26.2 kDa and Polidispersity (PDI) of 2.65 was used for evaluation of electrical conductivity, optical characterization and AFM characterization of films doped with most of the derivatives. A second batch with M_n of 37.3 kDa and Polidispersity (PDI) of 3.46 was used for characterization of films doped with PThBI and CBzBI and for all GIWAXS characterizations. Molecular weights of the polymers were evaluated via Gel Permeation Chromatography using an Alliance HPLC System (2690 Separation Module, by Waters). The instrument was equipped with a Tosoh TSKgel SuperHZM-N and a guard column (MW range: 200-700,000 g/mol), a Waters 2410 Differential Refractometer (RI) detector and a Waters 2998 Photodiode Array Detector (PDA).
Chloroform with 0.25% of triethylamine (TEA) was used as solvent. Polystyrene latex was used as reference.

4.5.6.1. Thin Films preparation procedure

All the procedure was performed inside an N_2 filled glove box (O_2 < 5 ppm). P(NDI2OD-T2) polymer was dissolved in anhydrous toluene at a concentration of 12 gL^{-1} and let stirring at 60°C for at least 12 hours to guarantee complete dissolution. The obtained solution was filtered through a 0.45 µm PTFE syringe filter just before use. N-DMBI-H, AnDMBI, 2C_4-DMBI, IStBI, PThBI and CBzBI solutions were prepared at room temperature at concentration of 10 gL^{-1}, 7 gL^{-1}, 13 gL^{-1}, 5 gL^{-1}, 2.8 gL^{-1}, 1.7 gL^{-1} respectively using anhydrous toluene as solvent. Aliquots of polymer and dopant solutions were mixed at room temperature just before the deposition to reach the desired dopant concentration. Toluene was added to each solution to reach the same polymer concentration (between 5 gL^{-1} and 8.75 gL^{-1} depending on the dopant used). The obtained solutions were used within 1 hour from preparation.
Microscope slides were cut into 15 mm × 15 mm pieces. Slides were cleaned with deionized water, acetone and 2-propanol (20 minutes in ultrasonic bath per each solvent) and then oven dried. For conductivity measurements, metallic contacts (5 nm Cr adhesion layer, followed by a 50 nm Au layer) were patterned on the substrates using a shadow mask and an Angrstrom engineering evaporator. Three active channels were obtained on each glass substrates having width (w) × length (l) respectively of 14 mm × 2.5 mm, 7 mm × 2.5 mm and 6 mm × 3 mm. The cleaning procedure was repeated and the obtained substrates were exposed to UV-Ozone treatment for 10 minutes. Thin polymer films were then spin-coated from the obtained solutions onto the substrates (1000 rpm for 60 seconds, 3000 rpm for 5 seconds) and annealed at 180 °C for two hours under inert atmosphere. Film thickness was measured either with an AMBIOS XP-100 profilometer or with AFM and was evaluated to be (on average) 50 ± 8 nm in

the case of N-DMBI-H, 37 ± 6 nm in the case of An-DMBI and 2C4-DMBI, 40 ± 7 nm in the case of IStBI, 26 ± 3 nm in the case of PThBI and 23 ± 6 nm in the case of CBzBI. Film used for the characterization of pristine polymer conductivity was prepared according to the same procedure using a 11 gL^{-1} polymer solution (film thickness 70±5 nm).

4.5.6.2. Electrical characterization

The I–V characteristics of the obtained films were collected using a two-point contacts configuration by means of a Signatone 1160 Series Probe-Station connected to a Keithley 4200 Semiconductor Parameter Analyzer. Measurements were performed at room temperature in a N_2-filled glovebox. Forward and backward scans were performed to exclude presence of hysteresis. The electrical conductivity σ was subsequently calculated using the formula $\sigma = l(Rwt)^{-1}$, where l is the active channel length, w is the channel width, t is the film thickness and R is the resistance values extrapolated from the I–V curves. Conductivity was evaluated as average of the values obtained from the three active channels patterned on each sample. Error bars were evaluated considering the standard deviation on the average value obtained and the error on the film thickness evaliation.

4.5.6.3. Optical characterization of thin films

Films for optical characterization were obtained using the same solutions and procedure of those prepared for electrical characterization but using 2 cm × 2 cm unpatterned glass substrates. UV-Vis-NIR absorption measurements of the obtained films were acquired in the 1200-300 nm range using a Lambda 750 UV/Vis Spectrometer by Perkin Elmer. Doped films were kept under inert atmosphere and were exposed to air just a few seconds before the spectrum acquisition.

4.5.6.4. AFM characterization

Film for AFM measurements were prepared according to the same procedure used for electrical characterization on plain glass substrates and then annealed at 180°C or dried under vacuum depending on the selected sample. AFM images were obtained using a Veeco-Bruker Multimode® AFM working in tapping mode and AFM tapping tip (BudgetSensors, Tap300-G) with a force constant of 40 Nm^{-1} and a resonant frequency of 300 kHz. Images were analyzed using Gwyddion software.

4.5.6.5. GIWAXS measurements

Samples for GIWAXS measurements were obtained following a procedure similar to the one described in section **4.5.6.1** but using silicon substrates instead of glass. All samples were obtained using solutions containing a dopant concentration of 40% in

moles with respect to the polymer repeating unit. Toluene was added to each solution so to reach the same polymer concentration, so to obtain films with similar thickness.

GIWAXS experiments were performed at the BL11, NCD-SWEET, beamline at ALBA Synchrotron, Cerdanyola del Vallès (Spain). The energy beam was set to 12.4 keV (λ = 0.1 nm), with a channel-cut Si (1 1 1) monochromator and a Rayonix LX255-HS area detector (pixel size of 88 microns). The sample to detector distance was 201.346 mm and the exposition time was 5 s. 2D-GIWAXS patterns were corrected as a function of the components of the scattering vector with a MATLAB script developed by Aurora Nogales and Edgar Gutiérrez.[65]

4.5.7. FET Mobility characterization

Corning glass (low alkali, 1737F) were cleaned according to the same procedure used for preliminary studies on IStBI. Gold contacts were printed on the glass, with horizontal and vertical alignment. Channel lengths: 60µm and 80µm.
P(NDI2OD-T2) solutions in toluene were prepared with a 7gL^{-1} concentration for the polymer batches having M_n of 37.3 kDa and of 26.2 kDa. Films were deposited on top of the patterned glass via off-centred spin coating (polymer thickness ~ 30-40 nm). Polymethyl methacrylate (dielectric) films were then deposited on top via off-centred spin-coating (solution: 80gL^{-1}, thickness ~ 500 nm). Gate contacts were printed on top in PEDOT:PSS. Mobility was extracted from the obtained I-V transfer curves in both linear and saturation regimes.

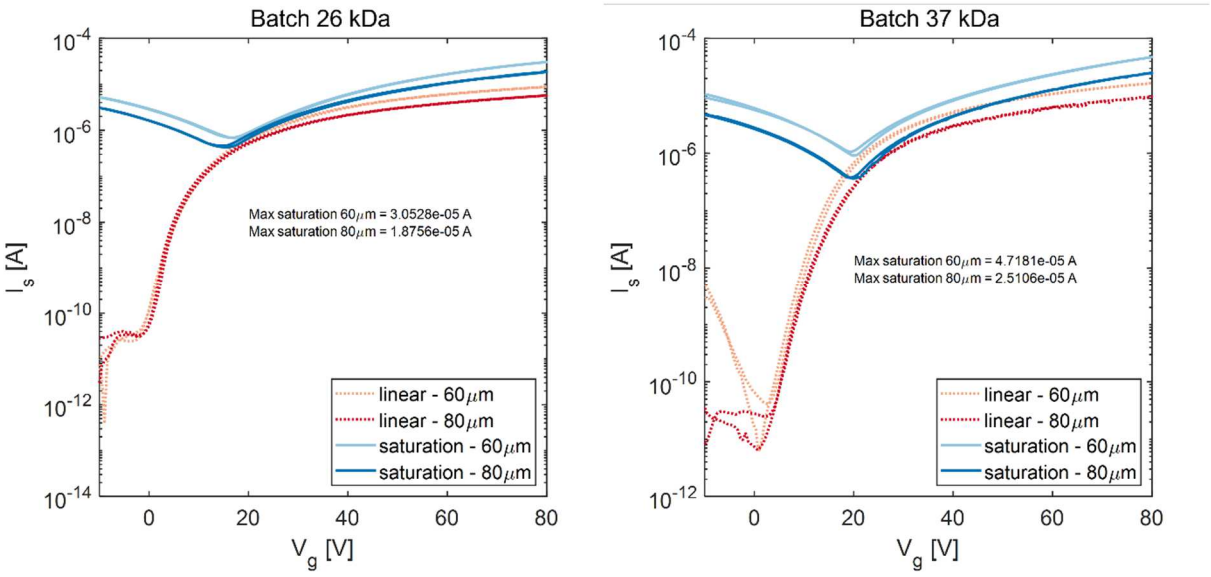

Figure 4.65 Transfer curves for different channel lengths

Batch	M_n 37 kDa		M_n 26 kDa	
Channel length	(60µm)	(80µm)	(60µm)	(80µm)
μ_{Linear} ($cm^2V^{-1}s^{-1}$)	0.17	0.09	0.19	0.07
$\mu_{Saturation}$ ($cm^2V^{-1}s^{-1}$)	0.24	0.15	0.21	0.11

4.5.8. Computational methods

All computational studies were performed by Giuseppe Mattioli (ISM-CNR).

Calculation of dopants energy level was performed via DFT using B3LYP functional.

Simulation of the diffusion of N-DMBI-H derivatives from P(NDI2OD-T2) matrix was performed according to a classic molecular dynamic approach based on the force-field GFN-FF.

Random spheroidal distributions containing 12 dopant molecules and 12 P(NDI2OD-T2) dimers (0.5 ratio between dopant and polymer repeat unit) were created to have the following features:

- the system is globular, so that it is possible to analyse it in a one parameter dependent radial symmetry;
- The system is big enough (> 3 nm in diameter) to have a clear differentiation between cluster surface and bulk;

The cluster geometry was optimized and the evolution of the cluster was monitored in a 3 ns simulation at a fixed temperature of 500 K.

Appendix B – Further studies on $2C_4$-DMBI and C_4C_6-DMBI dopants

In the case of $2C_4$-DMBI, we assessed the doping efficacy also in blends with P(NDI2OD-T2) processed from chlorobenzene. C_4C_6-DMBI (derivative **C9**) performances were characterized in such conditions as well. Proper TGA characterization and electrochemical characterization of C_4C_6-DMBI is still ongoing. However, due to the similar molecular structure, it is reasonable to expect this second dopant to have a redox behaviour and a thermal stability close to that of $2C_4$-DMBI. For these experiments we prepared solutions containing P(NDI2OD-T2) and the dopants at a dopant/repeating unit ratio (χ) between 0.1 and 0.85. After spin coating, we annealed the obtained films at 150°C for two hours. The measured conductivities are here reported in **Figure 4.66**. Values are compared to those of films doped with N-DMBI-H and obtained according to an analogue procedure. In agreement with the results of P(NDI2OD-T2)/$2C_4$-DMBI blends processed from toluene, data show that $2C_4$-DMBI is less performing than N-DMBI-H. Films doped with C_4C_6-DMBI show slightly higher conductivities with respect to $2C_4$-DMBI at low dopant concentration (χ = 0.25), but the measured values are comparable for the two dopants at higher doping levels. With respect to the electrical characterization shown in **section 4.4.4.1**, $2C_4$-DMBI results more performing in films processed from chlorobenzene, allowing to achieve a maximum σ of around 4×10^{-4} Scm^{-1}, four times higher with respect to that of films processed from toluene. P(NDI2OD-T2) polymer solution-state aggregation level decreases going from toluene to chlorobenzene.[66] The reason behind this conductivity enhancement might thus be an improved intermixing between the dopant and the semiconductor induced by the use of this solvent[4]. It is also worth mentioning that, in this case, we performed an annealing treatment at 150°C instead of 180°C. Dopant diffusion in semiconductor matrixes is known to be a thermally activated process.[32,33] Since we demonstrated that the dopant segregation happens mainly during thermal annealing, it is also possible that the lower annealing temperature used mitigated this phenomenon, with consequent higher doping efficiency.

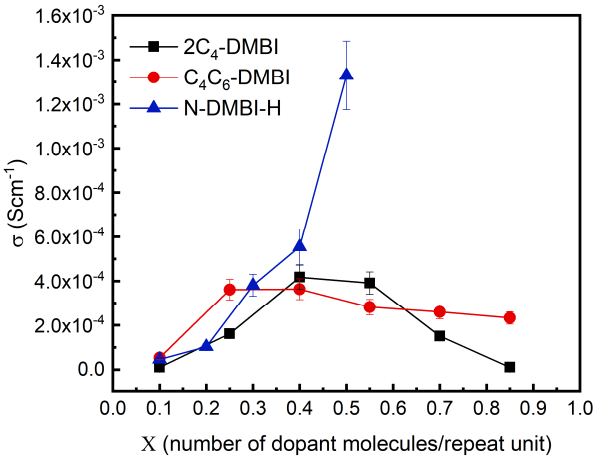

Figure 4.66 Conductivity of P(NDI2OD-T2) films doped with different molar concentration of $2C_4$-DMBI (black), C_4C_6-DMBI (red) and N-DMBI-H (blue).

In Chapter 2, we demonstrated via H_2 detection measurement that N-DMBI-H mediated doping of P(NDI2OD-T2) polymer can be successfully activated in solution via

thermal treatment. In a work by Xiong and coworkers, the authors also showed that the dopant/semiconductor intermixing can be improved via modulation of the polymer solution-state aggregation level via thermal treatment,[4] with a consequent positive effect on doping efficacy. We thus analysed the effect of a thermal pre-treatment of the polymer/dopant solution used for film preparation on the electrical performances of the obtained blends. For the purpose, we prepared P(NDI2OD-T2) films using the same solutions of the experiments shown in **Figure 4.66** but heating them for 30 minutes on a hot-plate at 90°C or at 120°C before spin coating. Films were then annealed at 150°C for 2 hours. The obtained results are reported in **Figure 4.67**.

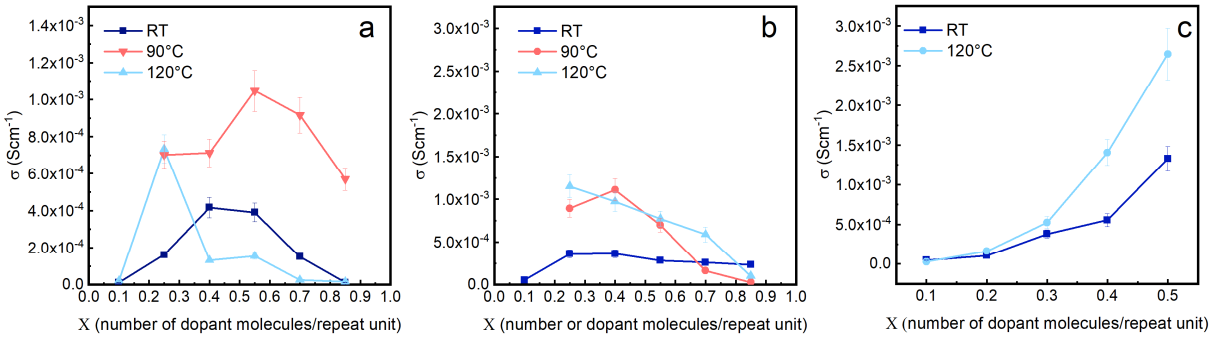

Figure 4.67 Conductivity of P(NDI2OD-T2) films doped with $2C_4$-DMBI (a), C_4C_6-DMBI (b) and N-DMBI-H (c) and spin coated from solutions kept at rt (blue) or heated at 90°C (pink) or 120°C (light blue) for 30 minutes before spin coating.

The solution pre-treatment always leads to a performance improvement. In the case of films doped with $2C_4$-DMBI and C_4C_6-DMBI, the thermal treatment allows to reach conductivities around 1.1×10^{-3} Scm^{-1}, in the same order of magnitude of those obtained for P(NDI2OD-T2) films doped with N-DMBI-H and processed from solutions kept at room temperature. For films doped with $2C_4$-DMBI, a 3-fold conductivity enhancement is reached at a χ of 0.55 by heating the solution at 90°C. Solution treatments at higher temperatures leads instead to a drop in performances. For films doped with C_4C_6-DMBI, the maximum conductivity shifts instead to lower χ as the pre-treatment temperature increase. In section **2.10.5** of chapter 2, we reported the optical characterization of P(NDI2OD-T2) neat polymer solution in chlorobenzene heated at different temperatures. According to such measurements, the polymer is completely disaggregated at temperatures higher than 80°C. Heating the polymer/dopant solution at higher temperature is thus not likely to induce any change in the two species intermixing at the solution level. We thus interpret the changes in conductivity obtained via solution pre-treatment at 120°C as associated to a more efficient activation of the dopant in solution. Previous works report that, if dopant counterion/polarons ion pairs are not soluble in solution, they can precipitate prior to casting, leading to heterogeneous films with poor conductive properties.[67] If this is the case also for our dopant/polymer systems, a possible explanation for the observed conductivity drop in films spin coated from solu-

tions heated at 120°C could thus be a higher microstructural disruption and film inhomogeneity. Further studies will be performed to confirm this hypothesis.

Samples were prepared according to the same procedure reported in Experimental methods section for the preparation of films characterized in preliminary studies of IStBI. Polymer dopants solutions were prepared mixing a P(NDI2OD-T2) 11.5 gL^{-1} solution and dopant solutions with a concentration of 13.4gL^{-1} ($2C_4$-DMBI and C_4C_6-DMBI) or 10gL^{-1} (N-DMBI-H).

Appendix C - Effect of nucleating agents on dopant segregation

The results discussed in Chapter 3 show that N-DMBI-H oxidation impurities can act as nucleating agent for the dopant, mitigating the impact of the phase segregation phenomenon on the doping efficiency. This effect might also explain the fast aggregates formation we observed via AFM on the surface of dried P(NDI2OD-T2) doped films once exposed to air (see section **4.4.4.3**). When the films are exposed to oxygen, dopant oxidation impurities can in fact form on their surface. Since the dopant tends to segregate from the polymeric matrix, the presence of oxidation impurities might accelerate the nucleation of dopant domains on the polymer film surface. To substantiate this hypothesis, we decided to investigate the effect of nucleating agents on the dopant segregation phenomenon via AFM. For the aim, we decided to introduce small amounts of a nucleating agent in P(NDI2OD-T2)/N-DMBI-H blends and to characterize the topography of the obtained films. We selected as nucleating agent the tert-butyl functionalized o-phenylenediamine (oPDA) reported in Chapter 3, since we demonstrated that this compound works as crystallization seed for N-DMBI-H. We then prepared P(NDI2OD-T2) films doped with 40 mol% of N-DMBI-H in the absence and in the presence of oPDA. According to the results reported in Chapter 3, 1 mol% of oPDA with respect to N-DMBI-H should be sufficient to efficiently nucleate the dopant within the polymeric film. We thus added this amount of nucleating agent to the blends.
We firstly analysed the topography of films annealed at 180°C for 2 hours. We carried out this experiment to confirm that the presence of a nucleation seed can reduce the dimension of the dopant segregated domains. The obtained images are reported in **Figure 4.68**. Coarse dopant segregates are inhomogeneously distributed on the surface of film containing only pure N-DMBI-H. Smaller, homogeneously distributed segregates are instead present on the surface of film containing oPDA. The obtained AFM images suggest that, when a nucleating agent is present in the material, the dopant segregated domains form preferentially where the nucleation seeds are localized. In such conditions, thermally activated phase separation happens, but the formed dopant aggregates are numerous, smaller in dimension and, according to the collected AFM images, also more homogeneously distributed. This result corroborates those reported in Chapter 3 and confirms that crystallization seeds can increase the interfacial area between dopant domains and the polymeric matrix, with consequent doping efficiency improvement.

Since N-DMBI-H oxidation impurities work as nucleating agents for the dopant, it is reasonable to expect the same effect also in the presence of these degradation products.

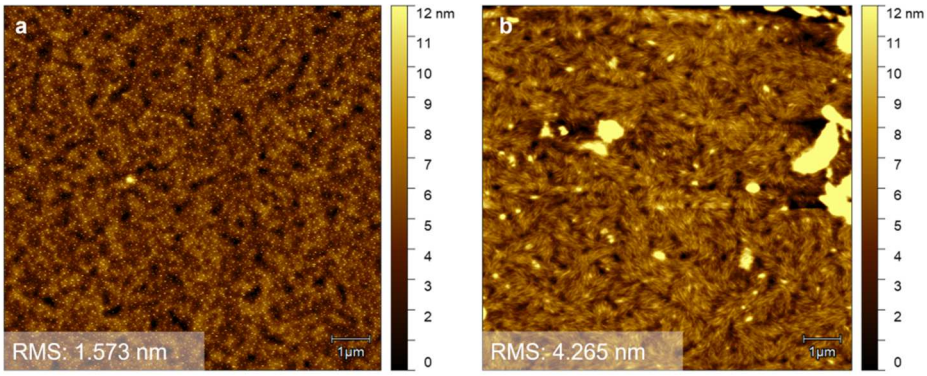

Figure 4.68 10×10 µm AFM images of P(NDI2OD-T2) films doped with 40 mol% of a N-DMBI-H:oPDA (99:1) mixture (a) and 40 mol % of pure N-DMBI-H (b). Films were annealed at 180°C for 2 hours before morphological characterization.

To demonstrate the role of N-DMBI-H oxidation impurities on the observed air promoted segregation, we prepared two more films, with the same features of the annealed ones, and dried them under vacuum. We then exposed the two films in air and monitored the evolution of the film surface in time via AFM. The obtained images are reported in **Figure 4.69**, together with an analysis of the evolution of the surface aggregates diameter and of the AFM images height distribution in time. The obtained images show surface aggregates formation and evolution in both samples. The phenomenon kinetics results faster in the film contaminated by oPDA, as the segregates become bigger in shorter times. This behaviour support our hypothesis on the role of oxidation impurities in accelerating dopant segregation once the film is exposed to air. The dopant segregation process in fact likely happens also at room temperature, due to the metastability of the dopant/semiconductor blend. The phase separation rate will be however slower if compared to a thermally activated process. In films contaminated with oPDA, the formation of dopant segregates on the film surface is accelerated, since a crystallization seed is already present within the material. In samples not containing oPDA, growth of segregates is instead likely seeded by oxidized dopant forming in time during air exposure and subsequently acting as nucleating agent. The oxidized dopant formation however requires some time, which explain the faster segregation in samples already containing a nucleating agent.

Samples were prepared according to the same procedure described in the experimental methods section related to AFM measurements. In the case of films containing oPDA nucleating agent, an oPDA solution in toluene (0.5 gL^{-1}) was prepared and an aliquot of this solution was added to that containing the polymer and 40 mol% of N-DMBI-H to reach an N-DMBI-H: oPDA molar ratio of 99:1.

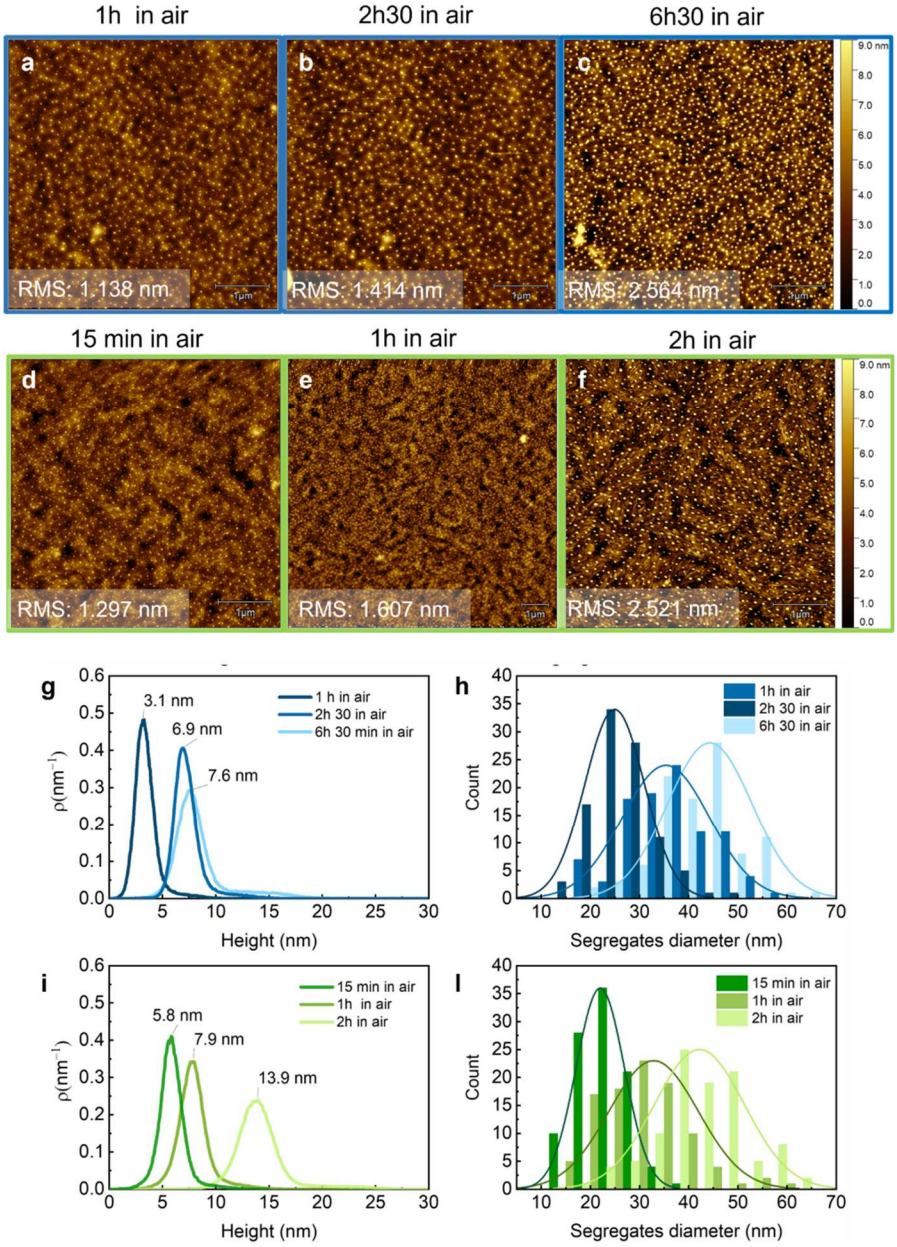

Figure 4.69 AFM images of P(NDI2OD-T2) films doped with 40 mol% of pure N-DMBI-H (blue) and with 40 mol% of a N-DMBI-H:oPDA (99:1) mixture (green) exposed to air for different time. The corresponding AFM image height distribution, expressed as density ρ, and segregate diameter distribution are reported as well. Distribution of segregates diameter dimension was evaluated on a sample of 100 surface aggregates.

4.6. Bibliography

1 J. Liu, L. Qiu, R. Alessandri, X. Qiu, G. Portale, J. J. Dong, W. Talsma, G. Ye, A. A. Sengrian, P. C. T. Souza, M. A. Loi, R. C. Chiechi, S. J. Marrink, J. C. Hummelen and L. J. A. Koster, *Adv. Mater.*, 2018, **30**, 1–9.

2 R. A. Schlitz, F. G. Brunetti, A. M. Glaudell, P. L. Miller, M. A. Brady, C. J. Takacs, C. J. Hawker and M. L. Chabinyc, *Adv. Mater.*, 2014, **26**, 2825–2830.

3 Y. Lu, Z. Di Yu, H. I. Un, Z. F. Yao, H. Y. You, W. Jin, L. Li, Z. Y. Wang, B. W. Dong, S. Barlow, E. Longhi, C. an Di, D. Zhu, J. Y. Wang, C. Silva, S. R. Marder and J. Pei, *Adv. Mater.*, 2021, **33**, 1–7.

4 M. Xiong, X. Yan, J. Li, S. Zhang, Z. Cao, N. Prine, Y. Lu, J. Wang, X. Gu and T. Lei, *Angew. Chemie*, 2021, **60**, 8189–8197.

5 L. Qiu, J. Liu, R. Alessandri, X. Qiu, M. Koopmans, R. W. A. Havenith, S. J. Marrink, R. C. Chiechi, L. J. Anton Koster and J. C. Hummelen, *J. Mater. Chem. A*, 2017, **5**, 21234–21241.

6 Y. Shin, M. Massetti, H. Komber, T. Biskup, D. Nava, G. Lanzani, M. Caironi and M. Sommer, *Adv. Electron. Mater.*, 2018, **4**, 1–8.

7 S. Deng, J. Liu, B. Meng, J. Liu and L. Wang, *ACS Appl. Mater. Interfaces*, 2023, **15**, 45190–45200.

8 J. Liu, L. Qiu, G. Portale, M. Koopmans, G. ten Brink, J. C. Hummelen and L. J. A. Koster, *Adv. Mater.*, 2017, **29**, 1–8.

9 D. Kiefer, A. Giovannitti, H. Sun, T. Biskup, A. Hofmann, M. Koopmans, C. Cendra, S. Weber, L. J. Anton Koster, E. Olsson, J. Rivnay, S. Fabiano, I. McCulloch and C. Müller, *ACS Energy Lett.*, 2018, **3**, 278–285.

10 A. Giovannitti, I. P. Maria, D. Hanifi, M. J. Donahue, D. Bryant, K. J. Barth, B. E. Makdah, A. Savva, D. Moia, M. Zetek, P. R. F. Barnes, O. G. Reid, S. Inal, G. Rumbles, G. G. Malliaras, J. Nelson, J. Rivnay and I. McCulloch, *Chem. Mater.*, 2018, **30**, 2945–2953.

11 R. M. Kluge, N. Saxena, W. Chen, V. Körstgens, M. Schwartzkopf, Q. Zhong, S. V. Roth and P. Müller-Buschbaum, *Adv. Funct. Mater.*, 2020, **30**, 1–9.

12 B. Saglio, M. Mura, M. Massetti, F. Scuratti, D. Beretta, X. Jiao, C. R. McNeill, M. Sommer, A. Famulari, G. Lanzani, M. Caironi and C. Bertarelli, *J. Mater. Chem. A*, 2018, **6**, 15294–15302.

13 C. LI, W. Wang, C. Zhan, Q. Zhou, D. Dong and S. Xiao, *J. Mater. Chem. C*, 2023, **11**, 15599–15607.

14 J. Han, A. Chiu, C. Ganley, P. McGuiggan, S. M. Thon, P. Clancy and H. E. Katz, *Angew. Chemie - Int. Ed.*, 2021, **60**, 27212–27219.

15 S. Riera-Galindo, A. Orbelli Biroli, A. Forni, Y. Puttisong, F. Tessore, M. Pizzotti, E. Pavlopoulou, E. Solano, S. Wang, G. Wang, T. P. Ruoko, W. M. Chen, M. Kemerink, M. Berggren, G. Di Carlo and S. Fabiano, *ACS Appl. Mater. Interfaces*, 2019, **11**, 37981–37990.

16 B. D. Naab, S. Guo, S. Olthof, E. G. B. Evans, P. Wei, G. L. Millhauser, A. Kahn, S. Barlow, S. R. Marder and Z. Bao, *J. Am. Chem. Soc.*, 2013, **135**, 15018–15025.

17 S. Bonacci, G. Iriti, S. Mancuso, P. Novelli, R. Paonessa, S. Tallarico and M. Nardi, *Catalysts*, 2020, **10**, 1–12.

18 O. Bardagot, C. Aumaître, A. Monmagnon, J. Pécaut, P. A. Bayle and R. Demadrille, *Appl. Phys. Lett.*, 2021, **118**, 1–6.

19 PCT/GB2016/053967, 2017, 1–62.

20 P. Gogoi, P. Hazarika and D. Konwar, *J. Org. Chem.*, 2005, **70**, 1934–1936.

21 R. C. Elderfield and V. B. Meyer, *J. Am. Chem. Soc.*, 1954, **76**, 1887–1891.

22 V. Hrobáriková, P. Hrobárik, P. Gajdoš, I. Fitilis, M. Fakis, P. Persephonis and P. Zahradník, *J. Org. Chem.*, 2010, **75**, 3053–3068.

23 A. Mederos, S. Dominguez, R. Hernandez-Molina, J. Sanchiz and F. Brito, *Coord. Chem. Rev.*, 1999, **193**–**195**, 913–939.

24 A. K. Sengupta, Y. Zhu and D. Hauze, *Environ. Sci. Technol.*, 1991, **25**, 481–488.

25 D. Yang, D. Fokas, J. Li, L. Yu and C. M. Baldino, *Synthesis (Stuttg).*, 2005, 47–56.

26 S. Oda, H. Shimizu, Y. Aoyama, T. Ueki, S. Shimizu, H. Osato and Y. Takeuchi, *Org. Process Res. Dev.*, 2012, **16**, 96–101.

27 E. Ghiglietti, S. Podapangi, S. Mecca, L. Mezzomo, R. Ruffo, M. Sassi, S. Mattiello, T. M. Brown and L. Beverina, *Energy Adv.*, 2022, 398–401.

28 C. Dardonville, M. L. Jimeno, I. Alkorta and J. Elguero, *Org. Biomol. Chem.*, 2004, **2**, 1587–1591.

29 D. Nava, Y. Shin, M. Massetti, X. Jiao, T. Biskup, M. S. Jagadeesh, A. Calloni, L. Duo, G. Lanzani, C. R. Mcneill, M. Sommer and M. Caironi, *ACS Appl. Energy Mater.*, 2018, **1**, 4626–4634.

30 H. Guo, C. Y. Yang, X. Zhang, A. Motta, K. Feng, Y. Xia, Y. Shi, Z. Wu, K. Yang, J. Chen, Q. Liao, Y. Tang, H. Sun, H. Y. Woo, S. Fabiano, A. Facchetti and X. Guo, *Nature*, 2021, **599**, 67–73.

31 L. Tang and C. R. McNeill, *Macromolecules*, 2022, **55**, 7273–7283.

32 S. Wang, T. P. Ruoko, G. Wang, S. Riera-Galindo, S. Hultmark, Y. Puttisong,

F. Moro, H. Yan, W. M. Chen, M. Berggren, C. Müller and S. Fabiano, *ACS Appl. Mater. Interfaces*, 2020, **12**, 53003–53011.

33 J. Li, C. W. Rochester, I. E. Jacobs, S. Friedrich, P. Stroeve, M. Riede and A. J. Moule, *ACS Appl. Mater. Interfaces*, 2015, **7**, 28420–28428.

34 G. C. Welch and G. C. Bazan, *J. Am. Chem. Soc.*, 2011, **133**, 4632–4644.

35 B. D. Naab, S. Zhang, K. Vandewal, A. Salleo, S. Barlow, S. R. Marder and Z. Bao, *Adv. Mater.*, 2014, **26**, 4268–4272.

36 S. Griggs, A. Marks, H. Bristow and I. McCulloch, *J. Mater. Chem. C*, 2021, **9**, 8099–8128.

37 M. M. Nahid, R. Matsidik, A. Welford, E. Gann, L. Thomsen, M. Sommer and C. R. McNeill, *Adv. Funct. Mater.*, 2017, **27**, 1–11.

38 D. Trefz, A. Ruff, R. Tkachov, M. Wieland, M. Goll, A. Kiriy and S. Ludwigs, *J. Phys. Chem. C*, 2015, **119**, 22760–22771.

39 J. Liu, Y. Shi, J. Dong, M. I. Nugraha, X. Qiu, M. Su, R. C. Chiechi, D. Baran, G. Portale, X. Guo and L. J. A. Koster, *ACS Energy Lett.*, 2019, **4**, 1556–1564.

40 A. Luzio, L. Criante, V. D'Innocenzo and M. Caironi, *Sci. Rep.*, 2013, **3**, 1–6.

41 O. Bardagot, Y. Kervella, A. A. Medjahed, S. Pouget, T. N. Domschke, A. Carella, C. Aumaître, P. Lévêque and R. Demadrille, *J. Mater. Chem. C*, 2023, 14108–14118.

42 I. E. Jacobs and A. J. Moulé, *Adv. Mater.*, 2017, **29**, 1–39.

43 V. Vijayakumar, P. Durand, H. Zeng, V. Untilova, L. Herrmann, A. Patrick, L. Nicolas and M. Brinkmann, *J. Mater. Chem. C*, 2020, **8**, 16470–16482.

44 M. Kang, J. S. Yeo, W. T. Park, N. K. Kim, D. H. Lim, H. Hwang, K. J. Baeg, Y. Y. Noh and D. Y. Kim, *Adv. Funct. Mater.*, 2016, **26**, 8527–8536.

45 R. Steyrleuthner, R. Di Pietro, B. A. Collins, F. Polzer, S. Himmelberger, M. Schubert, Z. Chen, S. Zhang, A. Salleo, H. Ade, A. Facchetti and D. Neher, *J. Am. Chem. Soc.*, 2014, **136**, 4245–4256.

46 J. Rivnay, R. Steyrleuthner, L. H. Jimison, A. Casadei, Z. Chen, M. F. Toney, A. Facchetti, D. Neher and A. Salleo, *Macromolecules*, 2011, **44**, 5246–5255.

47 S. Wang, S. Fabiano, S. Himmelberger, S. Puzinas, X. Crispin, A. Salleo and M. Berggren, *Proc. Natl. Acad. Sci. U. S. A.*, 2015, **112**, 10599–10604.

48 S. Spicher and S. Grimme, *Angew. Chemie - Int. Ed.*, 2020, **59**, 15665–15673.

49 C. Xu and D. Wang, *J. Mater. Chem. A*, 2023, 15416–15425.

50 N. Pataki, P. Rossi and M. Caironi, *Appl. Phys. Lett.*, 2022, **121**, 1–12.

51 K. Shi, F. Zhang, C. A. Di, T. W. Yan, Y. Zou, X. Zhou, D. Zhu, J. Y. Wang

and J. Pei, *J. Am. Chem. Soc.*, 2015, **137**, 6979–6982.

52 D. Beretta, P. Bruno, G. Lanzani and M. Caironi, *Rev. Sci. Instrum.*, 2015, **86**, 1–9.

53 M. Massetti, F. Jiao, A. J. Ferguson, D. Zhao, K. Wijeratne, A. Würger, J. L. Blackburn, X. Crispin and S. Fabiano, *Chem. Rev.*, 2021, **121**, 12465–12547.

54 G. Zuo, X. Liu, M. Fahlman and M. Kemerink, *Adv. Funct. Mater.*, 2018, **28**, 1–7.

55 M. Massetti, S. Bonfadini, D. Nava, M. Butti, L. Criante, G. Lanzani, L. Qiu, J. C. Hummelen, J. Liu, L. J. A. Koster and M. Caironi, *Nano Energy*, 2020, **75**, 104983.

56 K. Feng, W. Yang, S. Y. Jeong, S. Ma, Y. Li, J. Wang, Y. Wang, H. Y. Woo, P. Kwok, L. Chan, G. Wang and X. Guo, 2023, **2210847**, 1–9.

57 S. Wang, H. Sun, U. Ail, M. Vagin, P. O. Å. Persson, J. W. Andreasen, W. Thiel, M. Berggren, X. Crispin, D. Fazzi and S. Fabiano, 2016, 10764–10771.

58 S. Mattiello, G. Lucarelli, A. Calascibetta, L. Polastri, E. Ghiglietti, S. K. Podapangi, T. M. Brown, M. Sassi and L. Beverina, *ACS Sustain. Chem. Eng.*, 2022, **10**, 4750–4757.

59 G. M. Roberts, P. J. Pierce and L. K. Woo, *Organometallics*, 2013, **32**, 2033–2036.

60 S. H. Hausner, C. A. F. Striley, J. A. Krause-Bauer and H. Zimmer, *J. Org. Chem.*, 2005, **70**, 5804–5817.

61 H. Rao, H. Fu, Y. Jiang and Y. Zhao, *J. Org. Chem.*, 2005, **70**, 8107–8109.

62 T. H. Wang, R. Ambre, Q. Wang, W. C. Lee, P. C. Wang, Y. Liu, L. Zhao and T. G. Ong, *ACS Catal.*, 2018, **8**, 11368–11376.

63 Q. Zhou, S. Liu, M. Ma, H. Z. Cui, X. Hong, S. Huang, J. F. Zhang and X. F. Hou, *Synth.*, 2018, **50**, 1315–1322.

64 R. Matsidik, H. Komber, A. Luzio, M. Caironi and M. Sommer, *J. Am. Chem. Soc.*, 2015, **137**, 6705–6711.

65 A. Nogales and E. Gutiérrez, 2019, MathWorks File Exchange.

66 R. Steyrleuthner, M. Schubert, I. Howard, B. Klaumünzer, K. Schilling, Z. Chen, P. Saalfrank, F. Laquai, A. Facchetti and D. Neher, *J. Am. Chem. Soc.*, 2012, **134**, 18303–18317.

67 A. Dai, Y. Zhou, A. L. Shu, S. K. Mohapatra, H. Wang, C. Fuentes-Hernandez, Y. Zhang, S. Barlow, Y. L. Loo, S. R. Marder, B. Kippelen and A. Kahn, *Adv. Funct. Mater.*, 2014, **24**, 2197–2204.

68 L. L. Spangler, J. M. Torkelson and J. S. Royal, *Polym. Eng. Sci.*, 1990, **30**,

644–653.

69 P. Rossi, F. Pallini, G. Coco, S. Mattiello, W. L. Tan, L. Mezzomo, M. Cassinelli, G. Lanzani, C. R. McNeill, L. Beverina and M. Caironi, *Adv. Mater. Interfaces*, 2023, **10**, 1–9.

Conclusions

This work provides new insights on both the doping mechanism of N-DMBI-H like n-type dopants and the nature of the factors determining their doping efficiency when introduced in a semiconductor matrix.

Concerning N-DMBI-H promoted doping, our study presents the first experimental demonstration of H_2 evolution during uncatalyzed doping processes mediated by this compound and provides insight on the reaction mechanism and on the parameters impacting its outcome. Along with this result, it also introduces the innovative use of molecular H_2 detection techniques as direct tool to characterize organic semiconductor doping mediated by hydrogen atom transfers. The method proved to be general, allowing to extend the same results obtained for N-DMBI-H also to the p-type dopant trispentafluorophenylborane (BCF).

Our characterization of solution processed organic semiconductor/dopant mixtures instead deepens the correlation between doping performances and the blends microstructure. It indeed shows that these systems are metastable, confirming previous observations on the N-DMBI-H tendency to segregate from the semiconductor matrix and revealing that this phase separation is accelerated by the thermal treatments required to activate the dopant. Along with these insights, the work presents then two effective approaches to control the blend microstructure and its impact on the doping efficiency. One is the addition in the semiconductor/dopant mixture of a third element acting as nucleating agent for the dopant. This innovative strategy allows to tune the extension of the interfacial area between the N-DMBI-H segregated domains and the semiconductor matrix, consequently increasing the doping efficiency. The other is the tailored functionalization of the benzimidazoline structure. This second approach can serve to increase the dopant affinity for the host and consequently reduce the rate of the blend components phase segregation, thus improving their performances. Within the development of the latter approach, the thesis work also presents a new and promising iminostilbene functionalized N-DMBI-H derivative and provides new synthetic tools and design guidelines for the synthesis of more performing benzimidazoline based n-type dopants.

On the overall, we believe that this research represents a significant advancement in the understanding and controlling of n-type doping processes mediated by benzimidazoline derivatives and that it might have a meaningful impact in the development of

more performing n-type organic materials. Moreover, we suggest that some of the developed strategies could potentially be extended to the study of other semiconductor/dopant systems, with a wider impact in the field of organic semiconductors doping.

List of acronyms

AFM Atomic Force Microscopy

B3LYP Becke, 3-parameter, Lee-Yang-Parr

BHJ Bulk-Heterojunction

CB Conduction band

CoM Centre of Mass

CTC Charge Transfer Complex

CV Cyclic Voltammetry

DFT Density Functional theory

DPV Differential Pulse Voltammetry

DSC Differential Scanning Calorimetry

EA Electron Affinity

EPR Electron Paramagnetic Resonance

ET Electron Transfer

ETL Electron Transport Layer

FMO Frontier Molecular Orbital

GC Gas Chromatography

GC-MS Gas Chromatography-Mass Spectrometry

GFN-FF Geometries-Frequencies-Non-Covalent interaction Force-Field

GIWAXS Grazing-Incidence Wide-Angle X-Ray Scattering

GPC Gel Permeation Chromatography

HOMO Highest Occupied Molecular Orbital

HTL Hole Transport Layer

ICP-OES Inductively Coupled Plasma – Optical Emission Spectroscopy

IE Ionization Energy

IoT Internet of Things

LUMO Lowest Unoccupied Molecular Orbital

MW Microwave

NIR Near Infrared

NMR Nuclear Magnetic Resonance

OFET Organic Field-Effect Transistors

OLED Organic Light Emitting Diode

OPV Organic Photovoltaic

OSC Organic Semiconductor

OTEG Organic Thermoelectric Generator

PDI Polydispersity Index

PF Power Factor

RGA-MS Residual Gas Analysis-Mass Spectrometry

RMS Root Mean Square

RT Room Temperature

SOMO Singly occupied Molecular Orbital

TCD Thermal Conductivity Detector

TGA Thermogravimetric Analysis

TLC Thin Layer Chromatography

UV Ultraviolet

VB Valence Band

XRD X-Ray Diffraction

List of chemicals names

AcOEt Ethyl Acetate

AgOtf Silver triflate

BBL Poly(benzoimidazobenzophenanthroline)

BCF Trispentafluorophenylborane

BDOPV Benzodifurandione oligo(p-phenylene vinylene)

BDPPV Benzodifurandione- Poly(p-phenylene vinylene)

BEDT-TTF Bis(ethylenedithio)tetrathiafulvalene

BTA tris-tert-butyl-1,3,5-benzenetrisamide

DCM Dichloromethane

DMAB 4-(dimethylamino)-benzaldehyde

DMSO Dimethyl sulfoxide

DBuBI N,N-Dibutyl-4-(1,3-dimethyl-2,3-dihydro-1H-benzo[d] imidazol-2-yl)aniline

DEtBI 4-(1,3-Dimethyl-2,3-dihydro-1H-benzo[d]imidazol-2-yl)-N,N-diethylaniline

DiBuBI 4-(1,3-Dimethyl-2,3-dihydro-1H-benzo[d]imidazol-2-yl)-N,N-diisobutylaniline (DiBuBI)

DiPrBI 4-(1,3-Dimethyl-2,3-dihydro-1H-benzo[d]imidazol-2-yl)-N,N-diisopropylaniline (DiPrBI)

DPBI 4-(1,3-dime- thyl-2,3-dihydro-1H-benzimidazol-2-yl)-N,N-diphenylaniline

DPrBI 4-(1,3-Dimethyl-2,3-dihydro-1H-benzo[d]imidazol-2-yl)-N,N-dipropylaniline

EtOH Ethanol

Et_2O Diethyl ether

Fc Ferrocene

F4-TCNQ 2,3,5,6-tetrafluoro-tetracyanoquinodimethane

F6-TCNNQ 1,3,4,5,7,8-hexafluorotetracyanonaphthoquinodimethane

JLBI-H 9-(1,3-dimethyl-2,3-dihydro-1H-benzoimidazol-2-yl)-julolidine

LCV *Leuco* Crystal Violet

MeCN Acetonitrile

MeOtf Methyl trifluoromethanesulfonate

Mo(tfd)$_3$ Molybdenum tris(1,2-bis(trifluoromethyl)ethane-1,2-dithiolene)

N-DMBI-H 4-(1,3-Dimethyl-2,3-dihydro-1H-benzimidazol-2-yl)-N,N-dimethylaniline

NDI Napthalenediimide

oDCB o-dichlorobenzene

oPDA o-phenylendiamine

P3HT Poly(3-hexylthiophene-2,5-diyil)

PBFDO Poly(benzodifurandione)

PBTTT Poly(2,5-bis(3-alkylthiophen-2-yl)thieno[3,2-b]thiophene)

PCBM Phenyl-C61-butyric acid methyl ester

PCPDTBT Poly[2,6-(4,4-bis(2-hexadecyl)-4Hcyclopenta[2,1-b;3,4-b′]dithiophene)-alt-4,7(2,1,3benzothiadiazole)]

Pd(OAc)$_2$ Palladium (II) Acetate

PEDOT:PSS Poly(3,4-ethylenedioxythiophene) polystyrene sulfonate

PEG Polyethylene glycol

P(NDI2OD-T2) Poly{[N,N′-bis(2-octyldodecyl)-naphthalene-1,4,5,8-bis(dicarbo-ximide)-2,6-diyl]-alt-5,5′-(2,2′-bithiophene)

PNDTI-BBT-DT Poly-naphtho[2,3-b:6,7-b]dithiophenediimide benzobisthiadiazole-2-decyltetradecyl

PTFE Polytetrafluoroethylene

TAM Triaminomethane

TDAE Tetrakis (dimethylamino)ethylene

TEA Triethylamine

TEOA Triethanolamine

TP-DMBI 1,3-dimethyl-2-(3,4,5-trimethoxyphenyl)-2,3-dihydro-1H-benzo[d]imidazle

TTN Tetrathianaphthacene

XPhos [2-Dicyclohexylphosphino-2′,4′,6′-triisopropylbiphenyl]